Nuclear data for particle therapy

Lévana Gesson

UNIVERSITÉ DE STRASBOURG

École doctorale
Physique, chimie-physique
ED 182
Université de Strasbourg

ÉCOLE DOCTORALE de Physique et Chimie Physique

Institut Pluridisciplinaire Hubert Curien (IPHC), UMR 7178

THÈSE présentée par :

Lévana GESSON

soutenue le : **25 septembre 2024**

pour obtenir le grade de : **Docteur de l'université de Strasbourg**

Discipline/ Spécialité : Physique nucléaire appliquée

Données nucléaires pour la hadronthérapie

Aperçus expérimentaux et résultats de simulation

THÈSE dirigée par :

Mme. Marie VANSTALLE	Institut Pluridisciplinaire Hubert Curien (IPHC)
M. Ulrich WEBER	GSI Helmholtzzentrum für Schwerionenforschung GmbH

RAPPORTEURS :

Mme. Lydia MAIGNE	Laboratoire de Physique de Clermont
M. Vicenzo PATERA	Instituto Nazionale di Fisica Nuclear (INFN)

AUTRES MEMBRES DU JURY :

Mme. Michela MARAFINI	Instituto Nazionale di Fisica Nuclear (INFN)
M. Sébatien INCERTI	CNRS – IN2P3
Mme. Isabelle RIPP-BAUDOT	Institut Pluridisciplinaire Hubert Curien

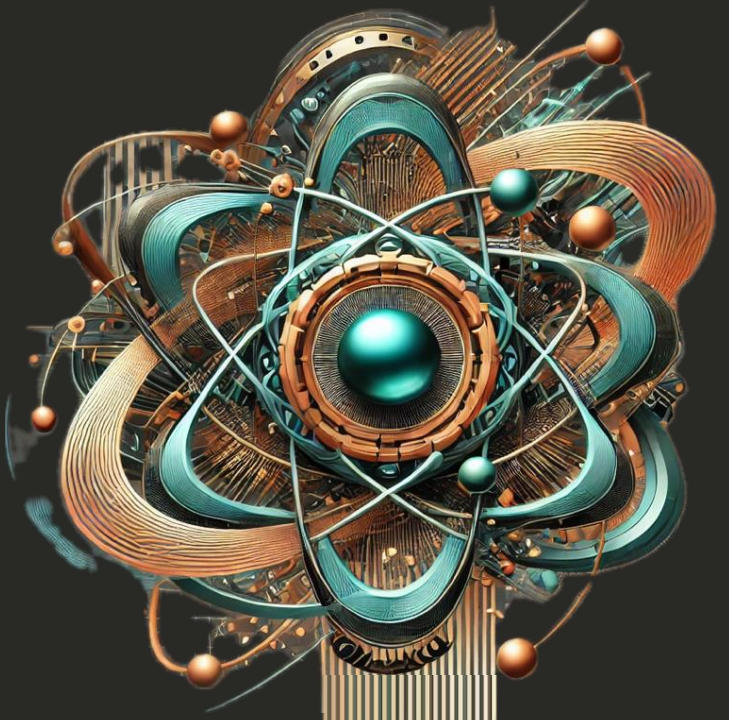

Nuclear data for particle therapy

Experimental insights and simulation outcomes

Lévana GESSON

PhD directed by Marie VANSTALLE and Ulrich WEBER

Referees:

Lydia MAIGNE

Vicenzo PATERA

Other jury members:

Michela MARAFINI

Sébastien INCERTI

Isabelle RIPP-BAUDOT

Remerciements

Nous y voilà ! La fin de ces trois années de doctorat, qui marquent aussi l'aboutissement de huit longues années d'études. Il est temps pour moi de remercier toutes les personnes qui m'ont accompagnée et, d'une manière ou d'une autre, ont contribué à ce travail et à la personne que je suis aujourd'hui.

Je souhaite d'abord remercier les membres du jury, Isabelle Ripp-Baudot, Sébastien Incerti, Michela Marafini, Vicenzo Patera, Lydia Maigne, pour avoir pris le temps de plonger dans cette thèse et pour votre participation à ma soutenance. Merci pour les questions et discussions qui ont suivies et pour la profonde bienveillance que chacun d'entre vous a eue envers moi.

Je tiens à te remercier Uli pour ton accueil au GSI et ton intérêt pour les pâtisseries françaises. Merci aussi à toutes les personnes du GSI, avec qui j'ai partagé sept mois de travail intense, de belles discussions, et quelques moments de stress inoubliables (mais on ne va retenir que le positif, promis).

Je ne peux pas continuer ces remerciements sans parler, bien sûr, de Marie, qui m'a encadrée pendant ces trois ans et avec qui j'ai eu la chance de partager bien plus qu'une relation de collègues, une relation d'amies. Ta bonne humeur, ton accueil chaleureux et ton soutien m'ont énormément aidée à prendre mes marques dans le monde de la recherche. Nos fous rires permanents qui résonnent dans les couloirs, nos discussions à rallonges et le fait qu'on se comprenne souvent sans même parler montrent à quel point on est sur la même longueur d'onde. Ta présence m'a été précieuse, surtout dans les moments difficiles, et j'espère que tu sais à quel point tu comptes pour moi.

Je ne peux pas oublier Christian, qui a lancé tout ça en m'accueillant en stage de M2. Grâce à toi, j'ai découvert ce projet de thèse, mais surtout, tu m'as redonné confiance en moi à un moment où j'en avais vraiment besoin. Ton soutien constant et ta bienveillance m'ont vraiment portée tout au long du chemin.

Je tiens aussi à remercier tous mes collègues avec qui j'ai partagé ces trois années, et des centaines de pauses café. Dès mon arrivée, des personnes d'autres équipes m'ont accueillie avec une chaleur et une amitié qui m'ont beaucoup touchée.

Dans l'équipe Radiochimie, j'ai trouvé des collègues qui sont vite devenus des amis. Sylvia, avec ta bienveillance infinie, ton aide précieuse, tes délicieux gâteaux et ton côté maternel. Quentin, tu resteras célèbre pour tes bourdes en expérience – « press to exit », ça te rappelle quelque chose, non ? - Antoine, toujours de bonne humeur, tu as su apporter de la légèreté et de l'amitié quand il le fallait. Lucie et tes hobbies originaux, et Mehdi, même si tu a manqué ma soutenance (pas de souci, le karma s'en est déjà chargé), tu m'as toujours soutenue comme personne.

L'équipe du Ramcher mérite aussi quelques mots. Addil, avec tes références parfois un peu trop bizarres et dérangeantes mais tellement drôles. Eric, avec tes blagues douteuses et ton Muppet Show avec Christian. Nicolas, toujours chaleureux et accueillant, Florent – oui, même avec ta BMW (« Bonjour, bonne soirée ! ») - , Micky et ta joie de vivre inébranlable, et enfin, Alexandre, toi qui ne manque jamais une occasion de plonger. Merci à vous tous pour ces moments inoubliables.

Et bien sûr, un grand merci à l'équipe DeSIs. Vous m'avez accueillie à bras ouverts et fait une vraie place parmi vous. Un merci à Séverine, pour ton aide précieuse et sa

chaleur humaine. Nicolas, malgré tes absences, tes retards, et tes anecdotes d'enfance plutôt discutables (« mais tout le monde fait ça, non ? »), tu as su apporter ta bonne humeur et ton humour au quotidien. Un remerciement spécial à Jonathan, alias « Dieu », pour tes présentations surprenantes, ton humour incroyable et ton infaillible motivation à ne jamais rater une opportunité de nourriture gratuite.

Enfin, un grand merci à tous les stagiaires qui ont croisé ma route, chacun apportant sa touche personnelle. Samuel, avec ton perfectionnisme en graphisme ; Carlotta, pour ta bonne humeur et ta chaleur ; Clara, avec tes imitations toujours bluffantes ; et Claire, avec ton franc-parler et avec qui les fous rires étaient nombreux. Merci aussi à Baptiste, vraie encyclopédie vivante sur les sujets les plus improbables (même si tu n'as pas daigné venir à ma soutenance), et bien sûr à Julie, dont la personnalité pétillante, l'intelligence et l'humour ont fait de toi un membre à part entière de notre groupe.

Je tiens maintenant à remercier sincèrement toutes les personnes rencontrées en conférence, qui ont transformé ces moments en souvenirs inoubliables. Un merci tout particulier à Gabriele, toujours de bonne humeur et toujours présent pour proposer ton aide. Sans oublier Jacinta, avec qui j'ai partagé des moments précieux à Miami et Singapour. Et enfin, merci à Nadine, toujours adorable, toi qui a fait de tes contacts une vraie carte VIP pour moi en conférence. Grâce à toi, ces événements ont pris une toute autre dimension !

Je voudrais adresser un remerciement tout spécial aux amis incroyables rencontrés à l'ESA-FAIR Summer School. Merci à Edward, Francesca, Laura, Mona, Olivia, Augusto, et Silvana pour toutes les aventures et les souvenirs inoubliables partagés lors de nos voyages. Un merci particulier à Esther et Vasily, avec qui j'ai ressenti une connexion immédiate et profonde, comme si on se connaissait depuis toujours.

En ce qui concerne les amitiés forgées pendant ces huit années d'études, je ne peux pas passer sous silence Paul et Hugo. Merci pour cette amitié sans faille depuis la Licence, votre bienveillance, nos discussions sans fin (oui, on a refait le monde plusieurs fois) et nos heures à enchaîner jeux de société et bières. Merci aussi à Clément, Clara, Aurélien et Boris, pour ces deux années de master où on a (contre toute attente) survécu ensemble.

Un grand merci aussi à mes amis rencontrés en doctorat, au volley ou ailleurs, notamment Wassim et PA (Docteur, Docteur), pour m'avoir accueillie dans vos vies et pour tous ces moments partagés ensemble. Vous êtes devenus presque plus que des collègues.

Enfin, le moment est venu de remercier ma famille, sans qui rien de tout cela n'aurait été possible. Merci pour votre soutien, votre amour, et cette éducation qui m'a donnée les clés pour affronter la vie (et les soutenances de thèse, ce qui est presque la même chose).

Maman, Papa, vous avez fait de moi une personne curieuse et vous avez toujours cru en moi, même quand j'avais du mal à le faire moi-même. Merci pour tout, vraiment. Merci à Iscia et Maéva, mes sœurs, vous êtes mes piliers sur qui je peux toujours compter. Aux grands-parents, cousins, cousines, tontons, tatas : votre présence, vos encouragements, m'ont donnée l'énergie et la confiance pour aller jusqu'au bout de cette aventure.

Je voudrais finir mes remerciements par Thibaut. Tu as été à mes côtés chaque jour pendant ces huit années. On a partagé notre amour de la physique, notre passion pour l'Univers, avec des discussions infinies sur les tous les sujets possibles. Les mots ne sauraient décrire la relation que l'on s'est construite tous les deux. On a su affronter toutes les épreuves ensemble, et notre relation en est devenue indestructible. Cette thèse, tu le sais, c'est la nôtre. Je veux te remercier pour tout ce que tu as fait pour moi, pour

tout ce que tu as fait de moi. Je ne serais pas ici sans toi.

À vous tous, un immense merci pour avoir fait partie de cette aventure. Sans vous, rien n'aurait été pareil, ni aussi mémorable. Merci d'avoir fait de ce moment le deuxième meilleur moment de ma vie (le premier restant bien sûr le concert de Taylor Swift).

Contents

List of Figures

List of Tables

Introduction

Cancer remains one of the leading causes of morbidity and mortality worldwide, presenting complex biological mechanisms and diverse clinical manifestations that pose significant treatment challenges. Traditional cancer treatments, such as surgery, chemotherapy, and conventional radiotherapy (X-rays), often face limitations in terms of precision and side effects. Therefore, innovative approaches like particle therapy have developed due to their enhanced targeting capabilities and reduced damage to healthy tissues, improving clinical outcomes and the quality of life for cancer patients.

Particle therapy, which includes both heavy ion and proton therapy, represents a significant advancement in the precise targeting of tumors while minimizing damage to surrounding healthy tissues. A critical component of improving particle therapy lies in understanding and leveraging the secondary particles produced during treatment. These secondary particles, generated from the fragmentation of the primary ion beam upon interaction with the target tissue, play a role in the overall dose distribution and, consequently, in the effectiveness and safety of the therapy. Therefore, accurate quantification and utilization of these secondary particles are essential for optimizing therapeutic outcomes.

The primary objective of this PhD thesis is to explore the secondary charged particles generated in heavy ion therapy, with a focus on their impact on dose distribution and treatment accuracy. Specifically, it aims to refine the detection and simulation of secondary particles, which arise from ion fragmentation. These particles influence the overall dose delivered and the biological effectiveness of the treatment, necessitating improved accuracy in simulations and experimental data.

The CLINM project (Cross-sections of Light Ion and Neutron Measurements), in which this thesis plays a pivotal role, seeks to address this challenge by investigating the complex interactions between ionizing radiation and biological systems. This interdisciplinary project, funded by the ANR (Agence Nationale de la Recherche), combines studies in physics and chemistry, including local collaboration with the radiochemistry team at IPHC, and an international partnership with CNAO therapy center in Italy. The CLINM project aims to improve the precision of Monte Carlo simulations and experimental measurements related to secondary particle behavior.

To achieve this, the integration of experimental data, gathered through advanced detectors such as scintillators and semiconductors, with Monte Carlo simulations. One key aspect of this work includes benchmarking simulation tools like Geant4 against exper-

imental data, and improving them through deep learning algorithms like DINo (Deep learning Intelligence for nuclear reactiOns) to enhance their predictive accuracy, particularly in clinical settings.

In addition to contributing to the CLINM project, this thesis explores the potential for novel detection technologies, such as CMOS tracking device, to enhance precision in lung cancer therapy, particularly in cases complicated by respiratory motion, aligning with the project's goal.

Chapter 1 provides an extensive overview of the importance and role of secondary particles in heavy ion therapy. It introduces the fundamental interactions between radiation and matter, detailing the production and behavior of secondary particles within tissues, which is crucial to understanding their impact on dose distribution and treatment accuracy. The chapter delves into the physics of ion-tissue interactions, the types of secondary particles produced, and their energy deposition patterns, which are critical for precise dose calculations.

To investigate the secondary charged particles produced during treatment, a comprehensive approach that combines detection and simulation of the involved physical processes is essential. Chapter 2 delves into the methodologies for detecting and identifying these particles, exploring the use of scintillator detectors, semiconductor detectors, and Geant4 simulation tools. The chapter outlines the characteristics of each detector type, their respective advantages, and limitations in the context of heavy ion therapy. It also discusses the role of Monte Carlo simulations in modeling the complex interactions and validating experimental data.

Focusing specifically on scintillator detectors, Chapter 3 presents detailed characterization studies and calibrations with heavy ions used in therapy. The chapter discusses the comparative advantages of plastic scintillators and $CeBr_3$ crystals, particularly in terms of detection efficiency, energy resolution, and temporal response. The calibration procedures and experimental results provide insights into optimizing detector performance for accurate secondary particle measurement in the particle therapy context.

The CLINM project aims to understand the complex interactions between ionizing radiation and biological systems thanks to an interdisciplinary project combining physics and chemical analysis. Chapter 4 will therefore present the CLINM project from the physical perspective, discussing the benchmarking of Monte Carlo simulations with experimental data to address potential inaccuracies and enhance the overall efficacy and safety of particle therapy treatments.

In Chapter 5, the application of deep learning algorithms in predicting nuclear reactions is explored, with a focus on the DINo algorithm. This chapter presents a detailed analysis of the algorithm's development, its predictive capabilities, and its implications for improving the accuracy of particle interactions in therapeutic contexts. The integration of such advanced computational tools is essential for refining dose calculation algorithms and enhancing treatment planning. The chapter also discusses the potential of DINo in reducing computational time while maintaining high predictive accuracy, thus making it a valuable asset in clinical and simulation settings.

Finally, Chapter 6 investigates the implementation of a CMOS tracking device for enhanced precision in lung cancer particle therapy. This chapter addresses specific challenges such as respiratory motion and high-density gradients in lung tissues, which complicate accurate dose delivery. Through detailed simulations and analyses, it demonstrates the potential of CMOS technology to improve treatment accuracy and patient outcomes in non-small cell lung cancer (NSCLC) therapy using secondary particles. The chapter elaborates on the device's design, its possible integration into existing therapy systems, and the results from preliminary experimental trials.

Chapter 1

Secondary particles in heavy ion therapy

"It's me, hi, I'm the problem, it's me."
– T. S.

Contents

I. Introduction to heavy ion therapy

Cancer's emergence: a changing health scenario

Over the last century, a decline in global mortality induced by infectious diseases appeared. This paradigm shift highlighted the emerging importance of cancer as an invasive global health concern, especially in Western countries and North America, appearing as a primary contributor to premature mortality alongside cardiovascular diseases. The graphical representations in Figure 1.1 show the global landscape of age-standardized incidence and mortality rates.

Figure 1.2, analyzing the predominant cancer types based on incidence and mortality rates in various countries, reveals that the frequency of new cases does not necessarily correlate with higher mortality. Numerous factors, including age, disease stage, and treatment modalities, contribute to the observed variations in mortality rates.

Reducing the global impact of cancer requires both effective prevention and nuanced treatment approaches, which this thesis will delve into.

From a biological point of view

Cancer is characterized by uncontrolled cell proliferation leading to the invasion and perturbation of normal tissue and organ functions. Fundamentally, cancer arises from the deregulation of diverse cellular mechanisms. The primary function of the cell is to replicate its genetic information stored in the DNA (double-stranded helix), within the cell nucleus. DNA is susceptible to various forms of damage, even under normal conditions, necessitating efficient repair mechanisms.

Cancer treatment: modalities and considerations

Contemporary cancer treatment consists mostly of surgery (removal of cancerous tumors through surgical procedures), chemotherapy (use of drugs to kill or control cancer cells throughout the body), radiotherapy (application of high doses of radiation to target and destroy cancer cells) and immunotherapy (stimulation of the body's immune system to recognize and combat cancer cells), often interwoven. The selection of a treatment modality relies on nuanced considerations, including cancer type, stage, and patient overall health. Multidisciplinary tumor boards often assess individual cases to determine the most effective treatment plan.

Despite advancements, cancer treatment may lead to various side effects, and one of the main challenges lie in reducing these effects while maximizing therapeutic benefits. Balancing treatment side effects with the patient's quality of life is a critical consideration. Access to various cancer treatment options differs around the world, resulting in disparities in outcomes and survival rates. Factors such as affordability, infrastructure, and the efficiency of healthcare systems significantly influence the accessibility of treatments.

Charged particle therapy emergence

Since the discovery of radioactivity in the late 19th and early 20th centuries, radiotherapy pioneered cancer treatment. Traditionally, this discipline has relied on the use of photons to deliver targeted doses of radiation to malignant tumors.

Within this framework, hadrontherapy has emerged as a promising substitute. Operating with charged particles, notably protons and carbon ions, it offers ballistic advan-

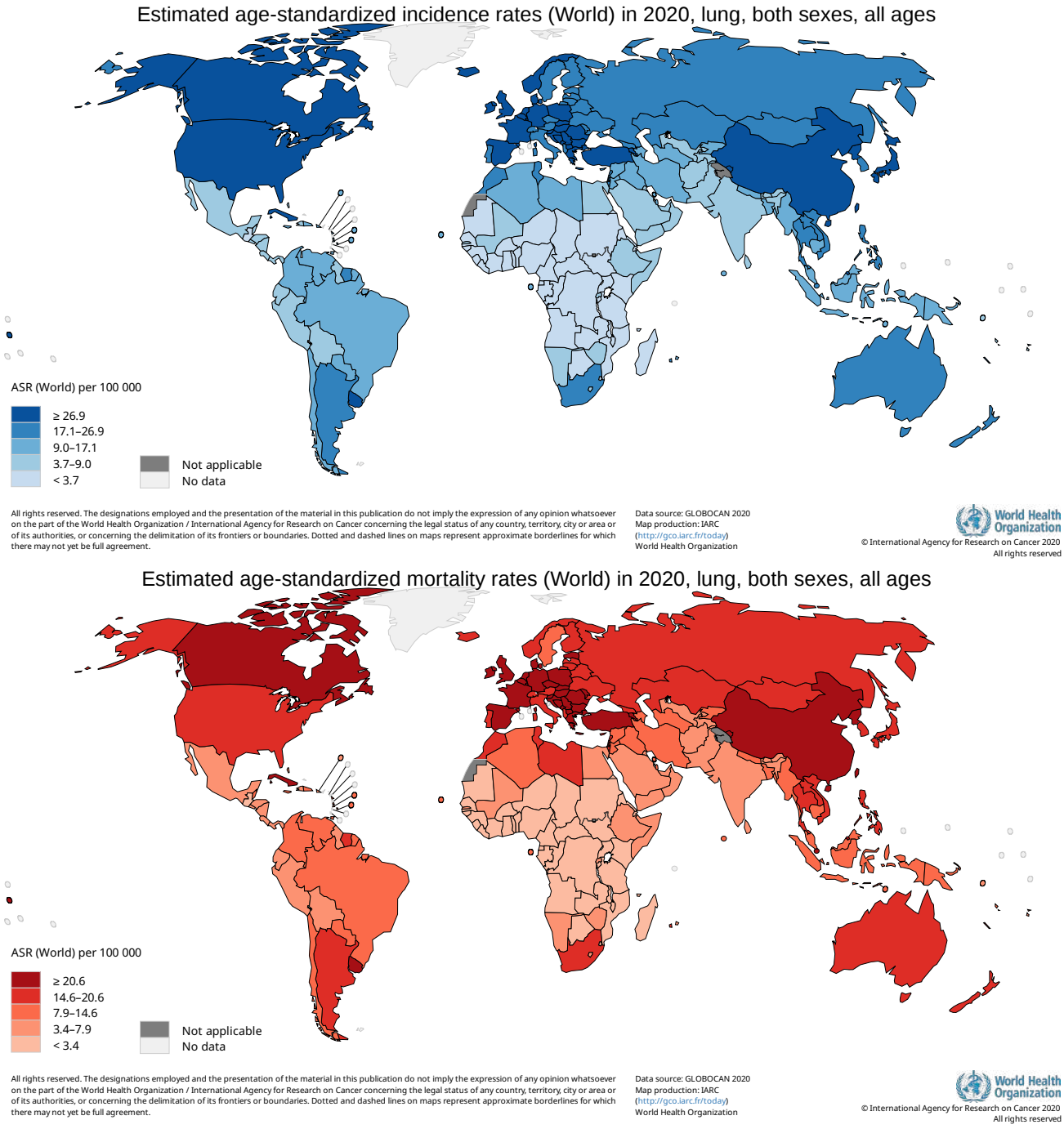

Figure 1.1: Estimated number of cases of cancer incidence and mortality rates worldwide age-standardized in 2020 [1].

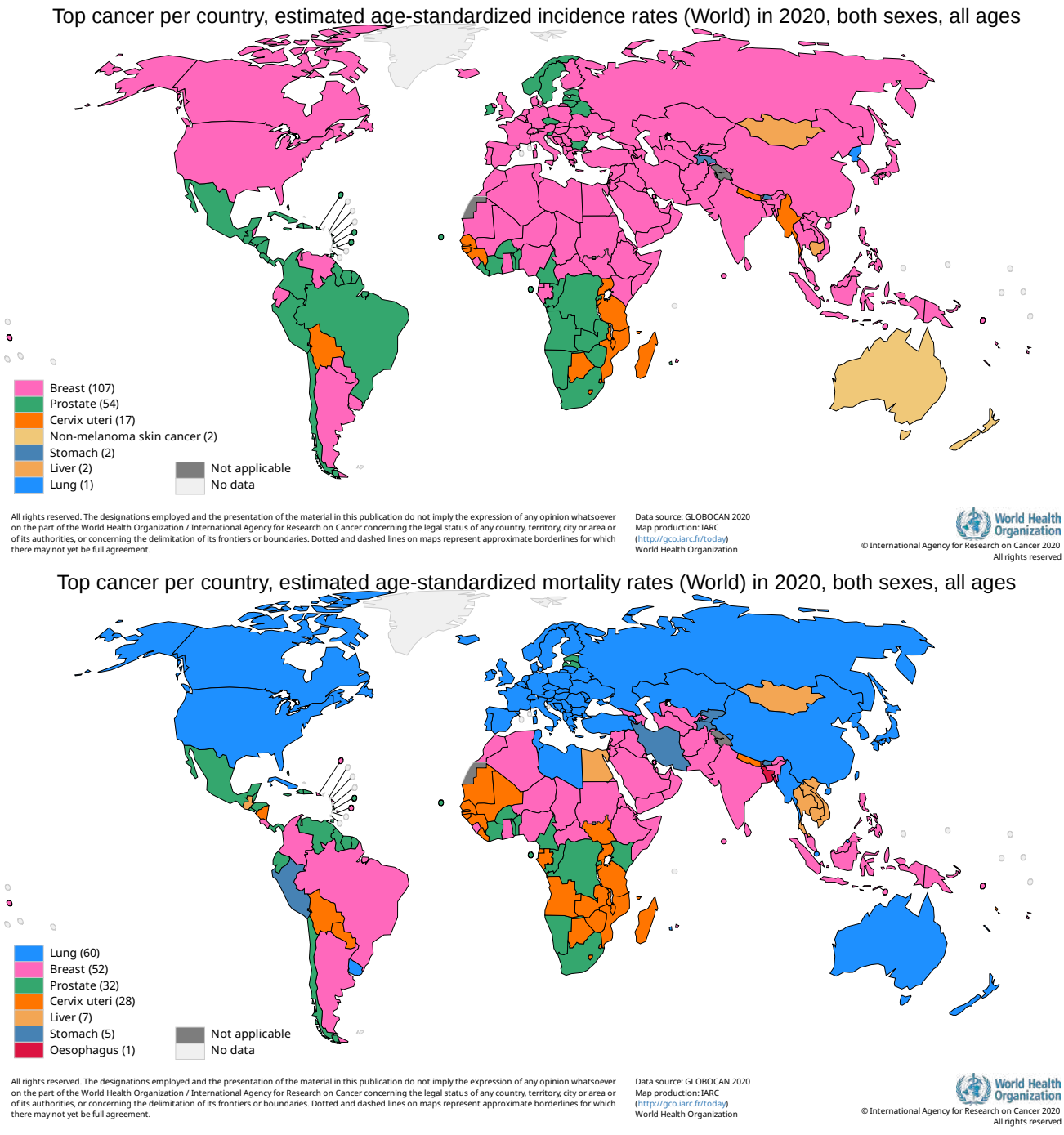

Figure 1.2: Estimated top cancer incidence and mortality rates per country age-standardized in 2020 [1]

tages over photon-based therapy. Despite its potential, hadrontherapy gained a significant extension only in recent decades, owing to advancements in particle acceleration and modeling of particle-matter interactions.

Integrating knowledge from nuclear physics, cancer biology, and medical engineering, hadrontherapy presents a promising approach with significant potential to enhance clinical outcomes in cancer patients.

Given the advantageous ballistic properties outlined in Section II.2.2, charged particle therapy presents the potential for a dual outcome. By the close of 2023, almost 312,000 patients worldwide [22] had undergone charged particle therapy, steadily rising annually. However, widespread adoption is blocked by the substantial costs associated with the requisite facilities, necessitating large accelerators and specialized personnel, resulting in treatment expenses 2 to 3 times higher than conventional therapy [23].

Nevertheless, the growing recognition of the benefits of hadrontherapy has promoted the establishment of clinical centers globally. Presently, 12 centers offer carbon-ion beam therapy [24], while 100 centers provide proton therapy. Exploration of other ions, including helium or oxygen, is under research and development.

Charged particle therapy indications and limitations

Recommended indications for charged particle therapy encompass scenarios involving tumors with intricate geometries proximate to critical organs, pediatric tumors, radiosensitive patients, and radio-resistant tumor sites. Figure 1.3 catalogs the recommended indications across various countries. Charged particle therapy emerges as a compelling alternative to conventional radiotherapy in diverse cancer cases.

It is crucial to acknowledge a major contraindication for charged particle therapy concerning tumor sites located in highly mobile regions, necessitating precise tracking methods, which remains a significant challenge in the field. Following this review of cancer's emergence and treatment approaches, especially focusing on radiation therapy, the next section will delve into exploring the fundamental physics behind the interaction of radiation and matter.

II. Interaction between radiation and matter

In this section, the radiation interactions with matter will be explored by examining charged particles. Including both light (such as electrons and positrons) and heavy particles (such as protons, alpha particles, and ions), as well as photons and neutrons, the interactions with all atomic components of the crossed material will be developed.

II.1 Important variables

II.1.1 Cross sections

The cross-section is employed to describe the collision or interaction between two particles, giving a probability for a reaction to occur. It can be written as follows :

$$\frac{d\sigma}{d\Omega}(E,\Omega) = \frac{1}{F}\frac{dN_s}{d\Omega} \tag{1.1}$$

with $\frac{d\sigma}{d\Omega}$ the average fraction of scattered particles into the solid angle $d\Omega$, N_s the average number of scattered particles, F the incident particles flux per unit area per unit time.

Country	Document	Group 1 (medically necessary)	Group 2 (potential indications)
USA	ASTRO[a] Model Policy	■ Eye tumors ■ Chordoma and chondrosarcoma ■ Spine tumors[b] ■ Hepatocellular carcinoma[c] ■ Pediatric tumors[d] ■ Patients with genetic syndromes[e]	All other solid tumors, including: ■ Head and neck cancers ■ Thoracic malignancies ■ Abdominal cancers ■ Pelvic cancers
UK	Clinical indications for treatment overseas by protons	■ Skull-base and spinal chordoma ■ Skull-base chondrosarcoma ■ Spine and paraspinal soft-tissue sarcomas[f] ■ Pediatric tumors	
Italy	AIRO[g] indications for government reimbursement	■ Skull base and spine chordomas and chondrosarcomas[h] ■ Adenoid cystic carcinoma of the salivary glands[h] ■ Mucosal malignant melanoma[h] ■ Ocular melanoma ■ Osteosarcomas[h] ■ Pediatric tumors	
Denmark	Aarhus University, Indications for the Danish National Center for Particle Therapy	■ Chordoma and chondrosarcoma ■ Ependymoma ■ Primitive neuroectodermal tumors ■ Pituitary adenoma ■ Acoustic neuroma ■ Arterovenous malformations ■ Germinoma ■ Eye tumors ■ Lymphomas ■ Selected sarcomas ■ Nasopharyngeal cancer recurrence ■ Pediatric tumors	
The Netherlands	Health Council of the Netherlands on Proton Therapy[i]	■ Skull base and spine chordomas and chondrosarcomas ■ Meningioma ■ Pediatric tumors	■ Re-irradiations ■ Paranasal sinus tumors ■ Nasopharyngeal carcinoma ■ Retroperitoneal sarcoma ■ Benign tumors of the CNS ■ Paranasal sinus and nasal cavity tumors
Canada	AHS[j] Proton Therapy Referral Committee Report	■ Chordomas and chondrosarcomas ■ Ocular melanomas[k] ■ Pediatric tumors	

[a] American Society for Therapeutic Radiation Oncology, 2013.
[b] When the spinal cord tolerance may be exceeded, or for re-irradiation.
[c] In hypofractionated schedules.
[d] When the treatment plan shows decreased normal tissue dose and therefore lower toxicity is expected.
[e] Radiosensitive syndromes such as retinoblastoma or NF-1.
[f] Non-Ewing.
[g] Italian Association for Radiation Oncology, 2015. Includes protons and C-ions.
[h] Unresectable or with post-surgery residual disease in critical volumes.
[i] An evidence-based model based on NTCP has been then accepted in The Netherlands (see figure 10).
[j] Alberta Health Services, 2014.
[k] Not suitable for plaque brachytherapy.

Figure 1.3: Recommended indications for charged particle therapy treatment in different countries [2]

Thus $d\sigma$ can be interpreted as the geometric cross-section of the target intercepting the target.

The quantity $\frac{d\sigma}{d\Omega}$ vary with the energy of the reaction and the angle at which the particle is scattered. A total cross section at an energy E is defined as :

$$\sigma(E) = \int d\Omega \frac{d\sigma}{d\Omega} \tag{1.2}$$

II.1.2 Mean free path

Considering now a distance x into matter, the probability of not having an interaction after this distance x can be described as :

$$P(x) = exp\left(\frac{-x}{\lambda}\right) \tag{1.3}$$

where λ is the mean free path, namely the mean distance traveled by the particle without having a collision.

II.1.3 Energy transfer

Frequently, radiation-matter interaction corresponds to energy transfer from the radiation to the atoms of the material, or in certain cases to the nucleus.

For a massive particle, a kinetic energy loss is observed, eventually an absorption (or neutron capture or annihilation for positrons). For non massive particle (photons) a diffusion or an absorption are observed.

The deposited energy in matter can induce at the end three phenomena :

- **atoms excitation** → the electrons from the atom are excited to higher energy levels, and then return to their ground state, releasing energy in the form of photons, leading to light emission.
- **atoms ionization** → the atom loses one or more electrons, resulting in positively charged ions. Those liberated electrons can move through the material, creating an electric field.
- **thermal agitation of atoms/molecules** → atoms or molecules are turned into motion, vibration, or collision, resulting in temperature rising and thus heat production.

II.2 Charged particle interaction

When using charged particles to treat tumor cancers in hadrontherapy, an understanding of how they interact with matter is essential. In the following section, the physics processes undergone by light and heavy charged particles will be described.

II.2.1 Light charged particles (electrons, positrons)

In the case of light charged particles like electrons or positrons, the trajectory deviates from a straight path, contrary to heavy charged ones. Those trajectories will follow a

broken line where each deviation corresponds to an interaction. Since the incident particle loses its energy, the probability of interaction increases together with the trajectory sinuosity. After the dissipation of their energy, the electrons are stabilizing at the level of thermal agitation.

Interaction with the electrons

When incident light charged particles interact with the electrons of the target, they are strongly deviated because they have the same mass (**inelastic collision**). Those light charged particles also can transfer an important part of their energy. This leads, like for heavy charged particles, to **ionization** of the atom or its **excitation**. Those three interactions are represented in Figure 1.4.

In the case where the incident electron ejects one electron from the target, it is impossible to distinguish between the two of them.

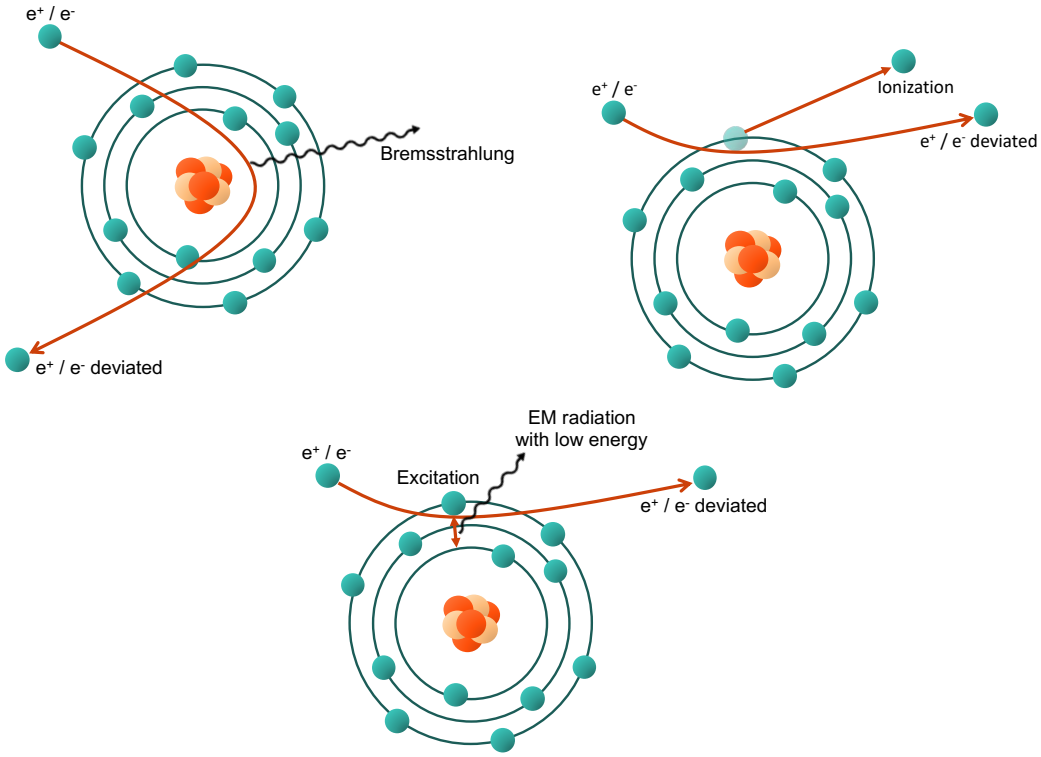

Figure 1.4: Scheme of light charged particle interaction with nucleus and electrons

Energy loss by collision

The Mott theory and its extension in the relativist case by Möller, similar to the Bethe-Bloch formula, give the energy loss by distance unit by collision with the electrons :

$$-\frac{dE}{dx} = 2\pi N_a r_e^2 m_e c^2 \rho \frac{Z}{A}\frac{1}{\beta^2}\left[\ln\frac{\tau^2(\tau+2)}{2(\frac{I}{m_e c^2})^2} + F(\tau) - \delta - 2\frac{C}{Z}\right] \tag{1.4}$$

where:

- r_e is the electron radius (physical constant)

- m_e is the electron mass
- ρ is the material density
- τ is the kinetic energy of a particle in units of $m_e c^2$
- I is the mean excitation potential of the material, typically on the order of a few tens of eV, which represents the average energy needed to ionize an atom in the material
- $F(\tau)$ is a correction factor that takes into account the behavior of stopping power at different energy regimes (typically a function of the particle's kinetic energy)
- σ is the density correction that takes into account the shielding of the electric field of the charged particle by the electrons in the material at higher energies
- $\frac{C}{Z}$ is a shell correction term that corrects the fact that the electron shell structure of atoms modifies the stopping power

An example inside water is presented in Figure 1.5, to show the proportion of ionization and radiation energy loss depending on the incident energy of the electron.

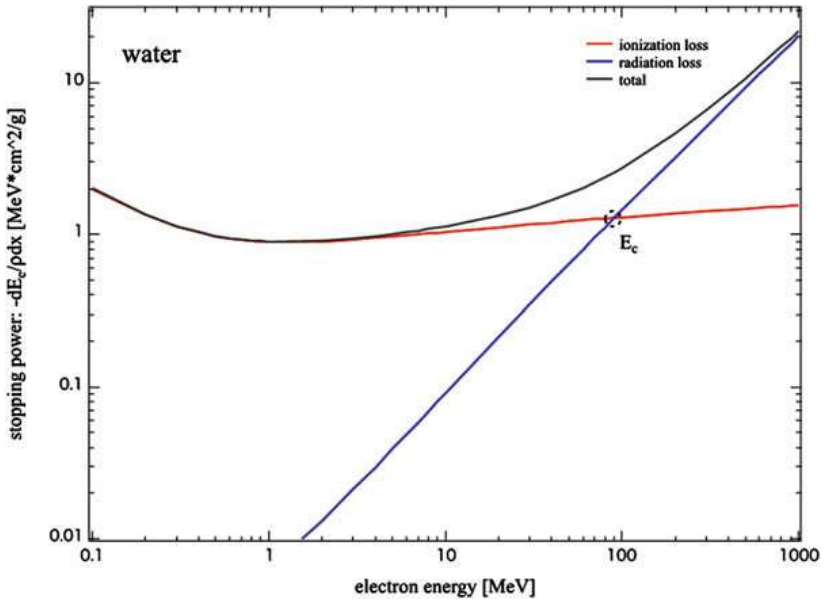

Figure 1.5: The mass-stopping power for water as a function of electron energy [3]

Interaction with the nucleus

As for heavy charged particles, which will be explored in the next section, the interaction with the nucleus can lead to an inelastic radiative diffusion with the Coulombian field of the nuclei, accompanied by a Bremsstrahlung emission, as shown in Figure 1.4.

Energy loss by breaking radiation

The energy loss by Bremsstrahlung is not negligible, especially at high energy and inside material with high Z. It can be described as:

$$-\left(\frac{dE}{dx}\right)_{rad} = n\Phi_{rad}E \tag{1.5}$$

where n is the number of atoms per volume unit, and Φ_{rad} is a term proportional to Z^2 and almost independent from E (the charged particle energy). Thus, the energy of the charged particles of high energy exponentially decrease by breaking radiation :

$$E = E_0 \exp\left(-\frac{X}{X_0}\right) \tag{1.6}$$

where X_0 is the radiation length of the material, and it can be described as the distance over which the electron energy is reduced by a factor of 1/e due to radiation loss only. A good approximation convenient for quick calculations can be:

$$X_0 = \frac{716,4\ g.cm^2.A}{Z(Z+1)\ln\left(\frac{287}{\sqrt{Z}}\right)} \tag{1.7}$$

Positron annihilation

When the energy of the positron tends toward zero at the end of its path, it will annihilate with an electron of the material, which will lead to the emission of two gammas of 511 keV at 180° one of the other as shown in Figure 1.6.

This emission is used in PET (positron emission tomography) in medical imaging, as it will be discussed in Section V.3.

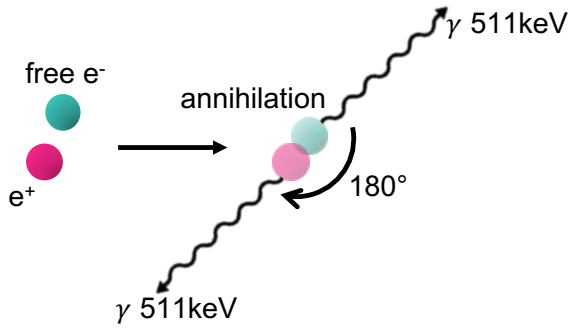

Figure 1.6: Scheme of positron annihilation with free electrons

II.2.2 Heavy charged particles (protons, alphas, ions)

In the case of heavy charged particles like protons or ions, they travel in an almost straight path in matter losing energy continuously through a large number of collisions with atoms nucleus or electrons.

Interaction with the electrons

The slowing down process of the heavy charged particles inside matter is dominated by their Coulombian interaction with the electrons from the target atoms :

- the electron can be ejected of the atoms (**ionization**) and may also ionize another atom if its energy is sufficient (**secondary ionization**).
- the electrons can be moved from one orbit to another, further from the nucleus (**excitation**).

Interaction with the nucleus

Under 100 MeV, a heavy charged particle can interact with the nucleus on its own as shown in Figure 1.7, by two phenomena:

- **inelastic diffusion** with Bremsstrahlung emission (braking radiation).
- **elastic diffusion** without energy transfer.

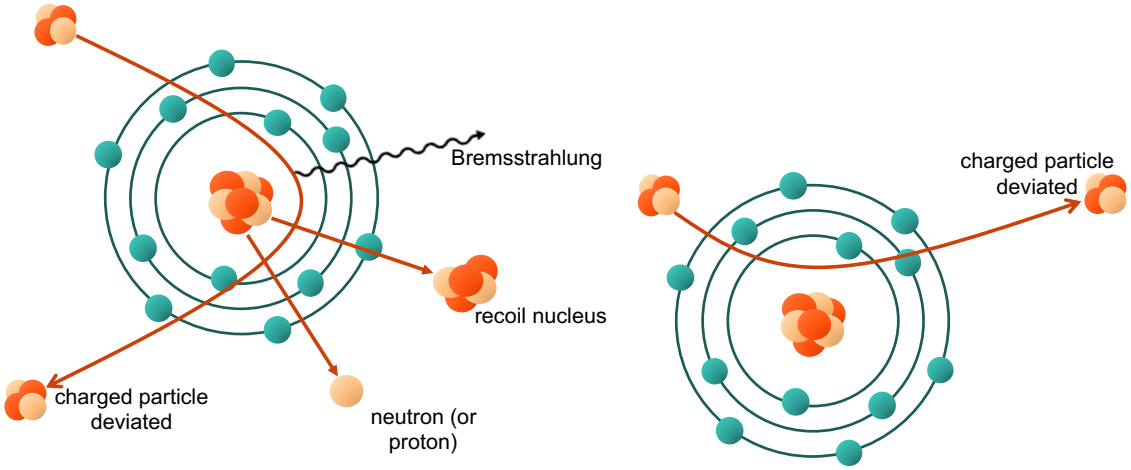

Figure 1.7: Scheme of heavy charged particle interaction with the nucleus.

Nuclear fragmentation plays a crucial role in the stopping process of high-energy ions, although its contribution is smaller compared to collisions with electrons. Nonetheless, it has significant effects at large penetration depths. At energies around several hundred MeV/u, violent (**nuclear spallation**) reactions occur, leading to the complete or partial disintegration of the projectile and target nuclei, as shown in Figure 1.8.

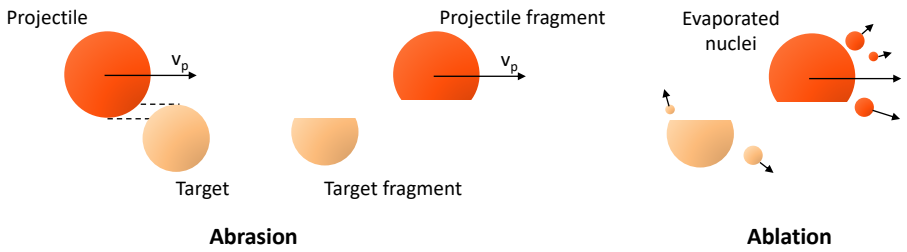

Figure 1.8: Scheme of fragmentation model with the abration and the ablation reactions.

Energy transfer during collision

If the incident particle is much heavier than the electron, its path will be equivalent to a straight line. The energy loss by the incident particle in a single interaction will then be :

$$\Delta T = \frac{2z^2e^4}{(4\pi\epsilon_0)^2 m_0 v^2 b^2} \tag{1.8}$$

where ϵ_0 is the permittivity of free space, a physical constant that describes how electric fields behave in a vacuum, m_0 the electron rest mass, v the velocity of the incident particle and b the impact parameter, which is the perpendicular distance between the incident particle's path and the electron.
In an extreme case of b=0 (really low probability), the energy loss will become :

$$\Delta T_{max} = \frac{4Mm_0}{(m_0+M)^2}T \tag{1.9}$$

where M the mass of the incident particle and T its kinetic energy.

Stopping power

Concerning the stopping power of high-energy ($\sim$ GeV) ions in patients, the ion beam needs to penetrate tissue up to a depth of 30 cm. Different types of ions are employed for this purpose. Protons and helium (^{4}He) ions, with energies reaching up to 220 MeV/u, and carbon (^{12}C) ions, capable of reaching energies up to 430 MeV/u. The velocity of these particles is approximately 0.7 ($\beta = \frac{v}{c} \sim 0.7$).

At this velocity $\beta \sim 0,7$, the slowing process is dominated by inelastic collisions with target's e^-, which is described by the Bethe-Bloch formula :

$$\frac{dE}{dx} = \frac{4\pi e^4 Z_t Z_p^2}{m_e v^2}\left[ln\frac{2m_e v^2}{<I>} - ln(1-\beta^2) - \beta^2 - \frac{c}{z_t} - \frac{\delta}{2}\right] \tag{1.10}$$

The maximum rate of energy loss occurs at the Bragg peak, as shown in Figure 1.9, which is reached when the velocity of the projectile (v_p) is approximately proportional to $v_p \sim z_p^{2/3} v_0$, with z_p the charge of the particle and v_0 its initial velocity.

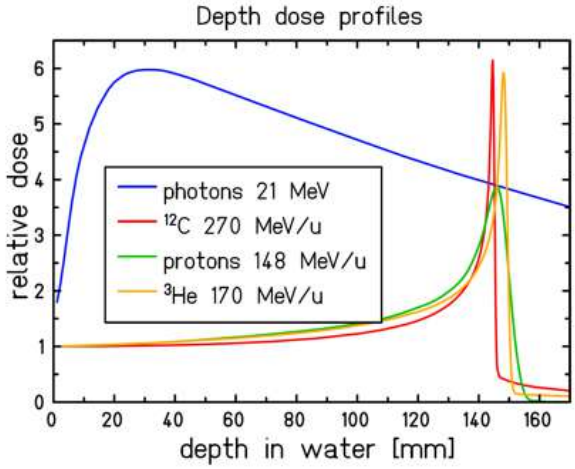

Figure 1.9: Depth dose profiles in water for different ion types compared to photons. [4]

Heavy charged particles (projectiles) typically travel in nearly straight lines. The statistical fluctuations in energy loss lead to the broadening of the Bragg peak, and in the limit of a large number of collisions, these fluctuations follow a Gaussian distribution. Additionally, the broadening of the Bragg peak can also be attributed to density inhomogeneities present in the penetrated tissue.

Nuclear fragmentation occurs throughout the trajectory of the incident particle within the material, leading to a progressive consumption of the beam. Consequently, primary beam particles are lost, resulting in the build-up of lower-Z fragments. Projectile fragments, moving at the same velocity, have longer ranges and create a dose tail behind the Bragg peak, as can be seen in Figure 1.9. Figure 1.10 illustrates the contribution of various fragments produced by the interaction of a ^{12}C beam in water to the dose profile. The majority of the produced fragments are ions ^{11}C, He, and B.

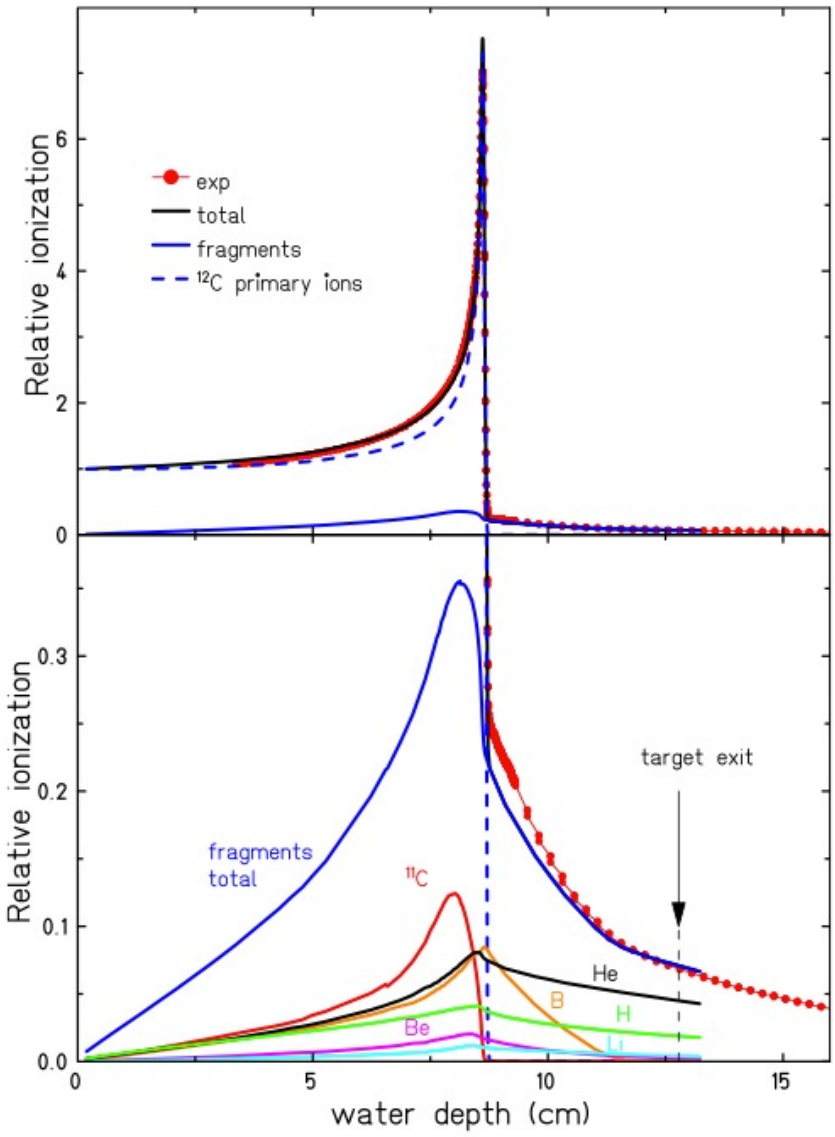

Figure 1.10: Ionization function (Bragg curve) of a 200 MeV/u ^{12}C ion beam in water. The lower part with a magnified ordinate scale shows the contribution of fragments with different atomic numbers Z as calculated with the Monte-Carlo code PHITS (particle and heavy ion transport code system).[5]

Linear stopping power

The linear stopping power $S = \frac{dT}{dx}$ corresponds to the energy loss of the incident particle per unit of distance, including the bremsstrahlung losses. For the heavy charged particles at particle therapy energies, those bremsstrahlung losses are negligible.

Mass stopping power

The mass stopping power is defined as $\frac{S}{\rho}$. Examples of mass stopping power for charged particles for various materials are presented in Figure 1.11.

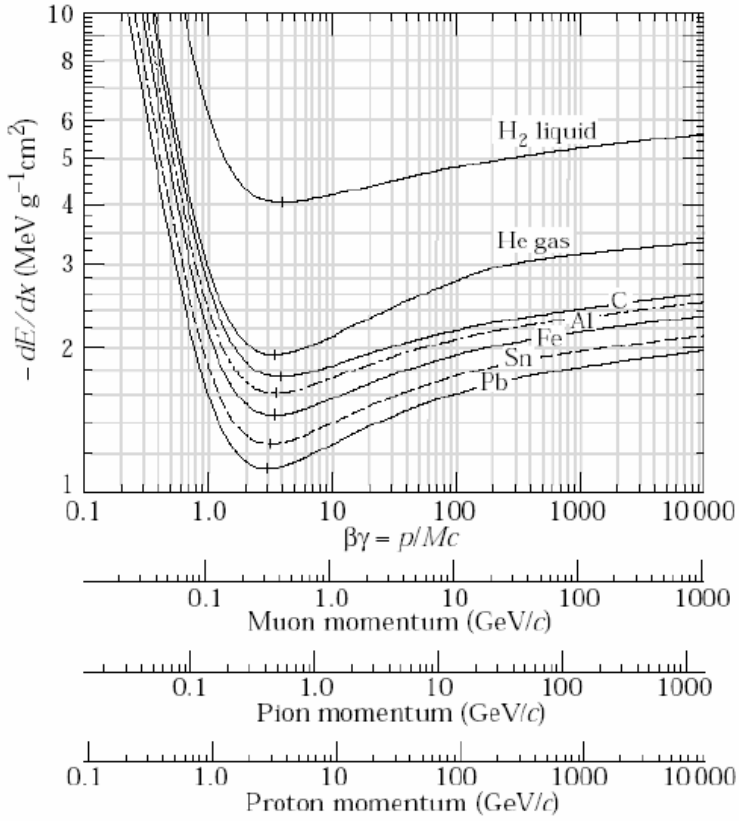

Figure 1.11: Mass stopping power graph for muons, pions, and protons in various materials. [6]

LET (Linear Energy Transfer)

The Linear Energy Transfer (LET) is a restricted local version of the stopping power described in the section above. The crucial distinction between stopping power and LET lies in their respective definitions: stopping power is delineated concerning the thickness of the attenuating medium, whereas LET is articulated about to the track length delineated by the traversing particle within the medium, mostly dominated by the electrons from ionization with sufficient energy.

In Figure 1.12 shows the structure of a proton and a carbon track in nanometre resolution compared to a schematic representation of a DNA molecule. The higher density

of the secondary electrons, produced by carbon ions, creates a large amount of clustered DNA damage.

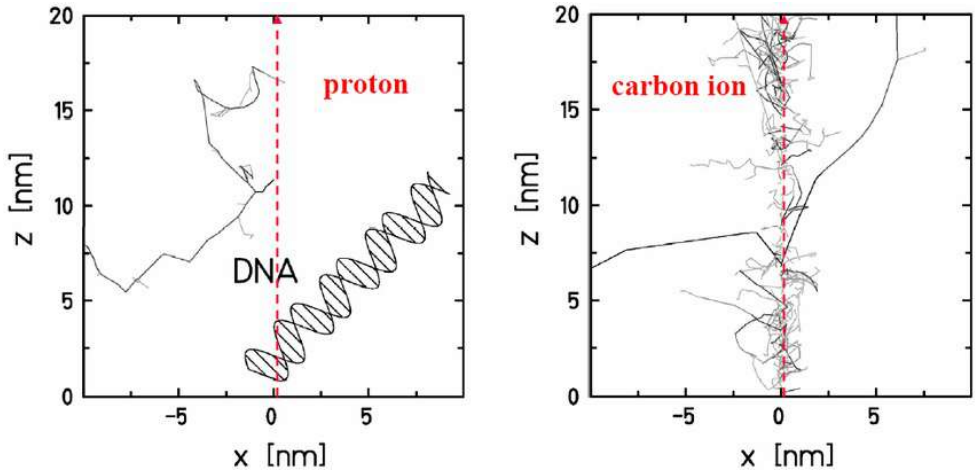

Figure 1.12: Structure of a proton and a carbon track in nanometre resolution compared to a schematic representation of a DNA molecule. [7]

The trajectory of the particle through the medium tends to exhibit a degree of randomness, and, consequently, the track length in the context of LET does not necessarily align with the thickness of the absorber. LET can thus be defined as :

$$LET = S_{el} - \frac{dE_{ke}}{dx} \tag{1.11}$$

where S_{el} is the linear electronic stopping power, and dE_{ke} is the mean sum of the kinetic energies of all the electrons released by the charged particle in traversing a distance dx.

II.3 Photon interaction

Photons are considered as indirect ionizing radiations which interact in three major different ways in our energy ranges (**photoelectric, pair production**, and **Compton**) and two less probable ones (**photonuclear** and **Thomson-Rayleigh**) as resumed in Figure 1.13. The probability of each interaction process depends on the energy of the photon and the type of material (atomic number Z) as can be observed in Figure 1.14.

II.3.1 Interactions with electrons

Photoelectric effect

The photoelectric effect is a phenomenon where electrons are emitted from a material's surface when the incident photons transfer all its energy. The linked electron will be emitted with a kinetic energy:

$$T_e = -W_s + h\nu \tag{1.12}$$

where W_s is the binding energy of the ejected electron and $h\nu$ is the energy of the incident photon. W_s must be inferior to $h\nu$ for this effect to appear.

The atom ionization is followed by a rearrangement of the electronic layers which induce an emission of a fluorescence photon or an Auger electron (from another layer).

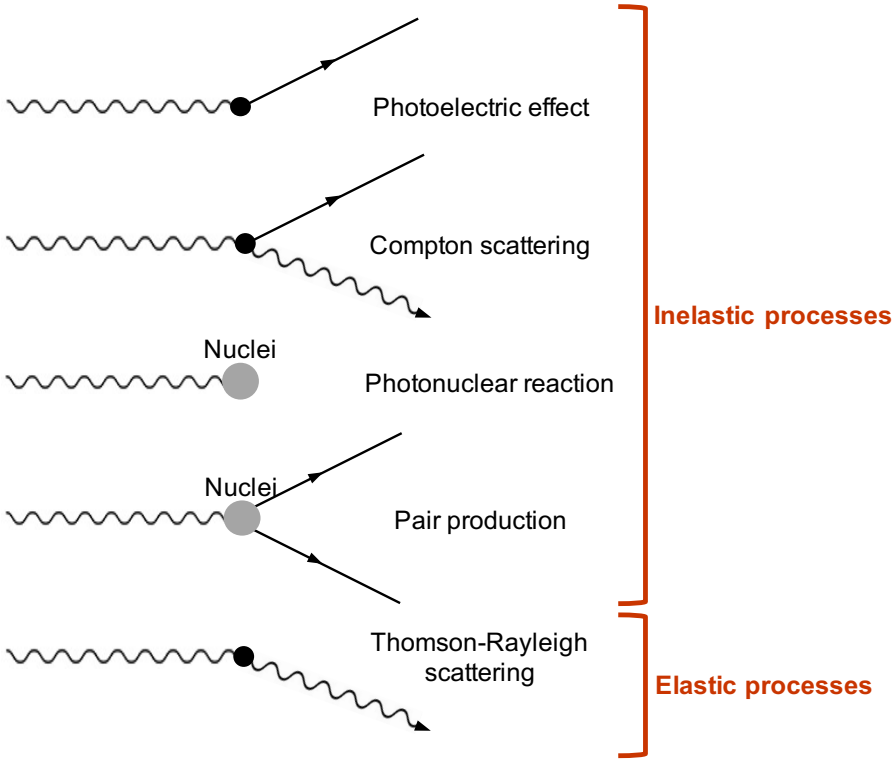

Figure 1.13: Review of interaction processes for photons in matter

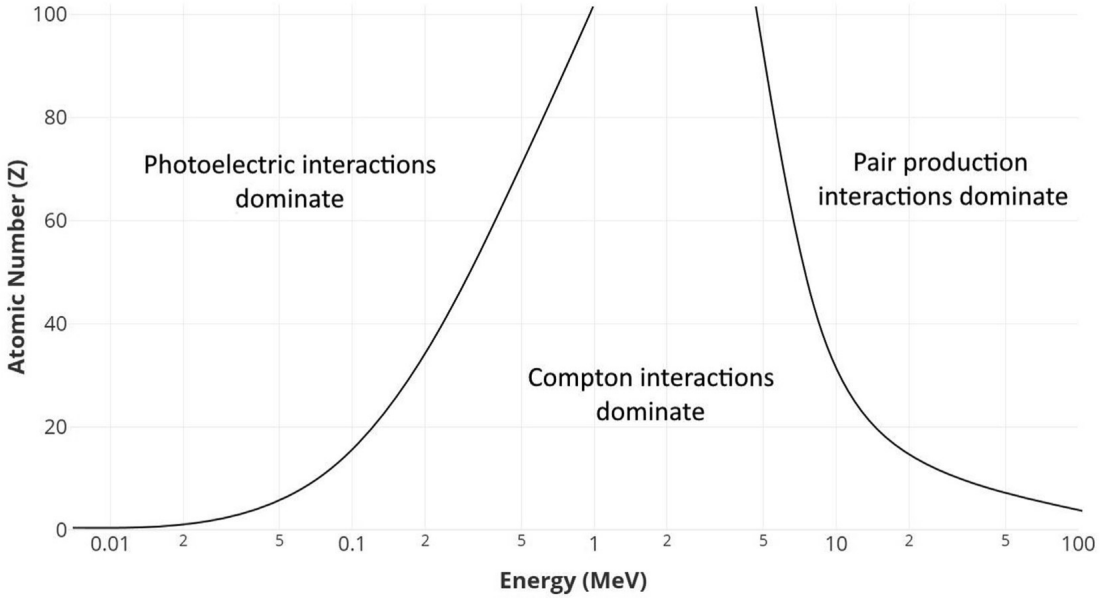

Figure 1.14: Relative importance of the three main photon interaction processes with atomic number (Z) and photon energy [8]

The photoelectric effect cross section is proportional to the atomic charge Z :

$$\sigma_{photoelec} \propto \frac{Z^N}{(h\nu)^{3.5}} \tag{1.13}$$

where N varies between 4 and 5.

Compton scattering

The Compton effect occurs when a high-energy photon collides with an electron, the photon scatters off the electron and transfers only a part of its energy and momentum to the electron. The kinetic energy of the scattered electron can be defined as:

$$T_e = \frac{E_1^2(1 - cos\theta)}{m_e c^2 + E_1(1 - cos\theta)} \tag{1.14}$$

where E_1 is the energy of the incident photon, m_e the electron mass, and θ is the angle between the scattered photon and the incident axis.

The cross-section for the Compton effect is described thanks to the Klein-Nishina formula :

$$\sigma = \sigma_0 \cdot \frac{Z}{A} \cdot \left(\frac{E}{m_e c^2}\right)^{-3} \cdot \left(\frac{E}{m_e c^2} + \frac{m_e c^2}{2E}\right) \cdot \left[1 - \beta^2 \sin^2(\theta)\right] \tag{1.15}$$

where σ_0 represents the classical Thomson cross-section, which is an approximation of the photoelectric cross section for low energy photons and small scattering angles.
Z is the atomic number of the target material, indicating the number of protons in its nucleus.
A is the atomic mass number of the target material, representing the total number of protons and neutrons in its nucleus.
E is the energy of the incident photon, and m_e is the rest mass of the electron.
c is the speed of light in vacuum, which is a fundamental constant.
β is a parameter that describes the velocity of the emitted photoelectron relative to the speed of light.
θ is the scattering angle of the emitted photoelectron, which indicates the direction in which the electron is ejected after the interaction.

Rayleigh-Thomson scattering

The Rayleigh-Thomson scattering is a limit case of Compton scattering at low energy.

It can be defined as the deviation of photons by free electrons in the classical limit. At low energies concerning the electron mass, the Klein-Nishina formula can be reduced to the Thomson cross-section :

$$\sigma = \frac{8\pi}{3} r_e^2 \tag{1.16}$$

On the other hand, the Rayleigh scattering is the scattering of photons by atoms as a whole. Both scattering are very small and most of the time neglected.

II.3.2 Interaction with the nucleus

Pair production

Pair production is a process that occurs if the photon energy is higher than 1.022 MeV (=$2m_e$). In pair production, a photon interacts with the coulombian field of a nucleus or another charged particle. The energy of the photon is converted into the mass energy of the particle-antiparticle pair. These newly formed particles carry away the energy of the original photon in the form of their rest mass energies.

The pair production cross section is proportionnal to Z :

$$\sigma_{paire} \propto Z^2 \tag{1.17}$$

Photonuclear reactions

Photonuclear reactions are of the type (γ,n), (γ,p) or photofission, which need the nucleon tearing or the transmission to big nuclei of an excitation energy, in which way it splits into two fragments. Those reactions appear with high energy photons but the cross-section of this reactions is small, almost negligible.

II.4 Neutron interaction

Neutrons are neutral particles and exhibit characteristics of indirect ionization as they interact with matter. Their classification is based on their energy ranges, and this categorization can be delineated for example as follows in Table 1.1.

Neutrons	Energy	Information
Thermal	$\sim$ 0.025 eV to $\sim$ 0.5 eV	Often used in nuclear reactors to sustain a controlled chain reaction.
Epithermal	$\sim$ 0.5 eV to $\sim$ 10 keV	Can undergo radiative capture.
Fast	$\sim$ 10 keV to $\sim$ 20 MeV	Valuable for neutron activation processes in various applications.
High energy	$>$ 10 MeV	Coming from cosmic rays or accelerators.

Table 1.1: Example of classification for neutrons according to their energy.

Neutrons can approach atomic nuclei closely enough to experience the effects of nuclear forces. This phenomenon gives place to three distinct interaction processes: **diffusion, capture,** and **fission**.

II.4.1 Neutron diffusion

Neutrons experience deviations in their trajectories upon interaction with nuclei. This deviation is accompanied by a partial loss of their energy.

Elastic scenario

In the elastic case, the energy exchanged with the nucleus ($E_{nucleus}$) is quantified by the difference between the initial energy (E_1) and the final energy (E_2) of the neutron. This

energy exchange can be expressed as:

$$E_{nucleus} = (E_1 - E_2) = \frac{4AE_1 \cos^2 \theta}{(A+1)^2} \tag{1.18}$$

where A represents the atomic mass number and θ denotes the angle of deviation in the interaction. This type of reaction is more likely when the Z of the target is low, and therefore with hydrogenated materials.

Inelastic scenario

In the inelastic case, the kinetic energy of the neutron is not conserved. A portion of this kinetic energy is used to excite the atomic nucleus. Consequently, the excited nucleus subsequently releases this excess energy by emitting γ radiation. This process involves a dynamic interplay between the neutron's energy and the nucleus's excitation and de-excitation mechanisms.

II.4.2 Neutron capture

In the context of neutron interactions with nuclei, a noticeable phenomenon occurs during neutron capture by a nucleus with a mass number A. This process yields the formation of a new nucleus with a slightly higher mass, specifically A+1. When the resultant nucleus is inherently radioactive, the term "activation" is employed to describe this transformation.

It is important to note that the neutron capture process can be categorized into two distinct types:

- **Radiative capture**: in this scenario, the newly formed nucleus undergoes de-excitation through the emission of γ radiation.
- **Non-radiative capture**: in cases where the excess energy attributed to the capture process is sufficient, a phenomenon arises wherein a particle extraction takes place. The types of extracted particles may include neutrons, protons, or alpha particles. Notably, this extraction mechanism primarily occurs in high-energy scenarios.

II.4.3 Fission

The phenomenon of nuclear fission can be categorized into two types: **spontaneous** and **induced**.

Induced fission represents a particular case of neutron capture processes. This process generates the rapid splitting or division of a nucleus into two smaller fragments or fission products. Induced fission can be initiated through interactions with neutrons. These neutrons can possess either thermal or high energy characteristics. Notably, a cascade effect may occur wherein emitted neutrons from a previous fission event induce the fission of additional nuclei, potentially leading to a self-sustaining chain reaction.

The fission products that emerge from this process carry a significant amount of energy. This energy content becomes important in the context of nuclear reactors, where the energy released by fission is exploited. This principle operates on the transfer of energy from fission products to the surrounding medium.

III. Biological aspects in heavy ion therapy

To discuss the radiation effects on the patient biology, variables like dose, relative biological effectiveness, and oxygen enhancement factors are used and need to be defined.

III.1 Important variables

III.1.1 Absorbed dose

The absorbed dose by a material is a quantity that measures the total energy absorbed per unit mass and can be defined as :

$$D = \frac{dE}{dm}[Gy] \tag{1.19}$$

where dE is the mean energy deposited by ionizing radiation through the mass element dm, and Gray unit ($[Gy]$) is J/kg.

The deposited dose can also be defined through a thin slice of an absorber material with a density ρ :

$$D[Gy] = 1,6.10^{-9}\frac{dE}{dx}\left[\frac{keV}{\mu m}\right]F[cm^{-2}]\frac{1}{\rho}\left[\frac{cm^3}{g}\right] \tag{1.20}$$

where F is the particle fluence. The dose stands out as the most frequently utilized reference variable in radioprotection, but it should be noted that this value does not take into account the radiation type, which plays an important role in biological responses. The LET defined in Section II.2.2 can also be defined as a function of the deposited dose :

$$D = \frac{\phi}{\rho}LET \tag{1.21}$$

III.1.2 Relative biological effectiveness (RBE)

To enable meaningful comparisons across diverse radiation modalities, the concept of relative biological effectiveness (RBE) has been introduced, to take into account the strong effect of the specific radiation type and its energy. This difference is induced by different LETs depending on radiation type.

RBE is quantified based on cellular survival curves and is defined as the ratio between a dose considered a reference, specifically in the context of conventional X-ray radiotherapy, and the dose of the radiation under investigation, yielding equivalent cellular survival:

$$RBE = \frac{D_{Xray}}{D_{ion}} \tag{1.22}$$

Thus, the more ionizing the particle the greater the local biological damage.

III.1.3 Equivalent and effective dose

In order to have a normalized value of the biological effect on a tissue or organ after irradiation, the equivalent dose H_T is defined as the multiplication of the absorbed dose

averaged over the entire tissue or organ D_R, with the radiation weighting factor w_R, defined for each organ of the body:

$$H_T = w_T \cdot D_R \tag{1.23}$$

To take into account the impact of organ or tissue type receiving the radiation on the probability of developing biological effects such as cancer or other genetic anomalies, the effective dose is defined as :

$$E = \sum H_T w_T \tag{1.24}$$

where the sum is over the different organ tissues exposed.

III.1.4 Oxygen enhancement factor (OER)

Another aspect of the multifactorial biological impact of radiation is the cellular oxygenation. Indeed, the majority of damages inflicted on cells arises from free radicals produced indirectly by ionizing radiations. A reduced concentration of oxygen within the cell will result in decreased radiation effectiveness. This radiosensitivity will consequently require a dose two to three times higher to destroy a hypoxic cell compared to an adequately oxygenated cell. This effect is quantified by the Oxygen Enhancement Ratio (OER):

$$OER = \frac{radiation\,dose\,in\,hypoxia}{radiation\,dose\,in\,air} \tag{1.25}$$

The less oxygen-enhancing the OER, the more efficient the radiation treatment for hypoxic tumors is considered.

In Figure 1.15 are summarized the RBE and OER values for different particles. Considering only those values, heavy ions seem to be very promising concerning their higher biological efficiency and lower OER than X-rays.

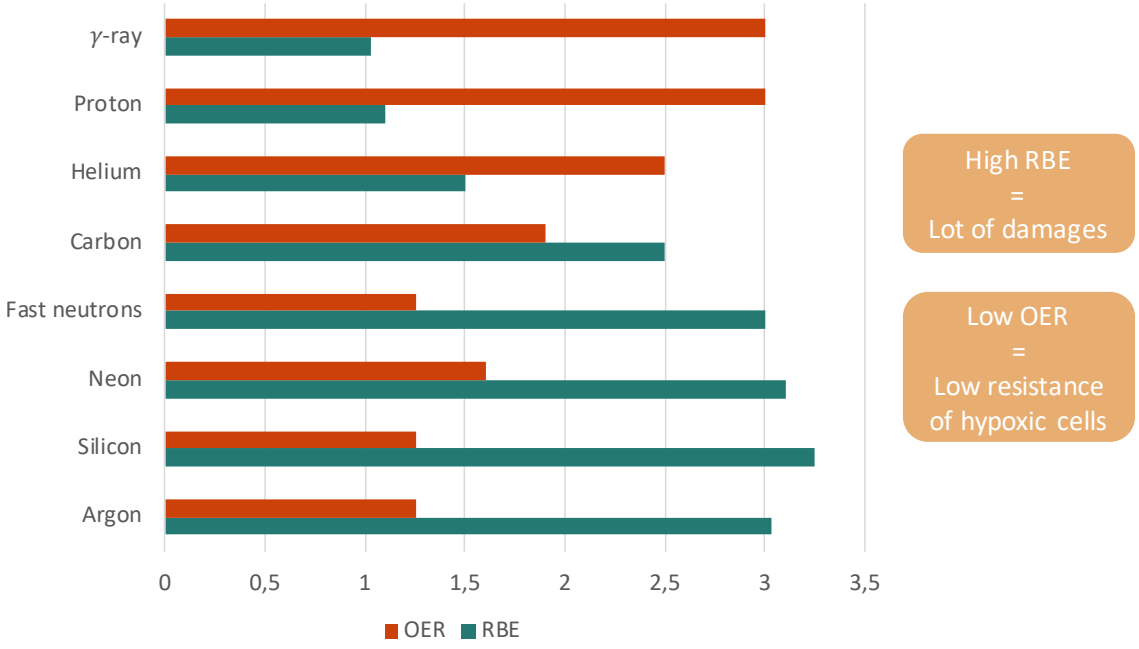

Figure 1.15: RBE and OER values for different particles. [9]

III.2 Effects on cells

III.2.1 Charged particle's effects

The cellular reaction to ionizing radiation depends on several factors, including the radiation dose, rate of dose delivery, LET, radiation type, cell type, and its immediate surroundings. When exposed, cells respond to DNA damage, which can occur within minutes, hours, or days after exposure. This damage is caused by two main processes which are represented in Figure 1.16:

- **Direct effects** occur when ionizing radiation directly interacts with atoms and molecules, leading to excitations and ionizations.
- **Indirect effects** happen when radiation causes water molecules to break down, generating reactive oxygen species like hydroxyl radicals (OH°) and hydrogen radicals (H°), that in turn can ionize the DNA helix.

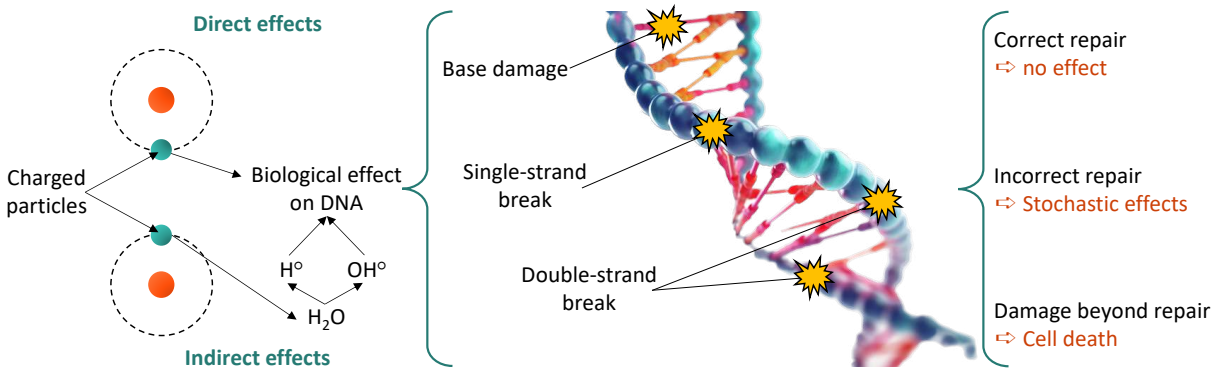

Figure 1.16: Scheme of direct and indirect effects on cells DNA of charged particles

DNA strands break

All components of a cell, such as water, DNA, proteins, lipids, and carbohydrates, can be affected and induce breaks in the DNA strands that can produce alterations in the chemical structure of its bases. The cellular response involves adjusting gene expression of relevant products, like those involved in DNA repair, and sometimes temporarily halting the cell cycle to allow for DNA repair. This response is called "early" because it occurs soon after exposure. These changes can lead to cell death through programmed cell death (apoptosis) or cell injury (necrosis) if repair mechanisms fail. Inaccurate repairs may cause cell death or mutations, potentially leading to radiation-induced cancers. Effective repair, however, ensures cell survival and diminishes the impact of radiation exposure.

Survival curve

To investigate cell sensitivity to radiation, assessing cell mortality in correlation with delivered radiation dose is frequently extressed by a cellular survival curve, denoted as S. This curve can be modeled using the linear-quadratic (LQ) model as follows:

$$\ln S = \alpha D + \beta D^2 \tag{1.26}$$

where D represents the absorbed dose, and α and β are experimentally determined parameters associated respectively with lethal damage (LD), leading to cell death without repair, and sub-lethal damage (SLD) which may either progress to cell death or be repaired. A typical survival curve for X-rays, as depicted in Figure 1.17, generally exhibits a shoulder at low doses followed by an exponential decrease.

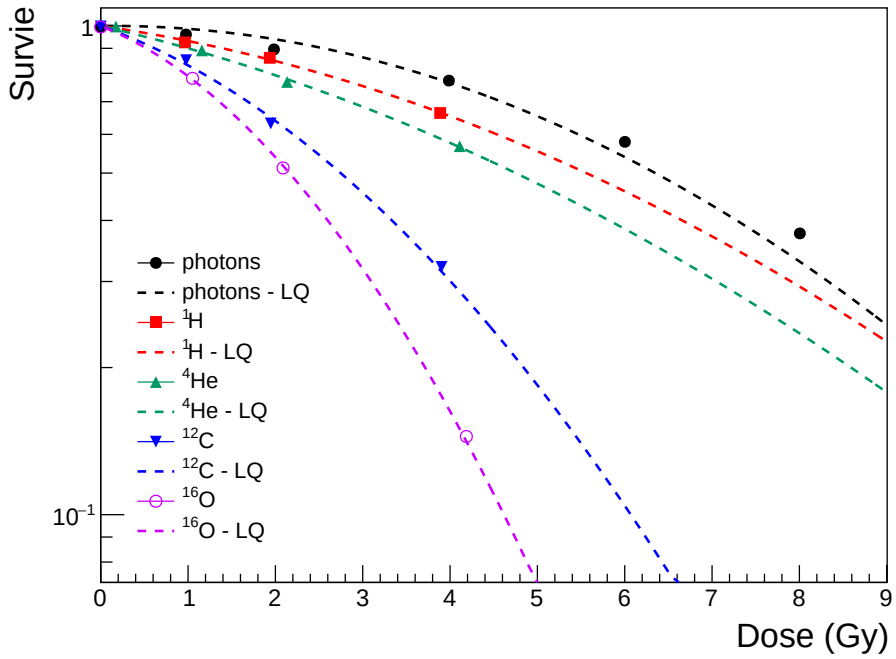

Figure 1.17: Cellular survival of A549 cells depending on the dose delivered for different types of ionizing radiation (photons, protons, ^{4}He, ^{12}C, and ^{16}O) [10]. The experimental data are extracted from[11].

In the case of high linear energy transfer (LET) particles, the curve is usually entirely exponential. Indeed, with increasing LET, the number of lethal lesions increases, and consequently, the ratio α/β also increases.

Advantages and applications

Considering the physical and biological properties of charged particles outlined in the preceding paragraphs, hadron therapy appears to offer clear advantages over conventional radiotherapy, particularly for heavier ions which exhibit increased biological effectiveness.

However, this observation quickly encounters the challenge of installation costs: treatment centers utilizing high linear energy transfer (LET) particles such as ^{12}C or ^{16}O entail costs 2 to 3 times higher than those using proton beams. Even proton therapy centers themselves require an investment of around \$50 million, which is approximately twice the investment needed for a conventional radiotherapy center. This significant cost disparity partly explains the relatively slow growth of hadrontherapy.

One notable application area is the treatment of pediatric cancers. This is particularly significant due to the inherent need to reduce the risk of radiation-induced secondary

cancers in young patients. Studies, such as those by Grassberger [15], have underlined the potential advantages of heavy ion therapy in this context.

However, a key consideration in delivering effective treatment while minimizing long-term risks is the management of the fragmentation tail associated with charged particle beams. While the Bragg peak enables precise targeting of tumors, the fragmentation tail can inadvertently irradiate surrounding healthy tissues, increasing the risk of secondary cancers.

Therefore, optimizing treatment planning techniques to reduce the impact on the short and long-term of the fragmentation tail is essential. Strategies may include refining beam delivery methods, such as intensity-modulated particle therapy (IMPT), which allows for more precise control over the distribution of radiation doses.

III.2.2 Neutron effects

The presence of neutrons need also to be considered as they may be produced through nuclear interactions within beam forming elements and the patient's body. Neutrons originating from the beam contribute significantly to the secondary dose.

Notably, heavy ions produce neutrons with characteristics similar to protons, with the energy spectrum reaching its maximum at half the velocity of the primary ions. The neutron dosage exhibits similarity in proton and carbon-ion therapy; however, the precise biological effects remain inadequately understood and considered.

IV. Clinical accelerators and beam delivery

Hadrontherapy requires the use of particle accelerators. There are two main types of particle accelerators utilized in clinical settings for this purpose: cyclotrons and synchrotrons. In this section, the role of those accelerators will be explored, in generating therapeutic ion beams with precise energy and intensity, alongside the modalities of beam delivery, which enables clinicians to shape dose distributions according to tumor volumes. Additionally, ions types commonly used in heavy ion therapy will be explored, highlighting their distinct advantages and clinical applications.

IV.1 Accelerator types

IV.1.1 Cyclotrons

Cyclotrons are circular particle accelerators commonly used in heavy ion therapy for proton and light ion (e.g., helium) treatments. These accelerators use a combination of electric and magnetic fields to accelerate charged particles along a circular path. A scheme of a cyclotron is represented in Figure 1.18. As the particles gain energy with each revolution, they reach the desired one for therapeutic applications.

Cyclotrons are particularly suited for generating beams of relatively low energy, which are well-suited for treating superficial tumors or tumors located near organs at risk. Their compact design and ability to produce continuous beams make them efficient for clinical use.

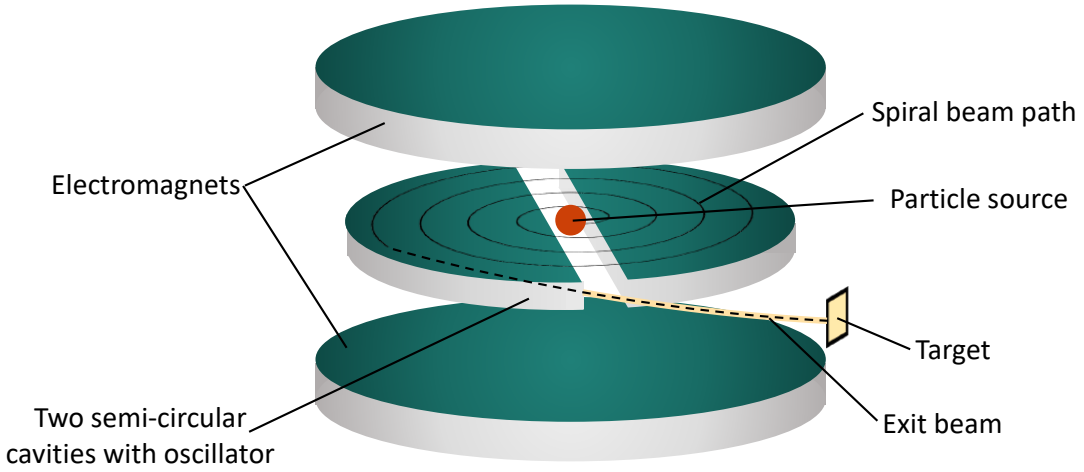

Figure 1.18: General scheme of a cyclotron

IV.1.2 Synchrotrons

Synchrotrons are another type of circular particle accelerator utilized in heavy ion therapy, particularly for generating high-energy beams such as carbon ions.

Synchrotrons employ alternating electric fields to accelerate particles while using magnetic fields to keep them in a circular orbit. A scheme of a synchrotron is represented in Figure 1.19. These accelerators are capable of accelerating particles to much higher energies compared to cyclotrons, making them suitable for treating deep-seated tumors with greater precision.

Synchrotrons can adjust beam energy and intensity, allowing modulation for clinicians in the treatment plan for each patient.

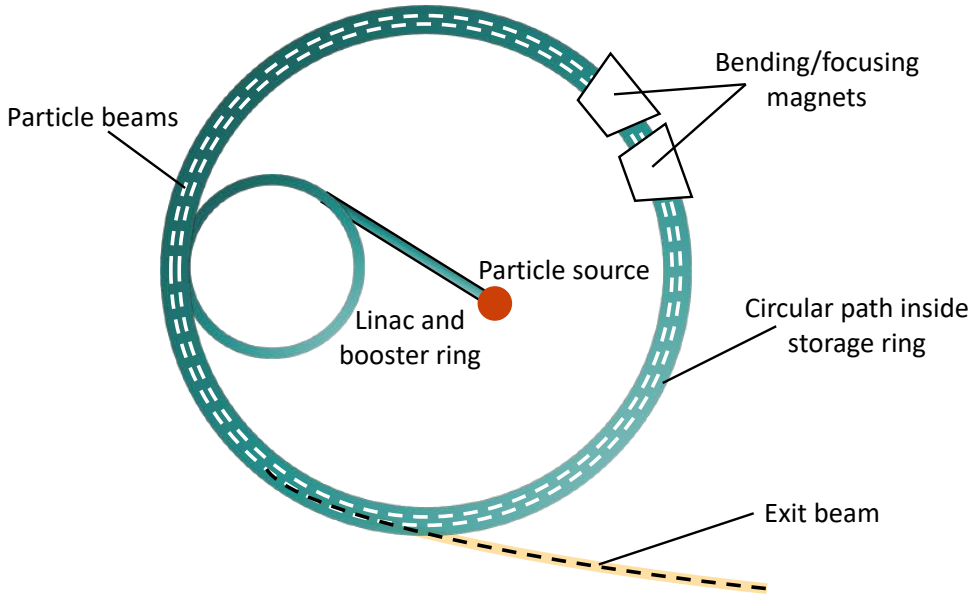

Figure 1.19: General scheme of a synchrotron

IV.2 Modalities of beam delivery

IV.2.1 Passive scattering

Passive scattering remains a fundamental technique in heavy ion therapy, employed with both cyclotrons and synchrotrons. This method utilizes physical scattering devices such as range modulators and compensators to shape the therapeutic beam before it enters the patient's body, as shown in Figure 1.20 (a).

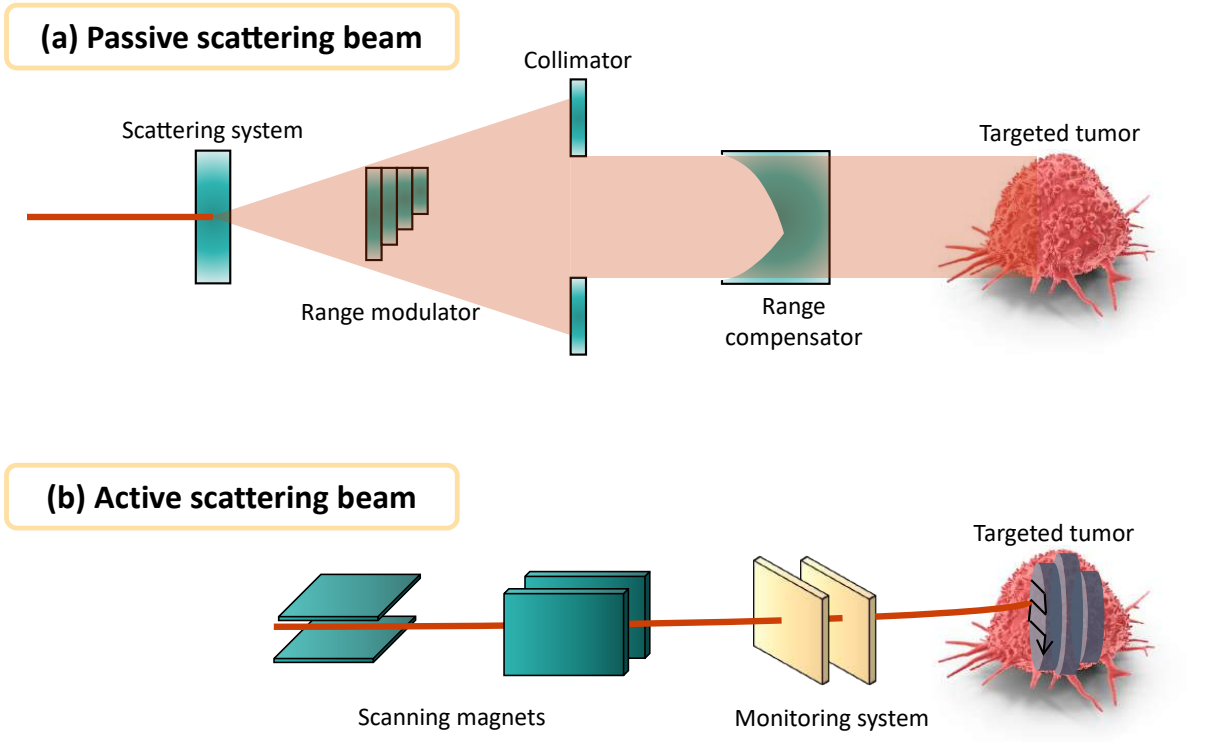

Figure 1.20: Scheme of passive (a) and active (b) scattering beam used in heavy ion therapy.

Range modulators adjust the energy of the incoming ions to align the Bragg peak with the tumor depth, while compensators compensate for variations in tissue density along the beam path. Passive scattering ensures a uniform dose distribution across the target volume, making it effective for treating relatively homogeneous tumors with well-defined geometries.

IV.2.2 Pencil beam scanning (PBS)

Pencil beam scanning, also known as spot scanning, is an advanced delivery technique that has gained prominence in heavy ion therapy, especially with synchrotron-based facilities. PBS involves scanning a narrow ion beam point by point across the tumor volume, with dynamic modulation of beam intensity and energy during delivery, as shown in Figure 1.20 (b).

This allows for precise dose deposition within the tumor while sparing surrounding healthy tissues. PBS offers advantages for treating irregularly shaped tumors or those located near critical organs, as it can conform closely to the tumor shape and size, delivering highly conformal dose distributions.

IV.3 Types of ions utilized

IV.3.1 Protons

Proton therapy, typically delivered using cyclotrons, remains a pillar of heavy ion therapy. Protons possess favorable physical properties for medical applications, including a finite range and a characteristic Bragg peak, making them suitable for precise tumor targeting while sparing healthy tissues. Proton therapy has demonstrated efficacy in treating various cancer types such as in tumors located near critical organs or in pediatric patients where minimizing radiation exposure to healthy tissues is primordial.

IV.3.2 Carbon ions

Carbon ion therapy, often delivered using synchrotrons, offers distinct advantages over proton therapy, particularly for treating radioresistant or deep-seated tumors. Carbon ions exhibit higher biological effectiveness, as shown in Figure 1.15, due to their increased mass and charge, as well as an enhanced ability to induce complex DNA damage in tumor cells. The sharp Bragg peak and high LET of carbon ions enable precise dose delivery, making them effective for treating challenging clinical scenarios.

IV.3.3 Other heavy ions

In addition to protons and carbon ions, other heavy ions such as helium, oxygen, lithium and neon are being investigated for their potential applications in heavy ion therapy. Each ion type offers unique physical and biological properties that can be tailored to specific treatment goals, expanding the therapeutic options available for clinicians and researchers.

V. Treatment plan, simulation codes, and models

In the previous section, we delved into the distinctive characteristics of high-energy photons and heavy ions within the context of radiation therapy. High-energy photons exhibit a dose buildup phenomenon, shifting the peak dose away from the body's surface due to scattered Compton electrons.

On the other hand, protons and heavier ions present a notable Bragg peak at the termination of their path, accompanied by a comparable biological effect. Understanding these features is important for optimizing radiation therapy, where precision and efficacy are interplayed.

V.1 Treatment planning generalities

The precision in treatment planning for hadrontherapy demands for accurate evaluation of uncertainties inherent to the ballistic trajectories of charged particles. These uncertainties arise from various sources, including imaging-related factors, patient positioning errors, and changes in tumor volume or patient anatomy.

V.1.1 Spread-Out Bragg Peak (SOBP)

Bragg peak allows for the deposition of maximum energy at a given depth. However, tumors often exhibit dimensions on the order of several centimeters, necessitating the

variation of the Bragg peak position to irradiate the entire tumor.

This modulation of the Bragg peak, called Spread-Out Bragg Peak (SOPB), can be achieved by employing a mono-energetic incident beam with various elements (such as scattering systems, range modulators, attenuators, etc.) to broaden the energy spectrum of incident ions and thus weighting the Bragg Peaks. Figure 1.21 illustrates the principle of the SOPB with an accumulation of peaks at different depths, the sum of which yields the plateau in dose distribution, the SOBP.

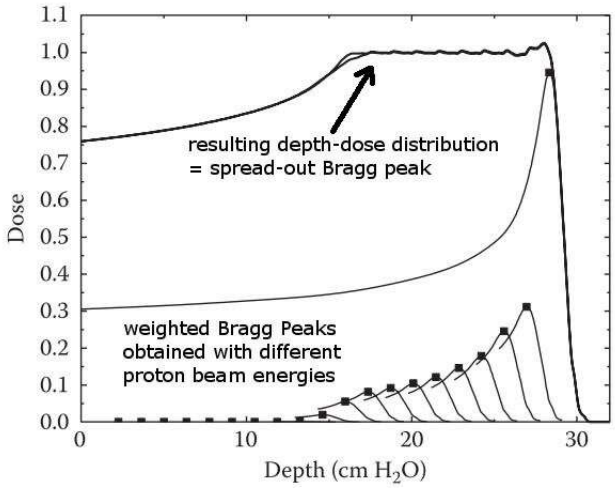

Figure 1.21: Scheme of passive (a) and active (b) scattering beam used in heavy ion therapy.

V.1.2 Target volume definition

One critical aspect is the definition of target volumes during tumor contouring. Internationally recognized guidelines distinguish between the Gross Tumor Volume (GTV), representing identifiable tumor mass, the Clinical Target Volume (CTV) to encompass invisible malignant cells, and the Planning Target Volume (PTV), accounting for machine-related uncertainties, as shown in Figure 1.22. The inclusion of margins accommodating these uncertainties are vital for treatment accuracy.

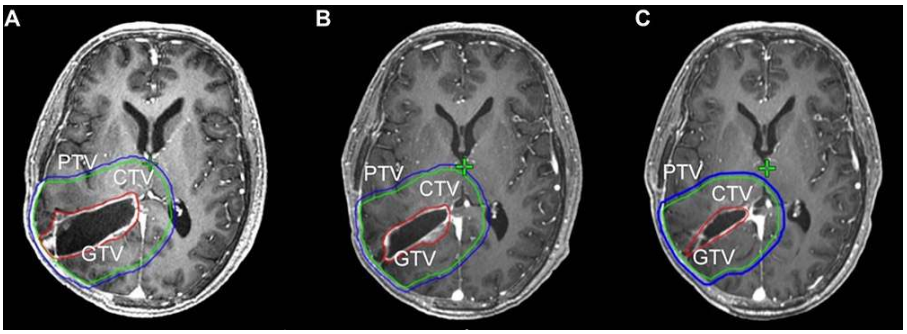

Figure 1.22: Target volumes example on head cancer. The GTV, CTV, and PTV are shown as red, green, and blue solid lines, respectively.[12]

V.2 Dose uncertainties

In conventional radiotherapy, slight changes in the traversed materials have limited impact on the delivered dose within the tumor volume and surrounding tissues due to the nature of the energy deposition profile of photons, as demonstrated in Figure 1.23.

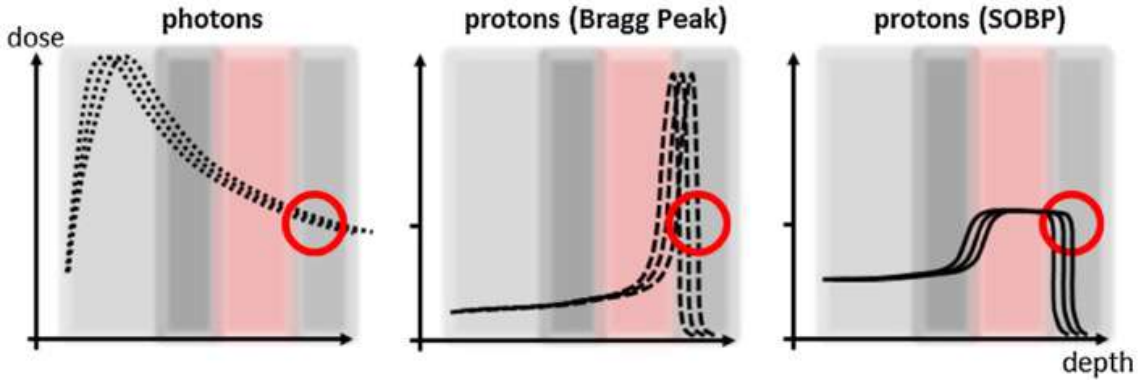

Figure 1.23: Scheme illustrating the impact of path uncertainties on dose distribution for both photons and protons.[13].

However, the consequences of such changes differ for charged particles: the significant dose gradient at the Bragg peak implies that even a slight deviation in the path of these particles within the material will result in over-irradiation of healthy tissues and under-irradiation of the tumor volume. The precision in particle path determination is conditioned by various parameters, including uncertainties related to imaging, patient positioning errors, tumor volume changes, and patient anatomy alterations.

V.2.1 CT scan uncertainties

In hadrontherapy, the specific ballistic characteristics of charged particles introduce additional uncertainties. While slight material changes minimally affect photon dose deposition, charged particles, due to their dose profile, are highly sensitive to variations in their path through tissues. Critical to this sensitivity is the conversion from X-ray CT images to Relative Stopping Power (RSP) used for treatment planning. This calibration, inherently imprecise due to differences in interaction mechanisms between diagnostic photons and therapeutic charged particles, contributes to uncertainties.

Uncertainties related to the image itself (voxel size, partial volume effects, beam hardening, potential artifact presence, etc.) contribute. Consequently, depending on the treatment centers, uncertainties in the paths of charged particles range between 2.4% and 4.6%, with corresponding margins ranging from 1 to 3 mm [25].

Reducing these margins is a major challenge in hadron therapy as they diminish the potential of this treatment technique. They necessitate selecting the beam direction to ensure no at-risk organ lies downstream of the distal edge of the Spread-Out Bragg Peak (SOBP) plane to avoid over-irradiation of critical structures. Beam directions are generally chosen to adjust the lateral penumbra to spare surrounding healthy tissues. Thus, the ballistic advantage of hadron therapy is not fully exploited. Figure 1.24 illustrates these various strategies for irradiating the same tumor volume.

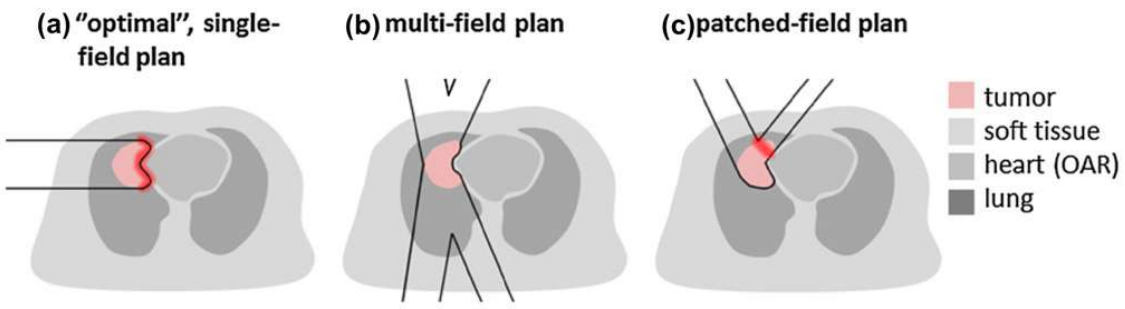

Figure 1.24: Different strategies for irradiation of the same tumor volume: (a) single-field irradiation with minimal irradiation of healthy tissues, but risk of over-irradiation of the OAR (organ at risk) located behind the volume target ; (b) multi-field irradiation reducing the risk of irradiation of the OAR but increasing the dose delivered to healthy tissues; (c) compromise between situations (a) and (b).[13].

V.2.2 Treatment planning simulations

Concerning the physical dose, Monte Carlo simulation codes play an important role in predicting and modeling the behavior of radiation beams within the human body. These sophisticated codes are powered by algorithms and computational models to simulate the interaction of radiation with tissues.

Simulation codes enable the accurate prediction of radiation dose distribution within the patient's anatomy. By implementing parameters such as beam energy, beam angles, and patient-specific anatomical data, these codes simulate the path of radiation through tissues, ensuring that the targeted tumor receives an effective dose while minimizing exposure to surrounding healthy tissues.

Clinicians can explore various scenarios by adjusting factors such as beam intensity, shape, and duration, seeking an optimal equilibrium between tumor control and healthy tissue sparing. Advanced simulation codes also facilitate real-time adaptation during treatment sessions. By integrating feedback from imaging modalities and treatment delivery systems, these codes can dynamically adjust treatment parameters to account for changes in patient anatomy or tumor position.

Jointly with simulation codes, computational models provide a theoretical framework for understanding the complex interactions between radiation and biological tissues. These models incorporate radiobiological physical and chemical principles to estimate the biological effectiveness of different radiation modalities. However, there is currently a lack of experimental data regarding nuclear reactions in particle therapy, which can introduce inaccuracies in dose calculations.

V.2.3 Dose calculation uncertainties

Both physical and biological dose uncertainties need to be considered during treatment planning. For instance, from a biological point of view, the RBE for treatment planning in proton therapy is considered as a constant value of 1 or 1.1. However, LET inscreases along the particle path, and the RBE will inscrease with it, as can be seen in Figure 1.25. The RBE consideration in the treatment plan could help to limit the dose uncertainties in healthy tissues, notably organs at risk.

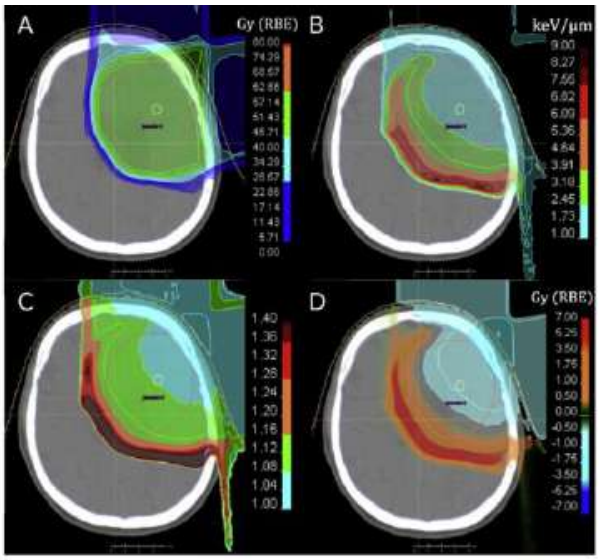

Figure 1.25: Proton treatment plan for a primary brain tumor patient with a prescribed dose of 60 Gy(RBE) to the CTV. (A) Absorbed physical dose D Phys ; (B) LET distribution; (C) variable RBE distribution based on measured in vitro RBE data, which depend on dose and LET; (D) difference in RBE-weighted dose [14].

Concerning the physical dose uncertainties in carbon ion therapy, the dose contribution from secondary particles generated through fragmentation is not taken into account. Indeed, inside the Bragg peak, they can contribute in the order of 5% of the total dose, and are responsible for the dose tail behind it. Generally, the LET of those secondary particles is higher, as can be shown in Figure 1.26 with the dose and LET distributions. Indeed, considering prostate cancer with proton treatment, the secondary protons dose contribution along the beam path reaches 6%, and delivers a higher LET than the beam at the end of their path. This contribution cannot be ignored because of the possible position or organs at risk behind the tumor and thus need to be simulated and predicted in the treatment plan algorithms.

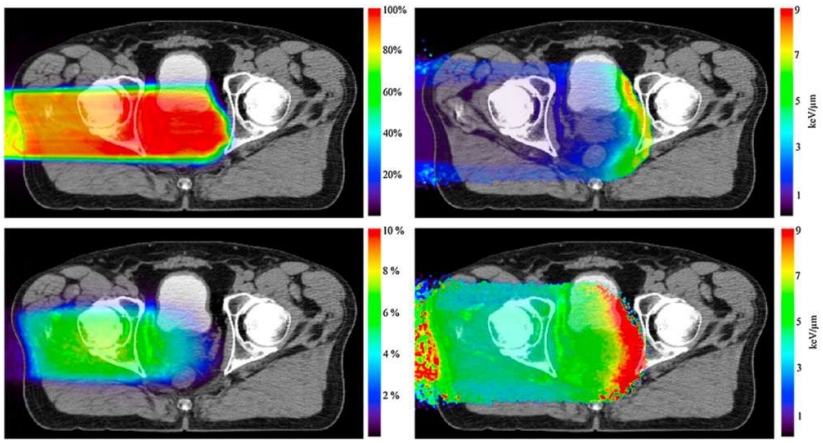

Figure 1.26: Dose and LET distribution for prostate cancer treatment with a proton beam. On (a) and (b) are presented the primary protons distributions and on (c) and (d) the secondary protons one, coming from nuclear reactions with the target. [15]

V.3 Margins and uncertainties reduction

Efforts to minimize margins in treatment planning are explored, aiming to exploit the full ballistic advantage of hadron therapy.

Imaging advancements, coupled with optimization techniques, offer opportunities to reduce margins and maximize the therapeutic potential of charged particle beams. Furthermore, real-time adaptation strategies during treatment sessions, exploiting the imaging feedback, promise to enhance precision.

V.3.1 Margins reduction

One possibility is to improve the imaging techniques used to obtain a more precise estimation of the Relative Stopping Power (RSP). Charged particle imaging (primarily proton, but also helium or carbon) could reduce uncertainties in RSP by employing the same probe for both diagnosis and treatment.

Several proton imaging prototypes are in development [26, 27, 28], with demonstrated precision of around 1% in proton path estimation [29, 30]. However, no prototype is currently used in clinical routine, mainly due to the high acquisition rates ($>$ 100 MHz) required by this imaging technique. Dual Energy Computed Tomography (DECT) imaging also drastically reduces RSP uncertainties to around 1% [31, 32], down to 0.4% depending on tissue type [33]. This imaging technique, already available clinically, uses two photon energies, unlike conventional X-ray imaging to scan an object.

The importance of margin reduction is illustrated in Figure 1.27, where two proton treatment plans are simulated with respective uncertainties of 1% and 3.5% on the path, showing the dose difference and thus significantly higher irradiation on radiosensitive brain part like the nerves.

V.3.2 Biological uncertainties reduction

Numerous studies focus on optimizing biological rather than physical dose in treatment plans. This optimization involves considering the variability of RBE along the path of charged particles. Accounting for this effect is particularly important for high-LET particles, such as helium or carbon.

Figure 1.28 presents a comparison between a fixed and a variable RBE on dose distribution and biological effects. This figure demonstrates that significant increases in LET values in the tumor and a significant reduction in normal structures is possible.

Treatment plan optimization based on biological rather than physical dose heavily depends on precise RBE measurement. Overestimation of RBE can lead to underdosing in the tumor volume. To mitigate RBE dependence, it has been proposed to combine optimization of physical dose and LET to deliver maximum LET in the tumor zone.

V.3.3 Nuclear reactions measurements

As demonstrated in the preceding paragraph, controlling the delivered LET distribution in the tumor zone is crucial to limit over-irradiation in critical areas. While the LET of incident particles must be considered for treatment plan optimization, the secondary particles produced by nuclear reactions of the incident beam with tissues must also be taken into account.

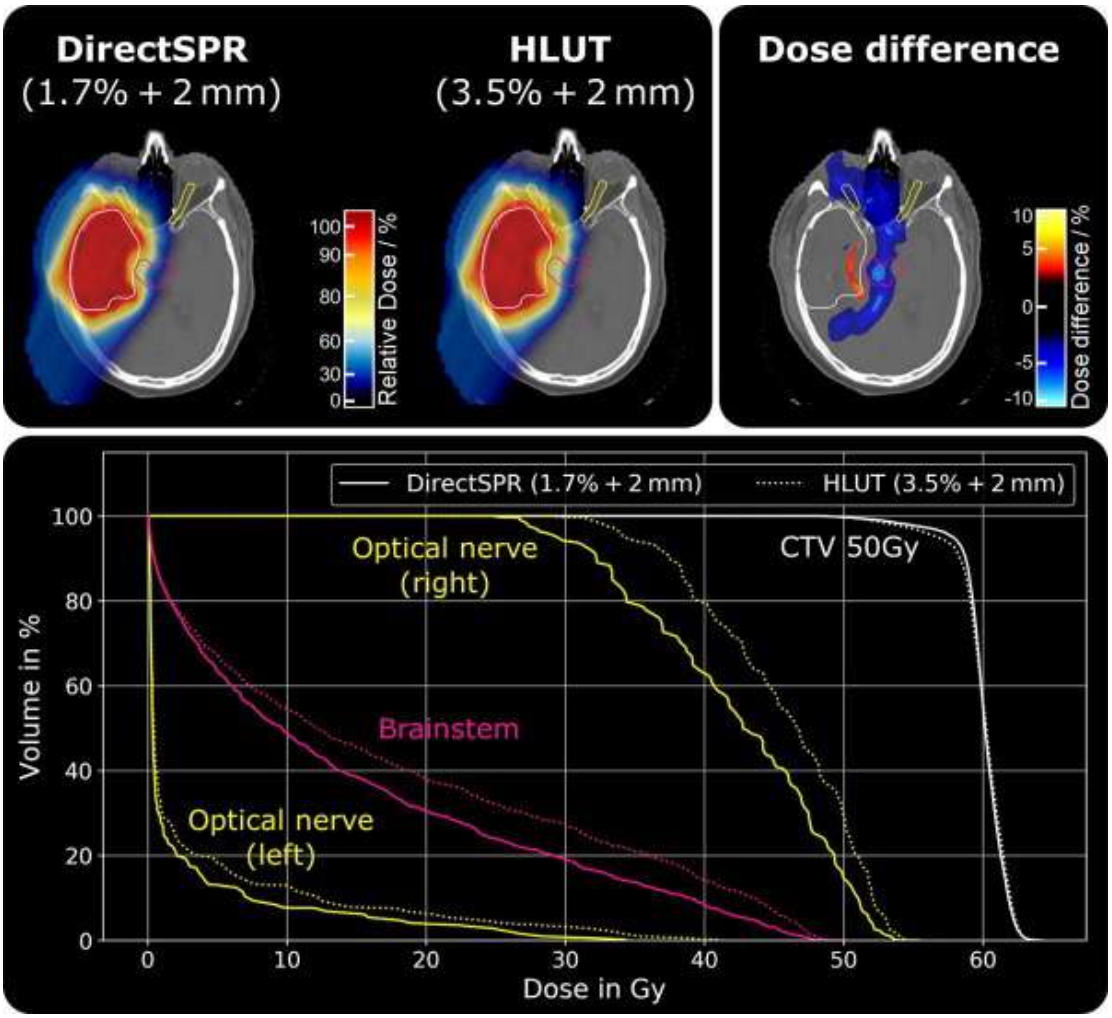

Figure 1.27: (Top) Clinical treatment plan of a glioblastoma patient calculated using the DirectSPR method with the reduced range uncertainty margin (1.7% + 2mm) in comparison to the use of a Hounsfield look-up table (HLUT) with the old clinical margin (3.5% + 2mm). (Bottom) Corresponding dose-volume histogram. The prescribed dose to the target is 60 Gy. Target volume (white), the brainstem (pink) and the optical nerves (yellow) are indicated. [16]

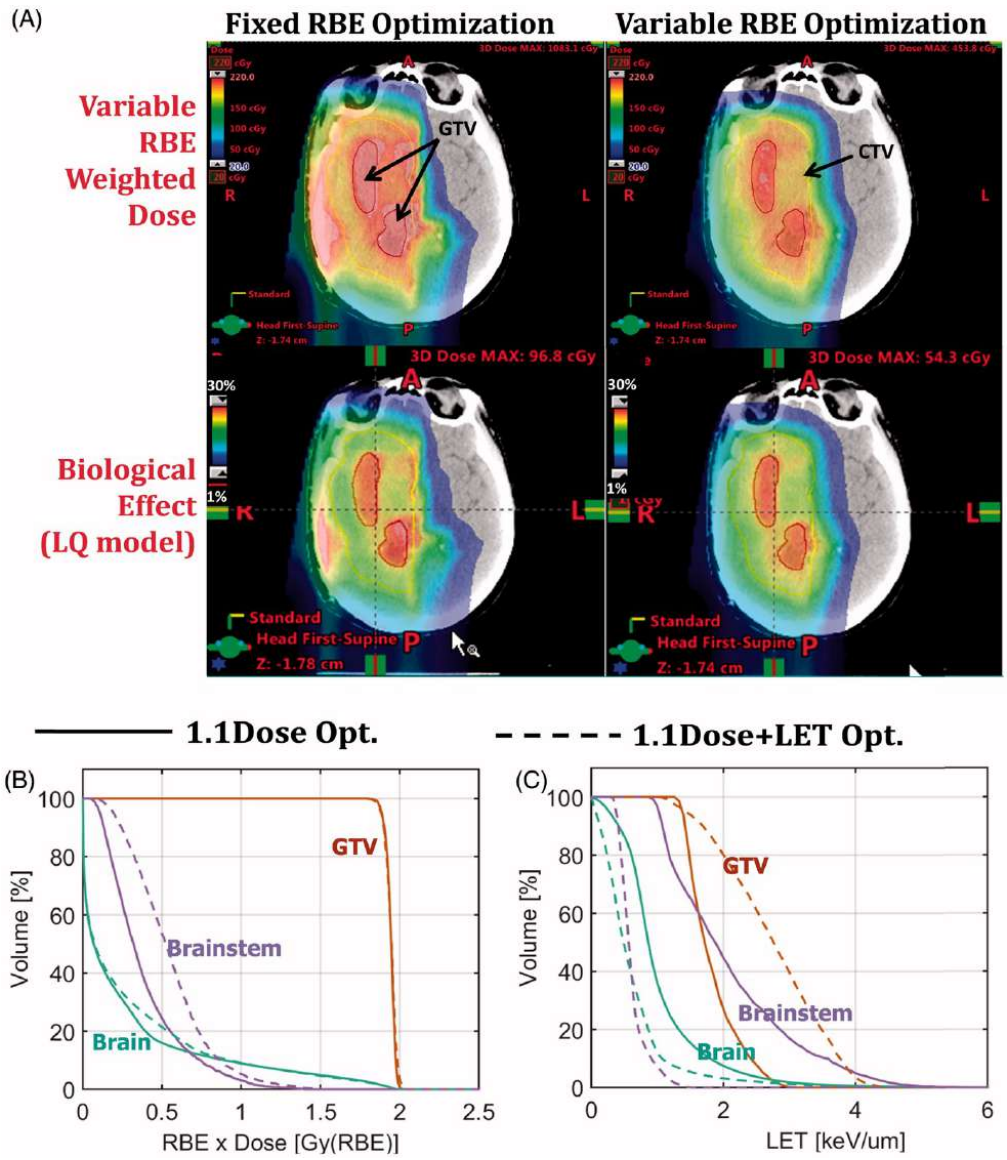

Figure 1.28: (A) Comparison of a glioblastoma IMPT plan optimized using criteria defined in terms of fixed RBE (RBE=1.1) vs. the plan optimized using criteria defined in terms of variable RBE. The top two panels display dose distributions in terms of variable RBE-weighted dose whereas the bottom two panels display biological effect in terms of (1-surviving fraction) calculated using the linear-quadratic model. Panels (B) and (C) compare a pediatric brain tumor IMPT plan optimized based on criteria defined in terms of RBE 1.1-weighted dose vs. a plan based on the same criteria plus additional terms that control LET in the target and normal structures. Panel (B) compares the RBE 1.1-weighted DVHs for the GTV, brainstem and normal brain, whereas panel (C) compares the corresponding LET-volume histograms. [17]

These lighter secondary particles generally have a much higher LET than the incident beam and can interact outside the tumor volume, potentially contributing to over-irradiation of healthy tissues. Currently, effective cross-section data of nuclear reactions responsible for producing these secondary particles are incomplete, especially for incidents involving carbon and oxygen. Measurements of these effective cross-sections are thus necessary to implement them in treatment plan calculations.

In Figure 1.29, a comparison between different simulation models and experimental data for absolute differential angular cross-sections on carbon target for different particles, shows discrepancies between data and models but also between models. Enhancing the measurements of nuclear reaction cross-sections within the simulation models is thus necessary.

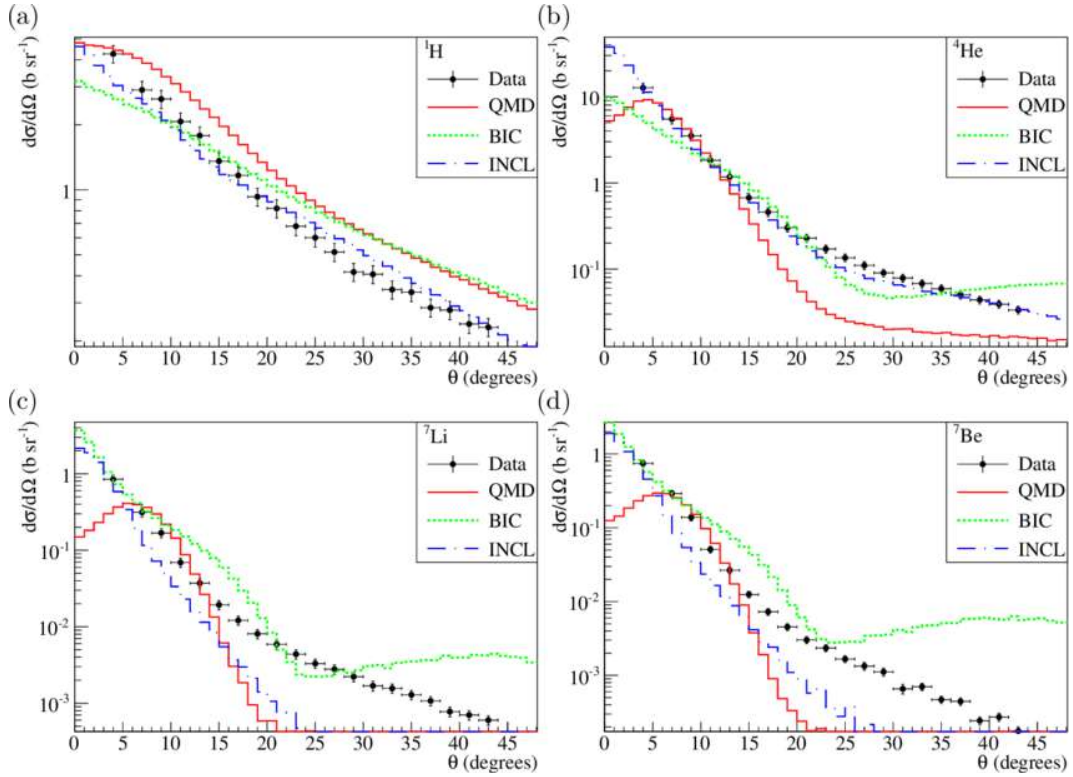

Figure 1.29: Absolute differential angular cross-sections of protons, ^{4}He, ^{6}Li, ^{7}Be, obtained for the carbon target. .[18]

Dose monitoring

The significant sensitivity of charged particle dose deposition to the composition of the traversed medium raises the question of verifying the conformity of the delivered dose to the tumor volume. Since secondary particles produced by nuclear reactions of the incident beam can potentially exit the patient, monitoring irradiation of the tumor volume can be considered, using the existing correlation between the production of these particles and the path of the primary beam.

A commonly cited advantage for implementing this monitoring is the possibility of doing it online, meaning in real-time during treatment. Among these path verification techniques are:

- **Prompt monitoring**, which utilizes the prompts photons produced by the de-excitation of nuclei resulting from nuclear reactions of the particle beam with the target.
- Secondary charged particle monitoring (or IVI, **Interaction Vertex Imaging**), mainly used for verifying the path of particles heavier than the proton.
- **Positron Emission Tomography** (PET) imaging, which benefits from the production of positron emitters along the path of the incident beam, and can also be performed "offline" (after treatment).
- **Detection of acoustic waves** generated by the energy loss of incident ions.

VI. Conclusion

Cancer treatment options typically include surgery, chemotherapy, radiotherapy, and immunotherapy, each chosen based on factors like cancer type, stage, and patient health. However, selecting the most suitable treatment involves a careful balance between benefits and potential side effects, influenced by factors like affordability and healthcare infrastructure, leading to global variations in accessibility.

Innovations in radiotherapy, particularly particle therapy utilizing charged particles such as protons and carbon ions, offer distinct advantages due to their ballistic properties. While the global adoption of charged particle therapy has increased, challenges remain, notably the high costs of dedicated facilities.

Charged particle therapy is particularly beneficial for treating tumors with complex geometries near critical organs, pediatric tumors, and radio-resistant tumor sites. However, addressing tumors in highly mobile regions requires precise tracking methods. Indeed, secondary particles are produced along the beam and create a dose tail after the Bragg peak.

Understanding the underlying nuclear physics interactions involving charged particles, photons, and neutrons is crucial, alongside their effects such as radiobiological effectiveness (RBE) and oxygen enhancement ratio (OER).

To mitigate margins and uncertainties in treatment planning, secondary particles need to be measured and characterized. It permits to predict the additional dose contributed by these particles and thus also comprehensively understanding their chemical and biological impact on the patient. Furthermore, leveraging secondary particles for dose monitoring offers the possibility of real-time monitoring in treatment delivery, thereby enhancing accuracy and patient safety.

Summary

Introduction à l'hadronthérapie

La hadronthérapie, ou thérapie par particules, est une méthode de traitement des cancers utilisant des particules chargées telles que les protons et les ions carbone. Contrairement à la radiothérapie conventionnelle, qui utilise des rayons X, la hadronthérapie permet de cibler les tumeurs avec une plus grande précision. Cette technique repose sur les propriétés balistiques uniques des particules chargées, qui déposent la majeure partie de leur énergie à une profondeur spécifique, formant un pic de Bragg. Cela permet de maximiser la dose délivrée à la tumeur tout en minimisant les dommages aux tissus sains environnants. Le développement de la hadronthérapie est motivé par le besoin de traiter des tumeurs résistantes aux traitements conventionnels et celles situées près d'organes à risque où les effets secondaires de la radiothérapie traditionnelle seraient dangereux.

Interaction entre les radiations et la matière

Les interactions entre les particules chargées (électrons, positrons, protons, ions lourds) et les particules neutres (neutrons) avec la matière sont variées et complexes. Ces interactions peuvent être classées en excitation et ionisation des atomes. Lors de l'excitation, les électrons des atomes sont poussés à des niveaux d'énergie plus élevés, tandis que l'ionisation entraîne l'éjection d'électrons, créant des ions positifs et des électrons libres. Les photons interagissent principalement via l'effet photoélectrique, la diffusion Compton et la production de paires. Les neutrons, étant des particules neutres, interagissent différemment, principalement par diffusion et capture. La compréhension de ces mécanismes est cruciale pour optimiser l'efficacité du traitement par hadronthérapie, car elle permet de prédire avec précision la distribution de la déposition d'énergie dans le corps du patient.

Variables importantes

La section efficace est une mesure clé de la probabilité qu'une interaction se produise entre deux particules. Elle est définie par la fraction moyenne des particules déviées par unité d'angle solide, prenant en compte le flux des particules incidentes par unité de surface et de temps.
Une autre variable importante est la trajectoire moyenne sans collision, ou le libre parcours moyen, représentant la distance moyenne parcourue par une particule avant une interaction. La perte d'énergie des particules lors de leur passage à travers la matière peut entraîner des phénomènes comme l'excitation, l'ionisation et l'agitation thermique des atomes et des molécules.

Aspects biologiques de la thérapie par ions lourds

La hadronthérapie provoque des dommages directs et indirects à l'ADN des cellules cancéreuses, provoquant une hausse de la mortalité cellulaire par rapport aux rayonnements conventionnels. Le modèle linéaire-quadratique (LQ) est souvent utilisé pour modéliser la survie cellulaire en fonction de la dose absorbée. Les particules à haute LET (Transfert Linéaire d'Énergie) telles que les ions carbone ont une efficacité biologique relative (RBE) plus élevée, ce qui renforce leur capacité à détruire les cellules tumorales. Ces effets biologiques doivent être pris en compte lors de la planification du traitement pour maximiser l'efficacité thérapeutique.

Dose absorbée et efficacité biologique

La dose absorbée est une mesure de l'énergie déposée par unité de masse de tissu, exprimée en Grays (Gy). La dose absorbée ne tient pas compte du type de radiation, ce qui est crucial car différentes particules ont des efficacités biologiques différentes. L'efficacité biologique relative (RBE) est utilisée pour comparer l'efficacité des différentes radiations à induire des dommages biologiques. Le RBE est défini comme le rapport de la dose d'une radiation de référence (comme les rayons X) à la dose de la radiation étudiée produisant le même effet biologique. La capacité des ions lourds à infliger des dommages complexes et irréparables à l'ADN des cellules cancéreuses leur confère un RBE élevé, les rendant particulièrement efficaces pour tuer les cellules tumorales.

Oxygène et radiosensibilité

L'oxygène joue un rôle crucial dans la radiosensibilité des cellules. Les dommages causés par les radiations sont amplifiés en présence d'oxygène, un phénomène connu sous le nom d'effet de rehaussement de l'oxygène (OER). Les cellules hypoxiques (pauvres en oxygène) sont plus résistantes aux radiations, nécessitant des doses plus élevées pour atteindre le même niveau de destruction cellulaire. Cela pose un défi particulier en radiothérapie, où l'hétérogénéité de l'oxygénation tumorale peut affecter l'efficacité du traitement. Les ions lourds, grâce à leur LET élevé, sont moins affectés par l'hypoxie, ce qui les rend particulièrement utiles pour traiter les tumeurs hypoxiques.

Accélérateurs cliniques et distribution des faisceaux

Deux principaux types d'accélérateurs sont utilisés en hadronthérapie : les cyclotrons et les synchrotrons. Les cyclotrons sont adaptés pour les protons et les ions légers, tandis que les synchrotrons peuvent accélérer des ions plus lourds comme les ions carbone. La distribution des faisceaux se fait par diffusion passive ou balayage fin, chaque méthode offrant des avantages spécifiques pour le traitement de différentes formes et localisations de tumeurs. La précision de ces techniques permet de cibler les tumeurs tout en réduisant l'impact sur les tissus sains environnants.

Types d'accélérateurs

Les cyclotrons et les synchrotrons jouent des rôles distincts dans la production de faisceaux de particules pour la thérapie par ions lourds. Les cyclotrons, avec leur conception compacte et leur capacité à produire des faisceaux continus de protons et d'ions légers, sont couramment utilisés pour les traitements nécessitant des énergies plus basses.

Les synchrotrons, en revanche, peuvent accélérer des particules plus lourdes à des énergies plus élevées, ce qui est essentiel pour traiter des tumeurs situées profondément dans le corps. Les synchrotrons permettent également une modulation précise de l'énergie et de l'intensité du faisceau, offrant une flexibilité supplémentaire dans la planification du traitement.

Modalités de distribution des faisceaux

La distribution des faisceaux en hadronthérapie peut se faire par diffusion passive ou par balayage fin. La diffusion passive utilise des dispositifs de modulation d'énergie et de compensation pour façonner le faisceau avant qu'il n'entre dans le corps du patient.

Cette méthode est efficace pour traiter des tumeurs relativement homogènes avec des géométries bien définies. Le balayage fin, ou pencil beam scanning (PBS), est une technique plus avancée qui implique le balayage d'un faisceau étroit point par point à travers le volume tumoral, avec une modulation dynamique de l'intensité et de l'énergie du faisceau. Cette technique permet une distribution de dose hautement conforme, minimisant l'exposition des tissus sains.

Planification du traitement, codes de simulation et modèles

La planification du traitement en hadronthérapie nécessite des simulations précises pour modéliser la distribution de la dose dans le corps du patient. Les codes de simulation Monte Carlo sont couramment utilisés pour prédire le comportement des faisceaux de radiations, intégrant les effets physiques, chimiques et biologiques. Ces simulations permettent d'optimiser la dose délivrée à la tumeur tout en minimisant l'exposition des tissus sains. Cependant, des incertitudes persistent, notamment en raison des réactions nucléaires secondaires et des variations biologiques et chimiques le long du trajet des particules.

Simulations Monte Carlo

Les simulations Monte Carlo sont des outils puissants pour la planification du traitement en hadronthérapie. Elles permettent de modéliser les interactions complexes des particules avec les tissus, en tenant compte des effets physiques comme la diffusion et l'ionisation, ainsi que des effets biologiques comme les dommages à l'ADN. Ces simulations nécessitent des calculs intensifs, mais elles fournissent des informations détaillées sur la distribution de la dose et les effets biologiques potentiels, permettant une planification du traitement plus précise et efficace.

Contributions des particules secondaires à la dose

Les particules secondaires produites lors des réactions nucléaires peuvent avoir un LET élevé, ce qui signifie qu'elles peuvent causer des dommages biologiques significatifs aux tissus sains. Il est donc crucial de prendre en compte ces contributions dans les algorithmes de planification du traitement pour éviter une irradiation excessive des organes à risque situés derrière la tumeur. Cependant, les models physiques actuels des réactions nucléaires sont en désaccord avec les données expérimentales, ce qui peut induire des incertitudes dans le calcul de dose.

Planification et incertitudes

La planification du traitement en hadronthérapie doit également tenir compte des incertitudes associées aux images de tomodensitométrie (CT) utilisées pour la planification, aux erreurs de positionnement du patient et aux changements de volume tumoral ou de l'anatomie du patient. Les incertitudes liées à la conversion des images CT en pouvoir d'arrêt relatif (Relative Stopping Power - RSP) peuvent entraîner des erreurs dans la distribution de la dose. Des techniques avancées d'imagerie et des algorithmes d'optimisation sont nécessaires pour réduire ces incertitudes et améliorer la précision du traitement.

Réduction des marges et des incertitudes

Pour maximiser l'efficacité thérapeutique tout en minimisant les risques pour les tissus sains, il est crucial de réduire les marges d'incertitude. Des techniques d'imagerie avancées, telles que l'imagerie par protons et la tomodensitométrie à double énergie, sont en développement pour améliorer la précision des estimations de la pouvoir d'arrêt relative (RSP). De plus, l'optimisation des plans de traitement en tenant compte des effets biologiques variables des particules lourdes est essentielle pour améliorer les résultats cliniques. La recherche continue et les améliorations technologiques sont nécessaires pour réduire ces incertitudes et exploiter pleinement le potentiel de la thérapie par ions lourds.

Imagerie avancée

L'imagerie avancée joue un rôle crucial dans la réduction des marges d'incertitude en hadronthérapie. L'imagerie par protons, par exemple, utilise les mêmes particules que celles utilisées pour le traitement, permettant une estimation plus précise du RSP. Bien que cette technique soit encore en développement, elle montre un grand potentiel pour améliorer la précision de la planification du traitement.

Optimisation biologique

L'optimisation des plans de traitement basée sur des considérations biologiques plutôt que physiques est une autre approche pour réduire les incertitudes. Cette méthode prend en compte la variabilité du RBE le long du trajet des particules, ce qui est particulièrement important pour les particules à haute LET comme les ions de carbone. En optimisant à la fois la dose physique et le LET, il est possible de maximiser l'efficacité thérapeutique tout en minimisant les dommages aux tissus sains.

Incertitudes physiques secondaires et réactions nucléaires

Les incertitudes physiques liées aux réactions nucléaires secondaires représentent un défi majeur en hadronthérapie. Lorsqu'un faisceau de particules chargées interagit avec les tissus, des réactions nucléaires peuvent se produire, produisant des particules secondaires telles que des neutrons, des protons secondaires et d'autres fragments. Ces particules secondaires peuvent contribuer à la dose totale reçue par les tissus sains et doivent être prises en compte dans la planification du traitement.

Mesures des sections efficaces de réaction nucléaire

Pour améliorer la précision des simulations de planification du traitement, il est essentiel de disposer de données précises sur les sections efficaces des réactions nucléaires. Ces sections efficaces déterminent la probabilité de production de particules secondaires lors de l'interaction du faisceau principal avec les tissus. Actuellement, les données disponibles pour certaines réactions nucléaires, notamment celles impliquant des ions lourds comme le carbone et l'oxygène, sont insuffisantes. Des mesures expérimentales supplémentaires sont nécessaires pour combler ces lacunes et améliorer les modèles de simulation.

Surveillance et vérification des doses
La sensibilité des doses de particules chargées à la composition du tissu traversé soulève la question de la vérification de la conformité de la dose délivrée au volume tumoral. Les particules secondaires produites par les réactions nucléaires peuvent potentiellement sortir du patient, offrant une opportunité de surveiller l'irradiation en temps réel pendant le traitement. Les techniques de surveillance incluent la détection des protons prompts, l'imagerie par émission de positrons (PET), et la détection des ondes acoustiques générées par la perte d'énergie des ions incidents.

Conclusion

La thérapie par ions lourds représente une avancée significative dans le traitement des cancers, offrant des avantages en termes de précision et d'efficacité par rapport à la radiothérapie conventionnelle. Cependant, des défis subsistent, notamment en ce qui concerne les coûts élevés et la nécessité de réduire les incertitudes liées à la planification du traitement. La poursuite des recherches et des développements technologiques est essentielle pour maximiser les bénéfices cliniques de cette approche thérapeutique. Les avancées dans les techniques d'imagerie, les simulations Monte Carlo et l'optimisation des plans de traitement basés sur des considérations biologiques, chimiques et physiques, sont des domaines clés pour améliorer la précision et l'efficacité de la thérapie par ions lourds.

Chapter 2

Secondary particle detection and simulation

"I'm a mirrorball, I'll show you every version of yourself tonight."
– T. S.

Contents

To investigate the secondary charged particles produced during a treatment, a complementary work of detection and simulation of the physical processes involved is necessary.

This chapter aims to delve into the technical methodologies employed for the precise detection and identification of these particles within the clinical context, focusing on scintillator detectors, semiconductors detectors, and Geant4 simulation tools. The efficiency of these detection techniques hinges upon the interaction processes of charged particles with matter, presented in the preceding chapter.

I. Secondary charged particle detection

Scintillator and semiconductor detectors are typical active media in secondary particle detection in hadrontherapy. This section provides a focused examination of those detectors, their composition and their response to charged particles, alongside their efficiency.

I.1 Scintillation detector

I.1.1 Generalities

When radiation passes through a scintillating material, it excites the atoms and molecules within it, resulting in the emission of light. The light output is directly proportional to the incident energy above a certain minimum threshold.

Scintillators offer a fast time response compared to other detectors, characterized by short response and recovery times. This allows for precise measurement of time intervals between two events and thus higher count rates.

Moreover, certain scintillating materials exhibit pulse shape discrimination capabilities, making it possible to distinguish between different types of particles by analyzing the pulses shape of the light pulses produced upon interaction with the material.

Pulse shape discrimination arises from the presence of various decay components within the scintillator materials. For instance, cesium iodide (CsI) and barium fluoride (BaF2) are two examples of scintillator materials known for their pulse shape discrimination properties. In these materials, different types of particles induce distinct fluorescence mechanisms, leading to characteristic shapes in the light pulses. By analyzing these pulse shapes, it becomes possible to discern between particles with varying ionizing power, thereby enhancing the capabilities of radiation detection and characterization.

Scintillators exhibit the property of absorbing and reemitting energy in the form of visible light. Fluorescence is the phenomenon observed when the reemission process occurs within a short time frame, typically on the order of atomic transitions ($\sim 10^{-8}s$) [34]. In cases where reemission is delayed due to an excited metastable state, phosphorescence or afterglow may occur, taking a few microseconds to hours.

The time evolution of the reemission process can be described by the equation :

$$N = A\ exp\left(\frac{-t}{\tau_f}\right) + B\ exp\left(\frac{-t}{\tau_s}\right) \tag{2.1}$$

where τ_f and τ_s are decay constants and A, B the relative magnitudes.

An effective scintillator detector should exhibit high efficiency in converting incident energy into fluorescent radiation, be transparent to its own fluorescent radiation, emit light in a spectral range consistent with existing photomultiplier tubes (PMTs) sensitivity, and possess a short decay constant for rapid decay of the scintillation signal.

I.1.2 Organic and inorganic scintillators

Organic scintillators

Organic scintillators are composed of carbon-based compounds, typically containing atoms such as carbon, hydrogen, and nitrogen.

Organic plastic scintillators exhibit a fast decay time, typically within a few nanoseconds or less, and demonstrate an extremely fast signal response, with a duration of 2-3 nanoseconds. Their behavior can be mathematically described by the equation $N(t) = N_0 f(\sigma, t) \exp\left(\frac{-t}{\tau}\right)$, which represents the convolution of a Gaussian function with an exponential decay.

One major advantage of organic plastic scintillators is their flexibility in various applications. For instance, these scintillators can be easily machined into a wide range of shapes and sizes, making them adaptable to diverse experimental setups and detection requirements. Additionally, their non-hygroscopic nature ensures consistent performance even in humid environments.

Further details regarding the specific characteristics of the scintillators used in this study will be provided in Section I.1.4.

Inorganic scintillators

Inorganic scintillators are made of crystalline or non-crystalline inorganic materials. These materials can include various compounds such as alkali halides, rare-earth oxides, or heavy metal halides.

Inorganic crystal scintillators exhibit a response time generally of to two three times slower than organic scintillators, approximately 50 ns. This slower response is due to phosphorescence effects. While inorganic crystal scintillators offer advantages such as greater stopping power (resulting from their higher density and atomic number) and higher light outputs, and some of them also have a notable disadvantage compared to organic ones which is hygroscopicity.

Nevertheless, they are compatible for detecting gamma rays, high-energy electrons and positrons, charged particles and neutrons. When a radiation enters the crystal, it can ionize the crystal by exciting an electron from the valence band to the conduction band, generating either a free electron and a free hole or an exciton, where the electron and hole remain bound together as a pair, capable of moving freely through the crystal.

Light output response

The light output response varies for different types of particles at the same energy. The efficiency of a scintillation detector must consider the efficiency of the photomultiplier (PMT) coupled with it, which typically has an overall efficiency, taking into account both quantum and collection efficiencies, of around 30%.

While the relationship between light output and energy deposition is not strictly linear, it can be approximated as $L \propto \Delta E$ for many applications [34]. Temperature dependence of scintillators is generally weak at room temperatures, with organic scintillators being almost independent from temperature, while inorganic scintillators exhibit some sensitivity.

Additionally, pulse shape discrimination is observed in certain materials, where a substantial slow component exists, and the overall decay time of the emitted light pulse varies with the type of incident radiation.

In Table 2.1 can be found examples of the most commonly used scintillators alongside with their properties.

Detection efficiency

In terms of intrinsic detection efficiency for various radiations, electrons are efficiently detected by most scintillators with an efficiency close to 100%. However, their small mass can lead to significant scattering angles in matter, resulting in incident electrons being

Scintillator	Type	Light Output (ph/MeV)	Rise time (ns)	Energy resolution (%) for 100-1000 keV	Decay time (ns)
Cerium Bromide [35]	Inorganic	70-100	2-5	5-7	10-20
Sodium Iodide [36]	Inorganic	28-55	1-2	7-10	230
Lanthanum Bromide [37]	Inorganic	70-85	2-5	6-8	25-50
Bismuth Germanate [38]	Inorganic	8-14	0.5-1	3-5	300
Plastic [39]	Organic	10-30	0.5-2	10-15	2-6
Cesium Iodide [40]	Inorganic	20-40	1-3	6-8	100-150
Gadolinium Oxysulfide [41]	Inorganic	30-50	1-3	8-10	50-100
Zinc Sulfide [42]	Inorganic	15-25	1-2	8-12	100-200

Table 2.1: Examples of most commonly used scintillators alongside with their properties

backscattered or scattered out of the detector before depositing all their energy.

Gamma rays are more efficiently detected by materials with high atomic numbers (Z), and the scintillator must favor the photoelectric and pair production processes over the Compton process.

Neutron detection requires transferring all or part of the neutron's energy to a particle capable of ionizing and exiting the scintillator material. Fast neutron detection primarily relies on detecting the recoil proton in (n,p) scattering processes, for which plastics and other organic materials are suitable. Thermal neutron detection is achieved through (n,γ) or (n,α) nuclear reactions, and scintillators containing elements with high cross-sections for these reactions, such as lithium and boron, are employed.

Scintillators are generally not suitable for detecting heavy ions, due to their reduced light output caused by high ionizing power, inducing quenching effects and nonlinearities in the pulse response. Indeed, the total collected energy is proportional to the amplitude following the Birks' law [43]):

$$A = \frac{S * E + p}{1 + k_B * E} \tag{2.2}$$

where A is the amplitude of the pulse (mV), E is the deposited energy in the detector (MeV), S represents the scintillation efficiency, k_B the Birks coefficient, and p is the de-

tector pedestal.

There are, however, scenarios and techniques where scintillator detectors can still be effectively used for charged particles, including heavy ions.

Specialized scintillator formulations and coatings are designed to mitigate quenching effects and nonlinearities associated with heavy ions. Additionally, advanced detector designs featuring segmentation and pulse shape discrimination techniques enable the selective identification of heavy ions among background noise. Adjusting the energy threshold of scintillator detectors allows for the focused detection of charged particles, effectively minimizing undesirable effects [44, 45].

Integration of scintillator detectors into hybrid systems with other detector types, such as gas detectors or solid-state detectors, provides complementary information and enhances overall detection capabilities.

Calibration and correction procedures are crucial for compensating the nonlinear response of scintillator detectors to heavy ions.

Understanding and characterizing the detector's response enables the development of correction algorithms, ensuring accurate measurements in the presence of heavy ions.

I.1.3 Photomultiplier

Electron tube devices are utilized to convert light into a measurable electric current. In Figure 2.1 is presented a general scheme of a scintillator paired with a photomultiplier (PMT), grouping all the elements discussed in the preceding sections.

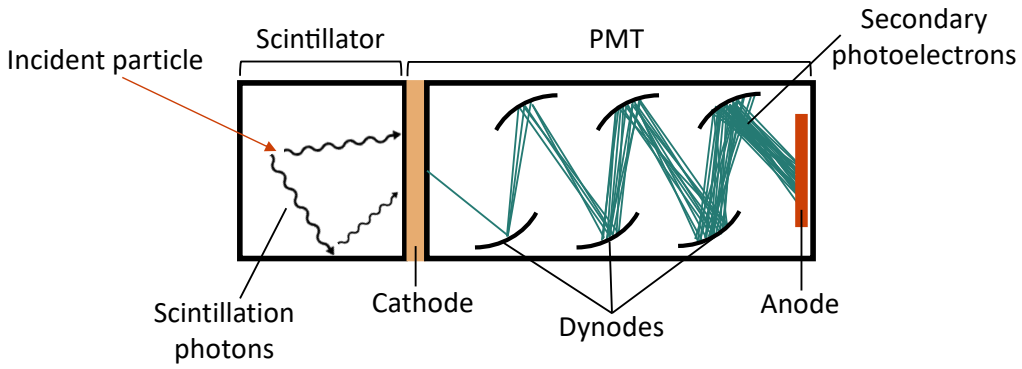

Figure 2.1: Scintillator detector coupled to a PMT simplified scheme

When an incident photon arrives on the photocathode, an electron is emitted through the photoelectric effect. Due to an applied voltage usually comprised between 500V and 2000V for all dynodes ladder, the electron is guided and accelerated towards the first dynode. Some of its energy is transferred to electrons within the dynode, leading to the emission and acceleration of secondary electrons towards the subsequent dynode. This process initiates an electron cascade.

The cascade of electrons is collected at the anode, resulting in an output current that can be amplified and analyzed. The relationship between the incident photon count and the current output is assumed to be linear for the cathode and dynode systems. Thus,

the current at the PMT output is directly proportional to the number of incident photons. By coupling the PMT with a scintillator that produces photons proportional to the deposited energy, information about the presence of particles and the remaining energy in the scintillator can be obtained.

The overall gain of the PMT, assuming equal division of the applied voltage among the dynodes, is given by the equation:

$$G = \delta^n = (kV_d)^n \tag{2.3}$$

where k is a constant and V_d the potential difference

Regarding time response and resolution, two primary factors influence the time resolution of the PMT. Firstly, variations in the transit time of electrons through the PMT play a role, and secondly, fluctuations due to statistical noise also affect the time resolution [34].

I.1.4 Detector setup: Plastic and $CeBr_3$ scintillators

In this thesis, a ΔE-E telescope composed of two scintillating detectors was employed: a thin plastic scintillator (ΔE) (organic plastic scintillator) and a thick crystal scintillator of Cerium Bromide, $CeBr_3$, (E) (inorganic crystal scintillator), big enough to stop ^{12}C ions up to 200MeV/u. A photo of this ΔE-E telescope is shown in Figure 2.2.

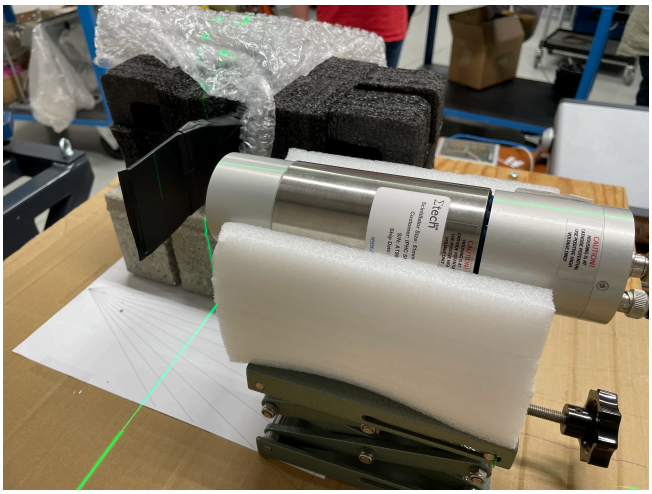

Figure 2.2: Photo of the ΔE-E telescope, made of the plastic scintillator (in black on the left) in front of the $CeBr_3$ scintillator in grey on the right.

The **$CeBr_3$ detector** is a cylindrical 2×2 inches crystal scintillator, from Advatech UK Ltd [19], coupled to a R6231-100 Hamamatsu photomultiplier (PMT). An entrance window in front of the crystal inside the $CeBr_3$ is made of 400 μm of aluminum and 1 mm of polytetrafluoroethylene (PTFE), used as a reflector. A scheme of this detector is shown on Figure 2.3.

To enable the detection of ions, such as ^{12}C, without inducing saturation within the system, a reduction in the high-voltage applied to the PMT was performed. Notably,

for protons and high-energy gammas, the voltage was attenuated from +600V to +350V, deviating from the customary operational voltage of approximately +1200V. This modification adheres to the recommendations outlined in [46, 47].

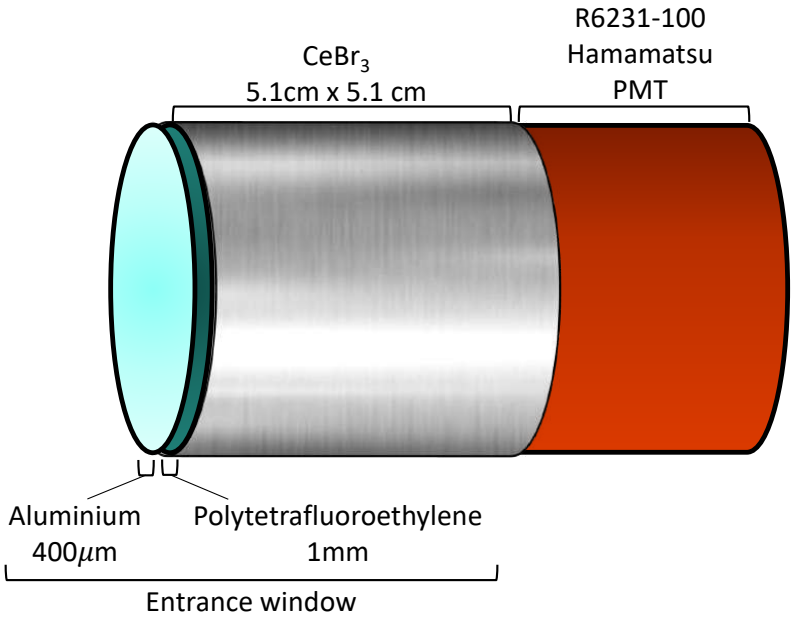

Figure 2.3: Side view scheme of the $CeBr_3$ detector from Advatech UK Ltd [19]

The **plastic scintillator**, from Eljen Technology (EJ-228), is a square of 6×6×0.2 cm^3, put in coincidence with the $CeBr_3$. Two different photomultipliers (PMT) from Hamamatsu, R7057 and XP3990, were tested, coupled with the plastic scintillator, supplied with -1100V and -1200V high-voltage respectively, in order to optimize the settings, i.e. minimize saturation while maximizing resolution. A scheme of this detector is shown on Figure 2.4.

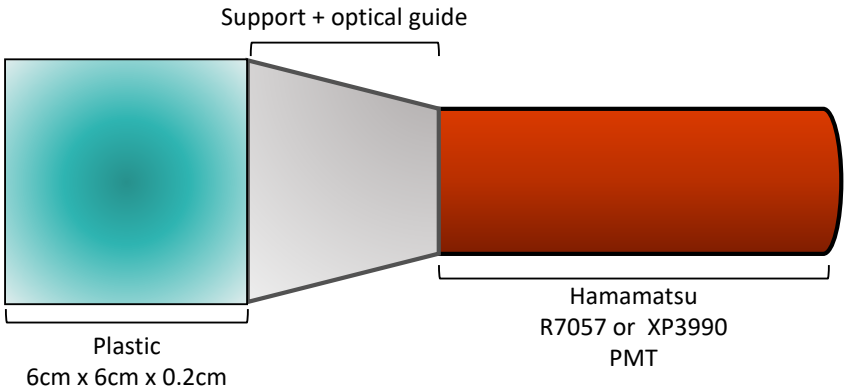

Figure 2.4: Up view scheme of the Plastic detector from Eljen Technology (EJ-228)

Both detector signals were acquired by a WaveCatcher digitizer module, developed by the LAL laboratory (Paris, France) [48]. The sampling frequency was set to be 3.2 GHz.

An example of digitized signals obtained from both detectors is presented in Figure 2.5. As expected, the pulse duration and the rising time of the plastic scintillator ($\sim$ 2 ns) are shorter than the ones from the $CeBr_3$ ($\sim$ 12 ns), in accordance with the intrinsic properties of both scintillators.

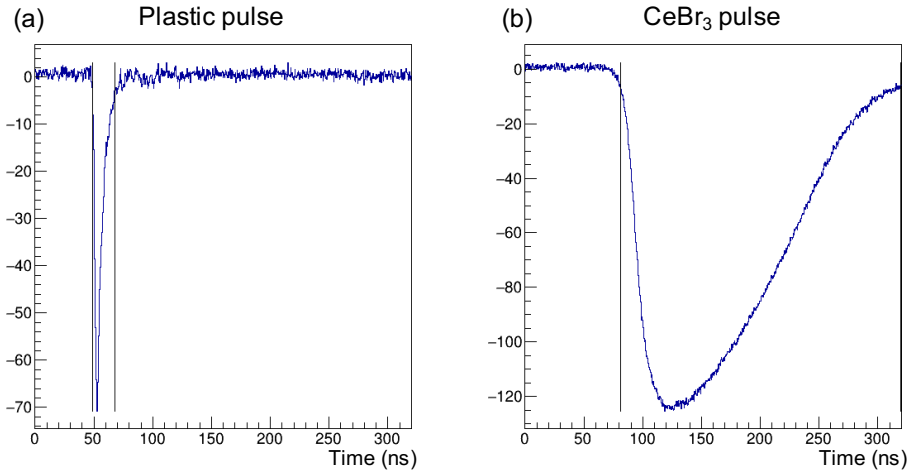

Figure 2.5: Pulse shape of the signal obtained with the plastic scintillator with -1200V applied (a) and $CeBr_3$ crystal with +350V applied (b) irradiated with 200 MeV/u ^{12}C.

I.2 Semiconductor detector

Another type of detector for detecting charged particles is semiconductor technology, and we will specifically focus here on silicon detectors.

I.2.1 Generalities

Complementary Metal Oxide Semiconductor (CMOS) sensors detectors play a crucial role in detecting ionizing radiation, and are constructed from crystalline semiconductor materials such as silicon and germanium. These detectors facilitate high spatial resolution and particle tracking capabilities.

The interaction of ionizing radiation with the semiconductor material results in the electron-hole pairs generation, which are then collected by an electric field.

A notable advantage of CMOS detectors lies in their efficiency, as the average energy required to create an electron-hole pair is around ten times smaller compared to gas ionization methods [49].

This efficiency, combined with their compact size, high density, and rapid response times, makes them valuable tools in various radiation detection applications.

Energy band structure

The energy band structure of crystalline semiconductors is depicted in Figure 2.6.

Energy bands represent regions with numerous discrete levels, closely spaced and treated as a continuum. The energy gap is a region devoid of available energy levels, arising from the periodic arrangement of atoms in crystals causing an overlap of electron

wavefunctions. The Pauli principle results in the breaking of degeneracy in the outer atomic shell energy levels, forming discrete levels slightly separated from each other.

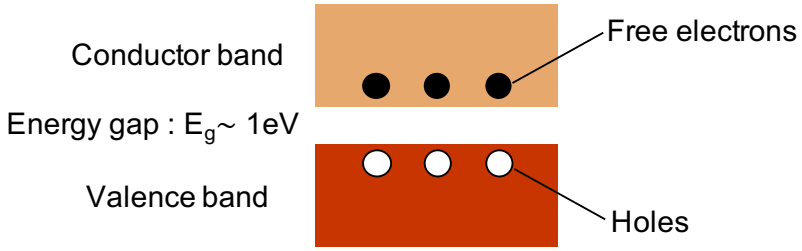

Figure 2.6: Energy band structure for semiconductors

The conduction band, the highest energy band, allows electrons to move freely throughout the crystal, detached from their parent atoms. Electrons in the valence band are more tightly bound, remaining associated with their lattice atoms.

The intermediate size of the energy gap ensures that only a limited number of electrons are excited into the conduction band by thermal energy. An electric field induces a small current, and cooling leads to electrons returning to the valence band, causing a decrease in semiconductor conductivity.

In semiconductors, electron-hole pairs are continuously generated by thermal energy, with a simultaneous recombination of a certain number of electrons and holes. Under stable conditions, an equilibrium concentration of electron-hole pairs (n_i) is established, given by the equation:

$$n_i = \sqrt{N_c N_v} \exp \frac{-E_g}{2kT} = AT^{3/2} \exp \frac{-E_g}{2kT} \tag{2.4}$$

where N_c is the number of states in the conduction band, N_v is the number of states in the valence band, and E_g is the energy gap at 0K. For example, at 300K, n_i is approximately 2.5 x 10^{13} cm^{-3} for germanium (Ge) and 1.5 x 10^{10} cm^{-3} for silicon (Si).

However, a critical consideration in the application of CMOS detectors is their sensitivity to radiation damage. This sensitivity imposes limitations on their long-term use, necessitating meticulous monitoring and potentially affecting their extended operational lifespan [34].

I.2.2 CMOS detectors

MOS generalities and operation principle

Metal-Oxide-Semiconductor (MOS) transistors are the main components of Complementary Metal-Oxide-Semiconductor (CMOS) technology. They are constructed using doped semiconductor material called substrate, either N-type or P-type, along with a thin insulating layer of silicon dioxide (SiO_2), and topped with a metal or polysilicon electrode. N-MOS transistors conduct via electrons, while P-MOS transistors conduct via holes, with N-MOS transistors generally exhibiting faster performance due to the higher mobility of electrons compared to holes.

A MOS transistor comprises four terminals: the source (S), emitting charge carriers; the drain (D), collecting the carriers; the gate (G), and the substrate (B), primarily serving as a doped support for the drain and source and as a potential reference (ground). The drain and source are positioned on opposite sides of the gate and are doped oppositely to the substrate [49]. A scheme of the MOS structure is represented in Figure 2.7.

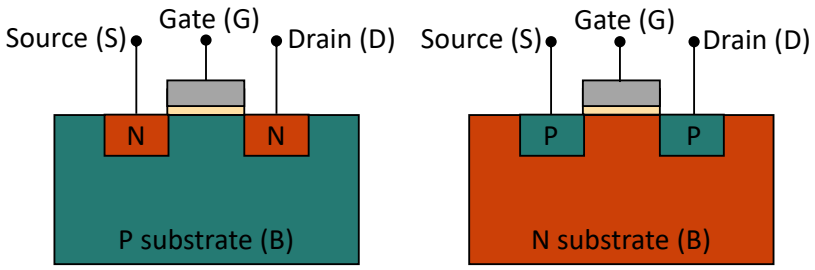

Figure 2.7: MOS sensor structure scheme

MOS transistors operate based on field-effect principles, where the density of mobile charges within the semiconductor is electrostatically modulated, by applying an electric field perpendicular to the movement of charges. The voltage applied to the gate (VGS) controls the quantity of charge carriers, while the voltage applied to the drain (VDS) puts them in motion.

To establish a conduction channel between the source and drain, the transistor must be biased under specific conditions. When the applied voltage exceeds a certain threshold (VT), electrons (in the case of N-MOS) present in the substrate as minority carriers are attracted by the electric potential of the gate oxide (GOX). They accumulate beneath the insulating layer, forming an inversion layer (where the doping of the semiconductor changes from P-type to N-type). Once this channel is created, electrons can flow from the source to the drain. The principle remains the same for P-MOS transistors.

CMOS sensors

The CMOS (Complementary Metal Oxide Semiconductor) technology originally found application in integrated circuits for computers and portable devices.

CMOS sensors incorporate both N-MOS and P-MOS transistors within a monolithic electronic circuit. Due to the inverted operation of these transistors, one is conducting while the other is blocking, inducing that CMOS designs ensure that all P-MOS transistors either have an output to the voltage source or connect to another P-MOS, and similarly, all N-MOS transistors are either connected to the ground or another N-MOS.

Various CMOS technologies exist, depending on the MOS used:

- N-well CMOS: the P-type silicon substrate contains an N-type well. P-MOS transistors are located within the well, while N-MOS transistors are in the substrate
- P-well CMOS technology: the inverse of N-well CMOS technology.
- Twin-well CMOS technology: the substrate of any type contains both N and P wells. Electronic circuits made in this technology are faster than others.

The energy consumption of CMOS is significantly lower compared to that of a conventional bipolar transistor. In a conventional bipolar transistor switch, unnecessary current flows, leading to energy dissipation and circuit heating [49].

I.2.3 MIMOSA-28

Detector description

The MIMOSA-28 (Minimum Ionizing cMOS) [50], an advanced CMOS active pixel sensor developed by the PICSEL (Physics with Integrated CMOS Sensors and Electron machines) group at IPHC, Strasbourg, France, has played a pivotal role as a particle tracker in the STAR HFT experiment. It operates in digital mode, capturing charges with a spatial resolution of 4 µm and achieving 100% efficiency with pions at 120 GeV. Notably, the sensor boasts two types of resistivity within its epitaxial layer: high-resistivity (400 Ω.cm) and low-resistivity (10 Ω.cm), a feature that significantly enhances signal-to-noise ratio and radiation tolerance.

Fabricated using the Austria Micro Systems (AMS) 0.35 µm CMOS process, the Mimosa-28 comprises 928 rows × 960 columns of square pixels, each with a length of 20.7 µm. It possesses a total thickness of 50 µm, with a 14 µm epitaxial layer. Employing line-by-line readout, it delivers a digital signal with an integration time of 186.5 µs (∼ 5 kHz frame rate), producing a binary output from fired pixels exceeding a user-defined threshold. A photo of the MIMOSA-28 sensor is shown in Figure 2.8.

Figure 2.8: MIMOSA-28 CMOS pixel sensor photo

Detection principle

The incident particle interacts with the sensitive layer, altering trajectory through multiple scatterings. Along this path, the particle deposits energy, ionizing the sensitive layer by generating electron-hole pairs, with energy loss dependent on particle kinetic energy and medium. Subsequently, created electrons undergo thermal drift through the sensitive layer, collected by pixels, where charge sharing among neighboring pixels activates clusters. A scheme of the CMOS and its detection principle is represented in Figure 2.9.

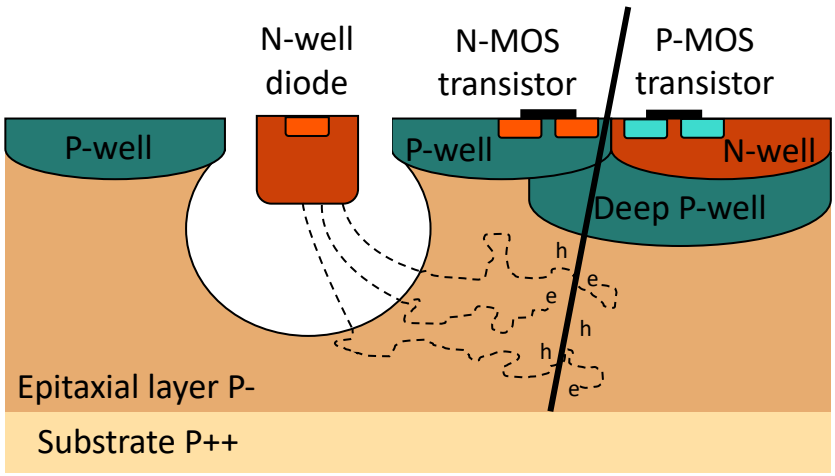

Figure 2.9: MIMOSA-28 CMOS pixel sensor structure scheme

The signal received by pixels is amplified and registered, facilitating continuous charge collection during acquisition. The system transfers previous signals to a discriminator, where user-set thresholds dictate pixel outputs. For each integration time, a 960 x 928 matrix containing the output is stored, with approximately 15 electrons activating a pixel in a dark chamber at 20°, representing the 1σ threshold.

Centroid determination

In particle tracking applications, a cluster denotes a grouping of pixels that have been activated by the same incident particle. To effectively identify clusters in the MIMOSA-28, an algorithm utilizing a first neighbor search methodology in an iterative method was implemented. Hits, or activated pixels, are deemed to belong to a cluster if they share a common edge.

The centroid, a crucial metric in cluster analysis, is determined as the center of gravity of all hits within the cluster. To achieve this, a program developed in C++, leveraging the ROOT library, facilitates the reconstruction of centroids for various clusters. For each integration time, the program parses the 960 x 928 pixel matrix, identifying and storing distinct clusters in memory.

Given the absence of access to deposited energy information, only activated pixels are utilized in cluster reconstruction. For each identified cluster, the program computes its centroid and records its position within a dedicated 960 x 928 histogram. This comprehensive approach ensures accurate localization and characterization of particle trajectories within the sensor array.

After discussing the secondary particle measurements using different detectors, the simulation tools will now be explored. These tools permit to simulate and thus understand particle behavior in ways that complement the experimental measurements.

While detectors provide us with real-world data and insights into particle interactions, simulation tools offer a virtual platform for detailed modeling and analysis, permitting a complementary understanding of the behavior of secondary particles in different contexts.

II. Simulation tools

In this section, simulation tools for modeling charged particle interactions such as Geant4 and OpenGATE will be explored, alongside their functionalities and applications.

II.1 Geant4 simulation code

Geant4 is an open-source Monte-Carlo simulation code [51, 52, 53] using object-oriented programming (C++), for the simulation of the passage of particles through matter. Developed by the CERN collaboration, Geant4 provides a flexible and extensible framework for simulating the interactions of particles with matter. It is widely used in various domains such as high-energy physics, medical physics, space science, and radiation protection.

II.1.1 Generalities

Geant4 employs a class-based structure encompassing various C++ classes for modeling simulation components such as geometry, materials, physical processes, events, and trajectories. Each class plays a crucial role in defining and simulating the behavior of particles as they interact with matter.

The simulation process in Geant4 typically begins with particle generation from a specified point source. This initial generation can represent various scenarios, such as particle beams from accelerators or natural radiation sources. Once particles are generated, Geant4 uses its comprehensive physics models to track their trajectories as they traverse through different materials or mediums.

The interactions between particles and matter are governed by a range of physical processes implemented in Geant4. These processes include electromagnetic interactions (such as ionization, bremsstrahlung, and multiple scattering), hadronic interactions (like elastic and inelastic scattering, nuclear reactions), decay processes, and transportation processes (like particle tracking and propagation).

It's important to note that for a given particle, multiple processes can occur simultaneously or sequentially as it interacts with the medium. Geant4 is designed to handle these complex scenarios, allowing users to customize the simulation to include specific processes of interest or to study the overall effects of various interactions on the particle's behavior.

Furthermore, Geant4 tracks not only primary particles but also secondary particles that may be generated during interactions. These secondary particles, including electrons, positrons, photons, and various hadrons, are tracked until their interaction decrease their energy below a preset threshold, or until they exit the defined simulation region. This comprehensive tracking capability enables to study cascading effects, energy depositions, and the overall evolution of particle showers within a given experimental setup or environment.

II.1.2 Overview of the functionalities

In Figure 2.10, the Geant class categories are presented, showcasing the hierarchical structure of the Geant4 toolkit. These categories are the main components in the simulation of particle-matter interactions and the behavior of particles within a defined geometry.

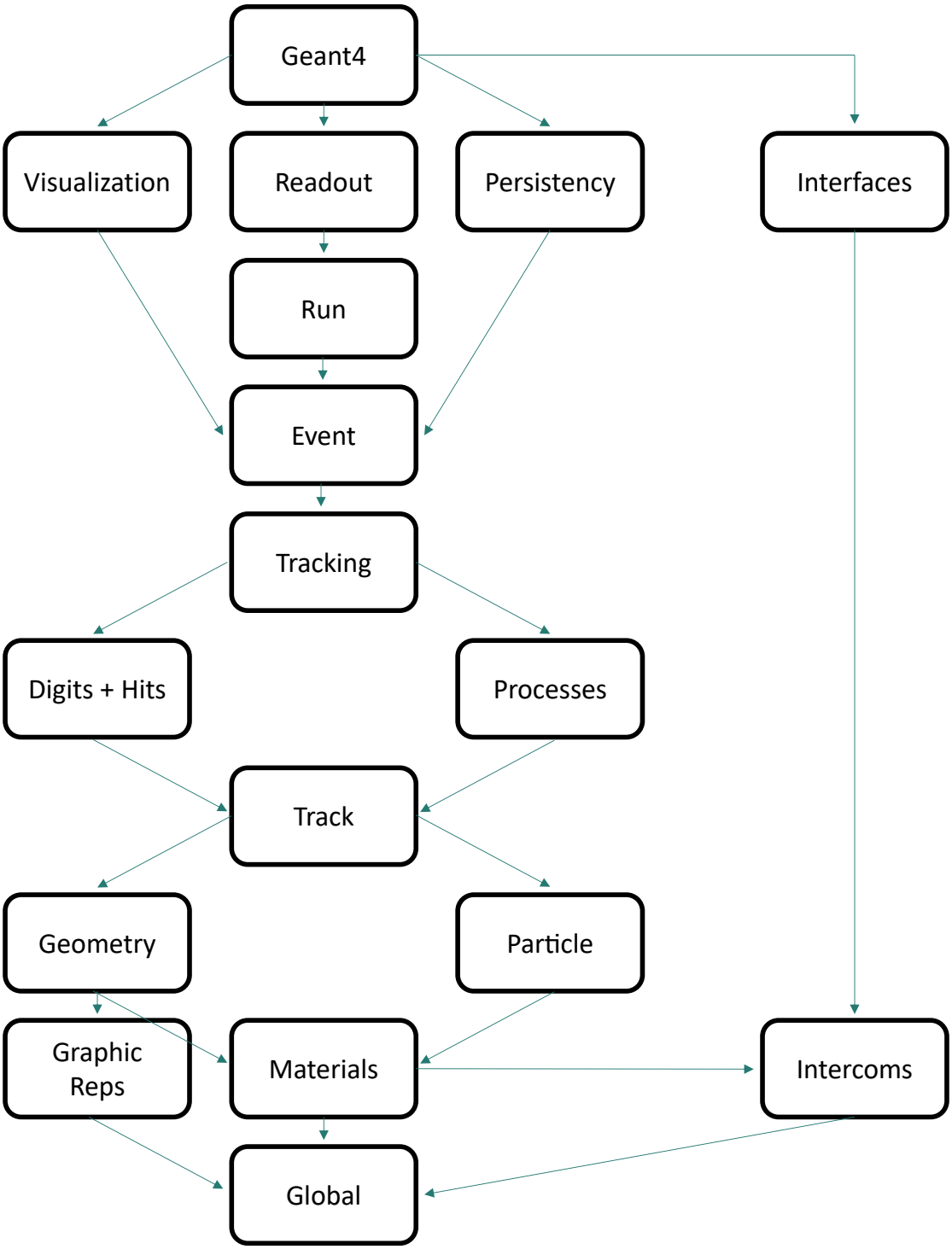

Figure 2.10: Geant4 class categories

At the foundation of the toolkit are the categories located at the bottom of the diagram. These categories are utilized by almost all higher categories and provide the fundamental building blocks for the toolkit's functionality.

The **global** category covers the system of units, physical constants, numerical handling and random number generation.

Moving up in the hierarchy, the **materials** and **particles** categories are responsible for implementing the necessary facilities to describe the physical properties of particles and materials. This includes characteristics such as mass, charge, energy loss, and interaction cross-sections.

The **geometry** module provides tools to define and manage the geometric structure of the simulation environment. It allows to create complex geometries, including solids, volumes, sensitive detectors, and efficient particle propagation through these geometries, taking into account interactions and boundary conditions.

Above these foundational categories are those essential for describing the tracking of particles and the physical processes they undergo during their trajectories. The **track** category includes classes for representing particle tracks and individual steps within those tracks. These elements are used by the **processes** category, which implements models of physical interactions such as electromagnetic interactions (for leptons, photons, hadrons, and ions) and hadronic interactions. These processes dictate how particles interact and evolve within the simulated space.

The **tracking** category manages the call of processes during particle tracking, ensuring their proper contribution to the evolution of a track's state. It also provides information regarding particle interactions within sensitive volumes, which is crucial for recording hits and following digitization processes.

Moving further up, the **event** category handles events within the simulation, organizing tracks and their associated data. The **run** category manages collections of events that share common parameters such as beam settings and detector configurations, providing an organized structure for simulations.

The **readout** category facilitates the handling of pile-up scenarios, where multiple interactions occur within a single event window, which is common in high-energy physics experiments.

Finally, the toolkit integrates capabilities from all these categories to connect with external facilities through abstract interfaces. This integration enables functionalities such as visualization, persistency (for storing simulation data), and user interface interactions. These capabilities enhance the usability and versatility of the Geant4 toolkit.

II.1.3 Geant4 physics models

Geant4's physics models cover a broad energy range (from a few eV to several PeV) and are based on theoretical models, experimental data, and parameterizations.

Physics processes in Geant4 are categorized into different groups such as hadronic, electromagnetic, optical, and other specialized processes. These processes are managed and organized by a "physics list" in Geant4, allowing users to select specific sets of physics models tailored to their simulation needs.

Hadronic processes

Hadronic processes in Geant4 are responsible for simulating the interactions of hadrons (such as protons, neutrons, and ions) with atomic nuclei. These processes encompass a

wide range of reactions, including elastic scattering, inelastic interactions, and nuclear reactions within the target material. Two prominent models utilized in Geant4 for hadronic processes are the BIC (Binary Cascade) model and the INCL++ (Liège Intranuclear Cascade) model. These models are selected based on their relevance and accuracy in various applications, including medical physics.

The BIC model is recommended by Geant4 developers for hadron therapy simulations. It describes the target nucleus as a collection of nucleons distributed according to specific nuclear density models, such as the Wood-Saxon model for heavier nuclei and an harmonic oscillator shell model for lighter nuclei:

- for A $>$ 16, a Wood-Saxon model is used :

$$\rho(r) = \frac{\rho_0}{1 + \exp(\frac{r-R}{a})}, p_0 = \frac{3}{4\pi R^3}\left(1 + \frac{a^2\pi^2}{R^2}\right)^{-1} \tag{2.5}$$

  with $a = 0.545$, $R = r_0 A^{1/3}$ and $r_0 = 1.16(1 - 1.16 \times A^{-2/3})$.

- for A $<$ 16, an harmonic oscillator shell model is used :

$$\rho(r) = (\pi R^2)^{-3/2} \exp\left(-\frac{r^2}{R^2}\right) \tag{2.6}$$

  with $R^2 = 0.8133 A^{2/3}$ fm^2.

The nucleon momentum is also defined as a random number between 0 and Fermi momentum, given by the previously defined nuclear density $p_F(r) = \hbar c(r\pi^2\rho(r))^{1/3}$.

During the cascade, a Runge-Kutta integration method is employed, where only particles propagate inside the target nucleus. The model incorporates strict Pauli blocking criteria during the cascade process, ensuring realistic nucleon interactions and energy thresholds for cascade initiation and termination. The cascade process ends when particles average energy falls below a threshold, with a minimum projectile kinetic energy of 45 MeV/u required for cascade initiation. Data from raw BIC and subsequent de-excitation models exclude intranuclear cascade effects, passing a composite nucleus directly to the pre-compound model.

On the other hand, the INCL++ model employs a diffuse nuclear surface representation based on a Wood-Saxon nuclear density distribution:

$$\rho(r) = \frac{\rho_0}{1 + \exp(\frac{r-R}{a})} \tag{2.7}$$

for $r < R_{max}$, with $R_{max} = R_0 + \delta a + r_{int}$, $a = 0.510 + 1.63x10^{-4}A$ fm, $R_0 = (2.745x10^{-4}A + 1.063)A^{1/3}$ fm and r_{int} a term linked to the total cross section for the interaction under consideration.

Nucleon position and momentum determination are not independent and again the momentum is taken as a random number between 0 and the Fermi momentum. Concerning the nucleons inside the target nucleus, they suffer from a constant potential defined by a radius depending on their momentum.

Like in the BIC model, a collision can be Pauli blocked. However, the depletion of the Fermi sphere is taken into account by looking at the local phase-space occupation probabilities.

One of the key aspects of the INCL model is its use of a coalescence model after a nucleon escapes the target nucleus: if other nucleons are sufficiently close in phase space, the initial nucleon can carry along the others, resulting in the emission of a light cluster.

Electromagnetic processes

Geant4's electromagnetic models encompass a range of processes essential for simulating interactions of charged particles and photons with matter. These processes include multiple scattering, ionization, bremsstrahlung, and Compton scattering, among others. Geant4 provides predefined physics lists validated against standards like the International Commission on Radiation Units and Measurements (ICRU) data, ensuring accuracy and consistency in electromagnetic simulations across different materials and energies.

Other processes

In addition to hadronic and electromagnetic processes, Geant4 incorporates various other physics processes crucial for comprehensive simulations. These include decay processes (both radioactive and non-radioactive), nuclear elastic collisions, muon physics, and relativistic effects of electromagnetic interactions. The selection of these processes in a physics list depends on the specific simulation scenario and the phenomena of interest, with decay processes often omitted in simulations where their impact is negligible or not relevant.

II.2 OpenGATE

OpenGATE [54] is an open-source software platform built upon the Geant4 toolkit and is specifically designed for simulating medical imaging systems such as PET, SPECT, Compton Cameras, X-ray alongside dosimetry studies encompassing external and internal radiotherapy and even advanced techniques like hadrontherapy. Both version 9 in C++ and version 10 in Python will be used in this thesis work.

OpenGATE allows to model and simulate the behavior of radiation within various medical imaging scenarios. It is an extension of Geant4 and provides a user-friendly interface and additional features tailored to the needs of the medical imaging community.

The software is used for tasks such as optimizing detector designs, understanding system performance, and studying the impact of different factors on image quality in medical imaging applications. It is particularly valuable in the development and testing of new imaging techniques and devices.

GATE, reliant on Geant4 for its Monte Carlo engine, offers three primary attributes:

- seamless access to Geant4 functionalities
- supplementary features such as variance reduction techniques
- collaborative development through shared source code, mitigating redundant efforts

The user interface, realized through macro files (.mac), streamlines the simulation process by employing Geant4-style macro commands, presenting a user-friendly alternative to direct Geant4 C++ coding. Comparable projects like Gamos or Topas adopt analogous principles.

III. Conclusion

In conclusion, the detectors discussed in this chapter, scintillation detectors and CMOS sensors, play crucial roles in the detection of secondary particles in hadrontherapy.

Scintillation detectors offer fast time responses and pulse shape discrimination capabilities, making them suitable for precise measurements and particle identification. Organic scintillators demonstrate fast decay times and high light outputs, while inorganic scintillators provide advantages in stopping power and light output, though with some disadvantages such as hygroscopicity. Both types of scintillators are effective in detecting various types of radiation, with specialized formulations and coatings enabling their use even for heavy ions.

On the other hand, CMOS detectors, based on Metal-Oxide-Semiconductor technology, offer high-resolution energy and particle tracking capabilities. Their efficiency and rapid response times make them valuable tools in radiation detection applications, despite their sensitivity to radiation damage.

Integration of these detectors into hybrid systems and careful calibration procedures are crucial for enhancing detection capabilities and ensuring accurate measurements, particularly in the presence of heavy ions.

All the experimental measurements were also simulated using Geant4 or OpenGATE, in order to do a comprehensive understanding of all the physical processes involved.

Simulation tools such as Geant4 and OpenGATE play essential roles in modeling charged particle interactions, particularly in medical physics and radiation protection. Geant4, an open-source Monte Carlo simulation code developed by CERN, permits to simulate the passage of particles through matter. Its object-oriented programming approach and extensive class-based structure allow for detailed modeling of particle interactions with various materials and physical processes. Geant4's physics models cover a broad energy range and are continuously updated and validated against experimental data to ensure accuracy.

OpenGATE, built upon the Geant4 toolkit, is specialized in simulating medical imaging systems and dosimetry studies. It provides a user-friendly interface and additional features for hadrontherapy simulation purposes. OpenGATE enables to optimize detector designs, assess system performance, and study the impact of different factors on treatment in hadrontherapy applications.

Summary

Introduction

Ce chapitre aborde les techniques employées pour la détection et la simulation précise des particules chargées secondaires produites lors des traitements en hadronthérapie. Il se concentre principalement sur les détecteurs à scintillation, les détecteurs à semi-conducteurs et les outils de simulation comme Geant4 et OpenGATE. L'efficacité de ces techniques de détection dépend des processus d'interaction des particules chargées avec la matière.

Détection des particules chargées secondaires

Les scintillateurs et les semi-conducteurs sont des détecteurs essentiels pour la détection des particules secondaires en hadronthérapie.

Scintillateur

Lorsque le rayonnement traverse un matériau scintillant, il excite les atomes et molécules du matériau, entraînant l'émission de lumière. La quantité de lumière émise est proportionnelle à l'énergie incidente, au-dessus d'un certain seuil minimal. Les scintillateurs offrent une réponse temporelle rapide comparée à d'autres détecteurs, caractérisée par des temps de réponse et de récupération courts. Cela permet des mesures précises des intervalles de temps entre deux événements et donc des taux de comptage plus élevés.

On peut catégoriser les scintillateurs en deux catégories: organiques et inorganiques. Les scintillateurs organiques sont composés de molécules contenant des atomes tels que des atomes de carbone, d'hydrogène et d'azote. Les scintillateurs plastiques organiques présentent un temps de décroissance rapide, généralement de quelques nanosecondes ou moins, et une réponse très rapide du signal. Un avantage majeur des scintillateurs plastiques organiques est leur flexibilité dans diverses applications, car ils peuvent être facilement façonnés en une grande variété de formes et de tailles, et ils ne sont pas hygroscopiques.
Les scintillateurs inorganiques sont composés de matériaux inorganiques cristallins ou non cristallins, incluant divers composés tels que les halogénures alcalins, les oxydes de terres rares ou les halogénures de métaux lourds. Les scintillateurs inorganiques cristallins ont un temps de réponse de deux à trois fois plus lent que les scintillateurs organiques, environ 50 ns. Ils offrent une plus grande puissance d'arrêt en raison de leur densité et de leur numéro atomique plus élevés, ainsi qu'une sortie de lumière plus élevée, mais certains présentent l'inconvénient d'être hygroscopiques.

La réponse lumineuse varie pour différents types de particules à la même énergie. L'efficacité d'un détecteur à scintillation doit prendre en compte l'efficacité du photomultiplicateur (PMT) associé, qui a une efficacité globale d'environ 30 %. Bien que la relation entre la sortie de lumière et le dépôt d'énergie ne soit pas strictement linéaire, elle peut être approximée comme $L \propto \Delta E$ pour de nombreuses applications. La dépendance à la température des scintillateurs est généralement faible à température ambiante, avec les scintillateurs organiques étant presque indépendants de la température, tandis que les scintillateurs inorganiques montrent une certaine sensibilité.

En termes d'efficacité de détection intrinsèque pour diverses radiations, les électrons sont efficacement détectés par la plupart des scintillateurs avec une efficacité proche de 100%. Cependant, leur faible masse peut entraîner des angles de diffusion significatifs dans la matière. Les rayons gamma sont plus efficacement détectés par des matériaux à numéro atomique élevé (Z), et le scintillateur doit favoriser les processus photoélectriques et de production de paires par rapport au processus Compton. La détection des neutrons nécessite le transfert de toute ou partie de l'énergie du neutron à une particule capable d'ioniser et de sortir du matériau scintillant.

Les photomultiplicateurs sont utilisés pour convertir la lumière en courant électrique mesurable. Lorsqu'un photon incident atteint la photocathode, un électron est émis par effet photoélectrique. En raison de la tension appliquée, généralement comprise entre 500V et 2000V, l'électron est guidé et accéléré vers la première dynode, initiant une cascade d'électrons. Le gain global du PMT, en supposant une division égale de la tension appliquée entre les dynodes, est donné par l'équation $G = \delta^n = (kV_d)^n$.

Dans le cadre de cette thèse, un télescope ΔE-E a été utilisé, composé de deux détecteurs scintillants : un scintillateur plastique mince (ΔE) et un scintillateur en cristal épais de bromure de cérium ($CeBr_3$) (E). Ce télescope est conçu pour stopper les ions carbone jusqu'à 200 MeV/u.

Scintillateur de bromure de cérium
Le détecteur $CeBr_3$ utilisé est un scintillateur cylindrique de 2×2 pouces fourni par Advatech UK Ltd, couplé à un photomultiplicateur R6231-100 de Hamamatsu. Une fenêtre d'entrée en aluminium de 400 μm et de polytétrafluoroéthylène (PTFE) de 1 mm agit comme réflecteur. Ce détecteur a été calibré pour permettre la détection d'ions sans induire de saturation dans le système, avec une réduction de la haute tension appliquée au PMT de +600 V à +350 V pour les protons et les gammas à haute énergie, par rapport à la tension de fonctionnement habituelle de +1200 V.

Scintillateur plastique
Le scintillateur en plastique, provenant d'Eljen Technology (EJ-228), est un pavé de 6×6×0.2 cm^3. Il est mis en coïncidence avec le $CeBr_3$. Deux photomultiplicateurs différents de Hamamatsu (R7057 et XP3990) ont été testés, couplés au scintillateur plastique, alimentés respectivement avec une haute tension de -1100V et -1200V, afin d'optimiser les paramètres, c'est-à-dire minimiser la saturation tout en maximisant la résolution.
Les signaux des deux détecteurs ont été acquis par un module de numérisation WaveCatcher, développé par le laboratoire LAL (Paris, France), avec une fréquence d'échantillonnage de 3,2 GHz.

Détecteur à semi-conducteur
Les détecteurs à semi-conducteurs, notamment ceux en silicium, offrent une haute résolution spatiale et des capacités de suivi des particules. Ces détecteurs génèrent des paires électron-trou lors de l'interaction avec le rayonnement ionisant, qui sont ensuite collectées par un champ électrique.

La structure de bande énergétique des semi-conducteurs se compose de la bande de conduction et de la bande de valence, séparées par un gap énergétique. La génération et la recombinaison des paires électron-trou sont régies par cette structure.
Les capteurs CMOS (Complementary Metal-Oxide-Semiconductor) sont essentiels pour la détection des radiations ionisantes. Ils fonctionnent sur des principes d'effet de champ où un champ électrique module la densité des charges mobiles dans le semi-conducteur.

MIMOSA-28
Le capteur MIMOSA-28 (Minimum Ionizing MOS Active pixel sensor) est un capteur CMOS à pixels actifs avancé, développé par le groupe PICSEL (Physics with Integrated CMOS Sensors and Electron machines) de l'IPHC, Strasbourg, France. Ce capteur a joué un rôle crucial en tant que trajectographe de particules dans l'expérience STAR HFT.
Le MIMOSA-28 fonctionne en mode digital, capturant les charges avec une résolution spatiale de 4 μm et atteignant une efficacité de 100 % avec des pions à 120 GeV. Le capteur présente deux types de résistivité dans sa couche épitaxiale, ce qui améliore significativement le rapport signal/bruit et la tolérance aux radiations. Fabriqué avec le procédé CMOS 0.35 μm d'Austria Micro Systems (AMS), le Mimosa-28 est constitué de 928 rangées $\times$ 960 colonnes de pixels carrés, chacun mesurant 20,7 μm de longueur. Le capteur a une épaisseur totale de 50 μm, avec une couche épitaxiale de 14 μm.

En ce qui concerne son principe de détection, la particule incidente interagit avec la couche sensible, altérant sa trajectoire par des diffusions multiples. Le long de cette trajectoire, la particule dépose de l'énergie, ionisant la couche sensible par la génération de paires électron-trou. Les électrons créés dérivent ensuite thermiquement à travers la couche sensible, collectés par les pixels, où le partage de charge entre les pixels voisins active des clusters. Le signal reçu par les pixels est amplifié et enregistré, facilitant la collecte continue des charges pendant l'acquisition.

Un cluster désigne un groupe de pixels activés par la même particule incidente. Un algorithme de recherche de premier voisin en méthode itérative est utilisé pour identifier efficacement les clusters dans le MIMOSA-28. Les hits, ou pixels activés, sont considérés comme appartenant à un cluster s'ils partagent un bord commun. Le centroïde, une mesure cruciale dans l'analyse des clusters, est déterminé comme le centre de gravité de tous les hits au sein du cluster. Pour chaque temps d'intégration, le programme analyse la matrice de pixels 960 x 928, identifiant et enregistrant les clusters distincts en mémoire.

Outils de simulation
Les outils de simulation comme Geant4 et OpenGATE sont essentiels pour modéliser les interactions des particules chargées, fournissant une plateforme virtuelle pour une analyse détaillée et une compréhension approfondie.

Code de simulation Geant4
Geant4 est un toolkit de simulation Monte Carlo open-source utilisé pour simuler les interactions des particules avec la matière. Il est extrêmement flexible et largement utilisé dans divers domaines scientifiques.

Développé par la collaboration CERN, Geant4 offre un cadre extensible pour la simulation des interactions des particules avec la matière, utilisé dans des domaines tels que la physique des hautes énergies, la physique médicale, la science spatiale et la protection contre les radiations.

Geant4 est structuré en plusieurs catégories de classes, chacune responsable de différents aspects de la simulation, tels que la géométrie, les matériaux, les processus physiques et le suivi des particules. Le processus de simulation dans Geant4 commence généralement par la génération de particules à partir d'une source ponctuelle spécifiée. Cette génération initiale peut représenter divers scénarios, tels que des faisceaux de particules provenant d'accélérateurs ou des sources de rayonnement naturel. Une fois les particules générées, Geant4 utilise ses modèles physiques complets pour suivre leurs trajectoires à travers différents matériaux ou milieux.

Les interactions entre les particules et la matière sont régies par une gamme de processus physiques implémentés dans Geant4. Ces processus incluent les interactions électromagnétiques (comme l'ionisation, le bremsstrahlung et la diffusion multiple), les interactions hadroniques (comme la diffusion élastique et inélastique, les réactions nucléaires), les processus de désintégration et les processus de transport (comme le suivi et la propagation des particules). Il est important de noter que pour une particule donnée, plusieurs processus peuvent se produire simultanément ou séquentiellement lors de son interaction avec le milieu. Geant4 est conçu pour gérer ces scénarios complexes, permettant aux utilisateurs de personnaliser la simulation pour inclure des processus spécifiques d'intérêt ou pour étudier les effets globaux de diverses interactions sur le comportement de la particule.

Modèles physiques de Geant4
Geant4 inclut un ensemble complet de modèles physiques couvrant les processus électromagnétiques, hadroniques et d'autres processus spécialisés. Ces modèles sont organisés en listes de physique que les utilisateurs peuvent sélectionner en fonction de leurs besoins de simulation.

Les processus hadroniques dans Geant4 sont responsables de la simulation des interactions des hadrons (comme les protons, les neutrons et les ions) avec les noyaux atomiques. Ces processus couvrent une large gamme de réactions, y compris la diffusion élastique, les interactions inélastiques et les réactions nucléaires au sein du matériau cible. Deux modèles importants utilisés dans Geant4 pour les processus hadroniques sont le modèle de cascade binaire (BIC) et le modèle de cascade intranucléaire de Liège (INCL++).

Les modèles électromagnétiques de Geant4 couvrent une gamme de processus essentiels pour la simulation des interactions des particules chargées et des photons avec la matière. Ces processus incluent la diffusion multiple, l'ionisation, le bremsstrahlung et la diffusion Compton, entre autres. Geant4 fournit des listes de physique prédéfinies validées par des normes telles que les données de l'ICRU.
En plus des processus hadroniques et électromagnétiques, Geant4 intègre divers autres processus physiques cruciaux pour des simulations complètes.

Ceux-ci incluent les processus de désintégration (radioactifs et non radioactifs), les collisions nucléaires élastiques, la physique des muons et les effets relativistes des interactions électromagnétiques. La sélection de ces processus dans une liste de physique dépend du scénario de simulation spécifique et des phénomènes d'intérêt.

OpenGATE
OpenGATE est une plateforme logicielle open-source basée sur le toolkit Geant4, spécifiquement conçue pour simuler les systèmes d'imagerie médicale tels que la TEP, la TEMP, les caméras Compton, les rayons X ainsi que les études de dosimétrie englobant la radiothérapie externe et interne et même des techniques avancées comme l'hadronthérapie. OpenGATE permet de modéliser et de simuler le comportement des radiations dans divers scénarios d'imagerie médicale. Il s'agit d'une extension de Geant4 et offre une interface facile d'utilisation et des fonctionnalités supplémentaires adaptées aux besoins de la communauté de l'imagerie médicale. Le logiciel est utilisé pour des tâches telles que l'optimisation des conceptions de détecteurs, la compréhension des performances du système et l'étude de l'impact de différents facteurs sur la qualité des images dans les applications d'imagerie médicale.

Conclusion
Ce chapitre souligne l'importance des détecteurs à scintillation et des détecteurs à semi-conducteurs pour la détection des particules secondaires en hadronthérapie. Il met en évidence l'intégration de ces détecteurs dans des systèmes hybrides et le rôle des outils de simulation comme Geant4 et OpenGATE dans la compréhension des interactions des particules et l'optimisation des conceptions de détecteurs pour des applications médicales. Ces outils de simulation permettent de modéliser et de comprendre les processus physiques impliqués, complétant ainsi les mesures expérimentales.

Chapter 3

Calibration of a ΔE-E telescope based on a $CeBr_3$ scintillator

"I don't wanna look at anything else now that I saw you."
– T. S.

Contents

I. General context

During a cancer treatment in particle therapy (heavy ion or proton beam), nuclear reactions of the primary beam with the targeted volume need to be quantified in order to compute properly the dose received by the patient, as discussed in Chapter 1.

Indeed, the primary beam and target fragmentation leading to the production of lighter fragments, and their contribution to an undesired dose in surrounding healthy tissues need to be predicted. As previously mentioned in Chapter 1 Section III.2, the dose calculations in particle therapy rely on high-performance algorithms which include physical, chemical

and biological processes. These calculations are based on data provided by the Monte Carlo, but the lack of experimental data regarding nuclear reactions in particle therapy, can introduce inaccuracies in dose calculations.

I.1 The CLINM project

I.1.1 Interdisciplinary study

The CLINM (Cross-sections of Light Ion and Neutron Measurements) project aims to understand the complex interactions between ionizing radiation and biological systems. This interdisciplinary project combines physics and chemical analysis to investigate the chemical effects of secondary ionizing radiation on water and biomolecules.

When primary carbon ions interact with biological matter, they produce secondary particles such as electrons, protons, neutrons, and gamma rays. These secondary particles can cause various types of damage, including ionization, excitation, and fragmentation of molecular bonds. This damage can affect cellular functions and lead to biological responses.

Currently, the softwares used for treatment planning are increasingly based on Monte Carlo simulations, which do not accurately reproduce the secondary particles generated by nuclear processes. This creates a gap that necessitates further research to improve the calculations of secondary particle production and their radiobiological effects.

Ionizing radiations, including primary beams and the resulting secondary particles, penetrate biological tissues and deposit most of their energy in water, which makes up about 65% of cells. This process, known as water radiolysis, leads to the formation of highly reactive species such as hydroxyl radicals ($HO^{\bullet}$), hydrated electrons ($e^{-}aq$), and hydrogen peroxide (H_2O_2). These reactive species can then interact with biomolecules, causing chemical damage as an indirect effect of the radiation. It is estimated that about 70% of cellular damage is due to these indirect effects, with the rest resulting from direct interactions of radiation with cellular material.

The yields of water radiolysis products (i.e., the number of molecules formed per unit of energy deposited) depend on both the type (γ-rays/electrons, ions, neutrons) and energy of the ionizing radiation. Thus, it is critical to precisely characterize the secondary particles produced during hadrontherapy treatments. Chemistry could bridge the gap between nuclear reactions and biological effects, enhancing our understanding and effectiveness of radiation therapy.

I.1.2 Experimental and simulation approach

This project integrates experimental measurements alongside simulations, in order to understand the radiation-induced damages and refine models for dose distribution estimation.

One key point of this project is to determine the yields, charge, and energy of the produced fragments, in the same conditions as the chemical experiment. Indeed, the secondary charged particle, the gammas, and the neutrons of high energy will be measured.

In this thesis, we will focus on the secondary charged particle identification. The use of a ΔE-E telescope for secondary charged particle identification is a technique that leverages the principles of energy loss and remaining energy to discriminate different particle charges. The thinner detector in the telescope measures the energy loss (ΔE)

of charged particles as they pass through, while the crystal scintillator measures the remaining energy (E) after the particle has traversed the detector. By analyzing the energy deposition patterns in these two components, we can identify and characterize secondary charged particles, as will be explored in the next Chapter.

I.2 ΔE-E telescope

The ΔE-E telescope utilized in this study comprises a plastic scintillator of 2 mm thickness and a $CeBr_3$ crystal scintillator of 5.1 cm thickness. These detectors possess distinct physical characteristics that contribute to their effectiveness in detecting and characterizing charged particles, gamma rays, and neutrons, as discussed in the previous Chapter.

I.2.1 Cerium Bromide choice

The $CeBr_3$ crystal scintillator was chosen to detect not only charged particles but also gamma rays and neutrons, aligning well with the general context of CLINM. Unlike some alternatives like $LaBr_3$, $CeBr_3$ does not exhibit internal radioactivity, which minimizes background noise and false coincidences, thus enhancing the precision of radiation detection. Additionally, $CeBr_3$ offers excellent energy resolution, of 3.6% at 662 keV with nominal tension of PMT of +1200 V, and rapid response, enabling precise time measurements critical for understanding particle interactions, as discussed in the preceding chapter.

The voltage applied on the R6231-100 Hamamatsu PMT coupled to the $CeBr_3$, the constructor recommended value is + 1200 V. However, the voltages applied were of + 400 V and + 350 V, in order to detect the high energy protons and ^{12}C without reaching the PMT saturation.

I.2.2 Plastic scintillator choice

The EJ-228 plastic scintillator is designed to deliver high performance in terms of timing resolution and light output, making it ideal for our specific needs.

The scintillator has a light output of 67% anthracene, with a scintillation efficiency of approximately 10,200 photons per 1 MeV of electron energy.

The rise time of the EJ-228 is 0.5 ns, and its decay time is 1.4 ns, contributing to a full width at half maximum (FWHM) pulse width of 1.2 ns. These fast timing properties are crucial for minimizing signal overlap and improving temporal resolution.

Compared to other scintillation materials, plastic scintillators provide a balance between performance and cost, making them an economical choice. Plastic scintillators like the EJ-228 are robust and less fragile compared to other types of scintillators and can be manufactured in a wide variety of shapes and sizes, permitting to have in this experiment a thin square piece for the ΔE-E detection method.

Concerning the PMT coupled to the plastic scintillator the applied voltage was the recommanded constructor value of -1200V (-1100V was also tested).

I.2.3 Data acquisition

Both detector signals were acquired in coincidence by a WaveCatcher digitizer module, developed by the LAL laboratory (Paris, France) [48]. The sampling frequency was set to be 3.2 GHz on the DAQ. Figure 2.5 in Chapter 2 Section I.1 illustrates digitized signals

obtained from the plastic scintillator and $CeBr_3$ crystal when irradiated with 200 MeV/u ^{12}C ions. As expected, the pulse duration and the rising time of the plastic scintillator ($\sim$ 1.4 ns) are shorter than the ones from the $CeBr_3$ ($\sim$ 19 ns), in accordance with the intrinsic properties of both scintillators. A gate of 80 ns was applied for the detector's coincidence.

I.2.4 Calibration

Calibrating the ΔE-E telescope with ions commonly used in clinical settings is essential for ensuring accurate particle identification and quantification. Calibration involves establishing a known relationship between the energy deposited in the detectors and the properties of the incident particles, such as their charge and energy.

In this Chapter, the calibration of this ΔE-E telescope with ions used in clinic will be presented.

II. Experimental setup

Data acquisition experiments were carried out in different facilities providing ions of various types and energies:

- Cyrcé cyclotron at IPHC (Strasbourg, France) [55], producing protons beam of 25 MeV, which can be attenuated by an aluminum wheel to lower energies.
- CAL (Centre Antoine Lacassagne, Nice, France) protontherapy center [56], specializes in proton therapy treatments for cancer, providing a proton beam of 62 MeV.
- cave M of GSI (Darmstadt, Germany), the heavy ion accelerator facility SIS-18 [57], using PMMA thickness variations to modulate carbon beam energies.
- CNAO hadrontherapy center (Pavia, Italy) [58], which offers advanced hadron therapy treatments using carbon ions and protons.

The characteristics of the beams that were used are summarised in Table 3.1 and the different experimental setups for each facility are presented in Figure 3.1.

At Cyrcé, aluminum attenuators from 0.147 mm to 1.424 mm were used to degrade the beam energy from 25 MeV down to 16 MeV, while at GSI, three different PMMA thicknesses were used in order to achieve carbon beam energy ranges of 120 MeV/u, 160 MeV/u and 180 MeV/u. At CAL and CNAO, the energy of the beam was not attenuated. Only one energy of 61 MeV/u was used at CAL, while several energies of ^{12}C and protons were used at CNAO, from 120 MeV/u to 200 MeV/u.

In the experimental setup at GSI, a plastic scintillator of 1 mm was placed in front of the beam for another experiment which was carried out at the same beam time.

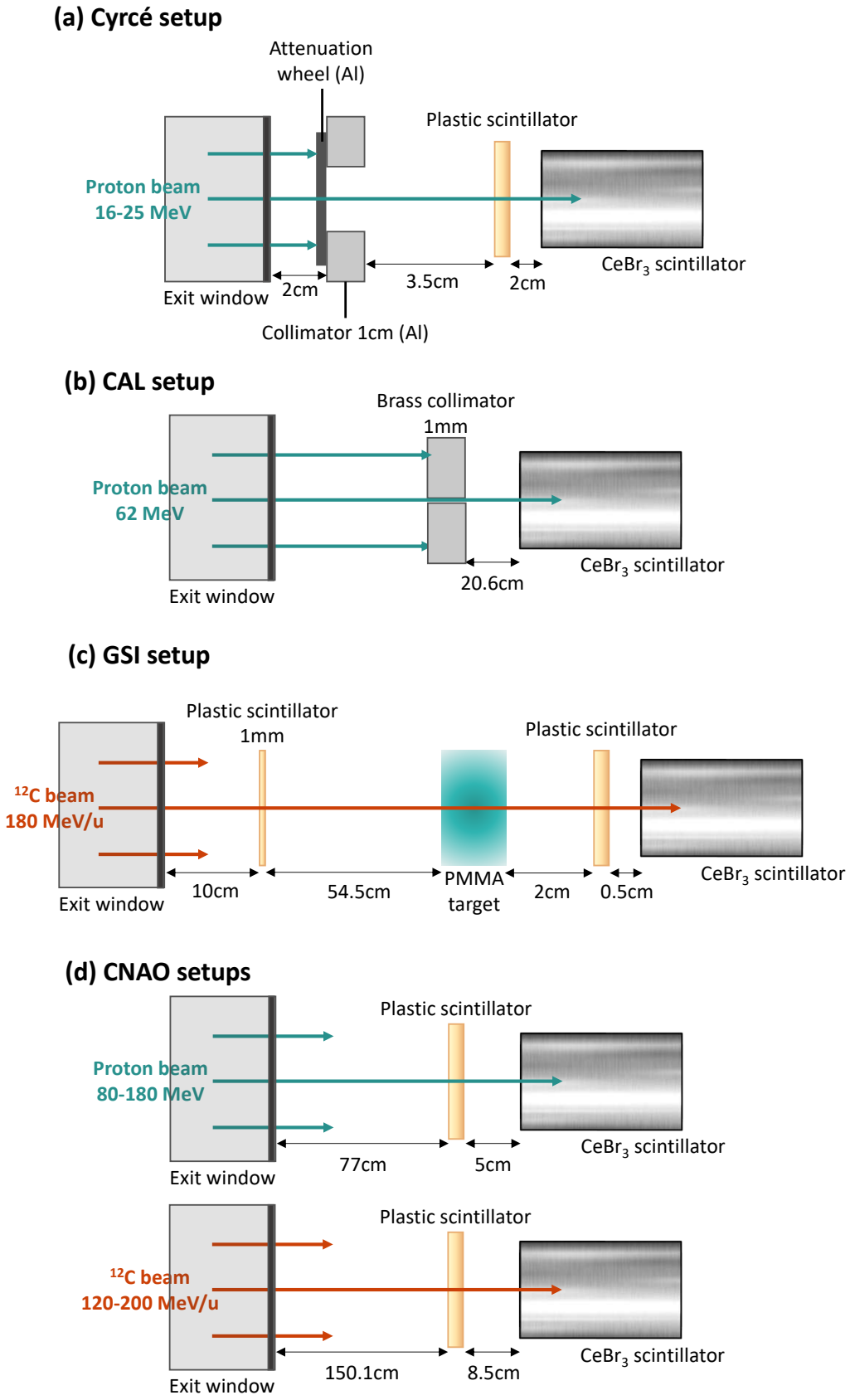

Figure 3.1: Schemes of the experimental setups used at Cyrcé (a), CAL (b), GSI (c) and CNAO (d).

Facility	Ion type	Energy range
Cyrcé	^{1}H	16-25 MeV
CAL	^{1}H	61 MeV
GSI	^{12}C	120-180 MeV/u
CNAO	^{12}C	120-200 MeV/u

Table 3.1: Beam types and energies that were used for the calibration of the $CeBr_3$ and plastic scintillators.

III. Data analysis and simulations

Continuing with the established experimental setups, we will delve into the methodology used for data analysis and the simulations conducted alongside the corresponding experimental data.

III.1 Data analysis method

The analysis software used for the data analysis was an extension of the QAPIVI software tool [59], called STIVI (for Software for Tracking of Ions and Vertex Imaging).

III.1.1 Baseline, amplitude, and charge determination

The baseline refers to the initial portion of the waveform where no significant signal is expected, representing the underlying noise level of the system. To establish the baseline of the waveforms, a method involving the projection of the first 10 bins in time was employed on the pulse shape (examples in Figure 2.5 in Chapter 2 Section I.1). Subsequently, the mean value and dispersion, indicative of the noise level, were computed for accurate characterization. The determination of the signal's rise and fall involved setting thresholds relative to the baseline, typically defined as the baseline minus 10 times the noise level. It's noteworthy that these thresholds are adjustable, facilitating adaptability to various experimental conditions. The integration of the signal giving the charge was then performed within the determined range, while the amplitude of the signal was identified as its maximum value.

The baseline of the waveforms was evaluated and subtracted to the signal, to isolate the signal from the background noise. The distributions of the amplitudes of the Waveforms (in mV) were fitted with Gaussian functions, in order to extract the mean amplitude value and its corresponding standard deviation.

III.1.2 Relation between amplitude and energy deposition

Birk's law describes the non-linear response of scintillators to ionizing radiation, particularly when light output is not directly proportional to energy deposition due to saturation effects. Initially formulated by J.B. Birk (1951), this law accounts for scintillation quenching, a phenomenon wherein scintillator efficiency decreases as the local ionization density along the particle track increases.

The classical formulation of Birk's law [43] is as follows:

$$\frac{dL}{dx} = \frac{S \cdot \frac{dE}{dx}}{1 + k_B \cdot \frac{dE}{dx}}$$

where $\frac{dL}{dx}$ is the light output per unit length, $\frac{dE}{dx}$ is the energy deposited per unit length by the particle, S is a proportionality constant that translates the energy deposited into light output (which can be attributed to scintillation efficiency), k_B is Birk's constant, representing the scintillator-specific quenching parameter, with typical values ranging from 10^{-2} to 10^{-3} cm/MeV for common scintillators [60].

However, this formulation assumes that $\frac{dE}{dx}$ is known, which is often not the case in practical applications where only the total energy deposited, E, and the resulting pulse amplitude produced by the scintillator are measured. Consequently, an adaptation of Birk's law that considers total deposited energy rather than differential energy loss is essential for experimental usage.

To suit practical constraints in experimental settings, we adapt Birk's law to use the total energy deposited, E, rather than $\frac{dE}{dx}$. In this adaptation, we replace S and K_B with modified constant S' and k'_B respectively, to distinguish it from the original formulation. The modified form of Birk's law then becomes:

$$A = \frac{S' \cdot E + A_0}{1 + k'_B \cdot E}$$

where A is the amplitude of the light signal measured (in mV), E is the total energy deposited (in MeV), S' is a conversion factor between the deposited energy and the amplitude, k'_B is a modified quenching parameter adapted to total energy (in MeV^{-1}), A_0 represents a pedestal or baseline signal (in mV) accounting for background noise or residual detector response.

Adjustable parameters

- **Adjusted conversion factor** S' serves as a proportionality factor to convert the deposited energy E into the expected amplitude A. Its value reflects both the light yield efficiency and the detector's response. In the literature, typical values of S' are $\sim 10^{-2}$ to 10^{0} (in mV.MeV^{-1}) [60][43][61]. Unlike S, which directly relates to differential energy loss, S' is experimentally calibrated to reflect the detector's pulse response to total energy deposition.

- **Adjusted quenching parameter** k'_B represents saturation or quenching effects in terms of total energy deposited. Typical values for k'_B are of 10^{-2} to $10^{-3}\,\text{MeV}^{-1}$ for inorganic scintillators [62] and of 10^{-3} to 10^{-4} MeV^{-1} for organic or plastic scintillators [63]. This parameter governs the non-linear light yield reduction at high energy deposition, aligning with quenching observed in Birk's original framework.

- **Pedestal** A_0 accounts for the baseline signal amplitude, capturing any residual detector response in the absence of energy deposition. Its expected values are in the low mV range.

The adapted version of Birk's law remains consistent with the theoretical basis of the original, preserving the quenching effect via the k'_B parameter while incorporating linear response at low energy depositions through S'.

For the next sections, the function will be used as follows, with p_0, p_1 and p_2 the variable parameters, and, for simplicity, S' and k'_B will be refereed to as S and k_B, respectively:

$$A = \frac{p_0 * E + p_1}{1 + p_2 * E} \tag{3.1}$$

These three parameters are dependent on the geometry of the scintillators and the high voltage applied to the PMT, they were considered as free parameters in the fit of the detector response to ions, and will represent the calibration parameters values of our detectors.

III.1.3 Time resolution

Lastly, the assessment of the time resolution of the telescope provides crucial information regarding the system's temporal capabilities. By quantifying the differences in detection times and determining the distribution's standard deviation, we evaluate the precision and accuracy of the detection system used in time-of-flight mode.

III.2 Monte Carlo simulation

The Monte Carlo code GEANT4 10.07 [64] with the INCL++ physic list [65] described in the Chapter 2 Section II.1.3, was used to evaluate the deposited energy in the plastic scintillator, and the energy of the ions reaching the $CeBr_3$, after its entrance window. While it is not necessary to take into account the thickness of this entrance window for γ-rays detection, it needs to be considered for ions detection, as they will lose a non-negligible amount of energy in it.

III.2.1 Beam straggling and scattering

Simulations were also used to evaluate the energy straggling and beam scattering. Indeed, contrary to gamma-rays measurements, where the standard deviation around the mean energy value corresponds to the detector resolution at the considered energy, charged particles encounter important straggling in the different materials that are crossed by the incoming ion, manifesting as a spread in the energy loss distribution, contributing to the observed broadening of the energy spectrum in detectors. Alongside, beam scattering, arising from multiple Coulomb scattering events experienced by charged particles, induces deviations from their initial trajectories, thereby influencing the spatial distribution of energy deposition.

In Figure 3.2 an example of energy deposition distribution of a ^{12}C beam of 120MeV/u, inside the $CeBr_3$ is shown, alongside the Gaussian fit parameters and thus the standard deviation from beam straggling and scattering.

III.2.2 Energy resolution

To rigorously quantify the intrinsic energy resolution of each detector, it is imperative to disentangle the contributions from energy straggling and beam scattering from the overall detector resolution. This requires subtracting the standard deviation derived from the Monte Carlo simulations, σ_{G4}, from the standard deviation obtained from the experimental data calibration, σ_{det}, as per the equation:

$$\sigma_E = \sqrt{\sigma_{det}^2 - \sigma_{G4}^2} \tag{3.2}$$

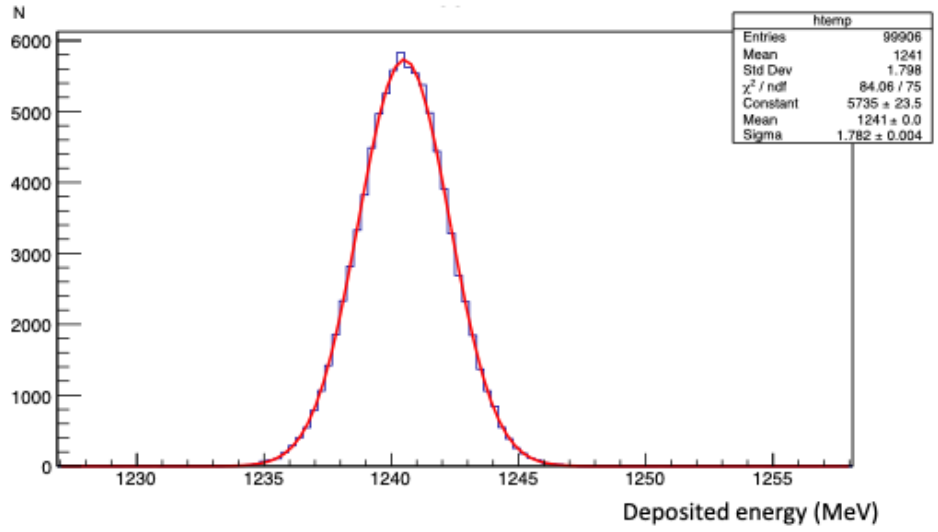

Figure 3.2: Geant4 simulation of deposited energy inside the $CeBr_3$ for ^{12}C beam of 120MeV/u, after the plastic scintillator and the entrance window.

where σ_{det} corresponds to the standard deviation of the energy distribution obtained after calibration of the raw data distributions, and σ_{G4} is the standard deviation of the energy distribution predicted by Geant4. This deviation does not take into account any detector response, and therefore corresponds only to the straggling and beam scattering.

Moreover, the fitting of detector resolution as a function of collected energy using the proposed equation facilitates a comprehensive characterization of the resolution behavior across varying energy depositions. The parameters a and b in the equation capture the nuanced dependence of resolution on energy deposition :

$$\frac{\sigma_E}{E} = a + \frac{b}{\sqrt{E}} \tag{3.3}$$

with a and b being free parameters for the fit.

IV. Detectors calibration and performance

IV.1 Response of $CeBr_3$ to ions

IV.1.1 Energy calibration

In Figure 3.3(a), the calibration curves of the $CeBr_3$ crystal scintillator obtained with both protons and ^{12}C, with an applied voltage of +350V are presented. For each ion type (carbon and proton), distinct calibration functions are applied. This differentiation is consistent with the findings in [66], where the scintillators' light output showed varying responses based on the isotope. Remarkably, the Birk's constant appears similar for both ions, reflecting a robust consistency in the calibration results.

Birk's law is followed up to 2350 MeV of deposited energy, corresponding to the energy deposited by ^{12}C of 200 MeV/u (after traversing 20mm of PMMA). Notably, the plotted points for protons and carbon ions exhibit a conformal distribution, suggesting a

consistent response of the scintillator across different particle types and energies.

In Figure 3.4(a) and (b), the calibration curves of the $CeBr_3$ crystal scintillator obtained with only protons with an applied voltage of +400V and +600V respectively, are presented.

All the fit parameters values collected for both plastic and $CeBr_3$ and for all applied voltage can be found in Table 3.2. It can be observed that, depending on the voltage and the photomultiplier gain, distinct Birk's constants are obtained for the plastic scintillator detector. Nevertheless, it is noteworthy that these discrepancies in Birk's constants across different conditions overlap within the margin of error and fall within the expected range reported in the literature, thereby indicating coherence in the data.

Detector	S ($mV.MeV^{-1}$)	k_B (MeV^{-1})
Plastic -1200V	8.4 ± 0.8	0.0074 ± 0.0026
Plastic -1100V	2.30 ± 0.16	0.0048 ± 0.0019
$CeBr_3$ +350V (Carbons)	0.1495 ± 0.0005	0.0008570 ± 0.0000024
$CeBr_3$ +350V (Protons)	0.3590 ± 0.0002	0.0008638 ± 0.0000024
$CeBr_3$ +400V	1.6510 ± 0.0012	0.010550 ± 0.000017
$CeBr_3$ +600V	20. ± 3.0	0.024 ± 0.008

Table 3.2: Obtained values of free parameters from Birks' law used to fit the detectors calibration curves.

IV.1.2 Energy resolution

In Figure 3.3(b) is presented the energy resolution distribution of the $CeBr_3$ for both protons and ^{12}C ions, obtained under a +350V applied voltage. Remarkably, a resolution in the order of 10 MeV is observed for both ion types, underscoring the precision of the crystal in measuring energy depositions.

IV.1.3 Energy distributions comparison

To validate the calibration of the $CeBr_3$ scintillator, experimental data in energy are compared with Geant4 simulations, as depicted in Figure 3.5. This comparison offers insights into the reliability of the methodology across both proton and carbon ion measurements.

Looking into the comparison of deposited energy in $CeBr_3$ between Geant4 simulations and calibrated experimental data, using a 120MeV/u ^{12}C beam as illustrated in Figure 3.5(a), the presence of a fragmentation tail is revealed in the experimental data, but less present in the simulation. However, the simulation accurately reproduces the energy peak distribution.

Similarly, Figure 3.5(b) depicts the comparison of $CeBr_3$ deposited energy between Geant4 simulations and calibrated experimental data using a 80MeV/u ^{1}H beam. Here, a discrepancy of less than 5 MeV in the energy peak can be observed. While this deviation is noticeable, it falls within an acceptable range for ensuring the reliability of our measurements.

This range, typically defined as ±5%, accounts for minor variations in experimental conditions and calibration inconsistencies. Specifically, a 5 MeV discrepancy in the context

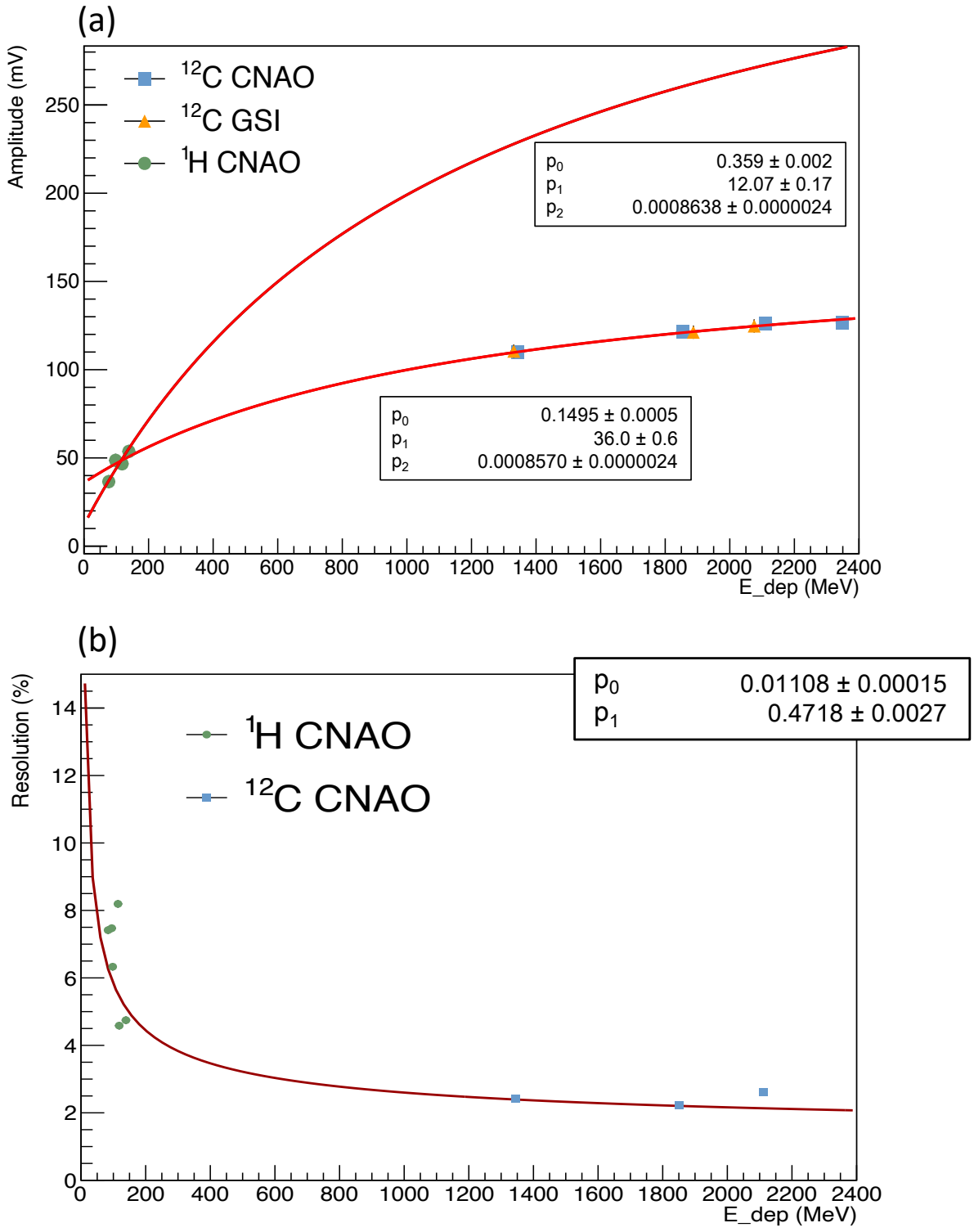

Figure 3.3: Calibration curve in amplitude (a) and energy resolution (b) of the $CeBr_3$ scintillator obtained with both protons and ^{12}C ions with a +350V voltage applied. Energies can be found on Table 3.1.

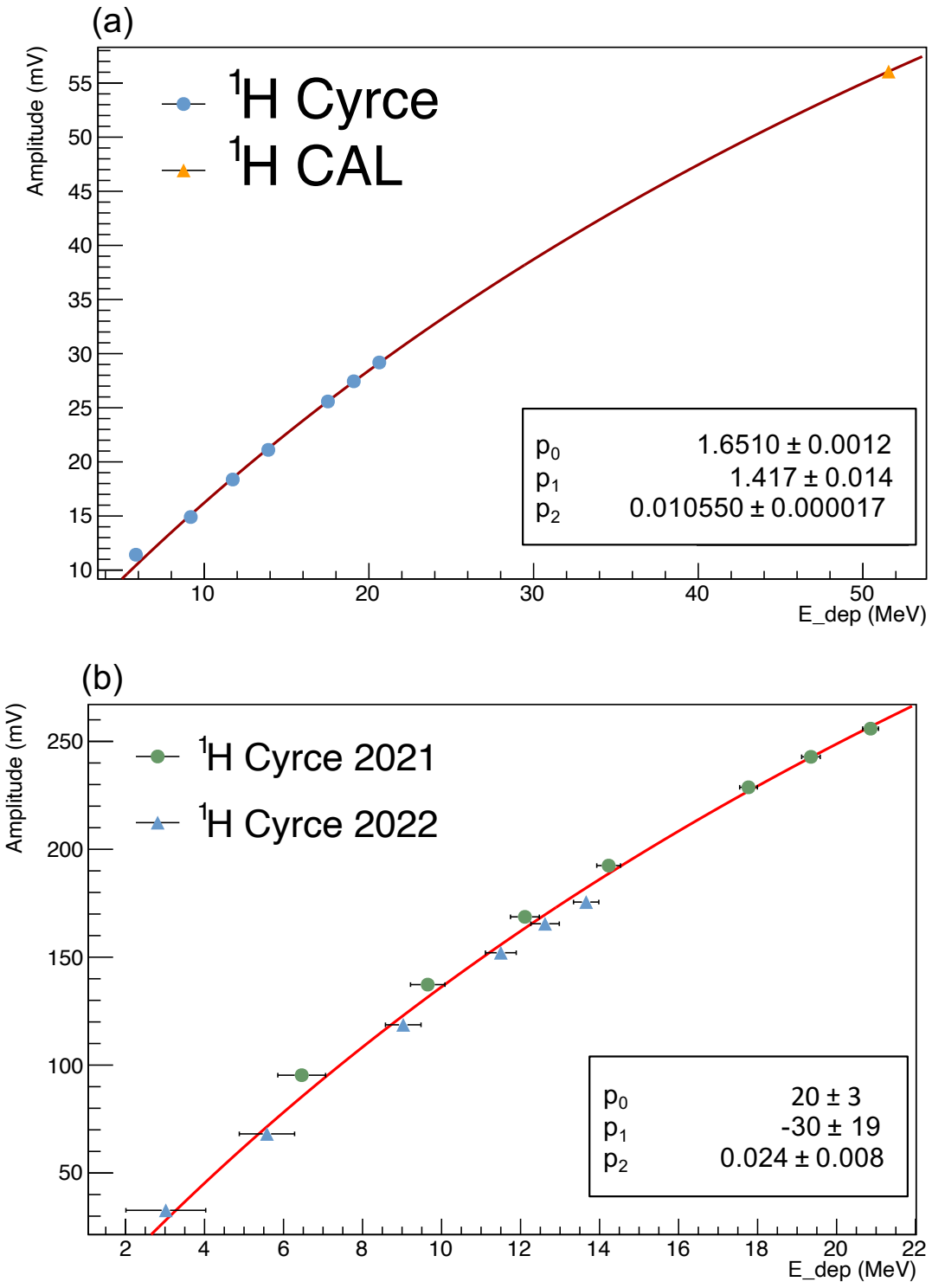

Figure 3.4: Calibration curve of the $CeBr_3$ obtained with both protons with a +400V (a) and a +600V (b) voltage applied with ^{1}H beam of Cyrcé and CAL. Energies can be found in Table 3.1.

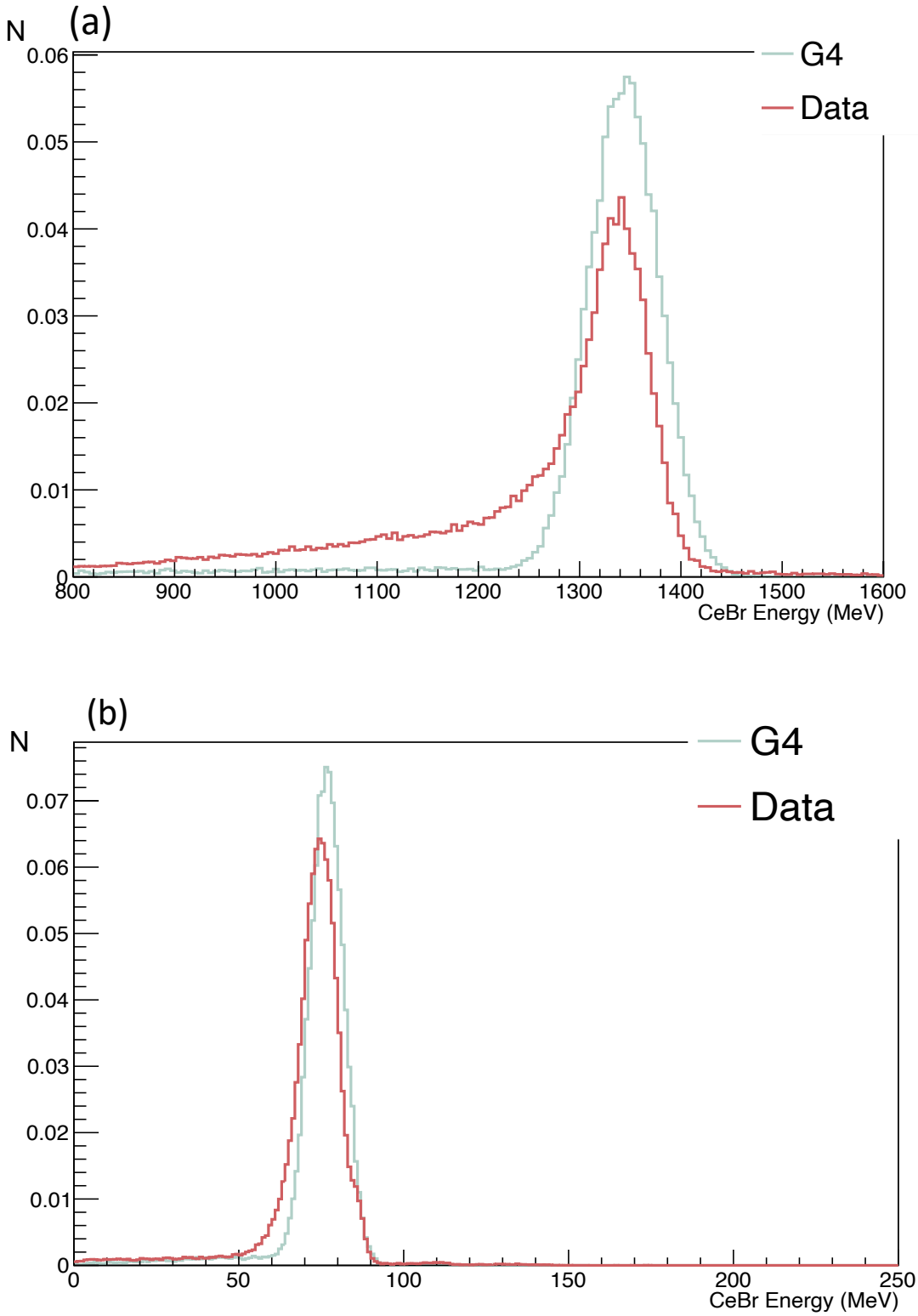

Figure 3.5: $CeBr_3$ deposited energy comparison between Geant4 simulation and calibrated data with a 120MeV/u ^{12}C beam (a) and a 80MeV/u ^{1}H beam.

of a 80 MeV/u ^{1}H beam represents a deviation of about 6%, which, while significant, remains manageable within the broader scope of experimental nuclear physics, where uncertainties can often span up to 10-20% depending on the complexity of the setup and the type of particles measured [67]. Moreover, radiolysis effects do not significantly change with slight variations in energy, maintaining relative consistency even with differences of a few percent [68].

IV.2 Response of plastic to ions

In this section, the calibration curves of plastic scintillators will be investigated, aiming to understand their response to both proton and ^{12}C ion beams, with a particular focus on two distinct photomultiplier setups.

The calibration curves of the plastic scintillator obtained with both protons and ^{12}C ions, are depicted in Figures 3.6 and 3.7(a) for both photomultipliers. Notably, both plots demonstrate adherence to Birk's law up to a deposited energy of 50 MeV. This range corresponds to energy depositions by ^{12}C ions of 110 MeV/u (after traversing 30 mm of PMMA) for Figure 3.6, and by ^{12}C ions of 120 MeV/u for Figure 3.7(a).

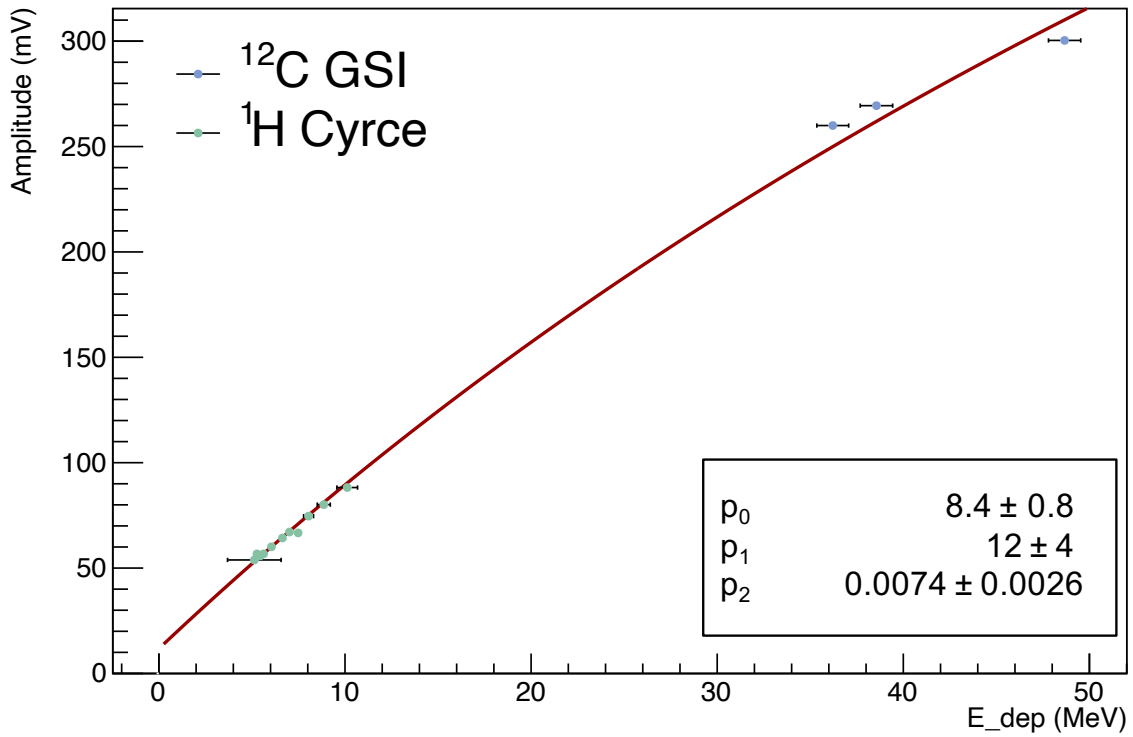

Figure 3.6: Calibration curve of the plastic scintillator with the R7057 PMT at -1100V, with ^{12}C beam of GSI and ^{1}H beam of Cyrce. Energies can be found on Table 3.1.

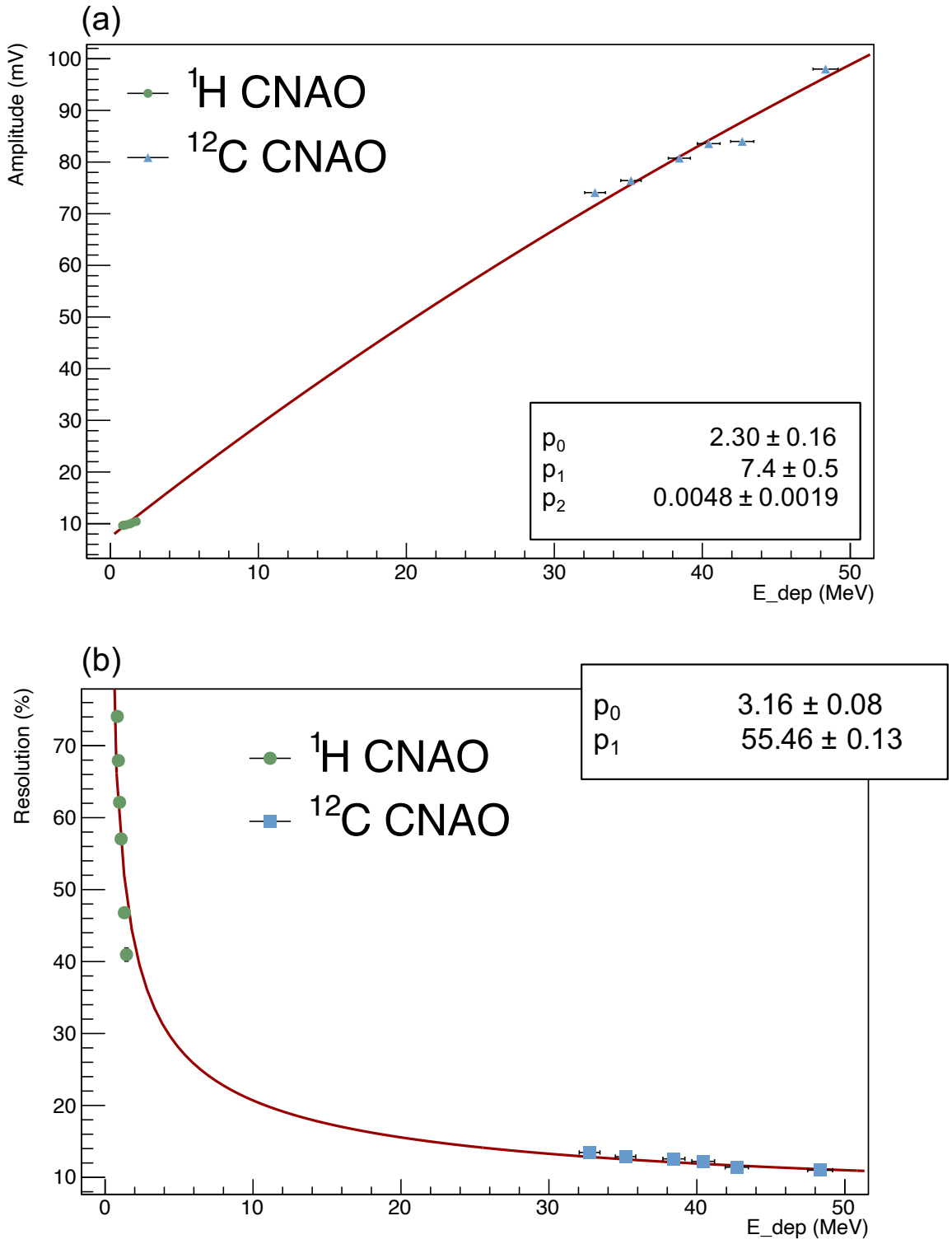

Figure 3.7: Calibration curve of the plastic scintillator with the XP3990 PMT at -1200V (a) and energy resolution as a function of the deposited energy (b), with ^{12}C and ^{1}H beam of CNAO. Energies can be found on Table 3.1.

It's important to highlight that direct comparison between the two calibration constants isn't feasible due to differences in the photomultiplier tubes (PMT) and applied voltages (-1200V and -1100V).

Furthermore, Figure 3.7(b) illustrates the energy resolution of the scintillator with the XP3990 PMT as a function of deposited energy. This analysis integrates considerations of experimental beam straggling effects, which may introduce uncertainties in the measured energy resolution. Indeed, the energy deposited by the ions can exhibit significant variation due to straggling, leading to a spread in the measured energy spectrum. The uncertainty in energy loss can be in the order of several MeV, depending on the thickness and composition of the material. Similarly, scattering can cause angular deviations up to a few degrees, impacting the spatial resolution of the detector.

IV.3 Time performance

A good time resolution ensures that the two measurements, energy loss and total energy, can be accurately correlated in time, aiding in precise particle identification. Moreover, this test is necessary as the telescope will also be used in ΔE-ToF measurements for high-energy ions, as well as for detecting gammas and neutrons, necessitating rigorous temporal performance assessments.

For instance, the FRACAS experiment achieved a time resolution of around 300 ps for similar high-energy ion beams [69]. These benchmarks illustrate the standards required for effective particle detection. The time resolution values were extracted from the experiments performed, with both protons and ^{12}C.

Figure 3.8 presents the time differences between the two detectors for a 25 MeV proton beam (a) and a 180 MeV/u ^{12}C ion beam (b). These plots permit to explore the temporal behavior of the detector system under different beam conditions.

From the experimental data, we determined the temporal resolution for the 180 MeV/u ^{12}C ion beam is 282 ± 1 ps. Similarly, for the plastic and $CeBr_3$ detectors with a 25 MeV proton beam, the time resolution was found to be 170 ± 1 ps. The increase of the time resolution value for carbon ions is mainly due to the low voltage that was applied to the cerium bromide PMT (+350 V).

These values represent crucial benchmarks in assessing the time performance of the detection system across varying beam energies and particle types. Such precise temporal resolution enables robust particle identification and TOF measurement, and enhances the overall capabilities of the experimental setup for the CLINM purpose.

IV.4 Overall discussion

The calibration of the plastic scintillator yielded a calibration curve with two different PMTs that followed Birks' law up to 50 MeV of deposited energy. This result demonstrates the reliability of the plastic scintillator's response to ion beams within this energy range. Furthermore, the energy resolution of the plastic scintillator was also examined, and it is noteworthy that the resolution improves as the deposited energy increases. This phenomenon aligns with expectations, as higher energy ions induce greater scintillation light, thus augmenting energy resolution.

The $CeBr_3$ crystal scintillator was calibrated using both proton and ^{12}C ion beams.

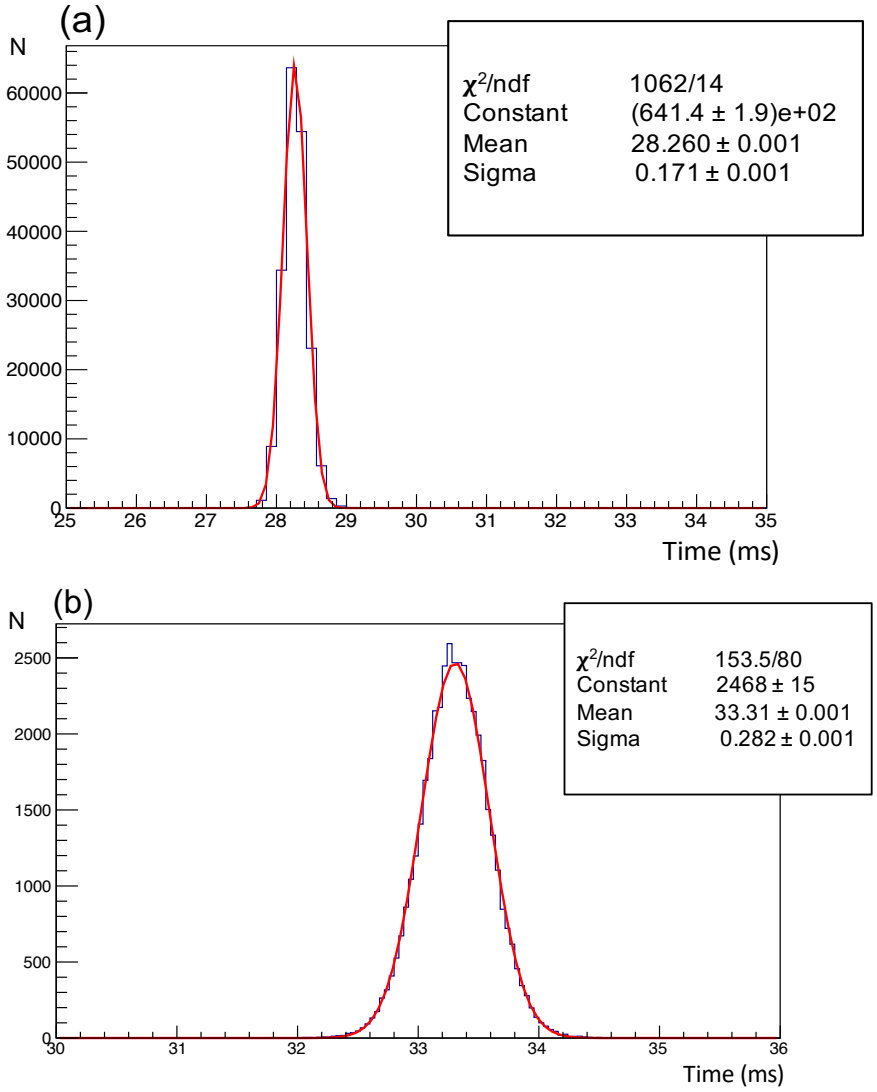

Figure 3.8: Resolution in time between the plastic with the $CeBr_3$ and R7057 PMT with a 25MeV ^{1}H beam (a) and XP3990 PMT with a 180MeV/u ^{12}C beam (b)

The calibration results show that the crystal scintillator follows the Birks' law up to 2350 MeV of deposited energy, which corresponds to the energy deposited by 200 MeV/u ^{12}C ions. This extended reliability is a valuable characteristic, as it allows accurate measurement across a broad spectrum of ion energies encountered in hadrontherapy treatment (80 - 200 MeV/u for ^{1}H beam and 12 - 400 MeV/u for ^{12}C beam).

Furthermore, examination of calibration curves obtained with protons at different voltages (+ 400 V and + 600 V) exhibited consistency with those obtained at + 350 V, indicative of the $CeBr_3$ scintillator's efficient response to varied voltage settings for ion detection.

Notably, the Birks' law reflected a quenching effect of the scintillators, with an increase in voltage corresponding to an increase in the Birks constant. This observation underscores the adaptability of the scintillator to diverse experimental conditions and provides options for optimizing its performance.

In addition to energy resolution assessment, the time performance of our ΔE-E telescope was also evaluated. Accurate time measurements enable the correlation of energy loss and total energy, facilitating particle identification and background rejection.

The time resolution measurements exhibit a resolution of 282 ± 1ps for ^{12}C ions of 180 MeV/u and 170 ± 1ps for 25 MeV protons. These results underscore the capability of this telescope to provide precise measurements in clinical conditions. The narrower time resolution for protons compared to ^{12}C ions can be attributed to the differences in their masses and velocities.

V. Conclusion

In the context of hadrontherapy, precision in measuring energy deposition stands as a fundamental requirement for optimizing treatment plan.

The calibration was carried out for both the plastic scintillator and the $CeBr_3$ crystal scintillator, resulting in accurate energy measurements. Notably, this marks the initial calibration for $CeBr_3$ in the context of various high energy ion beams. This calibration enhances the ability to accurately measure energy deposition and also improves the identification of various ion types in the CLINM project in order to improve data in Monte Carlo simulations.

Summary

Contexte général

Lors du traitement du cancer par thérapie par particules (faisceau d'ions lourds ou de protons), les réactions nucléaires du faisceau primaire avec le volume cible doivent être quantifiées pour calculer correctement la dose reçue par le patient. Ceci est crucial pour prévoir la production de fragments plus légers et leur contribution à une dose indésirable dans les tissus sains environnants. Les calculs de dose en thérapie par particules reposent sur des algorithmes haute performance intégrant des processus physiques, chimiques et biologiques, mais le manque de données expérimentales sur les réactions nucléaires peut introduire des inexactitudes sur les modèles utilisés.

Le projet CLINM

Le projet CLINM (Cross-sections of Light Ion and Neutron Measurements) vise à comprendre les interactions complexes entre les radiations ionisantes et les systèmes biologiques. Ce projet interdisciplinaire combine la physique et l'analyse chimique pour étudier les effets chimiques des radiations ionisantes secondaires sur l'eau et les biomolécules.

Lors de l'interaction des ions carbone primaires avec la matière biologique, des particules secondaires telles que des électrons, protons, neutrons et rayons gamma sont produites, pouvant causer divers types de dommages, y compris l'ionisation, l'excitation et la fragmentation des liaisons moléculaires, affectant les fonctions cellulaires et entraînant des réponses biologiques.

Les logiciels de planification des traitements, de plus en plus basés sur des simulations Monte Carlo, ne reproduisent pas fidèlement les particules secondaires générées par les processus nucléaires, créant des incertitudes nécessitant une recherche approfondie pour améliorer les calculs de production de particules secondaires et leurs effets radiobiologiques. Environ 70 % des dommages cellulaires sont dus à des effets indirects des espèces réactives formées lors de la radiolyse de l'eau, nécessitant une caractérisation précise des particules secondaires produites pendant les traitements.

Télescope ΔE-E

Le télescope ΔE-E utilisé dans cette étude comprend un scintillateur en plastique de 2 mm d'épaisseur et un scintillateur en cristal de $CeBr_3$ de 5,1 cm d'épaisseur. Ces détecteurs, choisis pour leurs caractéristiques physiques distinctes, contribuent à l'efficacité de la détection et de la caractérisation des particules chargées, des rayons gamma et des neutrons.

Le cristal de $CeBr_3$ a été choisi pour détecter non seulement les particules chargées mais aussi les rayons gamma et les neutrons. Contrairement à certaines alternatives comme le $LaBr_3$, le $CeBr_3$ ne présente pas de radioactivité interne, ce qui minimise le bruit de fond et les fausses coïncidences, améliorant ainsi la précision de la détection des radiations. Le $CeBr_3$ offre également une excellente résolution énergétique et une réponse rapide, permettant des mesures temporelles précises.

Le scintillateur plastique EJ-228 est conçu pour offrir des performances élevées en termes de résolution temporelle et de rendement lumineux. Il produit environ 10 200 photons par MeV d'énergie d'électron, avec un temps de montée de 0,5 ns et un temps de décroissance de 1,4 ns. Ces propriétés de synchronisation rapide sont cruciales pour minimiser le chevauchement des signaux et améliorer la résolution temporelle. Comparés à d'autres matériaux, les scintillateurs en plastique offrent un bon compromis entre performance et coût.

Les signaux des deux détecteurs ont été acquis en coïncidence par un module de numérisation WaveCatcher, développé par le laboratoire LAL (Paris, France), avec une fréquence d'échantillonnage de 3,2 GHz. Une fenêtre de 80 ns a été appliquée pour la coïncidence des détecteurs.

Calibration
La calibration du télescope ΔE-E avec des ions utilisés en clinique est essentielle pour assurer une identification et une quantification précises des particules. Elle implique d'établir une relation connue entre l'énergie déposée dans les détecteurs et les propriétés des particules incidentes, telles que leur charge et leur énergie.

Dispositif expérimental

Les expériences d'acquisition de données ont été réalisées dans différentes installations, avec les dispositifs expérimentaux présentés en Figure 3.1, fournissant divers types et énergies d'ions. Les énergies précises employées sont résumées dans la Table 3.1 :

- Cyclotron Cyrcé à l'IPHC (Strasbourg, France) : Faisceau de protons de 25 MeV, pouvant être atténué pour obtenir des énergies plus basses.
- Centre Antoine Lacassagne (Nice, France) : Centre de protonthérapie fournissant un faisceau de protons de 62 MeV.
- GSI (Darmstadt, Allemagne) : accélérateur d'ions lourds SIS-18, utilisant des variations d'épaisseur de PMMA pour moduler les énergies du faisceau de carbone.
- Centre CNAO (Pavia, Italie) : Offre des traitements de hadronthérapie avancés utilisant des ions carbone et des protons.

Analyse des données et simulations

Méthode d'analyse des données

Le code d'analyse utilisé était une extension de l'outil QAPIVI, nommé STIVI (Software for Tracking of Ions and Vertex Imaging). La ligne de base représente le niveau de bruit du système. La méthode impliquait la projection des 10 premiers points temporels du signal pour établir la ligne de base, puis la valeur moyenne et la dispersion étaient calculées. L'intégration du signal donnant la charge était ensuite réalisée dans la plage déterminée, tandis que l'amplitude était identifiée comme sa valeur maximale.

La loi de Birks (équation 3.1) établit une relation entre l'amplitude et la charge des impulsions et l'énergie déposée dans le détecteur. Les paramètres de la fonction de calibration ont été ajustés pour représenter les valeurs de calibration des détecteurs.

L'évaluation de la résolution temporelle fournit des informations cruciales sur les capacités temporelles du système. En quantifiant les différences de temps de détection et en déterminant l'écart type de la distribution, la précision du système de détection en mode temps de vol (ToF) peut être évaluée.

Simulation Monte Carlo
Le code Monte Carlo Geant4 10.07 avec la liste de physique INCL a été utilisé pour évaluer l'énergie déposée dans le scintillateur en plastique et l'énergie des ions atteignant le $CeBr_3$. Les simulations ont également permis d'évaluer la répartition de l'énergie déposée par un faisceau de ^{12}C de 120 MeV/u dans le $CeBr_3$, montrant les effets du straggling et de la diffusion du faisceau.
Pour quantifier la résolution énergétique intrinsèque de chaque détecteur, exprimée par l'équation 3.4, il est nécessaire de séparer les contributions du straggling énergétique et de la diffusion du faisceau de la résolution globale du détecteur. La résolution énergétique est ajustée en fonction de l'énergie déposée pour une caractérisation complète.

Calibration et performance des détecteurs

Toutes les valeurs des paramètres de la loi de Birk, pour le $CeBr_3$ et le plastique, sont données en Table 3.2, incluant les différentes tensions appliquées et les types d'ions.

Réponse du $CeBr_3$ aux ions
Les courbes de calibration du $CeBr_3$, en Figure 3.3, obtenues avec des protons et des ions ^{12}C à une tension de +350V montrent que la loi de Birks est suivie jusqu'à 2350 MeV d'énergie déposée. Les courbes de calibration obtenues avec des protons à différentes tensions (+400V et +600V), en Figure 3.4, ont montré une cohérence avec celles obtenues à +350V.

La résolution énergétique du $CeBr_3$ pour les protons et les ions ^{12}C à +350V montre une résolution de l'ordre de 10 MeV, soulignant la précision du cristal dans les mesures d'énergie. Les données expérimentales en énergie comparées aux simulations Geant4 pour un faisceau de ^{12}C de 120 MeV/u et un faisceau de ^{1}H de 80 MeV/u, représentées en Figure 3.5, montrent une bonne correspondance, validant ainsi la calibration du $CeBr_3$.

Réponse du scintillateur plastique aux ions
Les courbes de calibration du scintillateur en plastique, en Figures 3.6 et 3.7, obtenues avec des protons et des ions ^{12}C montrent qu'elles respectent la loi de Birks jusqu'à 50 MeV d'énergie déposée. La résolution énergétique du scintillateur en plastique s'améliore avec l'augmentation de l'énergie déposée.
La résolution temporelle mesurée pour un faisceau de ^{12}C de 180 MeV/u est de 282 ± 1 ps, et pour un faisceau de protons de 25 MeV, elle est de 170 ± 1 ps. Ces résultats montrent la capacité du télescope à fournir des mesures précises dans des conditions cliniques.

Conclusion

La calibration des scintillateurs en plastique et en cristal de $CeBr_3$ a permis d'obtenir des mesures énergétiques précises et d'améliorer l'identification des ions dans le cadre du projet CLINM. Cela permettra d'améliorer les données des réactions nucléaires dans les simulations Monte Carlo et d'ainsi mieux prédire les effets chimiques et biologiques.

Chapter 4

The CLINM experiment at CNAO

"The lights are so bright, but they never blind me."
– T. S.

Contents

As discussed in the previous Chapter 3, the CLINM (Cross-Sections of Light Ions and Neutron Measurements) project, funded by ANR (starting in January 2024), seeks to offer a global characterization of the secondary particles produced by fragmentation processes of ions on tissues, and their associated chemical effects.

The investigation of these chemical effects involves the measurement of the radiolysis products generated by the secondary particles, while the physical properties (energy, charge) of these particles is performed thanks to a ΔE-E telescope.

In this Chapter, we delve into the measurement of secondary particles produced during the experimental campaign at the CNAO hadrontherapy center.

It is important to emphasize that this is the very first experiment for the CLINM project, and issues were encountered with the beam, particularly its spread. Consequently, the detector's dead time information was not recovered. Although a relative study can be conducted, some crucial data is lacking, and improvements in future experiments need to be considered for further perspectives.

I. Material and methods

The objective is to characterize the secondary particles produced by carbon fragmentation, using a ΔE-E telescope setup. The following subsections detail the experimental setups, analysis procedures, and results obtained from the experiment conducted at CNAO hadrontherapy center (Pavia, Italy) in May 2023, and the achieved results of this campaign will be presented in this work.

I.1 Experimental setup

In this experiment, a ^{12}C ion beam with two energies, 200 and 400 MeV/u, was degraded by different thicknesses of the target, 5 and 23 cm respectively of RW3 (tissue equivalent material) [70], to achieve an energy of 120 MeV/u after the target. In the following chapter, we will refer to the setup involving a 200 MeV/u beam on a 5 cm target as **Config.1**, and the configuration with a 400 MeV/u beam on a 23 cm target as **Config.2**.

The experiment was conducted in two stages to thoroughly understand the effects of secondary radiation. The first stage involved the physics experiment to characterize the secondary particles, using the ΔE-E telescope. The second stage was the chemistry experiment, where water samples were placed after the target in order to study the water radiolysis generated by the beam and its resulting secondary particles. Both stages were carried out under identical irradiation conditions, enabling a direct correlation between the physical characterization data and the observed chemical impacts. This work will only focus on the physical part of the CNAO experiment, the chemical part being carried out in the context of another PhD.

The ΔE-E telescope is made of a thin plastic scintillator (2 mm) placed in front of a cerium bromide crystal scintillator ($CeBr_3$). The voltage applied was - 1200 V for the plastic and + 350 V for the $CeBr_3$ and all the detector specificities were presented in the previous Chapter 3. It was placed behind the RW3 target, and sets at two different angles (0° and 5°). The experimental setup is represented in Figure 4.1.

The calibration process presented in the Chapter 3 was conducted at various facilities, allowing to evaluate the response of the detectors over a wide range of energies encountered in this experiment (between 1 MeV up to several GeV).

I.2 Simulation with Geant4

The same experimental geometry and materials as illustrated in Figure 4.1 was implemented in a Geant4 simulation with the INCL++ physic list. The initial beam was created as a gaussian beam with 200 millions of particles. The cuts applied in the simulation are resumed in Figure 4.2.

Within this setup, the energy deposition in each detector was recorded and related to each event. By simulating the experimental conditions using Geant4, we aim to quantify the accuracy of the simulation physics model.

To take into account the detector response in the Geant4 simulation, the energy resolution of each detector presented in the previous chapter was integrated into the simulated recorded energy.

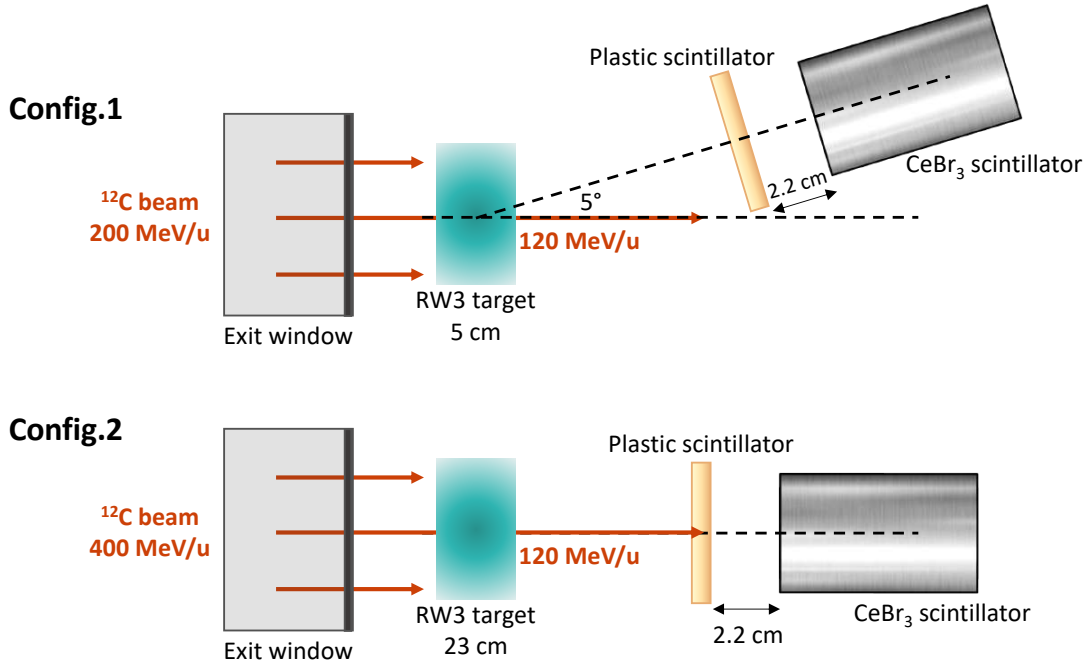

Figure 4.1: CNAO experimental setup with the ΔE-E telescope placed at 0° and 5° from the beam axes.

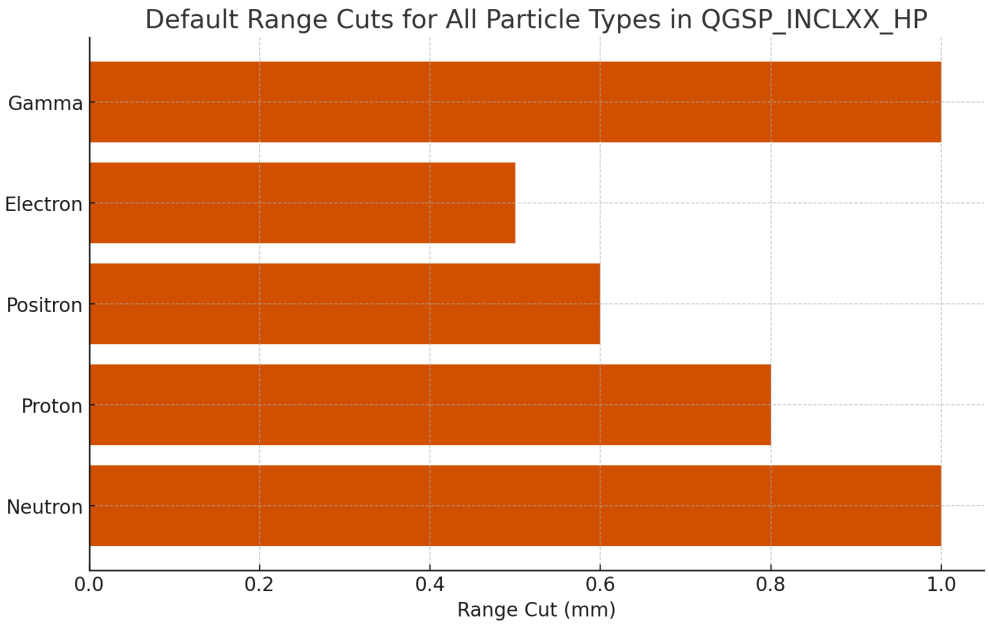

Figure 4.2: Geant4 particles cuts applied in the simulation of CNAO experiment.

I.3 Analysis tools

When secondary particles interact with the ΔE-E telescope, they lose a small amount of energy inside the plastic and deposit the rest of it inside the $CeBr_3$. From an acquisition point of view, we obtain amplitude or charge distributions in coincidence between the two detectors. Applying the calibration done in the previous Chapter, we can accurately convert the recorded signals into corresponding energy values and are thus able to obtain energy distributions of the energy deposited inside the detectors.

These values are then used to construct a plot of ΔE as a function of E for all detected events, as illustrated in Figure 4.3 for the two configurations, a ^{12}C beam of 200MeV/u on a 5cm target and the detectors at 5° and 400MeV/u on a 23cm target and the detectors at 0°. This plot serves as the primary tool for particle identification and analysis.

Different types of particles exhibit characteristic patterns or clusters in the ΔE-E plot due to variations in their energy loss characteristics in the detector materials. By analyzing these patterns and applying graphical cuts on data, we can identify and discriminate between various particle species (each Z). Experimental cuts applied to data are shown in black in Figure 4.3. This identification process may involve comparing experimental data with simulations to optimize each cut.

Once particles are identified, we can perform detailed analyses of their properties within specific regions of the ΔE-E plot. This may include studying the energy spectra, angular distributions, or other relevant parameters of individual particle populations. By comparing these properties to Geant4 simulation results, we will be able to validate and refine models describing particle production during beam fragmentation with the target.

Similar to the methodology employed for experimental data, for each particle event, the energy deposited ΔE in the plastic scintillator and the energy deposited E in the $CeBr_3$ scintillator are recorded, and permit to construct the ΔE-E plot as illustrated in Figure 4.4 where the energy deposited inside the plastic scintillator (ΔE) as a function of the energy deposited inside the $CeBr_3$ (E) for a ^{12}C beam of 200MeV/u on a 5cm target and the detectors at 5° (a) and a ^{12}C beam of 400MeV/u on a 23cm target and the detectors at 0° are presented.

To ensure a meaningful comparison between experimental and simulated datasets, the data cuts employed to isolate distinct Z populations on the ΔE-E experimental plot are applied to the simulated one, as presented in Figure 4.4 in black. This ensures consistency in analytical methodologies across experimental and simulated data, facilitating comparisons and enhancing reliability.

Despite efforts to replicate experimental conditions and because of inaccuracy in theoretical models, simulated Z populations may deviate from predefined data cuts, introducing disparities between simulated and experimental results.

Therefore, extracting the actual simulated Z populations is important to check the accuracy of the analysis and the cut errors.

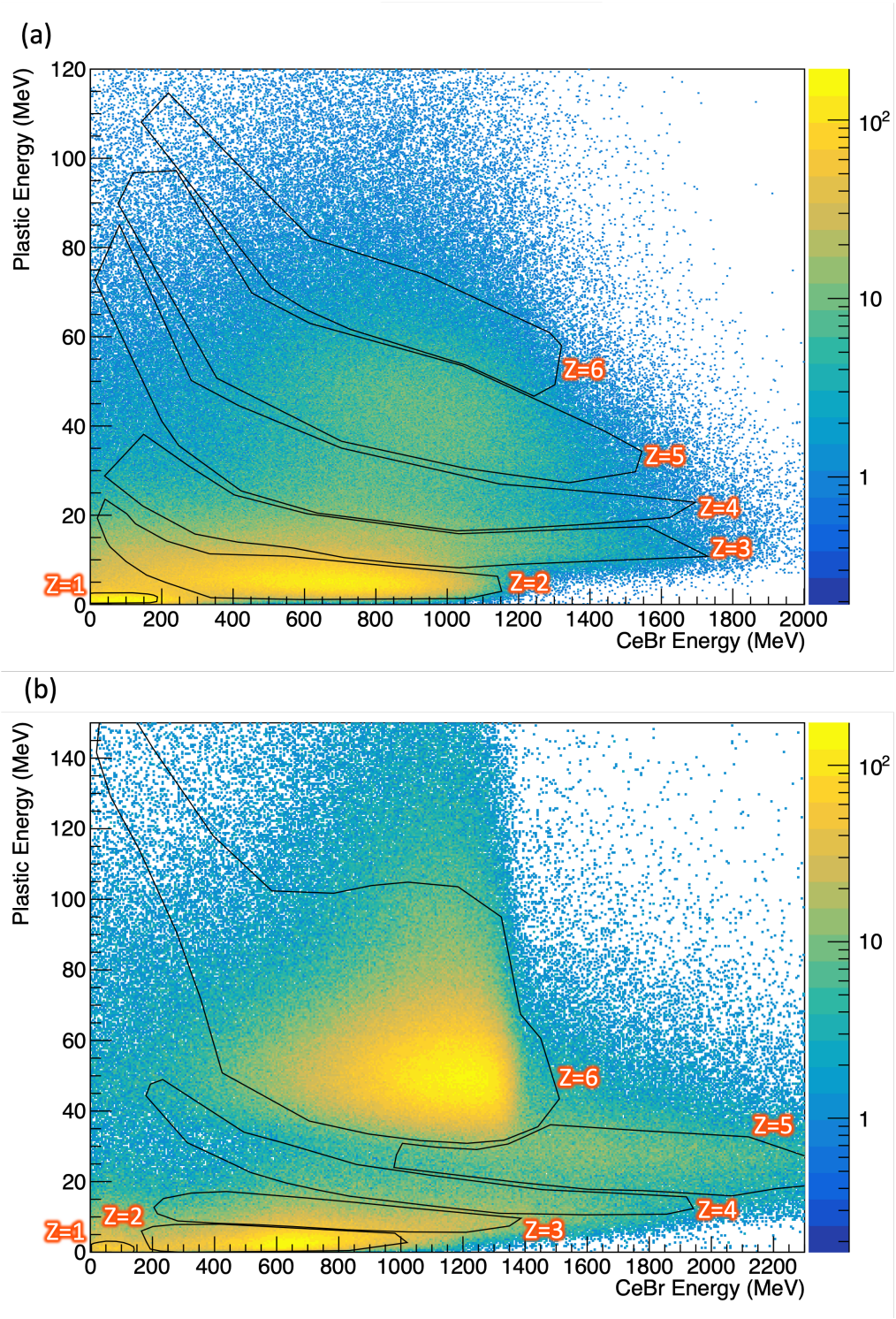

Figure 4.3: Energy deposited inside the plastic scintillator (ΔE) as a function of the energy deposited inside the $CeBr_3$ (E) for a ^{12}C beam of 200MeV/u on a 5cm target and the detectors at 5° (a) and 400MeV/u on a 23cm target and the detectors at 0° with the cuts applied to isolate each Z.

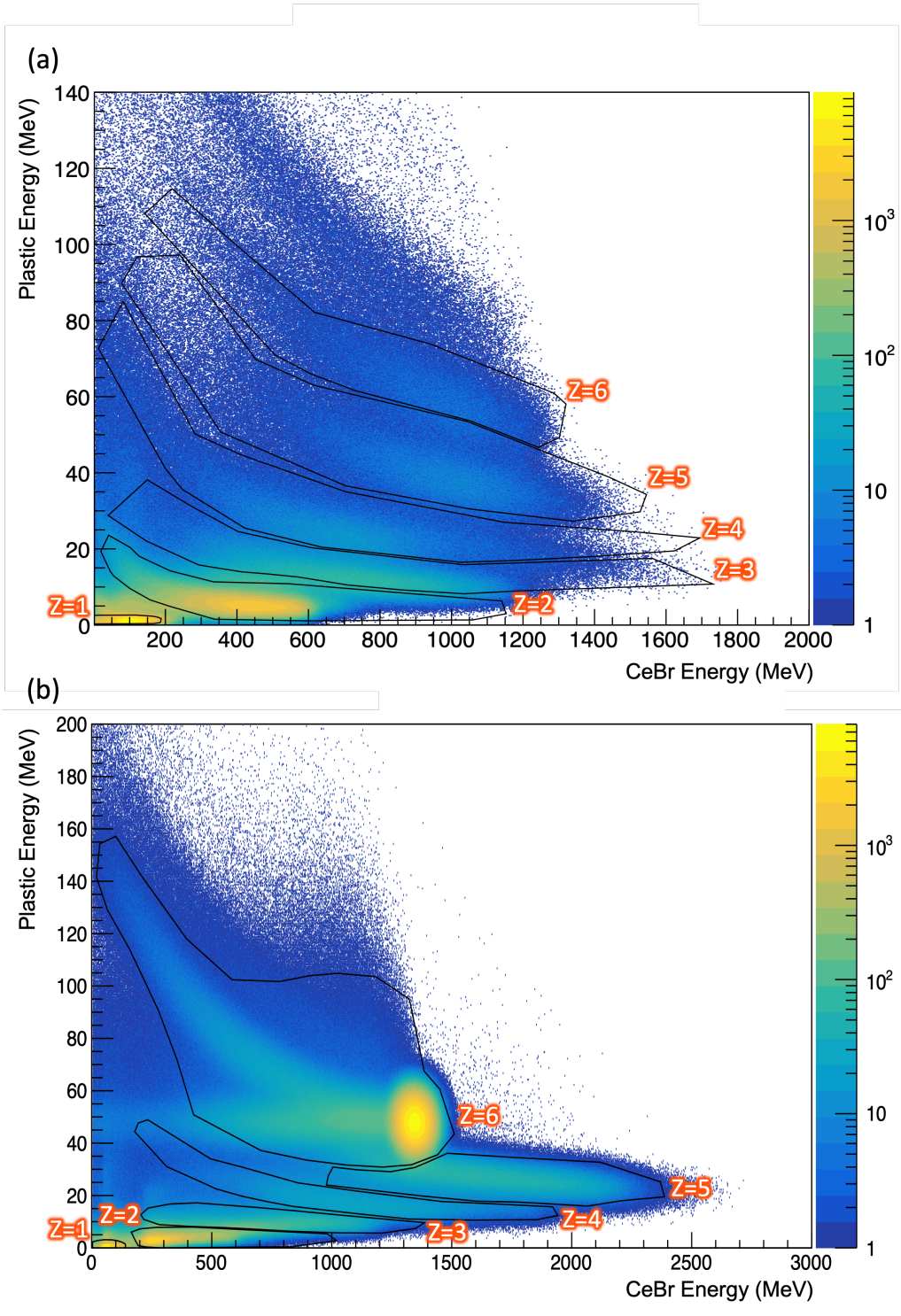

Figure 4.4: Geant4 simulated energy deposited inside the plastic scintillator (ΔE) as a function of the energy deposited inside the $CeBr_3$ (E) for a ^{12}C beam of 200MeV/u on a 5cm target and the detectors at 5° (a) and a ^{12}C beam of 400MeV/u on a 23cm target and the detectors at 0°. Applied cuts for each Z population are represented in black.

II. Results

In this section, the comparison between the simulated and experimental energy distributions and results will be presented.

II.1 Experimental results

Looking into each isolated Z population in our data, the total energy deposited distribution in the detectors of each secondary particle produced by the beam fragmentation inside the target can be analyzed.

In Figure 4.5 for Config.1 and Figure 4.6 for Config.2 are presented the energy distribution for each Z isolated from the ΔE-E distributions. Because of the plastic resolution, presented in Chapter 3 Section IV.2 (around 15% at 40 MeV down to 70% at few MeV), the isotope differentiation is not possible, making the identification more difficult than in simulation.

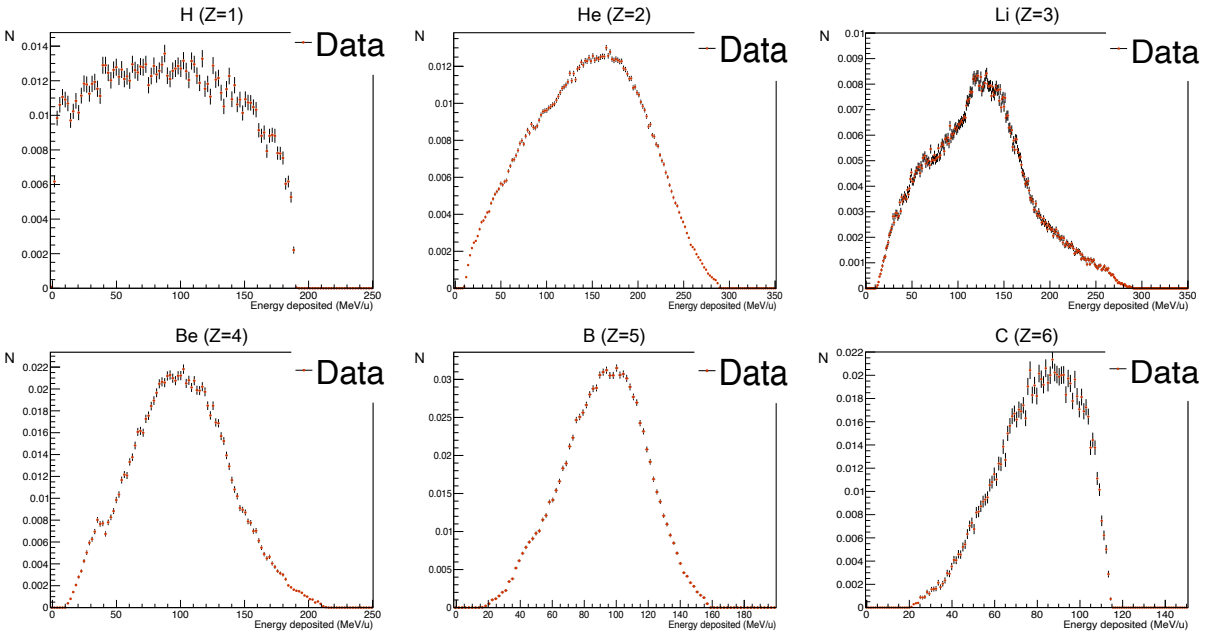

Figure 4.5: Total energy deposited inside the detectors distribution for each isolated Z from data cuts on the ΔE-E plot, for a ^{12}C beam of 200MeV/u on a 5cm target and the detectors at 5°

The energy distributions of the observed fragments provide valuable insights into the experimental results. These distributions are all centered around an average energy, which corresponds to the beam energy in MeV/u at the exit of the target. This outcome is consistent with expectations, as the majority of the observed fragments are from the projectile, carrying with them the energy of the original projectile.

II.2 Comparison with the simulation

In this section, the comparison between the energy distributions measured in the experiment with those predicted by Geant4 simulations will be presented. This comparison will allow to identify any discrepancies and understand their potential causes.

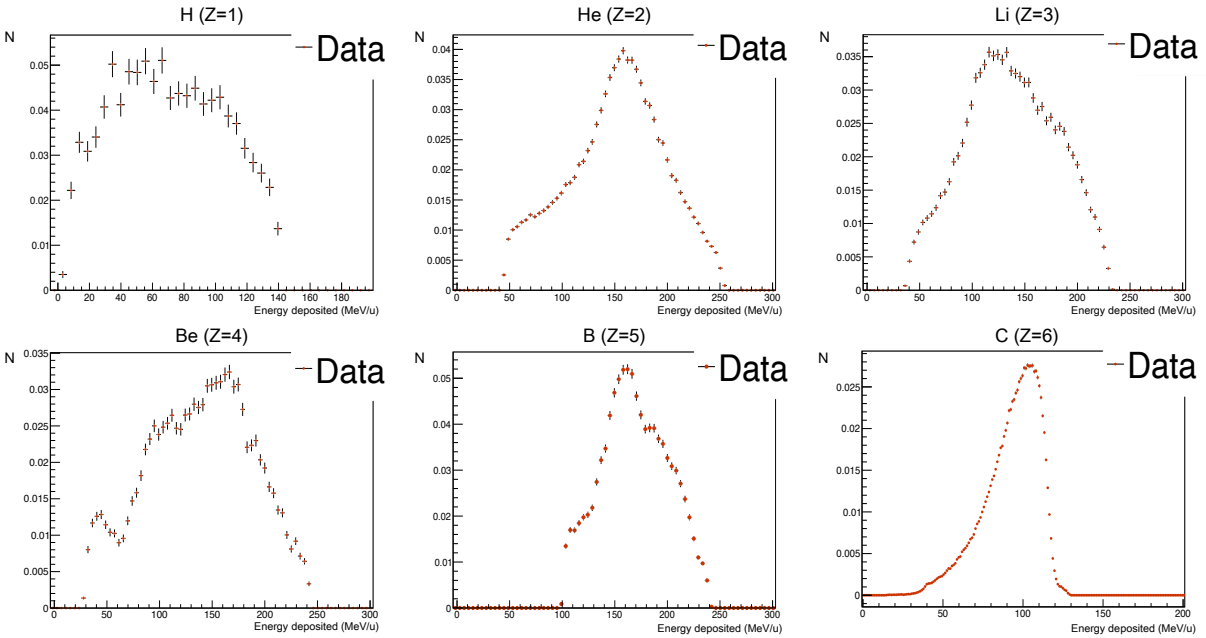

Figure 4.6: Total energy deposited inside the detectors distribution for each isolated Z from data cuts on the ΔE-E plot, for a ^{12}C beam of 400MeV/u on a 23cm target and the detectors at 0°

Looking into each isolated Z population in the simulated data, the deposited energy distribution of each secondary particle produced by the beam fragmentation inside the target can be extracted, and compared to the experimental ones.

In Figure 4.7 and Figure 4.8 are presented in blue the energy distributions for each Z isolated from the ΔE-E simulated distributions, with the cuts done on data applied to it.

Figure 4.7 presents the total energy deposited inside the detectors (ΔE in plastic + E in $CeBr_3$), for the Config.1. The figure includes experimental measurements in red referred to as Data, the Geant4 simulated data in blue for each isolated Z obtained from data cuts on the ΔE-E plot, referred to as MC_rec, and the Z distributions obtained by selecting the Z in Geant4 in beige, referred to as the MC_true. This allows to highlight the quality of the applied cuts, by comparing the MC_true to the MC_rec distribution. Precise efficiency, purity and errors on those cuts will be explored in Section II.4.

In general, it is notable that the experimental distributions are broader than those predicted by simulations. This discrepancy suggests that the beam spread at CNAO is bigger than anticipated. This observation highlights the need for further refinement in beam control to ensure more accurate alignment with simulated expectations. This discrepancies are also showing that the angular secondaries distributions are non accurate in the Monte Carlo simulation. Each Z species will now be analyzed between the experimental data, the MC_rec and the MC_true. Concerning the comparison between M_rec and M_truth, over or under estimation of particle number within the cut will be calculated as the ratio of the number of particles inside the cut over the total one detected in the simulation.

- **Z=1, Hydrogen**: Initial observations indicate a strong correspondence in energy between experimental data and Geant4 simulation MC_rec. However, the resolution of detectors at lower energies constrains a detailed investigation and quantification.

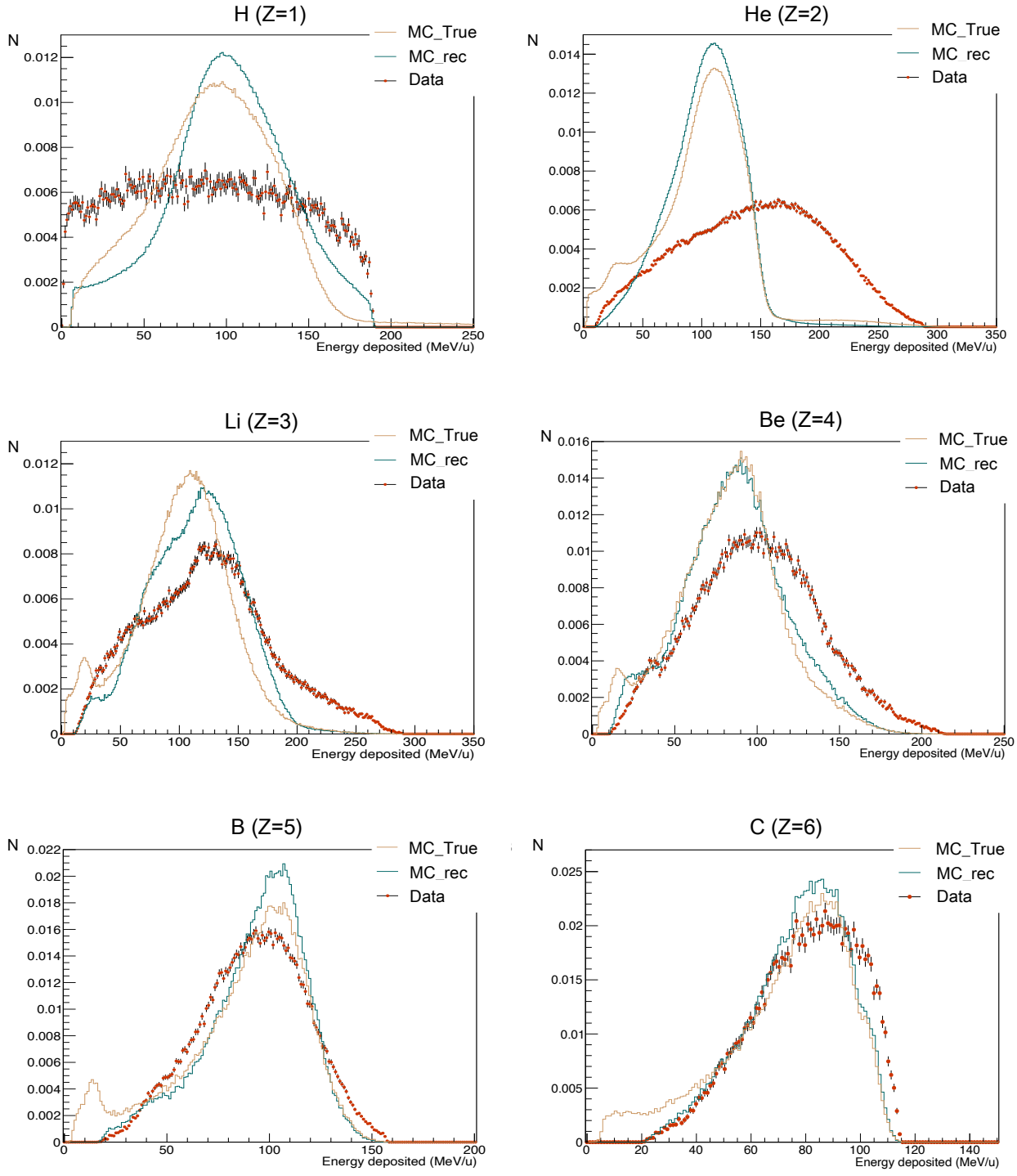

Figure 4.7: Total energy deposited inside the detectors comparison between experimental and simulated data, for each isolated Z from data cuts on the ΔE-E plot, for a ^{12}C beam of 200 MeV/u on a 5cm target and the detectors at 5°. Concerning the simulated data, the total Z distributions without data cut are also plotted.

It is also important to note the proton scattering, particularly alongside the beam spread. The beam spread significantly affects the accuracy of proton measurements, leading to a broader distribution and lower resolution in the data. This highlights the need for improved beam control to enhance measurement precision for those particles.

While an overall agreement is observed between the MC_rec and the MC_true protons produced, a minor distribution and energy shift, attributed to imprecision in cuts, is noted, approximately 5MeV/u. Geant4 simulation indicates an overestimation of hydrogen number by 39.31% within the cut, which will be discussed in detail, in the Section II.4.

- **Z=2, Helium**: A notable deviation in energy, approximately 60MeV/u, is observed between experimental results and Geant4 simulation MC_rec. This deviation probably originates from pile-up in the detectors, that detect two alphas at the same time. This question will be addressed in detail in the discussion Section II.3.1.

  Good accordance in distribution and energy is observed between MC_rec and MC_true. However, Geant4 simulation suggests a slight underestimation of helium number within the cut in MC_rec, by 6.02%.

- **Z=3, Lithium**: Because of the important statistical presence of Helium, isolation and identification of Lithium are difficult. Apart from energy resolution considerations, the agreement in energy, particularly around the maximum peak between experimental data and MC_rec, appears satisfactory.

  Similar to Hydrogen, a good agreement is achieved between MC_rec and MC_true, although a minor distribution and energy shift, around 10MeV/u. Geant4 simulation indicates an overestimation of Lithium within the cut in MC_rec, by 15.31%.

- **Z=4, Beryllium**: An energy shift of approximately 10MeV/u is observed between experimental data and MC_rec, coupled with a more accurate reproduction of calculated resolution.

  Good agreement in distribution and energy is noted between MC_rec and MC_true distributions, with Geant4 simulation indicating a slight underestimation of Beryllium number within the cut in MC_rec, by 4.65%.

- **Z=5, Boron**: A slight energy deviation of less than 10MeV/u is noted between experimental data and MC_rec, alongside improved reproduction of calculated resolution.

  Consistent agreement in distribution and energy is observed between MC_rec and MC_true distributions. Geant4 simulation suggests a marginal underestimation of Boron number within the cut in MC_rec, by 0.67%.

- **Z=6, Carbon**: Negligible energy shift, less than 5MeV/u, is observed between experimental data and MC_rec, with a close reproduction of calculated energy resolution within the Geant4 simulation.

  Similar to Boron, a consistent agreement in distribution and energy is obtained between MC_rec and MC_true distributions. However, Geant4 simulation indicates a significant underestimation of Carbon number within the cut in MC_rec, by 59.84%, which necessitates further discussion on efficiency and purity, in the Section II.4.

Figures 4.8 present the total energy deposited inside the detectors for the Config.2, comparing experimental and simulated data, including also both MC_true and MC_rec, with the precise efficiency, purity and errors discussed in Section II.4.

- **Z=1, Hydrogen**: It can be seen that the simulated MC_rec and experimental distributions are both centered on the same average energy of 70 MeV/u. However, like for the previous configuration, the resolution of detectors at lower energies constrains a detailed investigation and quantification.

  An overall energy agreement is observed between the MC_true and the MC_rec distributions. However, Geant4 simulation indicates an overestimation of hydrogen number by 55.09% within the cut in MC_rec, which will be discussed in the Section II.4

- **Z=2, Helium**: Similar to the data at 200MeV/u, a notable shift in energy, approximately 95MeV/u, is observed between experimental results and Geant4 simulation MC_rec, needing further investigation.

  Good accordance in distribution and energy is observed between the MC_true and the MC_rec distributions. However, Geant4 simulation suggests a slight underestimation of helium within the cut in MC_rec, by 7.25%.

- **Z=3, Lithium**: Because of the even more important statistical presence of Helium at 0° compared to 5°, isolation and identification of Lithium are difficult. Apart from energy resolution considerations, a small shift in energy of around 10MeV/u appears between the simulated MC_rec and experimental distributions.

  Similar to Hydrogen, a good agreement is achieved between MC_true and MC_rec, although a minor distribution and energy shift, around 10MeV/u. Geant4 simulation indicates a small overestimation of Lithium within the cut in MC_rec, by 6.75%.

- **Z=4, Beryllium**: An energy shift of approximately 25MeV/u is observed between the simulated MC_rec and experimental distributions, coupled with a more accurate reproduction of calculated resolution. However, the experimental distribution appears to be distorted compared to the simulation MC_rec.

  A good agreement in distribution and energy is noted between MC_true and MC_rec, with Geant4 simulation indicating an underestimation of Beryllium within the cut in MC_rec, by 13.09%.

- **Z=5, Boron**: A slight energy deviation of around 10MeV/u is noted between the simulated MC_rec and experimental distributions, alongside improved reproduction of calculated resolution.

  Consistent agreement in distribution and energy is observed between MC_true and MC_rec, although a small distribution and energy shift, around 10MeV/u. Geant4 simulation suggests a marginal underestimation of Boron within the cut in MC_rec, by 4.05%.

- **Z=6, Carbon**: Negligible energy shift, less than 5MeV/u, is observed, between the simulated MC_rec and experimental distributions.

  Similar to Beryllium, a consistent agreement in distribution and energy is observed between MC_true and MC_rec alongside an insignificant underestimation of Carbon within the cut in MC_rec, by 0.24%.

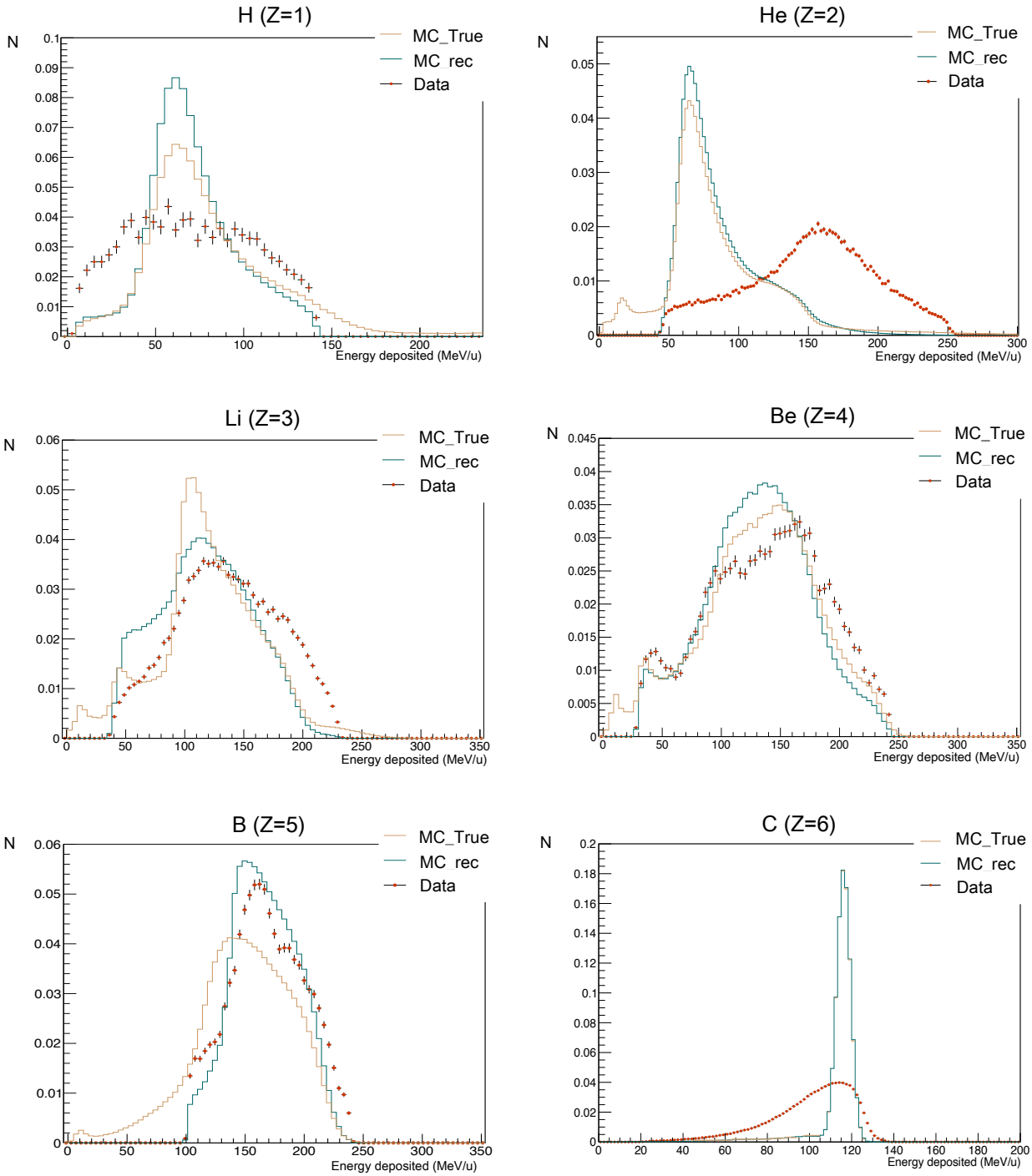

Figure 4.8: Total energy deposited inside the detectors comparison between experimental and simulated data, for each isolated Z from data cuts on the ΔE-E plot, for a ^{12}C beam of 400 MeV/u on a 23cm target and the detectors at 0°. Concerning the simulated data, the total Z distributions without data cut are also plotted.

Overall, the applied cuts at 0° are less accurate than those at 5°. This result is expected, as the beam contribution is more significant at 0°, leading to a higher physical background in the ΔE-E map. This increased background contributes to the reduced accuracy of the cuts at this angle.

Discussion

The investigation of energy distributions, particularly for Z=2, reveals significant discrepancies. These discrepancies can be attributed to the inability of the Geant4 simulation to accurately model the breakup of carbon nuclei into two or three alpha particles. The specific nuclear reactions involved are:

$$^{12}\mathrm{C} \rightarrow 3\alpha$$

$$^{12}\mathrm{C} \rightarrow 2\alpha + \text{residuals}$$

The residuals could include other particles such as protons, neutrons, or other light nuclei.

Figure 4.9 illustrates the kinetic energies of the alpha particles after the target as obtained from the Geant 4 simulation. Notably, the distribution is cleaner at 5° than at 0°, as the Z identification is easier due to reduced beam proportion at 5°, as previously explained. The maximum energy peak for Config.1 is approximately 130 MeV/u while for Config.2 is approximately 260 MeV/u. This suggests an initial energy for the alpha particles of around 200 MeV/u for Config.1 and 400 MeV/u for Config.2, which is inconsistent with the initial carbon energy of 200MeV/u and 400 MeV/u respectively. Indeed, the breakup into two or three alpha particles should result in each alpha particle possessing approximately half or third of the beam's initial energy. Moreover, at these energies, the alphas are expected to pass through the $CeBr_3$ without stopping inside, which explains why the energy deposited in it predicted by Geant4 is much lower than what is observed.

The observed discrepancy indicates a flaw in the simulation's ability to conserve energy correctly during the nuclear breakup process.

II.3 Yields study

In this subsection, the analysis of the particle yields for each atomic number Z will be studied, comparing experimental and simulation data. The relative yield will be calculated as the number of particle detected over the total number of estimated incident ^{12}C ions :

$$\Phi_Z = \frac{N_Z}{N_{\text{events}}} \tag{4.1}$$

The exact number of incident ^{12}C ions being experimentally unknown, it will be considered and estimated that each event in our detector corresponds to an initial incident ^{12}C ions. The simulated relative yield will be calculated similarly. The results are presented for the two configurations, permitting to study of the effect of detection angle and target thicknesses on the yields.

Figure 4.10 illustrates the yield as described above as a function of the atomic number (Z) of the detected particles, comparing the experimental to the simulated values.

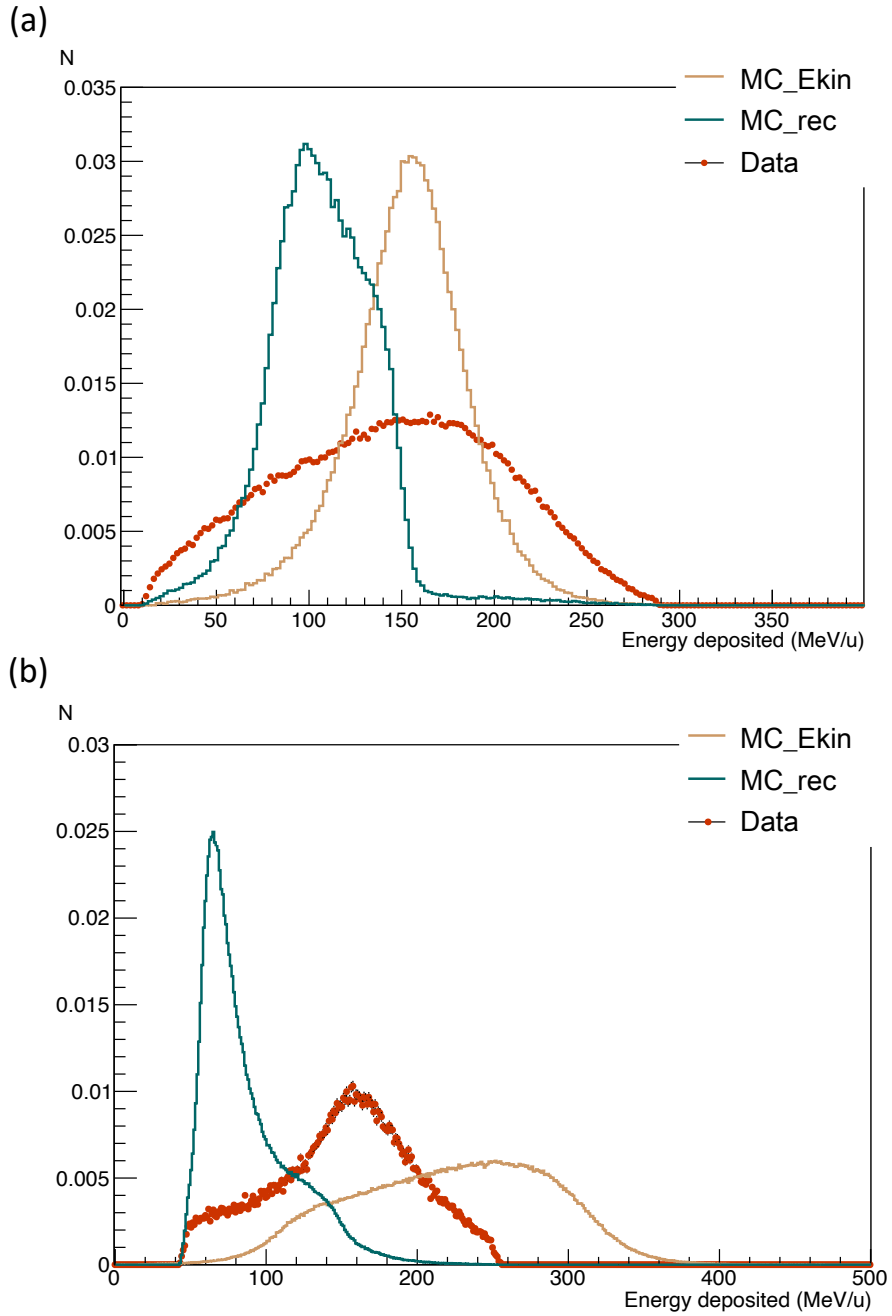

Figure 4.9: Kinetic energy of secondary alphas after the target, for a ^{12}C beam of 200MeV/u on a 5cm target and the detectors at 5° (a) and 400MeV/u on a 23cm target and the detectors at 0°

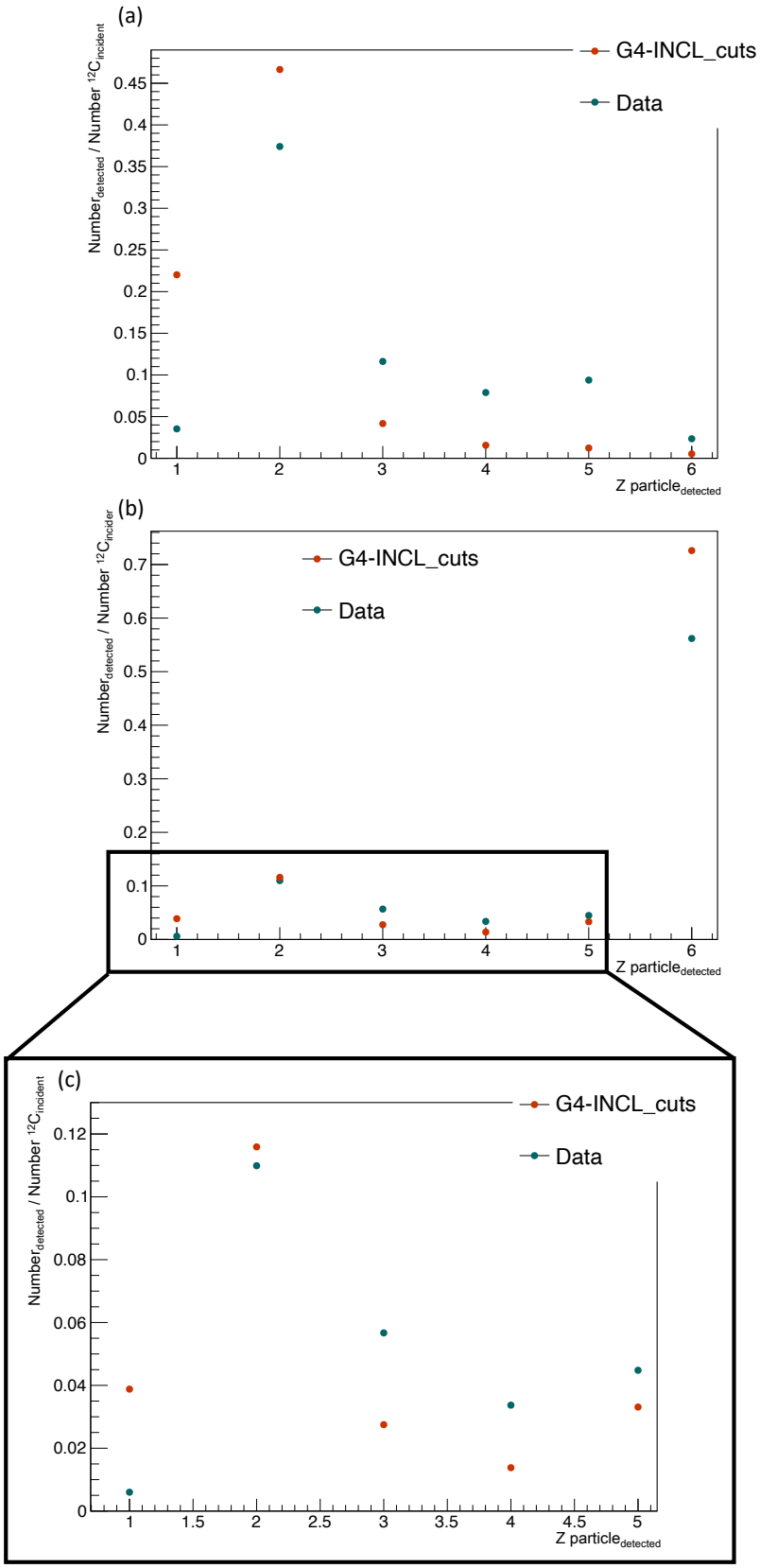

Figure 4.10: Number of particles detected over the total number of incident ^{12}C as function of each Z for a 200MeV/u beam on a 5cm target with the detectors at 5° (a), for a 400Mev/u beam on a 23cm target with the detectors at 0° (b) (c), Error bars are plotted but not visible due to their small size.

The three subfigures (a), (b), and (c) provide detailed views of the results under different conditions. **Subfigure (a)** shows the results for the 200 MeV/u beam on a 5 cm target with detectors at 5°. **Subfigure (b)** presents the results for the 400 MeV/u beam on a 23 cm target with detectors at 0°. **Subfigure (c)** zooms in on the data for atomic numbers Z = 1 to Z = 5 for the 400 MeV/u beam.

In Figure 4.10 (a), a higher relative yield of light fragments in simulation is observed. For Z=1, the simulated yield is close to 6 times higher than the experimental one, and for Z=2 the simulated yield is 1.2 times higher than the experimental. For heavier fragments (Z > 2), the experimental data (blue points) show higher yields for Z > 2. Indeed, for Z=3 it is 2.8 times higher, for Z=4 it is 5.1 times higher and for Z=5 it is 7.6 times higher. This result is in agreement with what was previously measured [18], where it was demonstrated that lighter particles are the most produced fragments.

Figure 4.10 (b) demonstrates a similar trend but with generally lower relative yields compared to the 200 MeV/u case. This is due to the fact that a bigger amount of secondaries can be detected at angles, where the beam is less predominant. The simulation demonstrates a better agreement with the experimental data than at 5°, however discrepancies with the same tendency - lower yields on experimental data for Z=1 of 6.5 times higher, Z=2 of 1.1 times higher, and Z=6 of 1.3 times higher, for Z=3 it is 2.1 times higher, for Z=4 it is 2.5 times higher, and for Z=5 it is 1.4 times higher - as for the previous configuration is observable, especially in subfigure (c), where a detailed view of the light fragments (Z=1 to Z=5) for the 400 MeV/u beam is provided. It is important to note that Geant4 predicts mainly only one alpha emitted in the carbon break-up, while in reality there are two or three alphas that are produced. The calculation of the yields does not take into account this effect.

The comparison of experimental data with simulation results provides valuable insights into the accuracy of the Geant4-INCL model in predicting particle yields from ^{12}C fragmentation on a target. The observation of the discrepancies indicates the underestimation of Geant4 in predicting particle productions during treatment and the need of improvement to accurately reproduce what happens in reality, particularly for heavier fragments and at angles.

II.4 Errors evaluation

To assess the precision of cut delimitations in ΔE-E detection, an analysis of both purity and efficiency will be done in this section. This analysis is similar to that conducted by the FOOT (Fragmentation Of Target) experiment [71].

Purity defines the ratio of particles correctly attributed to a specific Z within defined cut parameters, relative to the total particles encompassed by these cuts. It serves as a gauge of the fidelity of Z identification within the chosen criteria and gives clues about any unwanted particles that might be mixed in.

Efficiency, on the other hand, represents the efficacy of the cut criteria in isolating particles with a specific Z. It quantifies the proportion of particles falling within the predefined cuts and correctly identified as possessing the desired Z, relative to the total number of particles identified with that specific Z inside the detectors. Thus, efficiency clarifies the effectiveness of the cut parameters in capturing and correctly categorizing particles of interest, thereby influencing the overall reliability of the measurement process.

Table 4.1 lists the purity and efficiency of each Z cut for both ^{12}C beams of 200 Mev/u on a 5 cm target with the detectors at 5° and 400 MeV/u on a 23 cm target with the

detectors at 0°, with the errors estimated statisticaly.

Secondaries	200MeV/u on 5cm target, with detectors at 5°		400MeV/u on a 23cm target, with detectors at 0°	
	Cut purity	Cut efficiency	Cut purity	Cut efficiency
Z=1 (H)	45.52 ± 0.03 %	75.01 ± 0.03 %	36.54 ± 0.03 %	78.88 ± 0.04 %
Z=2 (He)	88.01 ± 0.01 %	83.01 ± 0.01 %	85.11 ± 0.01 %	79.36 ± 0.02 %
Z=3 (Li)	53.27 ± 0.06 %	62.90 ± 0.07 %	58.18 ± 0.04 %	62.39 ± 0.04 %
Z=4 (Be)	77.92 ± 0.09 %	74.46 ± 0.09 %	69.96 ± 0.05 %	61.86 ± 0.05 %
Z=5 (B)	80.05 ± 0.09 %	79.52 ± 0.10 %	92.16 ± 0.02 %	65.58 ± 0.03 %
Z=6 (C)	94.56± 0.08 %	59.16 ± 0.14 %	99.48 ± 0.01 %	98.71 ± 0.01 %

Table 4.1: Statistics about the data cuts purity and efficiency.

As mentioned above, purity and efficiency permit to assess of the effectiveness of the selection criteria applied to distinguish particles in both experimental setups.

Purity analysis

Purity represents the proportion of particles correctly attributed to a specific Z within the defined cut parameters, relative to the total particles encompassed by these cuts. High purity values indicate a high level of confidence that the particles identified within a given cut are predominantly of the specified Z. From Table 4.1, the purity values exhibit significant variability across different Z values and experimental conditions:

- **Z=1 - Hydrogen**: shows a cut purity of 45.52% at 200 MeV/u on a 5cm target with detectors at 5°, and 36.54% at 400 MeV/u on a 23cm target with detectors at 0°. These lower purity values suggest that a considerable number of other particles, mostly Helium, are mistakenly classified as Hydrogen, reflecting challenges in isolating protons effectively with these experimental setups.
- **Z=2 - Helium**: demonstrates high cut purity values of 88.01% and 85.11% for the two respective conditions, indicating robust identification criteria. This high purity is possible because of the high production rate of Helium during Carbon fragmentation.
- **Z=3 - Lithium**: shows moderate cut purity values of 53.27% and 58.18%, indicating a relatively higher likelihood of misclassification compared to Helium. This reflects the overlap in the energy loss characteristics of Lithium with Helium and Beryllium populations, complicating its isolation.
- **Z=4 - Beryllium and Z=5 - Boron**: also exhibit high purity values (77.92% and 80.05% at 200 MeV/u, and 69.96% and 92.16% at 400 MeV/u, respectively), with Boron demonstrating particularly high purity at the higher energy setting, also thanks to the detector resolution. This indicates effective discrimination criteria for these mid-range Z particles.

- **Z=6 - Carbon**: reaches the highest cut purity of 94.56% and 99.48%, underscoring good identification fidelity. The near perfect purity at 400 MeV/u on a 23cm target illustrates the precision with which Carbon can be isolated when the detectors are aligned with the beam.

Efficiency analysis

Efficiency, on the other hand, measures the proportion of particles with a specific Z that fall within the predefined cuts relative to the total number of particles identified with that Z inside the detectors. High efficiency values indicate that a large fraction of the relevant particles is being captured by the cuts, which is crucial for maximizing data acquisition without significant loss. However, in our experimental data, there is a notable abundance of scattered carbons that are often missed in our measurements.

- **Z=1 - Hydrogen**: efficiency values are 75.01% and 78.88%, which are relatively high. Despite lower purity, the high efficiency ensures that most of the Hydrogen particles are being included in the analysis, although a higher rate of contamination.

- **Z=2 - Helium**: maintains high efficiency alongside high purity, with values of 83.01% and 79.36%. This balance suggests an optimal cut parameter setting for Helium that successfully includes most Helium particles while maintaining low contamination rates.

- **Z=3 - Lithium**: shows lower efficiency values of 62.90% and 62.39%, indicating a significant fraction of Lithium particles may be excluded by the current cuts, which also reflects and confirms the overlapping in the energy loss characteristics of Lithium with Helium and Beryllium populations.

- **Z=4 - Beryllium and Z=5 - Boron**: have efficiency values in the range of 61.86% to 79.52%, with Boron again performing better at higher energy. These values reflect a reasonable balance between capturing most particles and maintaining purity.

- **Z=6 - Carbon**: exhibits a stark contrast in efficiency values: 59.16% at 200 MeV/u versus an excellent 98.71% at 400 MeV/u.

Implications

The data indicate that while the current cut parameters are highly effective for certain Z values (notably Helium and Carbon), there is variability in performance across different elements and experimental conditions. For elements such as Hydrogen and Lithium, where purity and efficiency are less optimal, further refinement of the detector's resolution, for example, is needed. This could involve adjusting the ΔE-E thresholds to reduce overlap with neighboring elements, incorporating additional detection parameters to enhance specificity, or using detectors with better resolution than the plastic scintillator such as silicium detectors. Moreover, the experimental setup, such as the target thickness and detector angles, plays a critical role in influencing these parameters. Thus, more data and analysis campaigns in various experimental setup and condition are needed to adjust the method.

III. Conclusion

Chapter 4 focused on the measurement and characterization of secondary particles produced by heavy ion fragmentation using a ΔE-E telescope setup as part of the CLINM project. The main objectives were to compare experimental data with Geant4 simulations to evaluate the accuracy and efficiency of the simulations in reproducing experimental results, considering various angles and target thicknesses. The results indicated notable discrepancies between the experimental data and the Geant4 simulations, revealing limitations in the current simulation models.

The study revealed significant discrepancies between the experimental data and the Geant4 simulations in several key areas. First, there were energy distribution discrepancies where initial observations showed a strong correspondence in energy between the experimental data and Geant4 simulations for protons (Z=1). However, detailed quantification was limited due to resolution constraints at lower energies. For helium (Z=2), a significant energy deviation of approximately 60 MeV/u and 95 MeV/u was observed depending on the configurations, suggesting inaccuracies in simulating carbon break-up into alphas.

Additionally, simulation models consistently underestimated the yields of secondary particles (Z=3, Z=4, Z=5, Z=6) across both experimental setups, which impacted dose calculations. Measurements at different angles (0° and 5°) and with varying target thicknesses (5 cm and 23 cm of RW3) further highlighted discrepancies in energy distributions and particle yields, particularly at 5°, emphasizing the need for improved simulation models across varying fragmentation conditions.

Summary

Introduction

Le projet CLINM (Cross-sections of Light Ions and Neutron Measurements), financé par l'ANR à partir de janvier 2024, a pour objectif de caractériser de manière globale les particules secondaires produites par les processus de fragmentation des ions sur les tissus, ainsi que les effets chimiques associés. L'examen de ces effets chimiques implique la mesure des produits de radiolyse générés par les particules secondaires, tandis que les propriétés physiques (énergie, charge) de ces particules sont déterminées grâce à un télescope ΔE-E. Ce chapitre se concentre sur la mesure des particules secondaires produites lors de la campagne expérimentale de mai 2023 au centre de hadronthérapie de CNAO, en Italie.

Matériel et méthodes

Configuration expérimentale

L'objectif est de caractériser les particules secondaires produites par la fragmentation du carbone en utilisant un télescope ΔE-E. Le télescope ΔE-E est composé d'un scintillateur en plastique mince (2 mm) devant un cristal scintillateur de bromure de cérium ($CeBr_3$). La tension appliquée était de -1100V pour le plastique et de +350V pour le CeBr3. Le télescope a été placé derrière la cible RW3 à deux angles différents (0° et 5°).

L'expérience a été menée au centre de hadronthérapie CNAO. Un faisceau d'ions ^{12}C avec deux énergies, 200 et 400 MeV/u, a été dégradé par différentes épaisseurs de cible, 5 et 23 cm respectivement de RW3 (matériau équivalent tissulaire), pour atteindre une énergie de 120 MeV/u après la cible. Le dispositif expérimental est présenté en Figure 4.1.

- **Config.1** : Faisceau de 200 MeV/u sur une cible de 5 cm, avec les détecteurs à 5° de l'axe du faisceau.
- **Config.2** : Faisceau de 400 MeV/u sur une cible de 23 cm, avec les détecteurs à 0° de l'axe du faisceau.

L'expérience a été réalisée en deux étapes pour comprendre les effets des radiations secondaires : l'expérience physique, qui consiste à caractériser les particules secondaires avec le télescope ΔE-E, et l'expérience chimique, qui étudie la radiolyse de l'eau générée par le faisceau et ses particules secondaires.

Lorsque les particules secondaires interagissent avec le télescope ΔE-E, elles perdent une petite quantité d'énergie dans le scintillateur plastique et déposent le reste dans le $CeBr_3$. Les signaux enregistrés en coïncidence entre les deux détecteurs sont convertis en valeurs énergétiques grâce à la calibration effectuée. Ces valeurs sont ensuite utilisées pour construire un diagramme ΔE en fonction de E, comme présenté en Figure 4.2, permettant l'identification et l'analyse des particules. Différents types de particules présentent des motifs caractéristiques dans ce diagramme, facilitant leur identification et leur discrimination.

Simulation avec Geant4
La même configuration expérimentale a été reproduite dans une simulation Geant4. Cette simulation a permis d'enregistrer le dépôt d'énergie dans chaque détecteur pour chaque événement. En simulant les conditions expérimentales, l'objectif est de quantifier l'exactitude des modèles physiques de simulation. Pour tenir compte de la réponse du détecteur dans la simulation Geant4, la résolution énergétique de chaque détecteur, présentée dans le chapitre précédent, a été intégrée aux énergies enregistrées simulées.

Résultats

Résultats expérimentaux
Les Figures 4.4 et 4.5 présentent les distributions d'énergie pour chaque numéro atomique Z isolé à partir des distributions ΔE-E pour les deux configurations expérimentales. La figure 4.4 montre les distributions pour la Config.1 avec les détecteurs à 5°, tandis que la figure 4.5 montre les distributions pour la Config.2 avec les détecteurs à 0°.

Comparaison avec la simulation
Les figures 4.6 et 4.7 comparent les distributions d'énergie mesurées expérimentalement avec celles simulées par Geant4. La figure 4.6 présente les résultats pour la Config.1, et la figure 4.7 pour la Config.2. Les résultats montrent que les distributions expérimentales sont généralement plus larges que celles prédites par les simulations, suggérant une diffusion du faisceau plus importante que prévu au CNAO. Chaque type de particule présente des écarts caractéristiques entre les résultats expérimentaux et les simulations.
Les résultats montrent une bonne correspondance en énergie pour l'hydrogène (Z=1), le lithium (Z=3), le béryllium (Z=4), le bore (Z=5) et le carbone (Z=6). En revanche, une grande déviation en énergie est observable pour l'hélium (Z=2), d'environ 60 MeV/u.

Les rendements relatifs des particules pour chaque Z sont calculés comme le nombre de particules détectées sur le nombre total d'ions ^{12}C incidents estimé. La Figure 4.9 présente les rendements pour les deux configurations expérimentales, comparant les données expérimentales aux simulations. Les résultats montrent des rendements plus élevés pour les fragments légers (Z=1 et Z=2) dans les simulations par rapport aux données expérimentales, cependant les rendements des fragments plus lourds (Z=3 à Z=6) sont sous-estimés dans les simulations Geant4, avec des écarts allant de 2,1 à 7,6 fois plus élevés dans les données expérimentales.

Évaluation des erreurs
L'analyse de la pureté et de l'efficacité des coupures ΔE-E est essentielle pour évaluer la précision des délimitations des coupures. La pureté représente la proportion de particules correctement attribuées à un Z spécifique au sein des paramètres de coupures définis, tandis que l'efficacité mesure la proportion de particules avec un Z spécifique capturées par les coupures. La Table 4.1 présente la pureté et l'efficacité pour chaque Z dans les deux configurations expérimentales.

La pureté des coupures montre une contamination élevée pour l'hydrogène (Z=1) avec des valeurs de 45,52 % (Config.1) et 36,54 % (Config.2), tandis que l'hélium (Z=2) atteint des niveaux élevés de pureté de 88,01 % (Config.1) et 85,11 % (Config.2), indiquant des critères de discrimination robustes. En termes d'efficacité, l'hydrogène capture la majorité des particules avec 75,01 % (Config.1) et 78,88 % (Config.2), et l'hélium montre des critères optimaux avec 83,01 % (Config.1) et 79,36 % (Config.2). Le carbone (Z=6) affiche une identification précise avec une pureté de 94,56 % (Config.1) et 99,48 % (Config.2) et une capture presque complète pour la Config.2 à des énergies plus élevées avec 98,71 %.

Discussion

L'analyse des distributions d'énergie révèle des écarts significatifs entre les résultats expérimentaux et les simulations Geant4. Les divergences dans les rendements relatifs indiquent que les modèles de simulation actuels sous-estiment la production de particules secondaires, nécessitant des améliorations pour mieux reproduire les phénomènes réels.

L'étude des distributions d'énergie, en particulier pour Z=2, révèle des écarts importants. Ces écarts peuvent être attribués à l'incapacité de la simulation Geant4 à modéliser avec précision la fragmentation des noyaux de carbone en deux ou trois particules alpha. Les réactions nucléaires spécifiques impliquées sont :

$$^{12}\mathrm{C} \rightarrow 3\alpha$$

$$^{12}\mathrm{C} \rightarrow 2\alpha + \text{residuals}$$

Les résidus peuvent inclure d'autres particules telles que des protons, des neutrons ou d'autres noyaux légers.

Pour Z=1, la correspondance énergétique initiale est bonne, mais la résolution limitée des détecteurs et la diffusion du faisceau créent des distributions plus larges et moins précises. La surestimation de la production d'hydrogène dans les simulations souligne la nécessité de mieux contrôler la diffusion du faisceau. Pour Z=3 et Z=4, les écarts énergétiques et les variations de pureté/efficacité indiquent une complexité dans l'identification de ces particules intermédiaires, nécessitant des ajustements dans les paramètres de coupure et une meilleure résolution des détecteurs. Pour Z=5 et Z=6, les résultats montrent une meilleure correspondance avec les simulations, mais des sous-estimations significatives des rendements indiquent la nécessité d'affiner les modèles pour les fragments plus lourds.

Conclusion

Le chapitre 4 a examiné la mesure et la caractérisation des particules secondaires produites par la fragmentation des ions lourds en utilisant un télescope ΔE-E dans le cadre du projet CLINM. Les résultats révèlent des divergences notables entre les données expérimentales et les simulations Geant4, révélant des limitations dans les modèles de simulation actuels. Les observations soulignent la nécessité d'améliorer les modèles pour reproduire avec précision les phénomènes observés, en particulier pour les fragments plus lourds et à différents angles.

Chapter 5

DINo - Nuclear reactions prediction by deep learning

"Can't you see that I'm the one who understands you?"
– T. S.

Contents

Persistent discrepancies between experimental data and hadronic models in particle therapy highlight the need for improved accuracy in nuclear reaction predictions. Traditional approaches often rely on measurements to address these gaps, and the CLINM project has been included in this effort.

The main objective is to utilize these precise measurements to improve Monte Carlo simulations, which are crucial for predicting nuclear reaction outcomes under various conditions. Indeed, an alternative strategy involves directly enhancing the predictive capabilities of the models themselves.

In this chapter, DINo (Deep learning Intelligence for Nuclear reactiOns) will be introduced, as a deep learning algorithm specifically designed to address these challenges, in the framework of the CLINM project. DINo operates by utilizing partial proton nuclear reactions cross-sections to extrapolate total cross-sections, aiming to predict experimental data with an improved accuracy compared to actual models.

DINo aims to use artificial intelligence and deep neural networks to learn complex patterns and relationships within the data. By focusing on incident protons, which play

a pivotal role in particle therapy applications, DINo benefits from an extensive representation in the TENDL nuclear model data library.

One of DINo's key strengths lies in its ability to adapt and learn from the latest advancements in nuclear data. By integrating with TENDL's 2021 model values, DINo aims to accurately predict total cross-sections even for unexplored initial energy regimes.

Preliminary evaluations and comparisons with the TENDL model suggest that DINo exhibits superior predictive capabilities, showcasing its potential to improve nuclear reaction modeling in particle therapy contexts.

I. Nuclear models and deep learning approach

In this section, the materials and methods employed in the development and application of DINo (Deep learning Intelligence for Nuclear reactions) will be outlined as an advanced deep learning algorithm designed to enhance the accuracy of nuclear reaction predictions.

I.1 Nuclear model and experimental data

I.1.1 TENDL 2021 nuclear model

TENDL (TALYS-based Evaluated Nuclear Data Library) [72] is a nuclear data library developed by the Nuclear Reaction Data Centre (NRDC) at the Institute for Reference Materials and Measurements (IRMM), a part of the Joint Research Centre (JRC) of the European Commission. TENDL is based on calculations using the TALYS nuclear reaction theoretical code, which is used to model nuclear reactions and generate evaluated nuclear data.

Nuclear data libraries like TENDL provide essential information about nuclear reactions, such as cross-sections, decay data, and other nuclear properties. These data are crucial for the simulations in various applications in nuclear science and technology, including nuclear reactor design, nuclear medicine, and nuclear security.

Each new version or update of a nuclear data library such as TENDL typically incorporates improved modeling techniques, updated experimental data, and corrections based on feedback from users and benchmarking against experimental results.

The library encompasses a great amount of proton data, leading to the choice of protons as the focal point for this study.

To collect all the TENDL21 model in the same format, with the same amount of energy steps, we used an algorithm developed by J.Collin, private communication.

I.1.2 EXFOR experimental data

EXFOR (Experimental Nuclear Reaction Data) is an international database that compiles experimental nuclear reaction data from various sources. It is maintained by the International Network of Nuclear Reaction Data Centers (NRDCs) with the support of the International Atomic Energy Agency (IAEA).

The primary purpose of EXFOR is to collect, organize, and disseminate experimental nuclear reaction data. These data include cross-sections, angular distributions, energy spectra, and other relevant information obtained from nuclear reactions studied in laboratories worldwide.

EXFOR gathers data from a wide range of experimental facilities, including accelerators, reactors, and other nuclear research facilities. Data contributors can include universities, research institutes, and national laboratories.

The data in EXFOR are stored in a standardized format to ensure compatibility and ease of use by researchers and nuclear data evaluators. The format includes detailed information about the experimental setup, target nuclei, incident particles, reaction products, and measured quantities.

The data are publicly accessible and can be accessed through various channels, including the EXFOR database website (https://www-nds.iaea.org/exfor/), which provides search and retrieval functionalities. Users can search for specific reactions, isotopes, energy ranges, and other parameters to retrieve relevant experimental data.

The data in EXFOR undergo quality checks and validation processes to ensure accuracy and reliability. This involves comparing experimental results with theoretical predictions, benchmarking against other experimental data, and reviewing data for consistency and completeness.

As for TENDL, a great amount of experimental data are available concerning proton, permitting to developp and test the algorithm on a well documented nuclear reaction.

I.1.3 Proton beam interactions with ^{12}C target

As mentioned in the previous section, we'll be focusing on proton interaction, and more especially on a proton beam on a ^{12}C target. Figure 5.1 illustrates the total and partial cross-sections for incident protons on a ^{12}C target from the TENDL 2021 nuclear model alongside the partial ones. Indeed, this choice is particularly relevant in the context of nuclear reactions in hadrontherapy.

Firstly, ^{12}C is often referred to as a "tissue-equivalent" material, meaning it has similar nuclear properties to biological tissues. This characteristic makes it an ideal target for simulating interactions that occur in human tissues during therapeutic procedures, such as in hadron therapy.

Secondly, the interaction of a proton beam with a ^{12}C target can produce secondary particles such as protons, neutrons, and fragments of carbon nuclei coming from the target. These secondary particles are crucial for understanding the dosimetry and biological effects of the radiation delivered to the patient. This choice of using a proton projectile on a ^{12}C target is justified because, in modern nuclear physics experiments that measure cross-sections, such as the FOOT experiment [71], direct measurement of carbon ion fragmentation in tissue is complex and challenging. This approach leverages the symmetry of nuclear interactions: the fragments produced when a proton hits a ^{12}C nucleus are similar to those produced when a ^{12}C ion hits a hydrogen nucleus (which is a major component of human tissue).

I.2 Deep learning generalities

I.2.1 Deep learning algorithms

Deep learning is a subset of machine learning that focuses on learning representations of data through neural networks with multiple layers. Unlike traditional machine learning algorithms that require handcrafted features, deep learning models can automatically learn hierarchical representations from raw data.

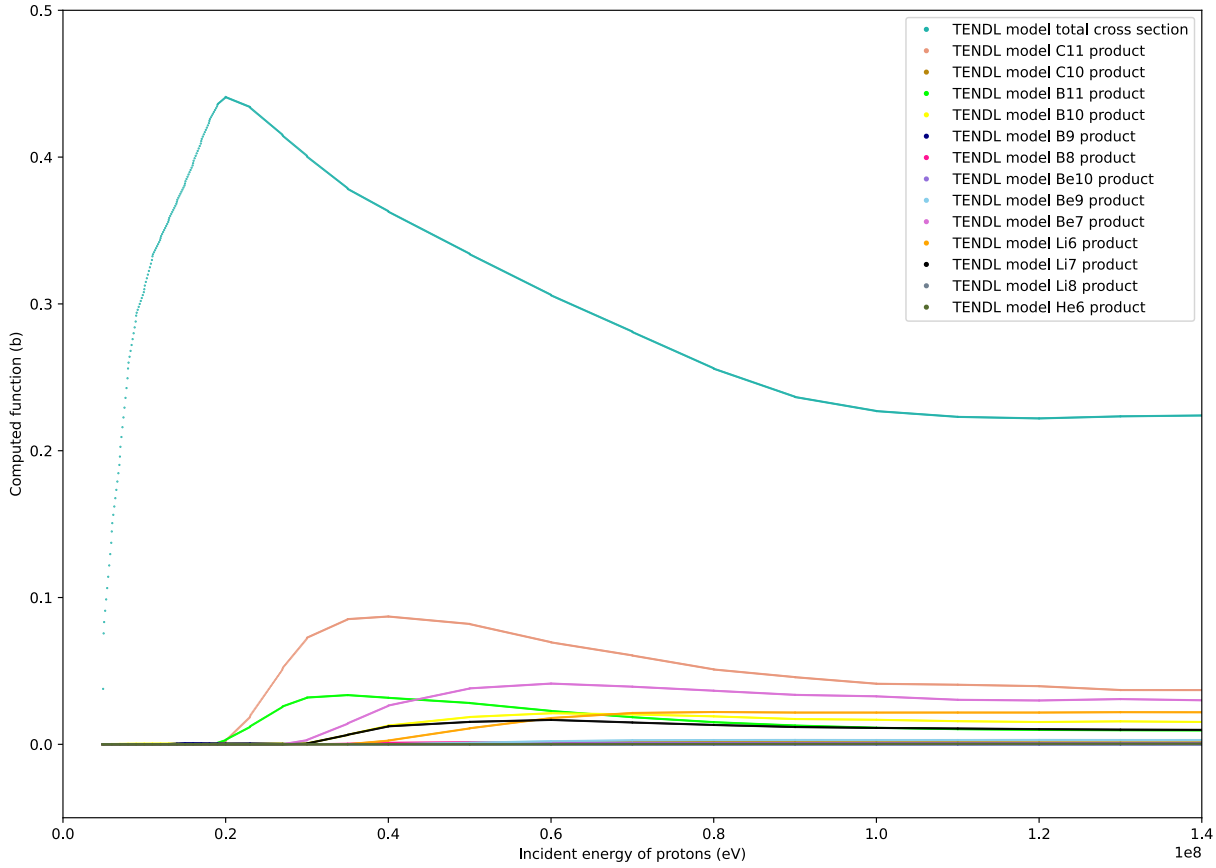

Figure 5.1: TENDL21 model of total and partial cross-sections of a proton beam on a ^{12}C target.

General structure

Neural networks are the building blocks of deep learning models. They are composed of interconnected nodes organized in layers. Each node, or neuron, takes input values, applies weights and biases, performs computations, and passes the result through an activation function to introduce non-linearity :

- The **Input Layer** receives raw data, which could be images, text, or numerical features. Each input is typically represented as a feature vector.
- The **Hidden Layers** are between the input and output layers. These layers perform transformations on the input data through weighted connections and activation functions. Deep networks have multiple hidden layers, allowing them to learn complex representations.
- The **Ouput Layers** produce the final predictions or classifications based on the processed information from the hidden layers. The structure of the output layer depends on the task (e.g., regression, classification).

Training process

The training process of a deep learning model involves several key steps:

- During **Forward Propagation**, input data is fed through the network layer by layer. Each layer computes a weighted sum of inputs, applies an activation function (e.g., sigmoid, ReLU-Rectified Linear Unit), and passes the result to the next layer. This process generates predictions or outputs. The ReLU function corresponds to $f(x) = max(0, x)$.

- During **Loss Calculation**, the output of the model is compared to the ground truth (actual) values using a loss function. Common loss functions include mean squared error (MSE) for regression tasks and categorical cross-entropy for classification tasks. The loss quantifies how well the model's predictions match the actual data.

- **Backpropagation** is used to update the model's weights and biases based on the loss value. It involves computing gradients of the loss with respect to each parameter in the network using the chain rule of calculus. The gradients guide the optimization process to minimize the loss.

- **Optimization algorithms** such as stochastic gradient descent (SGD), Adaptive Moment Estimation (Adam), and Root Mean Square Propagation (RMSprop) are used to update the model parameters iteratively. These algorithms adjust the weights and biases in the direction that reduces the loss, moving the model towards better performance. Adam computes adaptive learning rates for each parameter by keeping an exponentially decaying average of past gradients and their squares. RMSprop adjusts the learning rate for each parameter by dividing the gradient by a running average of the magnitudes of recent gradients, ensuring more stable and faster convergence.

- **Validation and Testing** phase. During training, a portion of the data is held out for validation. The model's performance on this validation set is monitored to avoid overfitting, where the model performs well on training data but poorly on new data. After training, the model is tested on a separate test set to evaluate its generalization ability.

I.2.2 TensorFlow and Keras

TensorFlow

TensorFlow [73] is an open-source deep learning framework developed by Google that facilitates building and training neural networks. It provides a flexible platform for numerical computations and supports both CPU and GPU acceleration, making it suitable for large-scale machine learning tasks.

- **TensorFlow's core** library provides fundamental building blocks for creating computational graphs, managing tensors (multidimensional arrays), and executing operations efficiently. It includes low-level APIs for tensor manipulation and graph construction.

- **TFX extends TensorFlow's** capabilities to support end-to-end machine learning workflows. It includes components for data preprocessing, model training, model evaluation, and model serving. TFX is designed for scalable and production-grade machine learning pipelines.

- **TensorFlow Serving** is a system for serving machine learning models in production environments. It provides APIs for serving trained models over RESTful endpoints, enabling real-time predictions for applications.

Keras

Keras [74], on the other hand, is a high-level neural networks API that simplifies the process of building and training models. It is integrated into TensorFlow as 'tf.keras' and offers a user-friendly interface for defining neural network architectures, specifying training parameters, and executing training and evaluation steps.

- **Modularity** - Keras allows developers to build neural networks by stacking modular layers. Layers can be easily added, removed, or modified, making it flexible for experimenting with different architectures.
- Keras provides a wide range of **pre-built layers** such as dense (fully connected), convolutional, recurrent, dropout, and normalization layers. These layers can be combined to create complex neural network architectures.
- Keras includes various **optimizers**(e.g., SGD, Adam, RMSprop) and **loss functions** (e.g., MSE, categorical cross-entropy) that can be specified during model compilation. This flexibility allows developers to customize training parameters based on the task and dataset.
- **Model Training and Evaluation** - With Keras, training a model involves specifying training data, validation data, batch size, number of epochs, and other parameters. After training, models can be evaluated on test data to assess their performance metrics such as accuracy, precision, and recall.

By leveraging the combined power of TensorFlow for efficient computations and Keras for streamlined model building, we can create and deploy deep learning models for a wide range of applications.

I.3 DINo structure

I.3.1 Dense Neural Network (DNN)

A dense neural network, also known as a fully connected neural network, is a fundamental type of artificial neural network (ANN) where each neuron in one layer is connected to every neuron in the adjacent layer. Dense layers are characterized by their dense connectivity pattern, where all neurons in one layer are connected to all neurons in the next layer. A summarizing scheme of an artificial neuron is presented in Figure 5.2.

Architecture of a Dense Neural Network

- **Input Layer:** The input layer represents the input features or data points. Each neuron in the input layer corresponds to a feature or dimension of the input data.
- **Hidden Layers:** Between the input and output layers, there can be one or more hidden layers in a dense neural network. Each hidden layer consists of multiple neurons, and all neurons in one layer are connected to all neurons in the next layer.

- **Output Layer:** The output layer produces the final predictions or outputs based on the information processed by the hidden layers. The structure of the output layer depends on the task at hand, such as regression (single neuron for continuous output) or classification (multiple neurons for categorical output).

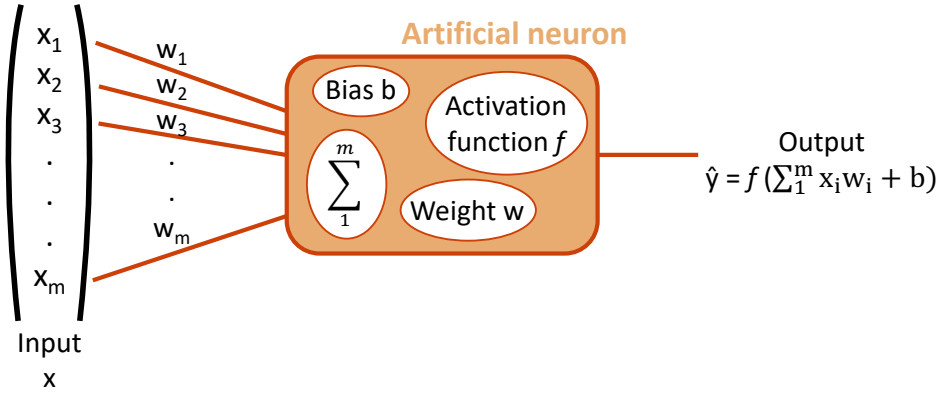

Figure 5.2: Scheme of an artificial neuron with the training process

How dense layers work

- **Weighted Sum Calculation:** In a dense layer, each neuron receives inputs from all neurons in the previous layer. For each neuron j in layer L, the weighted sum of inputs z_j is calculated as:

$$z_j = \sum_{i=1}^{n} (w_{ij} \cdot x_i) + b_j$$

  Where:

  - w_{ij} is the weight connecting neuron i in layer $L-1$ to neuron j in layer L.
  - x_i is the output of neuron i in layer $L-1$ (input to neuron j in layer L).
  - b_j is the bias associated with neuron j.

- **Activation Function:** After computing the weighted sum z_j, an activation function $f(z_j)$ is applied to introduce non-linearity into the network.

- **Output of Neurons:** The output a_j of neuron j in layer L is obtained by passing the result of the activation function:

$$a_j = f(z_j)$$

- **Forward Propagation:** This process of computing the outputs of neurons in each layer based on the inputs from the previous layer is repeated through the entire network in a forward propagation manner until the output layer is reached, as represented in Figure 5.3.

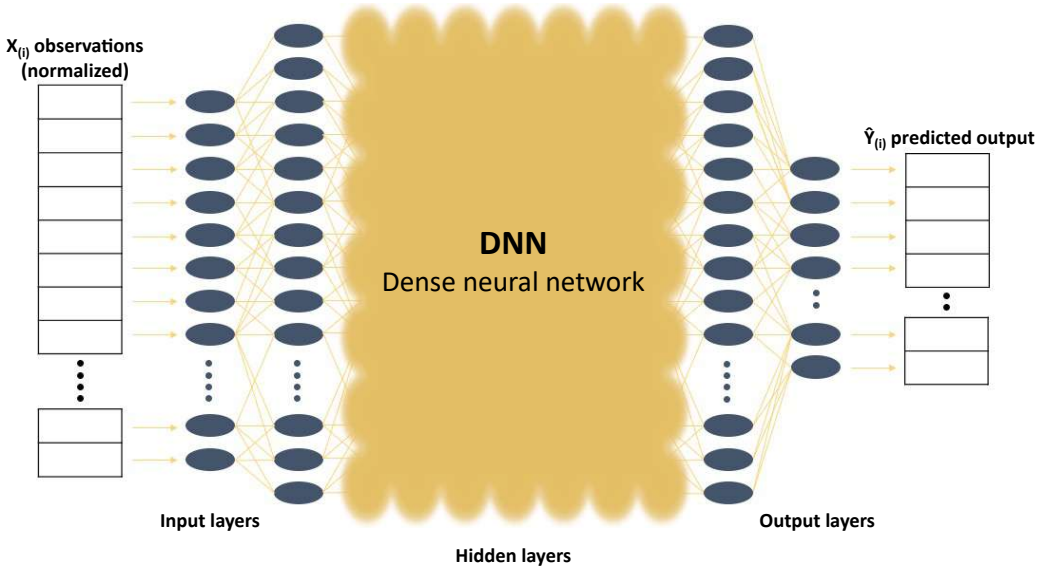

Figure 5.3: Scheme of the global structure of a Dense Neural Network structure

- **Training process:** The initial data are separated into a train set and a test set in order to evaluate the model at each step of learning, called epoch. The number of epoch is important in order for the network to accurately learn without overlearning and only reproducing the initial data. A scheme of this process is represented on Figure 5.4.

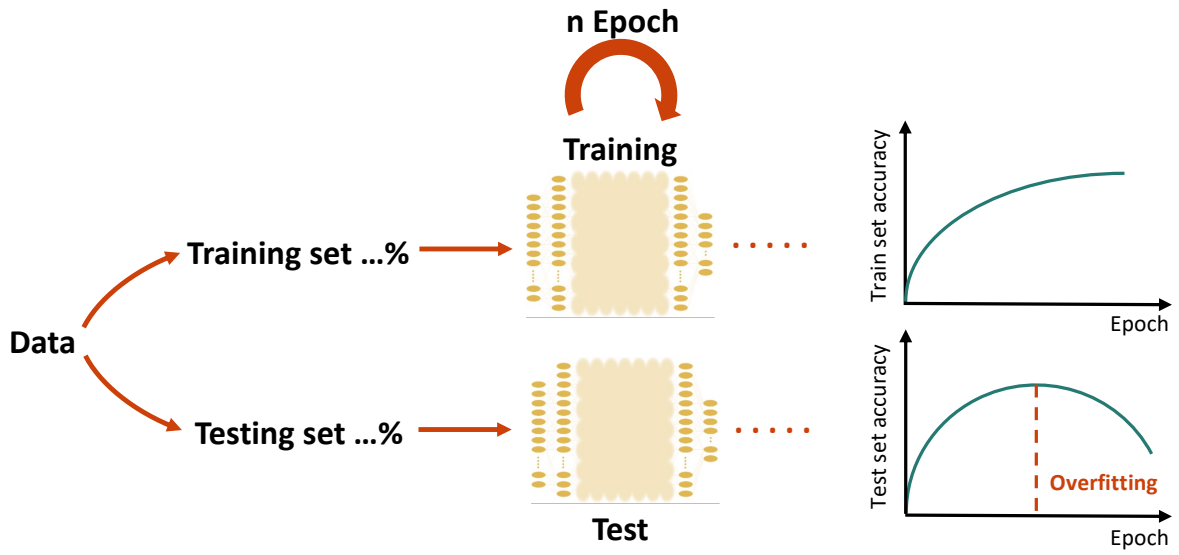

Figure 5.4: Scheme of the global structure of the training process of a Dense Neural Network

I.3.2 DINo

Introduced as a dense neural network (DNN), the DINo algorithm is designed to learn from the TENDL 2021 model values, with a specific focus on charge-changing cross-sections as a function of proton projectile initial energy on a ^{12}C target, as well as their corresponding total cross-sections.

The primary goal of DINo is to predict total cross-sections for initial energies that are not covered by current experimental data. This is crucial in hadrontherapy where accurate treatment plan predictions rely on understanding nuclear reactions and their implications. Figure 5.5 depicts the global structure of the DINo algorithm. The choices made for DINo model architecture are explained and justified in Annexe A.

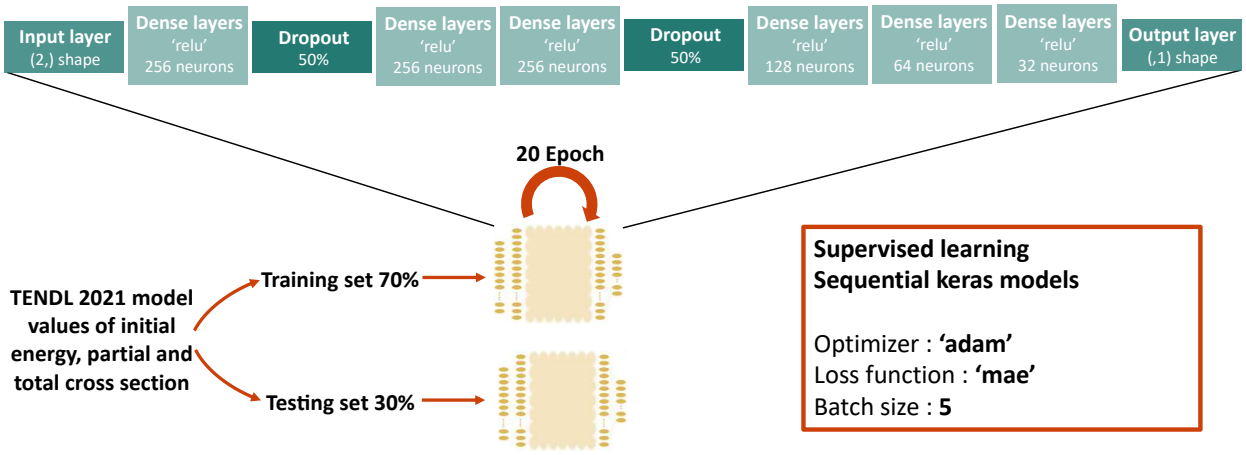

Figure 5.5: Global structure of the DINo algorithm.

During the learning phase of the algorithm, 70% of the TENDL model values for charge-changing cross-sections, along with their corresponding initial energy values, are used as input data. Simultaneously, the total cross-section values linked to these initial energies are designated as output. This setup enables the algorithm to learn the underlying patterns and relationships between input and output data, forming the basis for its predictive capabilities.

To assess the proficiency of the algorithm, the remaining 30% of the TENDL model values are reserved for testing purposes at each epoch. This rigorous testing process ensures that the algorithm generalizes well and can make accurate predictions on unseen data.

After undergoing 20 epochs of training, the DINo algorithm is deemed ready for application to experimental data. This transition from theoretical modeling to experimental prediction is a critical step in validating the algorithm's effectiveness and real-world applicability.

During the testing phase on experimental data, the algorithm receives actual values for charge-changing cross-sections along with their associated initial energies. Leveraging the knowledge gained during the learning phase, DINo can then predict the corresponding experimental values for total cross-sections at these specific initial energies. This predictive capability is essential in scenarios where direct experimental measurements are limited or impractical, allowing to extrapolate crucial information for various nuclear processes in simulation for example.

II. Results

In this section, the analysis will focus on comparing DINo's predictions with the established TENDL model. As an example, the ^{11}C product cross-sections will be explored, and the global results for all product cross-sections will be shown in the next section. This choice of charge-changing product was made due to the extensive data available for this cross-section in the EXFOR database, and thus permits to develop and better test our DNN algorithm.

To compare the DINo's prediction to the TENDL model one, the χ^2 values will be computed, which can be expressed as :

$$\chi^2 = \sum \frac{(predicted - expected)^2}{expected} \tag{5.1}$$

For each DINo χ^2 that will be given, the algorithm will be launched 100 times in order to have a reliable mean value and error associated, defined as the standard deviation.

The χ^2 statistic is a measure used to evaluate the goodness of fit between the predicted and expected values. It assesses whether there is a significant difference between the two sets of values, enabling a comparison of the efficiency of the two models. A lower χ^2 value indicates a better fit of the model to the experimental data, meaning the predictions are more accurate.

II.1 Detailed study of ^{11}C product

II.1.1 TENDL model comparison with experimental data

Figure 5.6 presents the total cross-section and ^{11}C product cross-section for incident protons on a ^{12}C target as a function of incident energy comparison between TENDL21 model and experimental data.

The χ^2 estimation concerning the TENDL21 model total cross-section prediction compared to experimental data is of 7.2 $\pm$ 1.1.

II.1.2 DINo predictions

Figure 5.7 presents an iteration example of the algorithm tested on the model values. The challenge in deep learning algorithms is that it needs to learn enough to be able to predict results, but not so much that it only replicates the model it was trained on.

Figure 5.8 presents the predicted experimental total cross-section values by DINo alongside TENDL model values and the experimental ones. This comparison is important for understanding how well DINo performs in predicting total cross-sections compared to existing models. Notably, within the energy range relevant for particle therapy (above 50 MeV), the predictions generated by the DINo model demonstrate significantly higher accordance to experiment data than those from the TENDL21 model.

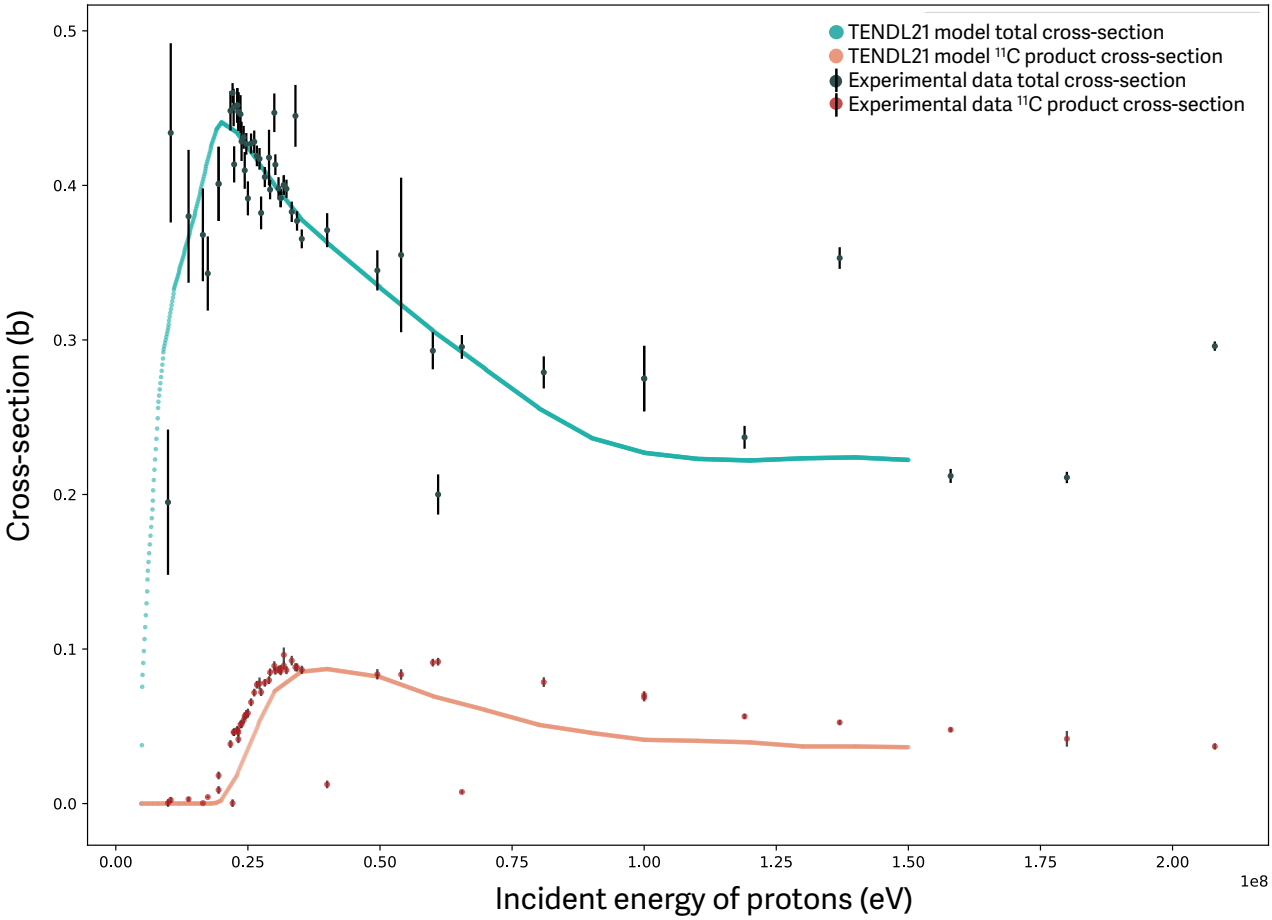

Figure 5.6: Total cross-section for incident protons on a ^{12}C target as a function of incident energy alongside with ^{11}C product cross-section: TENDL21 model predictions compared to experimental data.

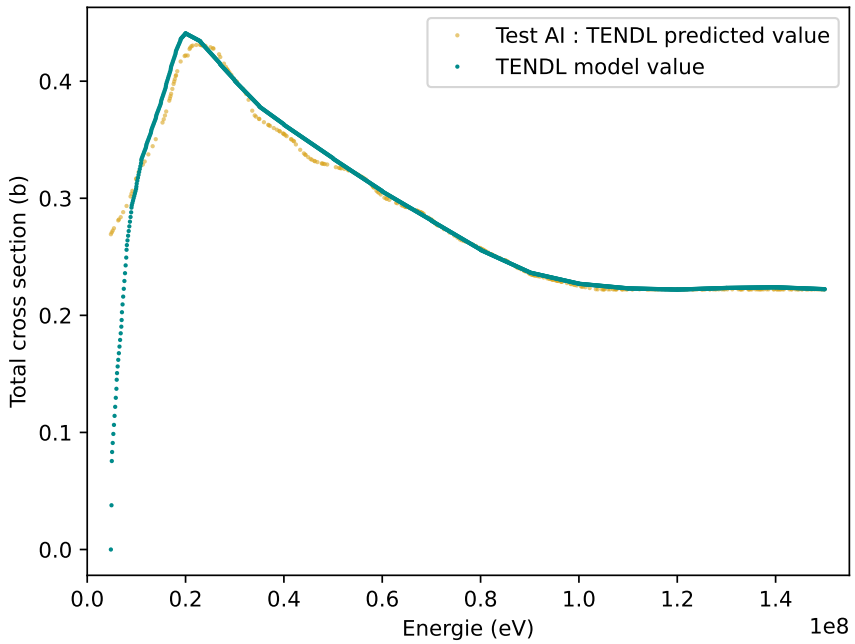

Figure 5.7: Algorithm test on total cross-section for incident protons on a ^{12}C target as a function of incident energy alongside: TENDL model results and DINo predictions.

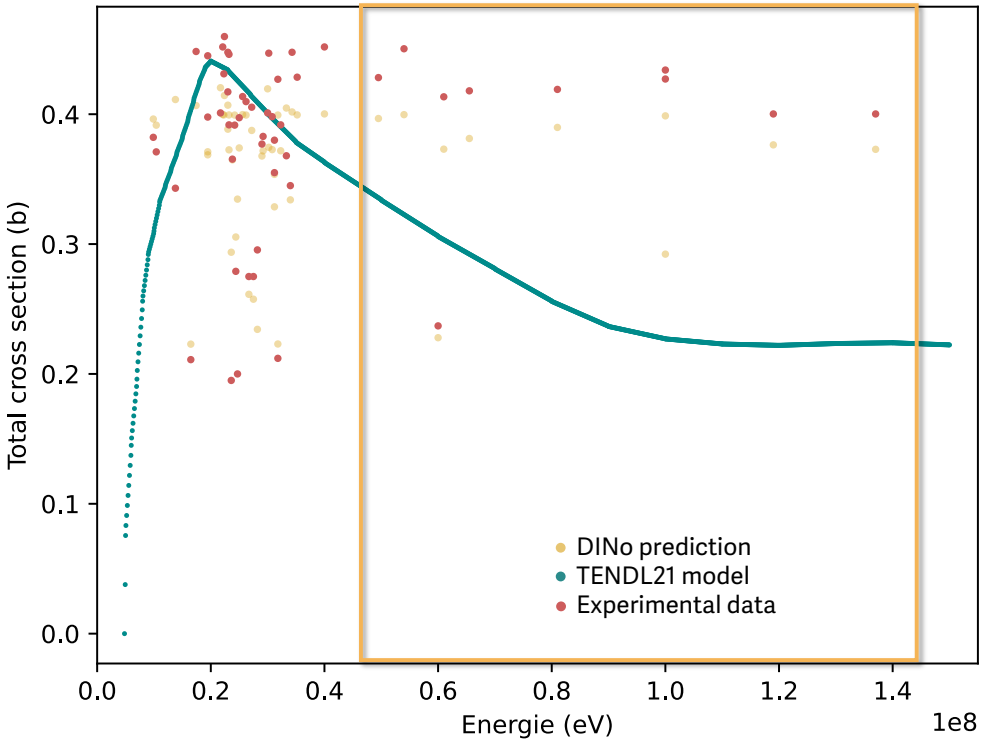

Figure 5.8: Total cross-section for incident protons on a ^{12}C target as a function of incident energy: TENDL model results and DINo predictions compared to experimental data.

II.1.3 Efficacy of DINo predictions

The effectiveness of DINo predictions is further analyzed in Figure 5.9, which compares total cross-sections for incident protons on a ^{12}C target between TENDL model results, DINo predictions, and experimental data. The predicted values from the model and the AI algorithm are plotted as a function of the experimental data values, for each incident energy. The black linear function represents the perfect case where the prediction is equal to the experimental value. The closer the points are from this line, the better the predictions are.

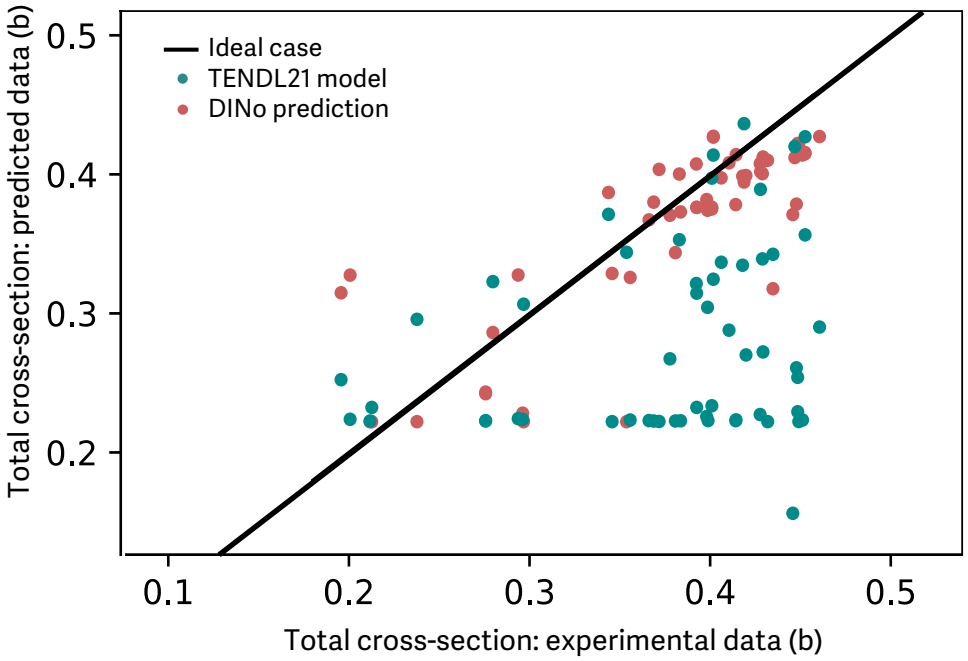

Figure 5.9: ^{11}C product cross-sections and total cross-section for incident protons on a ^{12}C target: TENDL model results and DINo predictions compared to experimental data.

The χ^2 values provide a quantitative measure of compatibility between the experimental data and the predictions. Notably, the χ^2 value between the experimental data and DINo predictions are reported as 5.2±1.0.

The results demonstrate that the deep learning algorithm DINo exhibits enhanced predictive capabilities for total cross-sections compared to the TENDL model for which the χ^2 value is 7.2 ± 1.1.

Even under the least favorable conditions, when DINo exhibits its lowest performance (indicated by a χ^2 value of 6.1), it still matches the best performance of the TENDL model. In optimal scenarios, DINo outperforms the TENDL model by a factor of almost 2 (1.98), showcasing its potential for accurate predictions in nuclear physics applications.

II.2 Tests with other products

Following the evaluation of the ^{11}C isotope, additional tests were performed on other isotopic products produced via proton-carbon nuclear reactions. The aim was to validate

the robustness and versatility of the DINo algorithm across different isotopes and to ensure its predictive accuracy was not limited to a single case.

II.2.1 Choice of products

When studying the fragmentation of protons on ^{12}C, the products of interest are those that are most likely to be produced in carbon ion therapy and have significant biological impacts. Here are the key products to focus on:

- ^{4}**He**: alpha particles, are significant due to their high LET, which can contribute to the therapeutic effect but also to potential side effects.
- ^{6}**Li**: Lithium isotopes are important to consider because they can result from the breakup of carbon nuclei and have specific biological impacts.
- ^{9}**Be**: Beryllium isotopes are less common but still relevant in understanding fragmentation patterns and dose calculations.
- ^{10}**B** : Boron isotopes are produced in fragmentation and are of interest, especially considering boron neutron capture therapy (BNCT) applications.

These choices ensure comprehensive modeling of relevant nuclear interactions, leveraging extensive data availability in TENDL-21.

II.2.2 Results

Table 5.1 presents the χ^2 values comparing the experimental charge-changing cross sections to the model predictions for various isotopes relevant to carbon ion therapy.

Isotope	DINo's prediction χ^2	TENDL21 Model χ^2
Helium-4 (^{4}He)	2.2 ± 0.4	3.0 ± 0.5
Lithium-6 (^{6}Li)	0.8 ± 0.3	1.0 ± 0.5
Boron-10 (^{10}B)	2.1 ± 0.3	2.5 ± 0.7
Beryllium-9 (^{9}Be)	0.7 ± 0.2	0.9 ± 0.5

Table 5.1: χ^2 Values for each charge-changing cross sections total cross-section DINo predictions compared to TENDL21 model

Across all tested isotopes, DINo demonstrated an ability to produce reliable predictions, although the accuracy was heavily influenced by the quality and quantity of the training data. The algorithm performed better in energy ranges with dense experimental data, indicating its potential for high accuracy in well-studied isotopes and reactions. Conversely, for isotopes with limited data, the model's predictive performance highlighted the need for more comprehensive datasets to improve accuracy.

This discussion aligns with the investigation presented in Chapter 4, which focuses on the measurement and analysis of secondary particles produced by ion fragmentation. It underlines the necessity of comprehensive studies between models and measurements to enhance overall accuracy and reliability, as these factors are intricately interconnected.

II.3 General efficiency and limits

The evaluation of DINo's efficiency involved comparing its computational performance and predictive accuracy against the TENDL 2021 model. Key metrics included computational time, mean squared error (MSE) for predictive accuracy, and the ability to generalize predictions from training data to unseen conditions.

II.3.1 Computational efficiency

DINo demonstrated significant computational efficiency advantages. Once trained, the deep learning model provided rapid predictions, typically in the order of µs, requiring substantially less computational time than traditional nuclear reaction models. This speed makes DINo particularly advantageous for simulations and real-time applications, such as in clinical settings for hadron therapy planning, where quick and accurate data is crucial.

II.3.2 Predictive accuracy

The model's predictive accuracy was rigorously tested using cross-validation methods. DINo's predictions for total cross-sections in proton-carbon interactions were consistently more accurate, with lower MSE values, compared to TENDL, especially within the well-represented mid-energy range (10-50 MeV). However, at the extremes of the energy spectrum (below 10 MeV and above 50 MeV), the model's accuracy was more variable. This variation can be attributed to the sparse data available for training in these regions, indicating a limitation that could be mitigated with more extensive experimental datasets.

II.3.3 Generalization capability

One of DINo's strengths is its ability to generalize from the training data to make predictions for unseen experimental conditions. This was particularly evident in isotopes with comprehensive datasets, where DINo provided reliable predictions even in extrapolated scenarios. However, for isotopes and energy ranges with limited experimental data, the model's generalization capability was less robust, often reflecting increased prediction variance.

II.3.4 Limitations

The primary limitation identified in this study is DINo's dependency on the quality and comprehensiveness of its training dataset. The algorithm performed best with isotopes and energy levels that had extensive and precise data. In contrast, its performance was less consistent for isotopes with sparse data, highlighting the need for continuous updates to the training datasets. Additionally, overfitting was observed when the training data was not sufficiently diverse, suggesting that future iterations of the model should incorporate techniques to mitigate this risk.

III. Conclusion

In conclusion, this chapter has presented an overview of the development and application of DINo, a deep learning-based algorithm for predicting nuclear reactions. By focusing on proton interactions, particularly within the context of hadrontherapy, DINo has

demonstrated substantial improvements in predictive accuracy and computational efficiency compared to TENDL 2021 model.

The analysis has shown that DINo's strength lies in its ability to learn complex patterns within nuclear data. However, the study also highlighted some limitations, particularly the dependency on the quality and comprehensiveness of training datasets. Performance was notably better for isotopes and energy levels with extensive data.

Furthermore, DINo should be viewed as a complementary tool to existing hadronic models rather than a replacement. It offers the potential to extrapolate values in data-sparse regions, but it's important to be cautious. Confidence in computational tools relies upon empirical validation through experimental measurements.

Overall, DINo could represent an advancement in nuclear reaction modeling, offering a promising tool for enhancing the accuracy of predictions in particle therapy and potentially other nuclear applications. Future work should focus on addressing the identified limitations and further refining the model to expand its applicability and robustness.

Summary

Introduction

Le chapitre 5 présente le développement et l'application de DINo (Deep Learning Intelligence for Nuclear reactions), un algorithme d'apprentissage profond conçu pour améliorer les prédictions des réactions nucléaires, particulièrement dans le cadre de l'hadronthérapie, où des divergences persistent entre les données expérimentales et les modèles hadroniques actuels. L'objectif principal est d'utiliser DINo pour améliorer la précision des prédictions des sections efficaces totales des réactions nucléaires critiques dans le contexte de la hadronthérapie.

Modèles nucléaires et approche d'apprentissage profond

Modèle nucléaire TENDL 2021

TENDL (TALYS-based Evaluated Nuclear Data Library) est une bibliothèque de données nucléaires développée par le Nuclear Reaction Data Centre (NRDC) à l'IRMM, faisant partie du Joint Research Centre (JRC) de la Commission Européenne. Basée sur des calculs utilisant le code théorique de réaction nucléaire TALYS, TENDL fournit des informations essentielles sur les réactions nucléaires, telles que les sections efficaces, les données de désintégration et d'autres propriétés nucléaires.

TENDL est particulièrement pertinent pour cette étude car il intègre une grande quantité de données sur les protons, rendant ce choix pertinent pour les applications d'hadronthérapie. Les modèles TENDL sont régulièrement mis à jour pour inclure des techniques de modélisation améliorées, des données expérimentales actualisées et des corrections basées sur des retours utilisateurs et des benchmarks expérimentaux.

Données expérimentales EXFOR

EXFOR (Experimental Nuclear Reaction Data) est une base de données internationale compilant des données expérimentales de réactions nucléaires provenant de diverses sources, maintenue par le réseau international des centres de données sur les réactions nucléaires (NRDCs) avec le soutien de l'AIEA. Elle collecte, organise et diffuse des données expérimentales sur les sections efficaces, les distributions angulaires, les spectres énergétiques et d'autres informations pertinentes obtenues lors d'expériences menées dans des laboratoires du monde entier.

Les données dans EXFOR sont stockées dans un format standardisé pour assurer la compatibilité et la facilité d'utilisation par les chercheurs et les évaluateurs de données nucléaires. Les données sont soumises à des contrôles de qualité et des processus de validation pour garantir leur précision et leur fiabilité.

Interactions des faisceaux de protons avec la cible ^{12}C

L'étude faite dans ce chapitre se concentre sur les interactions des faisceaux de protons avec une cible de ^{12}C. Le ^{12}C est souvent considéré comme un matériau "équivalent aux tissus", ce qui en fait une cible idéale pour simuler les interactions se produisant dans les tissus biologiques lors des traitements en hadronthérapie.

L'interaction d'un faisceau de protons avec une cible de ^{12}C peut produire des particules secondaires telles que des protons, des neutrons et des fragments de noyaux de carbone provenant de la cible. Ces particules secondaires sont cruciales pour comprendre la dosimétrie et les effets biologiques des radiations administrées aux patients. Ce choix est justifié car les fragments produits lorsqu'un proton frappe un noyau de ^{12}C sont similaires à ceux produits lorsqu'un ion ^{12}C frappe un noyau d'hydrogène, une composante majeure des tissus humains.

Généralités sur l'apprentissage profond

Algorithmes d'apprentissage profond

L'apprentissage profond est une sous-catégorie de l'apprentissage automatique qui se concentre sur l'apprentissage des représentations de données à travers des réseaux de neurones à multiples couches. Contrairement aux algorithmes d'apprentissage automatique traditionnels qui nécessitent des caractéristiques conçues manuellement, les modèles d'apprentissage profond peuvent automatiquement apprendre des représentations hiérarchiques à partir des données brutes.

Les réseaux de neurones sont les blocs de construction des modèles d'apprentissage profond. Ils sont composés de nœuds interconnectés organisés en couches. Chaque nœud ou neurone reçoit des valeurs d'entrée, applique des poids et des biais, effectue des calculs et passe le résultat à travers une fonction d'activation pour introduire de la non-linéarité.
Le processus d'entraînement d'un modèle d'apprentissage profond implique plusieurs étapes clés :

- **Propagation avant** : Les données d'entrée sont alimentées à travers le réseau couche par couche pour générer des prédictions.
- **Calcul de la perte** : La sortie du modèle est comparée aux valeurs réelles à l'aide d'une fonction de perte.
- **Rétropropagation** : Les gradients de la perte par rapport à chaque paramètre du réseau sont calculés pour mettre à jour les poids et les biais.
- **Optimisation** : Les algorithmes d'optimisation, comme la descente de gradient stochastique (SGD) ou Adam, sont utilisés pour ajuster les paramètres du modèle afin de minimiser la perte.

TensorFlow et Keras

TensorFlow est un framework open-source développé par Google pour la construction et l'entraînement de réseaux de neurones. Il offre une plateforme flexible pour les calculs numériques et prend en charge l'accélération par CPU et GPU, ce qui le rend adapté aux tâches d'apprentissage automatique à grande échelle. Keras, intégré à TensorFlow en tant que 'tf.keras', simplifie le processus de construction et d'entraînement des modèles en offrant une interface facile à utiliser pour définir les architectures de réseaux de neurones, spécifier les paramètres d'entraînement et exécuter les étapes d'entraînement et d'évaluation.

Structure de DINo

DINo est introduit comme un réseau de neurones dense (DNN) conçu pour apprendre à partir des valeurs du modèle TENDL 2021, en se concentrant spécifiquement sur les sections efficaces de changement de charge en fonction de l'énergie initiale du projectile de protons sur une cible de ^{12}C. L'objectif principal de DINo est de prédire les sections efficaces totales pour des énergies initiales non couvertes par les données expérimentales actuelles, à partir de section efficaces partielles.

La structure globale de l'algorithme DINo est détaillée en Figure 5.5, avec des couches denses utilisant la fonction d'activation ReLU, des couches de dropout pour éviter le surapprentissage (overfitting), et des couches de sortie pour produire les prédictions finales. Le processus d'apprentissage utilise 70 % des valeurs du modèle TENDL pour l'entraînement et 30 % pour les tests, afin d'assurer que l'algorithme peut généraliser correctement et faire des prédictions précises sur des données non vues.

Résultats

Étude détaillée du produit ^{11}C

L'efficacité des prédictions de DINo est analysée en comparant les sections efficaces totales pour les protons incidents sur une cible de ^{12}C entre les résultats du modèle TENDL, les prédictions de DINo à partir de la section efficace du produit ^{11}C, et les données expérimentales. Les valeurs χ^2, calculées suivant l'équation 5.1, fournissent une mesure quantitative de la compatibilité entre les données expérimentales et les prédictions.

La Figure 5.9 montre que les prédictions de DINo sont plus proches des données expérimentales que celles du modèle TENDL, avec une valeur χ^2 de 5.2 $\pm$ 1.0 pour DINo contre 7.2 $\pm$ 1.1 pour TENDL, démontrant une amélioration significative des performances de DINo par rapport au modèle TENDL. Les résultats montrent que même dans les conditions les moins favorables, DINo performe aussi bien que le modèle TENDL, et dans les conditions optimales, DINo surpasse le modèle TENDL par un facteur de presque 2.

Tests avec d'autres produits

Les produits clés étudiés incluent ^{4}He, ^{6}Li, ^{9}Be et ^{10}B, en raison de leur pertinence dans la thérapie par ions carbone et leur impact biologique significatif. Ces produits sont choisis pour assurer une modélisation complète des interactions nucléaires pertinentes, en s'appuyant sur la disponibilité extensive des données dans TENDL-21.

Les valeurs χ^2 pour chaque section efficace de changement de charge des produits, résumées dans la Table 5.1, montrent que DINo produit des prédictions plus fiables, surpassant souvent le modèle TENDL. Par exemple, pour l'^{4}He, DINo a une valeur χ^2 de 2.2 $\pm$ 0.4 contre 3.0 $\pm$ 0.5 pour TENDL, et pour le ^{6}Li, DINo a une valeur χ^2 de 0.79 $\pm$ 0.34 contre 0.97 $\pm$ 0.45 pour TENDL. Ces résultats montrent que DINo est capable de fournir des prédictions précises pour divers isotopes et dans différentes conditions énergétiques.

Efficacité générale et limites

Efficacité computationnelle

DINo démontre des avantages significatifs en termes d'efficacité computationnelle. Une fois entraîné, le modèle d'apprentissage profond fournit des prédictions rapides, généralement de l'ordre de microseconde, nécessitant beaucoup moins de temps de calcul que les modèles traditionnels de réactions nucléaires.
Cette rapidité rend DINo particulièrement avantageux pour les simulations et les applications en temps réel, telles que la planification de l'hadronthérapie où des données rapides et précises sont cruciales.

Précision prédictive

La précision prédictive du modèle a été rigoureusement testée en utilisant des méthodes de validation croisée. Les prédictions de DINo pour les sections efficaces totales dans les interactions proton-carbone sont constamment plus précises, avec des valeurs de l'erreur quadratique moyenne (MSE) plus faibles, comparées à TENDL, en particulier dans la gamme d'énergie bien représentée (10-50 MeV). Cependant, aux extrémités du spectre énergétique (en dessous de 10 MeV et au-dessus de 50 MeV), la précision du modèle est plus variable. Cette variation peut être attribuée à la rareté des données disponibles pour l'entraînement dans ces régions, indiquant une limitation qui pourrait être atténuée avec des jeux de données expérimentales plus complets.

Capacité de généralisation

DINo démontre une capacité de généralisation forte à partir des données d'entraînement pour faire des prédictions dans des conditions expérimentales non vues. Cette capacité est particulièrement évidente pour les isotopes avec des ensembles de données complets, où DINo fournit des prédictions fiables même dans des scénarios extrapolés. Cependant, pour les isotopes et les plages d'énergie avec des données expérimentales limitées, la capacité de généralisation du modèle est moins robuste, souvent reflétant une variance accrue des prédictions.

Limites

La principale limitation identifiée dans cette étude est la dépendance de DINo à la qualité et à l'exhaustivité de ses jeux de données d'entraînement. L'algorithme fonctionne mieux avec des isotopes et des niveaux d'énergie disposant de données extensives et précises. En revanche, ses performances sont moins cohérentes pour les isotopes avec des données limitées, soulignant le besoin de mises à jour continues des jeux de données d'entraînement. De plus, le surapprentissage a été observé lorsque les données d'entraînement n'étaient pas suffisamment diversifiées, suggérant que les futures itérations du modèle devraient incorporer des techniques pour atténuer ce risque.

Conclusion

Le chapitre présente DINo comme un outil complémentaire aux modèles hadroniques existants, offrant des améliorations significatives en termes de précision prédictive et d'efficacité computationnelle pour les réactions nucléaires. En se concentrant sur les interactions des protons, en particulier dans le contexte de la thérapie hadronique, DINo a démontré des améliorations substantielles par rapport au modèle TENDL 2021.

L'analyse a montré que la force de DINo réside dans sa capacité à apprendre des motifs complexes au sein des données nucléaires. Cependant, l'étude a également mis en évidence certaines limitations, en particulier la dépendance à la qualité et à l'exhaustivité des jeux de données d'entraînement. Les performances étaient notablement meilleures pour les isotopes et les niveaux d'énergie avec des données étendues.

En fin de compte, DINo devrait être considéré comme un outil complémentaire aux modèles existants plutôt que comme un remplacement. Il offre le potentiel d'extrapoler des valeurs dans des régions de données rares, mais il est important de rester prudent. La confiance dans les outils computationnels repose sur une validation empirique par des mesures expérimentales.

Globalement, DINo pourrait représenter une avancée dans la modélisation des réactions nucléaires, offrant un outil prometteur pour améliorer la précision des prédictions en thérapie par particules et potentiellement d'autres applications nucléaires. Les travaux futurs devraient se concentrer sur la résolution des limitations identifiées et sur l'affinement du modèle pour étendre son applicabilité et sa robustesse.

Chapter 6

CMOS tracking device for enhanced precision in lung cancer particle therapy

"They'll be chasing their tails trying to track us down."
– T. S.

Contents

Having discussed the nuclear models benchmarking with CLINM and the improvement achieved through deep learning with DINo, we will now explore how these secondary particles can be used in clinical conditions to enhance treatment efficacy. The integration of these advanced models and technologies has paved the way for more precise and effective cancer treatments by improving our understanding and prediction of particle interactions. In this chapter, we focus on the practical application of these insights, specifically in the context of lung cancer therapy.

Lung cancer remains one of the most prevalent and deadly forms of cancer worldwide. Traditional treatment modalities, including surgery, chemotherapy, and radiation therapy,

have shown limited success in improving long-term survival rates. Advances in particle therapy, particularly using heavy ions, have opened new possibilities for targeting cancer cells with greater precision and reduced collateral damage to healthy tissues. In this context, the development of novel tracking devices is crucial to enhance the accuracy and efficacy of particle therapy to treat lung cancer.

This chapter explores the implementation of a CMOS tracking device specifically designed to improve precision in lung cancer particle therapy. In this context, we propose a concept for 4D-online monitoring tailored to high-density gradient scenarios, focusing on a simplified lung tumor case. Utilizing the IVI (Interaction Vertex Imaging) technique [75], we aim to detect density gradients induced by tumor/bone and lung tissues, both statically and during simulated intrafractional motion. Through statistical analysis and computation of vertex distributions, we seek to assess the method's efficacy in accurately monitoring range shifts induced by motion, particularly at the edges of the target volume where high-density gradients are most pronounced.

I. Non-small cell lung cancer particle therapy

I.1 Generalities on non-small cell lung cancer

Non-small cell lung cancer (NSCLC) represents the predominant category in the lung cancer types, constituting around 80% of all diagnosed cases [76]. In 2020, lung cancer stands as the second most frequently diagnosed cancer worldwide, with a number of 2.2 million new cases and 1.8 million associated deaths [77].

Despite advancements in diagnostic and therapeutic modalities, the overall mortality rate remains high, standing at 22% across all histological types and disease stages [77].

NSCLC encompasses various types of tissue structures, primarily adenocarcinoma, squamous cell carcinoma, and large cell carcinoma, each with distinct molecular and clinical characteristics [78].

Adenocarcinoma, for instance, is the most prevalent subtype of NSCLC, particularly among nonsmokers and younger individuals, and often presents as peripheral lesions with glandular differentiation [79].

Notably, NSCLC is often detected at an advanced stage, with a median 5-year survival rate of only 26% [77]. This statistic concerns particularly patients presenting stage III disease and beyond, on which we'll be focusing in this chapter, characterized by locally advanced tumors with sizes ranging between 3 and 7 cm in diameter [80].

I.2 Particle therapy as a perspective

In recent years, advanced techniques have been developed to treat lung cancer, particularly non-small cell lung cancer (NSCLC), using particle therapy. As discussed in previous chapter, particle therapy, which includes both proton and carbon ion therapy, offers several advantages over conventional photon-based radiotherapy due to its ability to deliver highly conformal dose distributions with a Bragg Peak, thereby sparing surrounding healthy tissues. However, treating moving tumors with ion beams remains a significant challenge due to movement of respiratory motion.

I.2.1 Respiratory motion

In lung cancer treatment, the patient's respiratory motion can cause significant inhomogeneities in the delivered dose and range shifts during both planning and treatment. The high-density gradients between the lung, tumor tissue, and bones, coupled with motion, can cause the high-dose profile to narrow, the penumbra to widen, and dose shifts of up to 10-15% in the caudal direction. This motion leads to uncertainties in the range and position of the particle beam, which can result in either underdosing the tumor or overdosing the surrounding healthy tissues.

An example of a range overshoot is presented in Figure 6.1. Indeed, this Figure shows on the left panel the dose distribution for a treatment plan which was planned at the end of inhale. On the right panel, the dose distribution of the same treatment plan but appearing at the end of exhale shows range overshoot and even exposure to the heart.

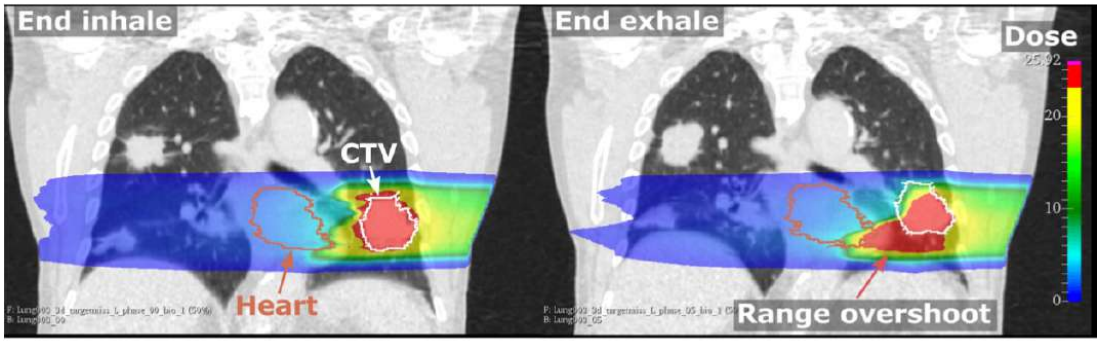

Figure 6.1: Left panel: dose distribution of a single-field uniform dose (SFUD) plan, optimized on the end inhale phase of a 4D-CT of lung cancer patient without safety margins. Right panel: same SFUD plan applied on the end exhale phase. Due to periodic tumor motion and the density gradient between tumor and surrounding lung tissue, considerable range changes are generated for the end exhale phase, causing dose deteriorations which increase the dose exposure to the heart. [20]

I.2.2 Impact of dose uncertainties

Underdosing of the tumor

Underdosing can occur if the tumor moves out of the high-dose region during treatment. This can result in insufficient radiation being delivered to the tumor, potentially leading to tumor recurrence. A study by Bert et al.[81] have shown that a 5 mm motion can lead to a dose reduction of up to 20% in some regions of the tumor.

Overdosing of healthy tissues

Overdosing can occur if the high-dose region moves into healthy tissues due to respiratory motion. This can lead to significant damage to healthy tissues, increasing the risk of radiation-induced side effects. For instance, movement-induced dose shifts can result in the adjacent organs at risk (OARs) receiving doses higher than their tolerance levels. For instance, a study by Seppenwoolde et al.[82] have quantified that for lung tumors, a 10

mm motion can lead to an increase in dose to healthy lung tissue by up to 15%, which significantly raises the risk of radiation pneumonitis.

Range uncertainty

Respiratory motion causes range uncertainty in proton and carbon ion therapy. This uncertainty can cause the beam to stop either before or after the tumor. Parodi and Enghardt [83] indicated that for a typical lung tumor, respiratory motion can cause a range uncertainty of 4-5 mm, potentially leading to a 10% variation in the expected dose distribution.

I.2.3 Advanced beam delivery techniques

Current advancements in cancer therapy, particularly in the treatment of lung cancer, have seen the integration of new beam delivery techniques such as beam scanning, particularly when combined with carbon ion beams. This approach allows for the precise administration of radiation, delivering a highly conformal dose distribution to target tissues. However, challenges arise due to geometric variations between planned irradiation and patient anatomy, potentially leading to under- or overdosage in tumor and healthy tissues, respectively. These variations stem from factors like patient movement, positioning uncertainties, and organ motion, necessitating the incorporation of additional margins into treatment plans.

I.2.4 Motion mitigation strategies

Efforts to mitigate motion effects have included breath-hold techniques, abdominal pressure, external motion tracking via cameras, and internal tumor tracking using fiducial markers or fluoroscopy. However, these methods may not be universally applicable, particularly in cases where patients are physically incapable of complying, such as those with advanced lung cancer. Additionally, certain techniques, like fluoroscopy, incur high additional doses to healthy tissues.

- **Breath-Hold Techniques**: These techniques involve having the patient hold their breath during radiation delivery to minimize motion. This can reduce tumor movement to less than 2-3 mm, significantly improving dose accuracy. Minohara et al. [84] demonstrated that breath-hold techniques could reduce motion-related uncertainties in dose delivery of 5-10mm.

- **Abdominal Compression**: Using abdominal compression devices can restrict diaphragm movement, thus limiting respiratory-induced tumor motion. This method can reduce the extent of tumor movement by up to 50%, as shown in a study by Wong et al. [85].

- **Gating and Rescanning**: Combining gating (delivering the radiation only at specific phases of the respiratory cycle) with rescanning strategies can help minimize motion-related dosimetric degradation. This approach can improve dose delivery precision by ensuring the tumor remains within the high-dose region during treatment delivery. Bert and Rietzel [81] demonstrated the effectiveness of gating and rescanning in reducing dose uncertainties caused by respiratory motion.

I.2.5 Real-time monitoring and advanced optimization

Advanced optimization techniques, including 4D-robust optimization, have been developed to account for intrafractional motion during treatment planning. Real-time monitoring techniques, such as MRI-guided radiotherapy and photoacoustics, hold the potential for verifying delivered doses without imposing additional constraints on patients. Another method is the use of secondary radiation produced during treatment, such as positron emission tomography (PET) imaging. PET imaging can detect annihilation photons from positron-emitting isotopes produced by nuclear reactions of the incident ions, permitting to visualize and verify the dose distribution post-treatment.

I.2.6 Emerging techniques

Emerging techniques like interaction vertex imaging (IVI) [75] offer novel approaches to online range monitoring, particularly relevant for cases with high-density gradients, such as lung tumors. By reconstructing trajectories and emission points of secondary charged particles produced during nuclear fragmentation, IVI allows for real-time assessment of range shifts induced by anatomical variations or motion during treatment.

I.3 Conclusion

In conclusion, while significant challenges remain in treating lung cancer with particle therapy due mainly to respiratory motion, ongoing research and technological advancements continue to improve the precision and efficacy of this modality. The integration of advanced imaging techniques, robust treatment planning algorithms, and real-time monitoring technologies permit more effective and personalized lung cancer treatments. The project presented in this chapter aims to build on these advancements by developing a novel approach that addresses the specific issue of dose delivery uncertainties caused by respiratory motion in lung cancer treatment with particle therapy.

II. Tracking device project - preliminary experiment

II.1 Generalities

This study aims to propose and evaluate a method for 4D-online monitoring of high-density gradients, applied to a simplified lung tumor model.

The production of lighter fragments within a specified volume varies with its density. This characteristic is leveraged to detect density gradients in a phantom composed of materials representing tumor/bone and lung tissues across several static scenarios, and scenarios simulating intrafractional motion.

When treatment is delivered as planned, the vertex (production points) distributions of the different secondary particles exhibit specific profiles in the x-y-z dimensions. However, intrafractional motion, such as movement during treatment, can cause significant range shifts due to the strong density gradients between bone/soft tissues in the thoracic wall or tumor tissues compared to lung tissues, leading to notable differences in the vertex distributions.

In this experiment, a phantom mimicking tumor and lung tissues was irradiated with a clinically relevant spherical treatment plan of 2 Gy. Respiratory motion was simulated using a remotely controlled motorized table. Four particle trackers made of 3 CMOS

sensors each, were positioned at various angles relative to the beam axis, and vertices were reconstructed under different conditions. The CMOS sensors were described in Chapter 2 Section I.2. A statistical analysis was conducted and vertex distributions were computed for all recorded measurements and presented across the different scenarios.

The study also focused on the high-density gradients induced by the spherical edge of the target, assessing the method's efficiency based on the scanned beam spots. Additionally, the feasibility of detecting the motion phase of the target using the proposed concept was examined.

II.2 Experimental setup

The first experimental campaign was performed at the MIT ion-beam therapy center in Marburg, Germany, in May 2022, in a patient room, and an overview of the results will be presented.

The measurements were performed with a ^{12}C ion scanning pencil beam. The general experimental setup is presented in Figure 6.2, and each part of the setup will be detailed in the next subsections.

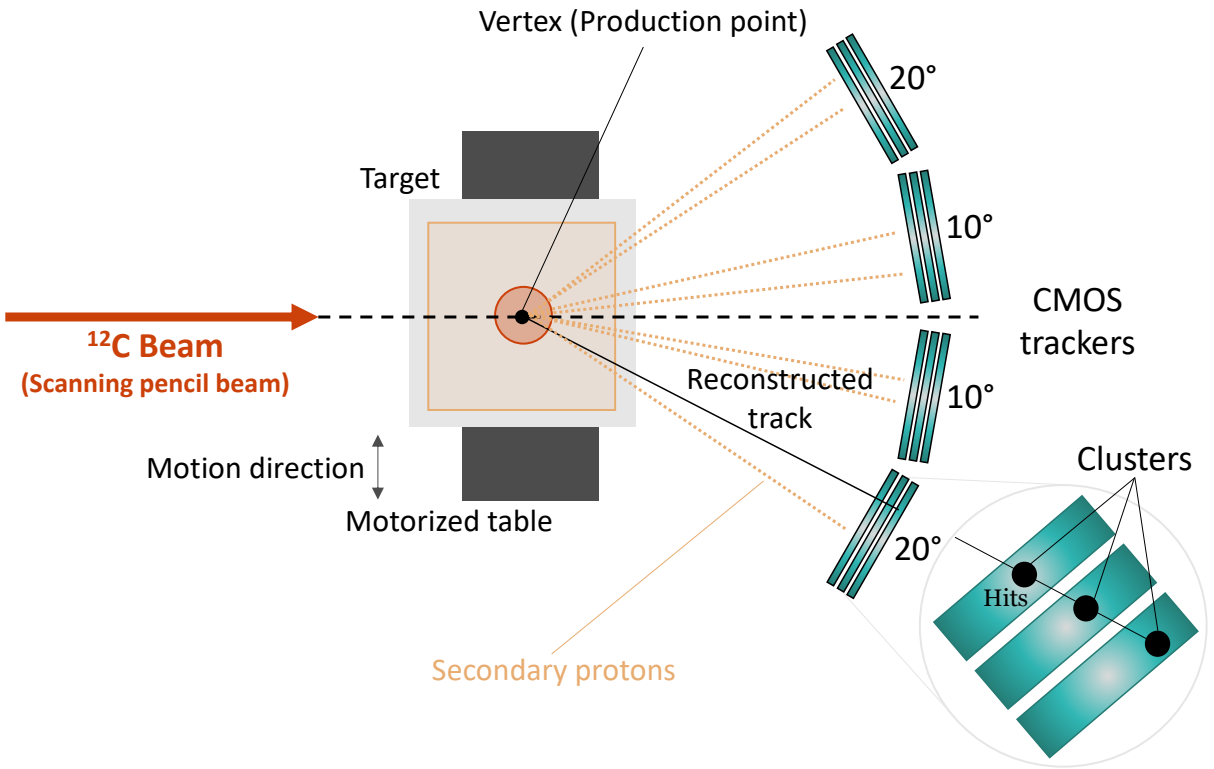

Figure 6.2: Experimental setup of the experiment at MIT, with the CMOS trackers measuring secondary protons produced by the beam inside the target.

II.2.1 Moving target phantom

The target was made of a PMMA aquarium of 26 × 26 × 26 cm^3, filled with a 24 × 25 × 25 cm^3 cube made of foam material of 0.23 g/cm^3 density, comparable to the lung tissue.

A hole in the center of the foam cube allows to insert a PMMA cylinder of 5 cm diameter with a spherical shape at one end, representing the tumor volume.

The phantom was positioned on a motorized table, controlled by a software designed to reproduce the respiratory motion of the patient. The motion pattern as proposed by [86] of 3 s period and 20 mm amplitude was used. The table is initially positioned to match in order that the center of the PMMA spherical end is the isocenter of the treatment room.

II.2.2 CMOS tracking device

The detection of secondary protons resulting from beam fragmentation with the target employed four tracker systems. Each system consisted of three MIMOSA-28 pixel sensors, described in Chapter II Section I.2, positioned at specific angles relative to the beam axis, $\pm$ 10.5° and $\pm$ 21°, located at 24.8 cm away from the target center. These angles and distances were determined through Geant4 Monte Carlo simulations to optimize vertex reconstruction and resolution.

As described earlier in Chapter II Section I.2 the MIMOSA-28 pixel sensors operate by detecting ionizations in their epitaxial layers, generating charges that are collected by activated pixels. An event is recorded when the signal is higher than a predefined threshold, forming clusters whose centroids determine the positions of interest.

Track reconstruction with analysis software QAPIVI [87], involves linking clusters across the three CMOS sensors within each tracker to establish straight-line trajectories. The vertices, denoting interaction points such as those from nuclear fragmentation, are subsequently computed. This calculation utilizes the minimal distance between the average projected track from the multi-wire proportional chambers (MWPCs) upstream of the target and the back-projected track from the CMOS tracker behind the target.

To enhance tracking precision, alignment of the trackers is crucial. This is achieved through a software alignment procedure, compensating for any mechanical misalignments detected during dedicated calibration runs without a target [88]. A detailed explanation of the vertex reconstruction procedure is given in Section II.3.

II.2.3 Treatment planning

Treatment plans for all investigated scenarios were generated using the TRiP (Treatment planning for particles) system, originally developed at GSI for carbon ion therapy [89]. These plans were computed based on a virtual CT scan, where the geometry and densities of materials mimicked those of the experimental phantom. The target volume was defined as a sphere slightly smaller than the spherical end of a PMMA cylinder, with 3 mm margins to accommodate potential target misalignments during the experiment.

The treatment plan focused on applying a homogeneous dose of 2 Gy within this volume, following the base data from MIT for carbon ions. The planning process involved creating 18 iso-energy layers spanning energies from 125.91 to 203.69 MeV/u of ^{12}C ion beam, utilizing a total of 8360 beam spots.

Figure 6.3 presents the treatment planned dose on the virtual CT when the treatment is delivered as planned and when the target is moved of 20mm in x direction.

II.3 Analysis

In order to reconstruct the spatial distributions (x-y-z coordinates) of the secondary protons produced during the nuclear fragmentation of primary beams within the phantom

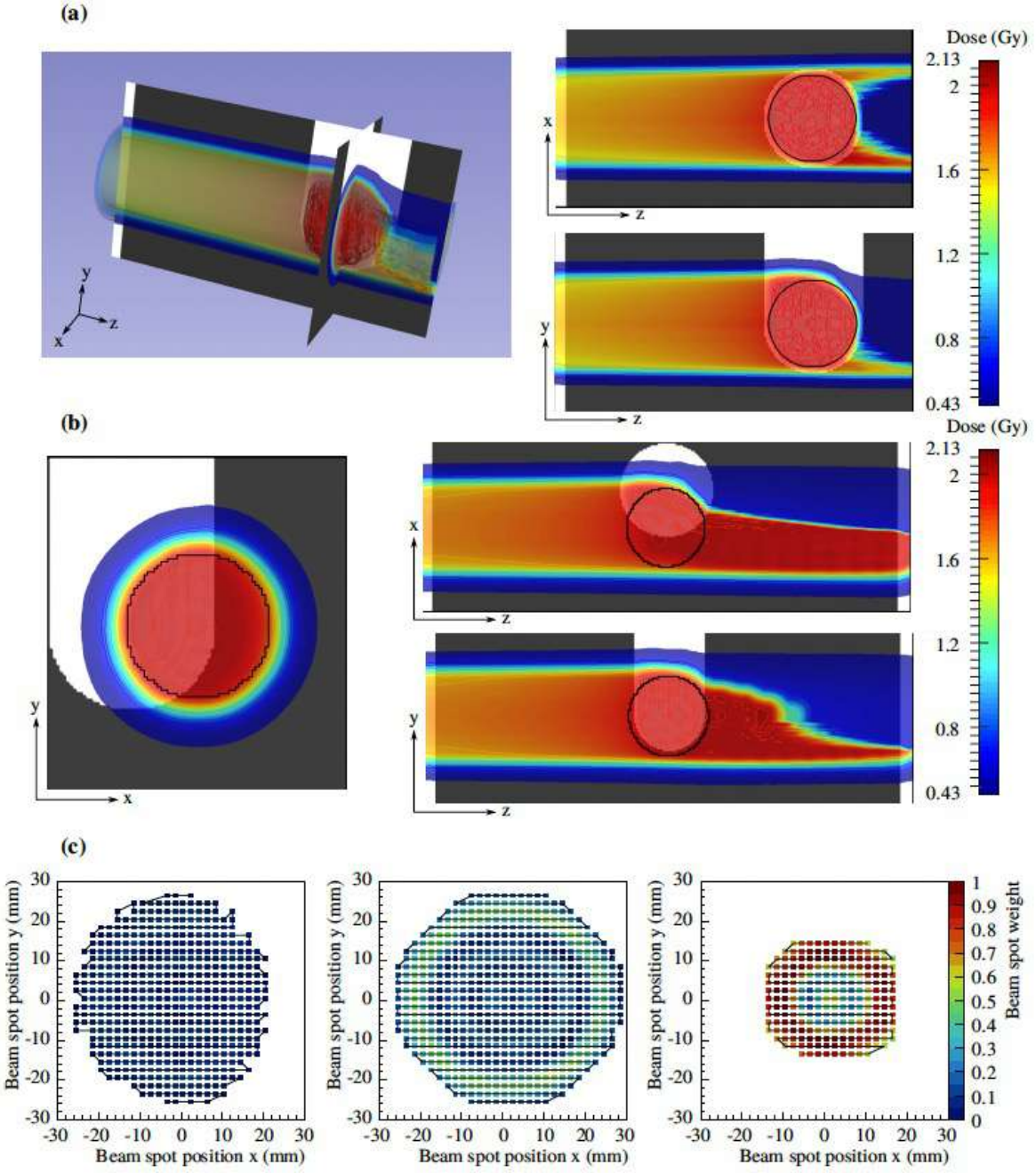

Figure 6.3: Delivered dose superimposed to the virtual CT as a 2D and 3D views when the treatment is delivered as planned (a), while in (b) the treatment is delivered at a motor position of 20 mm in x direction. In (c), x-y views of three single iso-energy layers that were extracted from the 3D treatment plan for 131.32, 170.11 and 195.65 MeV/u containing 495, 603 and 219 beam spots, respectively. The black line shows the trajectory of the irradiation, and the particles per beam spot were normalized to the maximum value of the 195.65 MeV/u treatment plan. [21]

volume, the correlation between the 3 CMOS (composing each set of tracker) detected clusters is necessary to rebuild the protons track and then be able to determine their production point, called vertex.

II.3.1 Track reconstruction

Considering sets of 3 CMOS as a tracking device, a track is described as linear regression which matches between clusters in each plane, following those steps:

- **Track candidates**: All combinations between the valid clusters from the first and the last plane are considered and a straight line is computed for each, creating track candidates.
- **Adding third plane**: For the plane in between, the closest cluster to the track candidate is added to it, and the track parameters are updated considering all three clusters.
- **Track validation**: Track candidates undergo validation against specific criteria:
  - A valid track includes three clusters, with allowance for one missing cluster to accommodate potential sensor insensitivity. This accounts for situations where deposited energy is insufficient to trigger a signal above the threshold or where pixels fail to register any signal (dead pixels).
  - Residuals, computed as the differences between cluster and track positions at each plane, must fall below predefined thresholds. These thresholds are individually estimated for each plane using a weighted calculation.
  - The deviation of cluster sizes from all identified clusters must be within a specified limit.
  - Non-valid tracks are reassessed with relaxed residual constraints, iteratively adjusting until a user-defined threshold is met.
  - If valid clusters persist, the process is repeated with a lower resolution for the last sensor plane used in the initial track selection.
  - The algorithm stops when no valid clusters or track candidates remain.

II.3.2 Vertex reconstruction

In a first step, the CMOS pixel sensor data were analyzed independently of the other systems. Each tracker was locally and globally aligned using the dedicated alignment run and all recorded tracks were reconstructed for the four individual trackers. Next, all files were merged based on the timing signals logged in the FPGA. Each reconstructed track from the CMOS sensors was back projected to the target, referred to as secondary track, and associated with the extrapolated front track based on the center of mass of the primary carbon ion beam spot measured by the two nozzle MWPCs, and is referred to as primary track.

Due to the readout time differences between the nozzle detectors and the CMOS sensors, multiple individually measured secondary tracks are assigned to a single primary track per beam spot. Last, the vertex reconstruction was performed by computing the interaction point between the primary and secondary tracks. The vertex is then defined as the point of coordinates (x, y, z), where the distance between primary and secondary tracks is minimum.

II.4 Results

The comprehensive temporal analysis for each beam spot plane of the treatment plan will not be explored in this thesis and was addressed in a separate study. However, a brief overview of proton distribution results will be provided. This comparison simplifies the scenarios into two cases: the static centered target, for which the treatment plan is designed, and the moving target with breathing, for which the treatment plan is not optimized.

In Figure 6.4, the proton production point (vertex) distributions are shown along the beam axis for the same treatment planning (sphere of 44 mm diameter with optimized plan of 2 Gy of 2.5min). Two cases were studied, one when the target (PMMA cylinder) is exactly where the beam is scanning according to the treatment plan (in blue) and the other with the moving target, where the beam is not delivered properly in the target (in green). The distributions are shown for a CMOS tracker placed at a 10° angle to the beam axis and the measurement was integrated over the time across all movement.

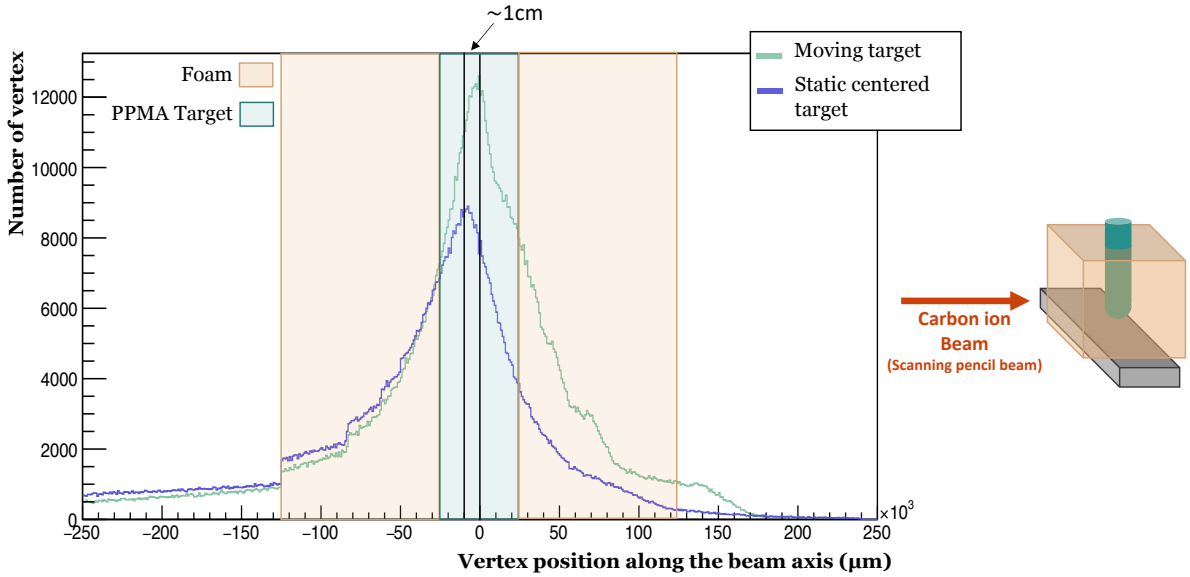

Figure 6.4: Vertex distributions of secondary charged particles along the beam axis reconstructed with the CMOS-tracker placed at 10° with respect to the beam axis, during a full treatment plan of 2 Gy on a PMMA sphere of 50mm diameter. The zero position represents the center of the target.

Significant differences between the two distributions are measured due to the high density gradients between the foam and the PMMA. For the case where the PMMA cylinder is centered as planned, the amount of vertices increases until dropping down around the zero position, as expected since the carbon ions fully stop in the PMMA cylinder. In the case where the beam is not delivered where it is planned to, the decrease of vertices number is less pronounced around zero because the carbon ions have a longer range when not passing through the PMMA cylinder, and thus continue to produce a bigger amount of secondary particles until the end of the target.

For the static centered target, the vertex distribution exhibits a more confined and

symmetric profile around the center of the target. This indicates a more predictable and concentrated pattern of secondary particle production.

In contrast, the moving target scenario shows a broader and more dispersed vertex distribution. This dispersion is attributed to the respiratory motion, causing significant range shifts and variations in density gradients encountered by the beam.

The broader distribution in the moving target highlights the challenges in achieving precise dose delivery in the presence of respiratory motion. The motion causes fluctuations in the density encountered by the beam, leading to a wider spread of secondary particle production points. This dispersion can potentially reduce the accuracy of the treatment, as the intended high-dose region may not consistently cover the tumor throughout the breathing cycle.

Figure 6.5 presents the total 2D vertex distributions of secondary charged particles, reconstructed using all the CMOS trackers during a full treatment plan of 2 Gy on a PMMA sphere with a diameter of 50 mm. The distributions are shown in three different planes: Vertex X vs. Y, Vertex X vs. Z, and Vertex Y vs. Z. The analysis compares the cases of a static centered target and a moving target and the measurement was integrated over the time across all movement.

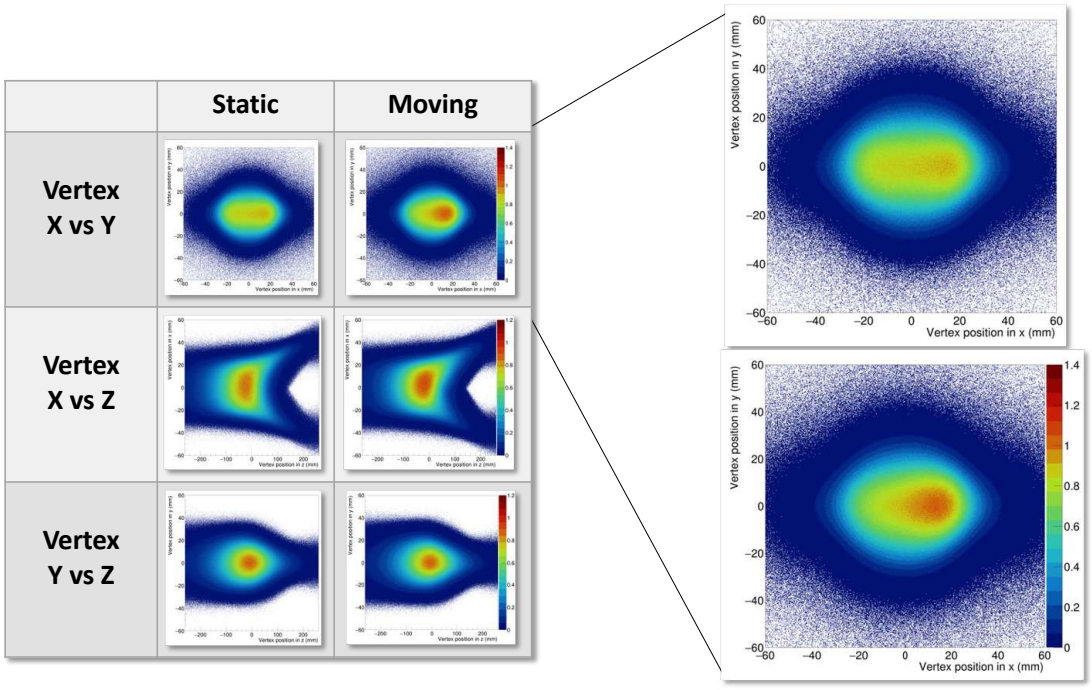

Figure 6.5: Total 2D vertex distributions of secondary charged particles reconstructed with all the CMOS-trackers, during a full treatment plan of 2 Gy on a PMMA sphere of 50mm diameter. [21]

The lateral spreads in the X and Y directions highlight the beam's divergence and the subsequent scattering of secondary particles. This is crucial for understanding the beam's behavior as it penetrates the target.

For the static centered target, the treatment plan is optimized, and the radiation beam is precisely delivered to the intended location. This results in a highly concentrated vertex distribution, indicating that the secondary charged particles are produced where expected. The vertices are primarily clustered around the target center, reflecting the

successful delivery of the treatment dose to the planned target volume.

In the case of the moving target, which simulates breathing motion, the treatment plan is not optimized to account for these movements. Consequently, the vertex distribution is more dispersed compared to the static target. This dispersion suggests that the secondary particles are produced over a wider area, indicating that the beam does not consistently hit the target as intended. The motion of the target causes a misalignment between the beam delivery and the target position, leading to a less efficient treatment.

Looking more in detail, for instance in vertex X vs. Y distributions, in the static case the distribution is concentrated around the origin, indicating precise targeting. However, in the moving target case, the distribution is spread out, and shows non homogeneous distributions, reflecting the misalignment due to motion. Concerning vertex Y vs. Z, the moving target case distribution extends further along the Z-axis, showing that the beam penetrates beyond the intended target due to movement.

In summary, the preliminary experiment using the CMOS tracking device demonstrated the potential for high-precision 4D-online monitoring of high-density gradients in a simplified lung tumor model. By utilizing CMOS pixel sensors and a motorized table to simulate respiratory motion, the study successfully reconstructed vertex distributions under various conditions. The results highlighted significant differences in vertex distributions due to intrafractional motion, emphasizing the importance of accurate motion tracking for effective particle therapy.

III. Tracking device project - simulation perspective

III.1 Generalities

The ultimate objective of this project is to develop a conceptual version of this detector system for use in clinical centers equipped with carbon ion beam facilities featuring scanning pencil beams and gantries, as illustrated in Figure 6.6.

This system intends to offer real-time monitoring of the beam position inside the patient and the movement of high-density gradient areas. Additionally, it could enable real-time data processing and surveillance, including the implementation of interlock mechanisms.

The data collected by the device will enhance treatment control by improving gating accuracy, facilitating beam correction via scanners, and refining 4D treatment plans to minimize margins. This improvement aims to increase treatment precision and reduce unnecessary radiation exposure to healthy tissues.

To explore the feasibility of this concept in a clinical setting, the proposed work includes a proof of concept of a comprehensive Monte Carlo simulation on a clinical scenario using GATE10 [90] on real patient 4D-CT data which includes breathing movements. This simulation will incorporate a pencil beam scanning treatment plan. The CMOS device will be integrated into this clinical case to optimize its geometry and technical characteristics, assessing its practicality and effectiveness in a realistic clinical environment. The investigation will involve detailed simulations to determine the optimal configuration and performance parameters of the CMOS detector system.

By conducting these simulations and analysis, the goal is to establish a robust proof of concept that demonstrates the clinical applicability of the CMOS-based detector system. This preliminary research will lay the groundwork for future experimental validations and

potential clinical trials, ultimately aiming to integrate the system into standard clinical practice for carbon ion beam therapy.

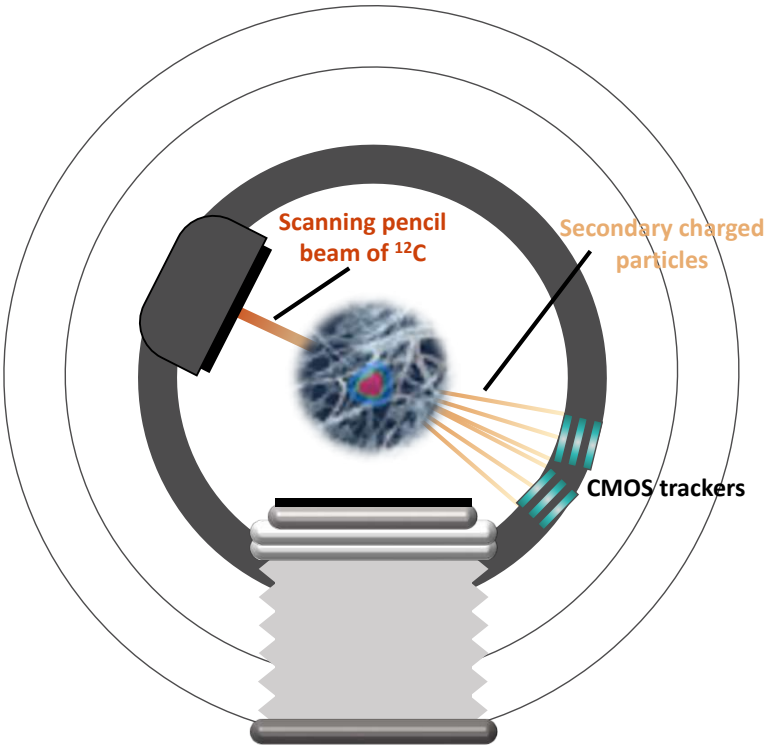

Figure 6.6: Schematic representation of the CMOS tracking device on a gantry facility for clinical application.

III.2 Simulation setup

III.2.1 Patient 4D-CT

In this study, a 4D-CT scan of a patient with lung cancer was employed, and was implemented in the GATE simulation. The 4D-CT imaging involves capturing 3D images of the patient's thorax at multiple time points throughout the breathing cycle, providing a comprehensive view of the tumor's dynamics over time. Specifically, ten distinct time steps were analyzed to understand the tumor's movement and deformation due to respiratory motion.

Figure 6.7 focuses on the initial time step (0.0) of the 3D-CT scan, highlighting the gross tumor volume (GTV) with contouring in red. The axial, coronal, and sagittal views collectively offer a precise localization and characterization of the tumor.

Figures 6.8 and 6.9 illustrate the 3D-CT images of the patient's thorax across these ten time steps. Each row represents a different time step, capturing the variations in the tumor's position and shape as the patient breathes. The left column shows axial slices, the middle column displays coronal slices, and the right column presents sagittal slices.

The integration of these 4D-CT images into the GATE simulation facilitates a realistic and dynamic modeling of the tumor's behavior under respiratory motion, and permit to study our proof of concept in clinical conditions.

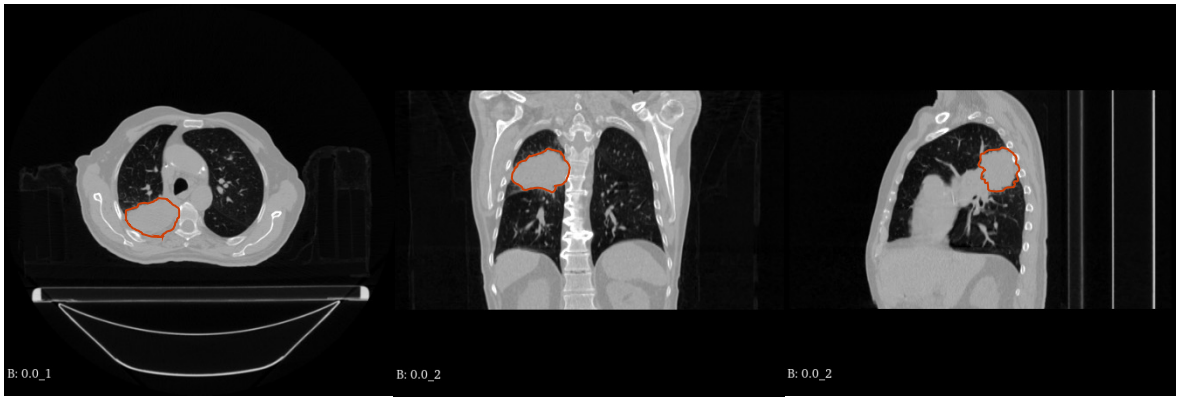

Figure 6.7: 3D-CT patient with a lung tumor for the first time step, with the GTV contouring in red.

III.2.2 Optimized treatment plan

The creation of personalized treatment plans that accommodate breathing movements aims to be tested in this proof of concept, in order to compare it in this case to a personalized treatment plans without any accommodation for breathing movements.

Personalized treatment plans tailored for breathing movements dynamically adjust the radiation beam to follow the tumor's position throughout the breathing cycle. This method ensures that the maximum dose is delivered to the tumor regardless of its location within the patient's body, thereby increasing treatment efficacy and reducing side effects.

Initially, two treatment plans are generated. The first plan is static, assuming no movement, while the second incorporates breathing patterns, typically obtained from the 4D-CT scans.

Implementation in OpenGATE 10 with Python

To implement a treatment plan that adapts to breathing movements within the OpenGATE framework, a specialized Python code was developed. This code reads treatment plan files and configures the simulation to generate a pencil scanning beam that precisely targets the moving tumor.

The process begins by parsing the treatment plan file to extract critical parameters such as beam energies, full width at half maximum (FWHM) values, and the coordinates of beam spots. These parameters are then used to create a series of beam spots in the simulation. Each spot is configured with specific energy, position, size and direction attributes to ensure accurate targeting.

The implementation involves creating a series of sources in the simulation, each representing a beam spot. The sources are assigned appropriate energies and positions based on the treatment plan. By systematically processing each spot, the simulation replicates the treatment plan, allowing for precise delivery of radiation that accounts for tumor movement.

III.2.3 CMOS digitized detectors

The digitizer in OpenGATE is a component that simulates the response of detectors to the interactions of particles. It converts the physical events (e.g., energy deposits) into

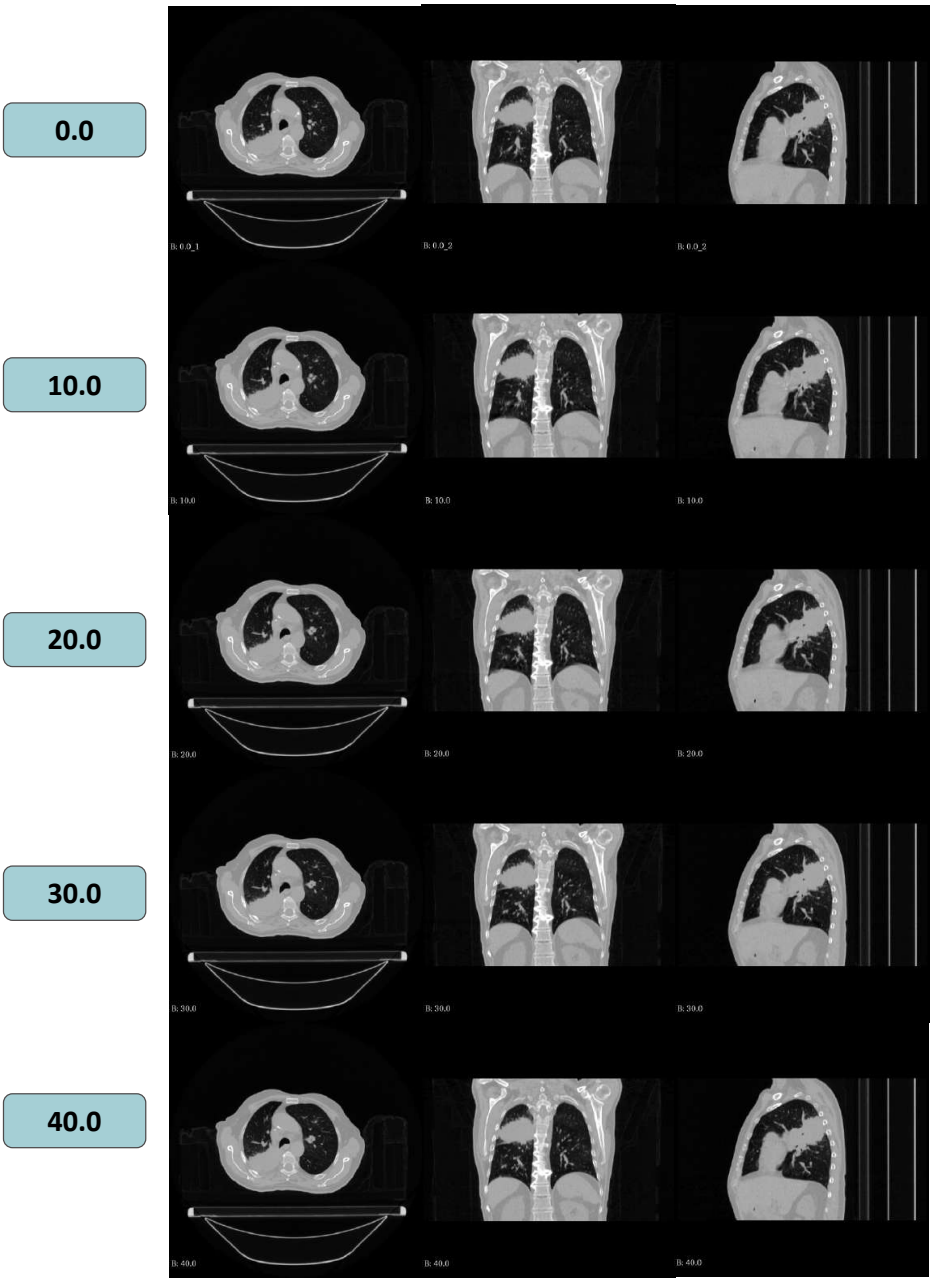

Figure 6.8: 3D-CT patient with a lung tumor for each step of time. Each row corresponds to a different time step during the breathing cycle, providing a dynamic view of the tumor's movement within the thorax.

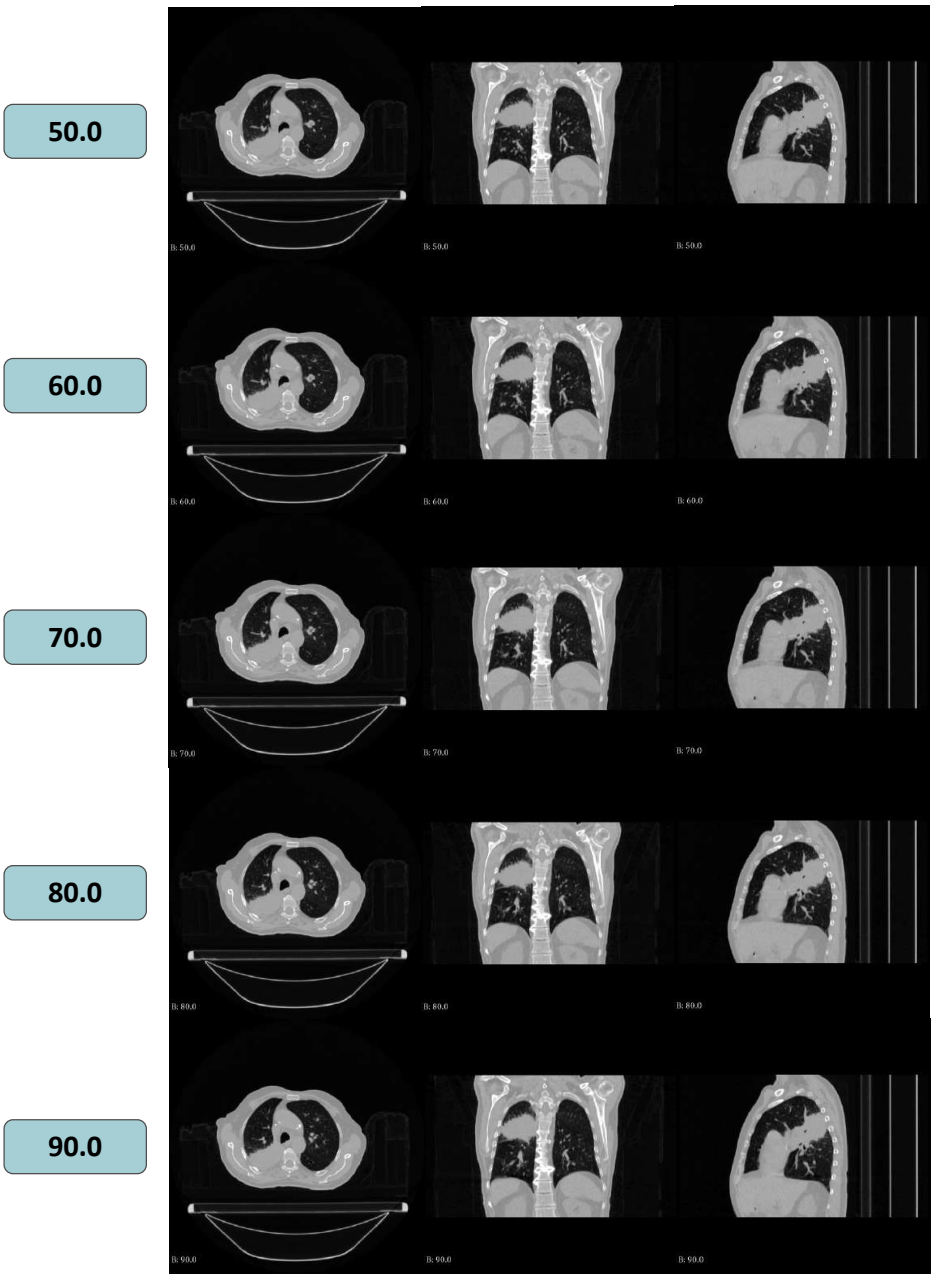

Figure 6.9: 3D-CT patient with a lung tumor for each step of time. Each row corresponds to a different time step during the breathing cycle, providing a dynamic view of the tumor's movement within the thorax.

a digital signal that mimics what an actual detector would record. This is crucial for bridging the gap between simulation and real-world measurements, allowing for more accurate comparisons and validations of simulation results.

Overview of digitization in OpenGATE

In OpenGATE version 10, digitization involves several key steps:

- **Energy Deposition**: This step records the total energy deposited by particles within the detector volume.
- **Signal Generation**: The deposited energy is converted into an electronic signal, typically involving processes like charge collection and signal amplification.
- **Analog-to-Digital Conversion (ADC)**: The analog signal is digitized, converting it into a discrete digital format that can be stored and analyzed. The ADC was not added in our case because the CMOS sensors do not exhibit ADC.

These steps ensure that the data obtained from simulations closely resembles what would be measured in a real detector.

Application to CMOS detectors

In our proof-of-concept simulation, the digitizer is configured to simulate the response of CMOS detectors, to accurately model and analyze the detector's response to the secondary protons. This setup is designed to capture detailed information about the particle interactions within the detector volume. The CMOS detectors were configured to record various attributes of the interacting particles, such as:

- Total energy deposit
- Kinetic energy
- Position and direction (both before and after interaction)
- Volume information
- Time-related attributes
- Particle and event identification details

By digitizing these attributes, the simulation produces a dataset that can be used to evaluate the performance of the CMOS detectors to detect differences in the secondary proton distributions.

III.2.4 Conceptual implications and future directions

The proposed simulation setup serves as a proof-of-concept, demonstrating the potential of the CMOS tracking device to improve the precision of particle therapy for lung cancer. This theoretical framework is rooted in several key insights from our preliminary experiments.

Firstly, the CMOS tracking device's ability to detect secondary particles with high spatial resolution provides a promising avenue for real-time monitoring of respiratory-induced motion. This capability is crucial given the significant dose uncertainties and

range shifts observed during treatment due to respiratory motion, as detailed in Section I.2. Our simulation anticipates that the device can effectively address these challenges by providing precise measurements of dose distribution and range shifts, particularly in high-density gradient scenarios. Secondly, by reconstructing the trajectories of secondary particles, IVI can potentially detect anatomical variations and motion-induced range shifts in real-time. This approach, as discussed in Section I.2.7, could significantly enhance the accuracy of dose delivery in particle therapy.

While the current work is primarily theoretical, it sets the stage for future experimental validation. The insights gained from this proof of concept are intended to guide subsequent studies and inform the development of robust clinical protocols. Future research should focus on empirically testing the proposed simulation setup on clinical case, optimizing the CMOS tracking device's performance, and integrating these technologies into clinical practice. Due to the delay to obtain an operational treatment plan, a finalized simulation cannot be shown in this manuscript. This will be done in a future work.

IV. Conclusion

Particle therapy, particularly with heavy ions, emerged as a promising alternative for lung cancer treatment due to its superior targeting capabilities and reduced side effects.

In this chapter, we have presented a comprehensive study on the development and application of a CMOS tracking device designed to enhance the precision of lung cancer particle therapy. This innovative approach addresses several key challenges associated with the treatment of non-small cell lung cancer (NSCLC) through particle therapy.

The preliminary experiments focused on the design and implementation of the CMOS tracking device. Experimental results have validated the device's performance on a simplified phantom, showing that it can reliably track particles with a high degree of accuracy. The subsequent simulations could reinforce these findings and highlight the potential for further enhancements. The integration of such a device into clinical practice could permit to optimize treatment outcomes for patients with non-small cell lung cancer.

Following the experimental validation, a proof of concept of an extensive simulation studies to explore the potential of the CMOS tracking device under various clinical scenarios was proposed.

Despite the promising results, further research and development are necessary to fully realize the clinical potential of the CMOS tracking device. Future work will focus on the following areas:

- **Optimization of device performance**: Refining the design and operational parameters of the CMOS tracker to enhance its precision and reliability.
- **Integration with clinical systems**: Ensuring seamless integration of the CMOS device with existing particle therapy equipment and protocols.
- **Clinical trials**: Conducting extensive clinical trials to validate the efficacy and safety of the CMOS tracking device in real-world settings.
- **Long-term monitoring**: Developing methods for long-term monitoring of treatment outcomes to assess the sustained impact of the CMOS tracker on patient health.

Summary

Introduction

Ce chapitre explore la mise en œuvre d'un trajectographe CMOS spécifiquement conçu afin d'améliorer la précision de la thérapie par particules dans le traitement du cancer du poumon. Après avoir discuté des modèles nucléaires et des améliorations apportées par l'apprentissage profond, nous nous concentrons sur l'application clinique de ces connaissances pour améliorer l'efficacité des traitements. Le développement de nouveaux dispositifs de suivi est crucial pour améliorer la précision et l'efficacité de la thérapie par particules pour traiter le cancer du poumon.

Thérapie par particules pour le cancer du poumon non à petites cellules

Généralités sur le cancer du poumon non à petites cellules (NSCLC)

Le cancer du poumon non à petites cellules (NSCLC) représente environ 80 % des cas de cancer du poumon diagnostiqués. En 2020, il y avait 2,2 millions de nouveaux cas et 1,8 million de décès associés. Malgré les avancées diagnostiques et thérapeutiques, le taux de mortalité reste élevé à 22 %. Les sous-types de NSCLC incluent l'adénocarcinome, le carcinome épidermoïde et le carcinome à grandes cellules, chacun avec des caractéristiques moléculaires et cliniques distinctes. L'adénocarcinome, par exemple, est le plus répandu, notamment chez les non-fumeurs et les jeunes.

Thérapie par particules comme perspective

La thérapie par particules, utilisant des protons ou des ions carbone, offre des avantages par rapport à la radiothérapie conventionnelle en délivrant des doses très conformes grâce au pic de Bragg, réduisant ainsi les dommages aux tissus sains. Cependant, le traitement des tumeurs en mouvement reste un défi significatif en raison du mouvement respiratoire du patient.

En effet, le mouvement respiratoire du patient peut causer des inhomogénéités significatives dans la dose délivrée et des décalages de portée pendant la planification et le traitement. Les gradients de densité élevés entre les tissus pulmonaires, tumoraux et osseux peuvent causer des changements de portée de 10 à 15 % dans la direction caudale. Lors par exemple d'une insuffisance de dose dans la tumeur, une récidive tumorale peut survenir, tandis que lors d'une surdose de tissus sains, une augmententation des effets secondaires peut être observée. Par exemple, un mouvement de 10 mm peut augmenter la dose au tissu pulmonaire sain jusqu'à 15 %, augmentant le risque de pneumonite radiologique.

Stratégies actuelles pour réduire les marges

Les techniques actuelles, comme le balayage du faisceau, permettent une administration précise de la dose, mais les variations géométriques dues au mouvement du patient nécessitent l'ajout de marges supplémentaires dans les plans de traitement.

D'autres techniques incluent de bloquer la respiration du patient, par la compression abdominale, le suivi externe des mouvements et le suivi interne des tumeurs. Ces méthodes peuvent réduire les incertitudes de mouvement, mais ne sont pas toujours applicables à tous les patients.

Les techniques de surveillance en temps réel, comme la radiothérapie guidée par IRM et la protoacoustique, permettent de vérifier les doses délivrées sans imposer de contraintes supplémentaires aux patients. La tomographie par émission de positons (PET) peut également détecter les photons d'annihilation des isotopes émetteurs de positrons produits par les réactions nucléaires des ions incidents.
L'imagerie par vertex d'interaction (IVI) offre de nouvelles approches pour la surveillance en ligne de la portée, particulièrement pertinente pour les cas avec des gradients de densité élevés. Cette méthode permet une évaluation en temps réel des décalages de portée induits par les variations anatomiques ou le mouvement pendant le traitement.
Malgré les défis persistants, les avancées technologiques continuent d'améliorer la précision et l'efficacité de la thérapie par particules pour le traitement du cancer du poumon. Ce projet vise à développer une approche novatrice pour aborder les incertitudes de dose causées par le mouvement respiratoire dans le traitement du cancer du poumon avec la thérapie par particules.

Projet de dispositif de suivi - expérience préliminaire

L'objectif de cette étude est de proposer et d'évaluer une méthode de surveillance en ligne 4D des gradients de densité appliquée à un modèle simplifié de tumeur pulmonaire. La production de fragments plus légers varie avec la densité du volume spécifié, permettant de détecter les gradients de densité dans un fantôme représentant les tissus tumoraux, osseux et pulmonaires, à la fois statiquement et pendant un mouvement simulé.

Configuration expérimentale

Une campagne expérimentale a été réalisée au centre de thérapie par ions du MIT à Marburg, Allemagne, en mai 2022. Le dispositif expérimental utilisé est présenté en Figure 6.2. Les mesures ont été effectuées avec un faisceau de balayage d'ions ^{12}C. Le dispositif de suivi CMOS est composé de quatre systèmes de suivi, chacun composé de trois capteurs de pixels MIMOSA-28, positionnés à des angles de 10° et de 20° par rapport à l'axe du faisceau. Le fantôme est constitué d'un aquarium en PMMA rempli de mousse de densité comparable à celle du tissu pulmonaire, avec un cylindre en PMMA représentant le volume tumoral. Le fantôme est placé sur une table motorisée reproduisant le mouvement respiratoire du patient. Le dispositif de suivi détecte les protons secondaires résultant de la fragmentation du faisceau dans le fantôme. Les capteurs de pixels MIMOSA-28 détectent les ionisations dans leurs couches épitaxiales, générant des charges collectées par les pixels activés. Les plans de traitement sont générés à l'aide du système TRiP, basé sur une tomodensitométrie virtuelle du fantôme. Le volume cible est défini comme une sphère légèrement plus petite que l'extrémité sphérique du cylindre en PMMA, avec des marges de 3 mm.

Analyse

L'analyse implique la reconstruction des distributions spatiales des protons secondaires produits pendant la fragmentation nucléaire du faisceau primaire avec la cible. Cela nécessite de faire une corrélation entre les clusters détectés par les capteurs CMOS pour reconstruire les trajectoires des protons et déterminer leur point de production (vertex). En effet, les trajectoires sont calculées par une régression linéaire entre les clusters de chaque set de 3 CMOS. Les trajectoires candidates sont validées par des critères spécifiques, tels que la taille des clusters et les écarts résiduels.

Les données des capteurs CMOS sont analysées indépendamment pour chaque système de suivi. Les trajectoires reconstruites sont projetées en arrière vers la cible et associées aux trajectoires extrapolées du faisceau primaire. Le vertex est défini comme le point de coordonnées où la distance entre les trajectoires primaires et secondaires est minimale.

Résultats
Les résultats, présentés en Figure 6.3 et 6.4, montrent des différences significatives dans les distributions de vertices entre une cible statique et une cible en mouvement. Dans le cas de la cible statique, les vertices sont principalement concentrés autour du centre de la cible, suggérant une interaction homogène du faisceau avec la cible. Pour la cible en mouvement, les vertices montrent une distribution plus étendue, reflétant les variations de densité et le mouvement respiratoire simulé.

Projet de dispositif de suivi - perspective de simulation

L'objectif final de ce projet est de développer une version conceptuelle de ce système de détection pour une utilisation clinique dans les centres équipés de faisceaux d'ions carbone avec portiques, comme représenté en Figure 6.5. Cela inclut une simulation de preuve de concept dans un scénario clinique en utilisant GATE10 sur des données de tomodensitométrie 4D réelles de patient ayant un cancer du poumon.

Configuration de la simulation
Une tomodensitométrie 4D d'un patient atteint de cancer du poumon non à petites cellules est utilisée pour modéliser de façon réaliste et dynamique le comportement d'une tumeur sous l'effet du mouvement respiratoire. Deux plans de traitement sont générés : un plan statique et un plan prenant en compte les mouvements respiratoires, ajustant dynamiquement le faisceau de radiation pour suivre la position de la tumeur. Le digitaliseur dans OpenGATE simule la réponse des détecteurs CMOS aux interactions des particules, convertissant les événements physiques en signaux numériques similaires à ceux enregistrés par un détecteur réel.
En raison du retard dans l'obtention d'un plan de traitement opérationnel, une simulation finalisée ne peut être montrée dans ce manuscrit. Le dispositif de suivi CMOS pourrait améliorer la précision et réduire les marges de la thérapie par particules en offrant une surveillance en temps réel des mouvements induits par la respiration. Les simulations pourraient montrer que le dispositif peut détecter les variations anatomiques et les décalages de portée induits par le mouvement en temps réel.

Conclusion

La thérapie par particules, en particulier avec les ions lourds, constitue une alternative prometteuse pour le traitement du cancer du poumon en raison de sa capacité de ciblage supérieures et de ses effets secondaires réduits. Ce chapitre présente une étude sur le développement et l'application d'un dispositif de suivi CMOS pour améliorer la précision de cette thérapie. Les résultats expérimentaux préliminaires valident les performances du dispositif dans un modèle simplifié, tandis que les simulations proposent de renforcer ces résultats. Les recherches futures porteront sur l'optimisation des performances du dispositif, son intégration dans les systèmes cliniques, et la réalisation d'essais cliniques pour valider son efficacité et sa sécurité en conditions réelles.

Conclusion

This PhD thesis provides an analysis of secondary particles produced during heavy ion therapy, focusing on their impact on dose distribution and treatment accuracy. Through experimental and simulation studies, the necessity of improving the nuclear reaction models through experiments and AI was highlighted, alongside the significance of secondary particles in optimizing treatment plan.

The experimental data analysis employed a ΔE-E telescope, which consisted of a thin plastic scintillator and a cerium bromide crystal scintillator, to identify and differentiate secondary particles produced by beam fragmentation. The telescope, positioned at angles of 0° and 5°, recorded energy deposition for various secondary particles. By applying data cuts to ΔE-E plots, different particle species (Z) were successfully isolated. This method allowed for the detailed examination of energy distributions for these isolated Z species.

The Geant4 simulation setup replicated experimental conditions to measure energy loss (ΔE) and residual energy (E), integrating detector energy resolution. The comparison between simulated and experimental energy distributions revealed notable deviations, especially for helium (Z=2), highlighting Geant4's limitations in accurately reproducing the carbon break-up process. These discrepancies emphasize the need for refining theoretical models to improve the accuracy of simulations. The successful particle identification and separation based on energy loss characteristics demonstrate the telescope's effectiveness in providing the necessary information for the CLINM project.

Moreover, the application of deep learning algorithms, specifically the DINo (Deep learning Intelligence for Nuclear reactions) algorithm, was developped to predict nuclear reactions using experimental data, thus improving simulation accuracy. This computational tool exhibits potential in improving the predictive accuracy of nuclear reactions, making it a possible valuable asset in simulation and thus in dose calculation algorithms and treatment planning.

Additionally, the implementation of a CMOS tracking device for enhanced precision in lung cancer particle therapy was investigated. The research demonstrated the potential of CMOS technology to improve treatment accuracy and patient outcomes in non-small cell lung cancer (NSCLC) therapy using secondary particles. The detailed simulations and analysis highlighted the device's design and its integration into existing therapy systems, supported by preliminary experimental trials. This technology shows promise in addressing specific challenges such as respiratory motion and high-density gradients in lung tissues, which complicate accurate dose delivery.

Perspectives

Concerning the CLINM project, the discrepancies observed between simulated and experimental results underscore the need for continuous refinement of nuclear reaction models. Future work should focus on integrating more experimental measurements and implement those data in simulations directly in order to enhance the accuracy of nuclear models, particularly in the context of secondary particle production and behavior.

The successful application of the DINo algorithm demonstrates the potential of deep learning to enhance the predictive accuracy of nuclear reactions. Moreover, developing DINo to encompass a wider range of nuclear reactions and conducting wider statistical testing and error evaluation with existing experimental data could enable the integration of this tool into simulations, thereby achieving more accurate results for simulating nuclear reactions.

The promising results from the use of CMOS tracking devices suggest that further innovation in detector technologies could greatly enhance the precision of particle therapy. Future research should explore the integration of advanced detectors with existing therapeutic systems to improve overall treatment efficacy. By addressing specific challenges such as respiratory motion and high-density gradients in lung tissues, these technologies can improve treatment accuracy and patient outcomes in NSCLC therapy using secondary particles.

Appendices

A DINo

Model architecture

The neural network used in the DINo algorithm is a dense, fully connected, sequential model. The model architecture is presented in the Table A.1, highlighting each layer's output shape and the number of parameters used. The total number of parameters is 175 617, all trainable, with a memory usage of 686 kB.

Layer type	Output shape	Parameter number
Input	(2,)	
Dense 1	(,256)	768
Dropout 50%		
Dense 2	(,256)	65 792
Dense 3	(,256)	65 792
Dropout 50%		
Dense 4	(,128)	32 896
Dense 5	(,64)	8 256
Dense 6	(,32)	2 080
Output	(,1)	33
Total		175 617

Table A.1: DINo model architecture

This architecture employs dropout layers (with 50% dropout) to mitigate overfitting by introducing noise and preventing the model from becoming overly dependent on specific neurons during training. This adds additional variability in the model training process.

Error metrics

The model performance is evaluated using two main error metrics: Mean Absolute Error (MAE) and Mean Squared Error (MSE). These metrics are defined as follows:

- Mean Absolute Error (MAE):

$$MAE = \frac{1}{n}\sum_{i=1}^{n}|y_i - \hat{y}_i|$$

  MAE measures the average magnitude of errors, treating all errors equally, regardless of whether they are positive or negative. It is easier to interpret because the average error is in the same unit as the target variable.

- Mean Squared Error (MSE):

$$MSE = \frac{1}{n}\sum_{i=1}^{n}(y_i - \hat{y}_i)^2$$

  MSE squares the errors, which places more weight on larger errors, making it more sensitive to outliers than MAE. However, MSE is harder to interpret because its unit is the square of the target variable's unit.

Model Performance Evaluation

Figures A.1 and A.2 illustrate the model's performance over 100 epochs using both training and validation sets for the MAE and MSE metrics.

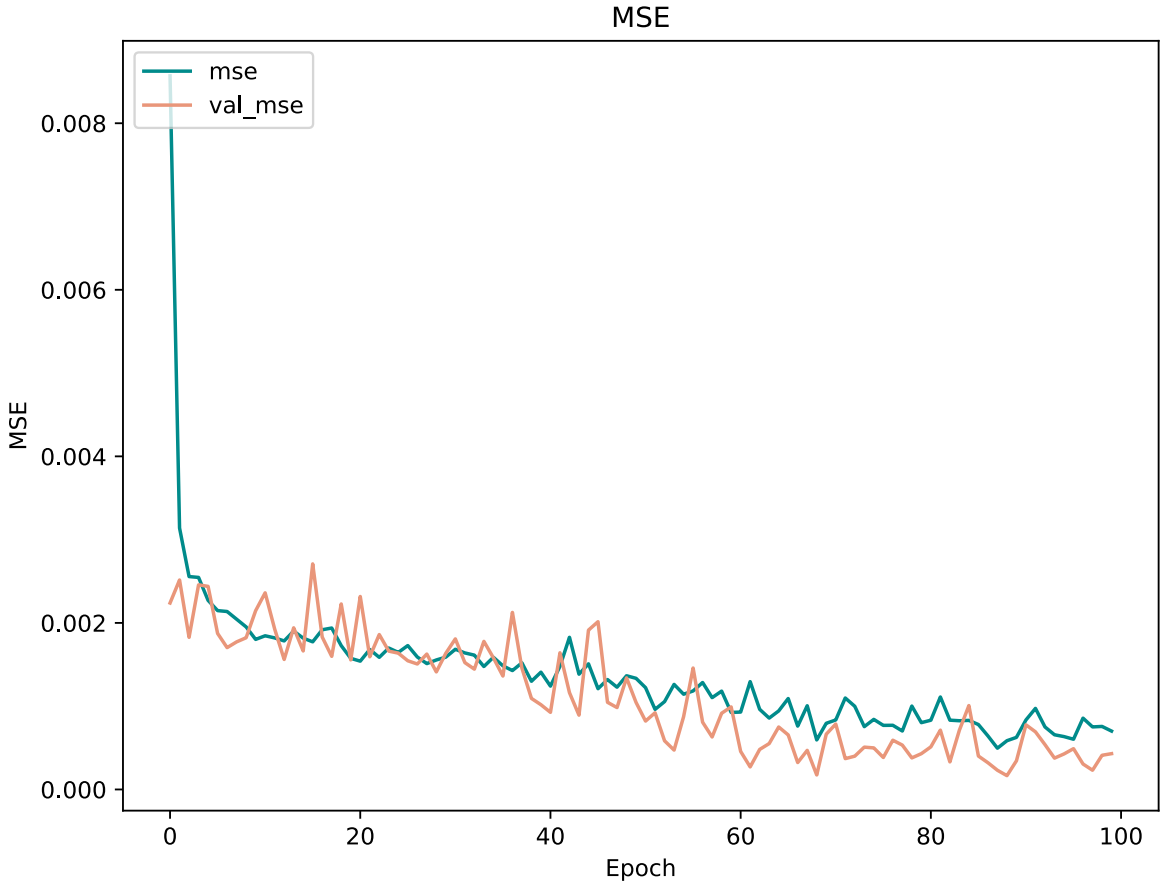

Figure A.1: DINo MSE performance over 100 epochs for both training and validation values.

Mean Squared Error (MSE)

The MSE on training values and on validation ones is monitored throughout the training process. The validation MSE shows more fluctuations compared to the training curve, indicating validation data variability. Depending on the particular batch of validation data being used in each epoch, the model's validation performance can be better or worse. This is caused by variability in the sample selection for validation, where each sample may not fully represent the complete validation set.

The MSE plot on Figure A.1 shows the convergence of the training and validation MSE values, indicating that the model is generalizing well. Both curves decrease steadily, and for the final epoch choice number of 20, a validation MSE value of approximately 0.0017, indicating strong performance.

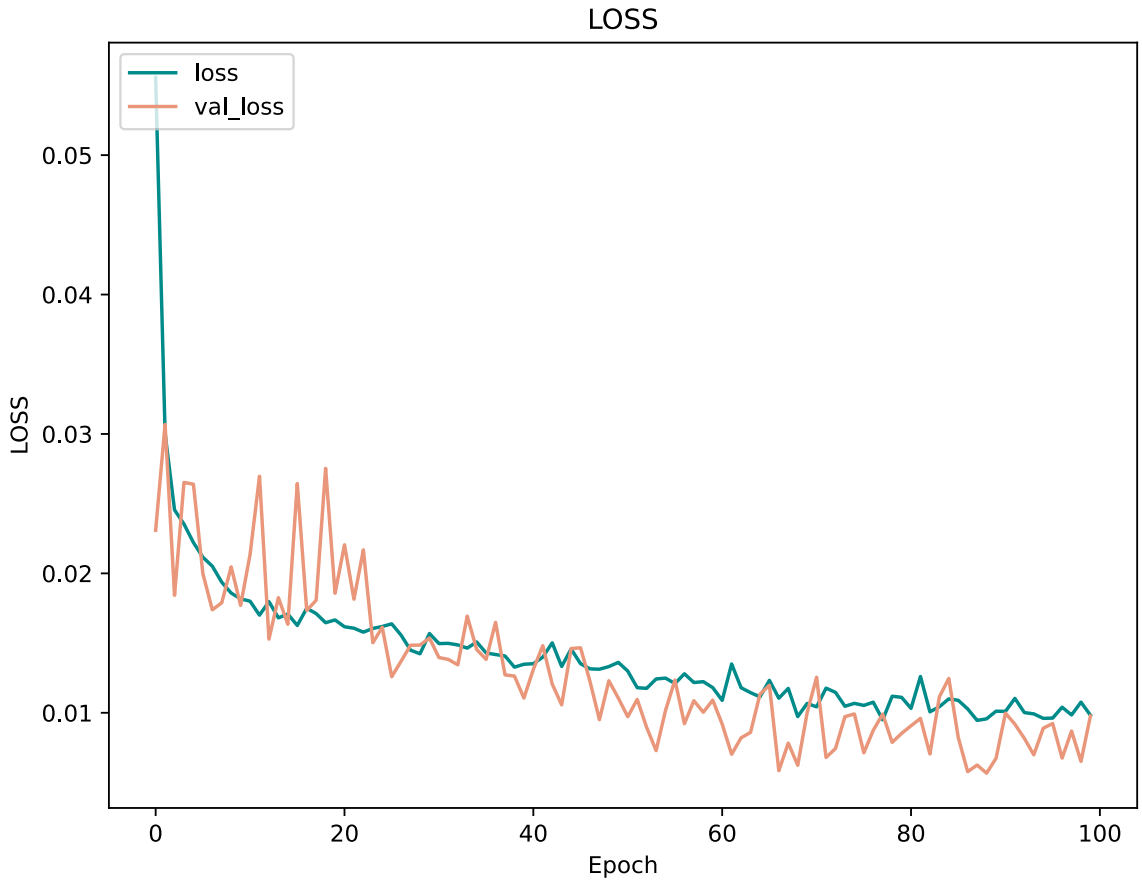

Figure A.2: DINo MAE performance over 100 epochs for both training and validation values.

Mean Absolute Error (MAE)

The MAE on training values and validation values is used to adjust model weights. Similar to the MSE curve, the MAE validation loss shows fluctuations, driven by variability in the validation samples per epoch. The MAE plot on Figure A.2 shows the loss function values for both training and validation data. The model converges for the final epoch coive number of 20 to a validation MAE value of approximately 0.0146. This level of error is considered acceptable.

Performance benchmark

A good range of values for MSE and MAE for this type of algorithm is considered to be between 0 and 0.5. Based on this range, MSE values less than 0.01 are considered acceptable. In this case, an MSE of ∼0.0017 indicates strong performance. MAE (loss function) values around 0.01 are also considered good enough, and the model achieves a final MAE of ∼0.0146. MSE typically results in smaller values than MAE due to the squaring of errors, which leads to lower final values in comparison to MAE.

Optimization process

The DINo model uses the Adam optimizer, which is a stochastic optimization algorithm. Adam adjusts the model weights by computing gradients based on small batches of data, rather than the entire dataset. This process introduces stochastic behavior during training, where the model weights are updated based on each small batch.

The stochastic nature of the Adam optimizer, particularly with smaller batch sizes, results in more fluctuations in the loss and MSE curves. Each weight update reflects only a small sample of the total data, which leads to variability in the MSE and MAE at each epoch. Although larger batch sizes can reduce this variability, they tend to slow down the convergence of the model.

Dropout further contributes to this variability as during each epoch, some neurons are randomly disabled, forcing the model to learn more robust patterns that are not dependent on any specific set of neurons.

Conclusion

This annex details the neural network architecture and performance evaluation of the DiNo algorithm. The architecture consists of multiple dense layers with dropout applied for regularization. The Adam optimizer, using small batch sizes, introduces stochasticity in the training process, which can be observed in the fluctuating validation curves. Performance metrics show the model is effectively minimizing both MSE and MAE, indicating good generalization to unseen data.

Bibliography

[1] Cancer today: data of the world global health organization, https://gco.iarc.fr/today/home, accessed: 2024-01-15.

[2] M.Durante, H.Paganetti, Nuclear physics in particle therapy: a review, Reports on Progress in Physics 79 (Aug. 2016). doi:10.1088/0034-4885/79/9/096702.

[3] Shibamoto, Yuta, Miyakawa, Akifumi, Iwata, Hiromitsu, Otsuka, Shinya, Radiobiology of sbrt, Stereotactic Body Radiation Therapy (2015) 11–25doi:10.1007/978-4-431-54883-6_2.

[4] W.Tinganelli, M.Durante, Carbon ion radiobiology, Clinical Oncology (Oct. 2020).
URL https://tuprints.ulb.tu-darmstadt.de/16188/1/cancers-12-03022-v2.pdf

[5] K. Gunzert-Marx, H. Iwase, D. Schardt, R. S. Simon, Secondary beam fragments produced by 200 mev/u 12c ions in water and their dose contributions in carbon ion radiotherapy., New Journal of Physics (July 2008). doi:0.1088/1367-2630/10/7/075003.
URL http://stacks.iop.org/1367-2630/10/i=7/a=075003?key=crossref.d8c5fe2733dc0eb15571a822575b9130

[6] M. Plum, Interceptive beam diagnostics-signal creation and materials interactions (Nov. 2004). doi:10.1063/1.1831132.

[7] U. Amaldi, G. Kraft, Radiotherapy with beams of carbon ions, Reports on Progress in Physics 68 (aug. 2005). doi:10.1088/0034-4885/68/8/R04.

[8] J. Mott, J. Daniel, Interactions of electromagnetic radiation and subatomic particles with matter e part 1, Clinical Oncology (Feb. 2021). doi:10.1016/j.clon.2021.02.004.
URL ://linkinghub.elsevier.com/retrieve/pii/S0168900215003101

[9] D. Cussol, Nuclear physics and hadrontherapy (2011).
URL https://hal.in2p3.fr/in2p3-00623351

[10] M.Vanstalle, Survie cellulaire de cellules a549 en fonction de la dose délivrée pour différents types de rayonnements ionisants (photons, protons, 4he, 12c et 16o)., IPHC - UMR7178, ED182 Strasbourg Thèse d'habilitation à diriger des recherches (2019).

[11] I. Dokic, A. Mairani, M. Niklas, F. Zimmermann, N. Chaudhri, D. Krunic, T. Tessonnier, A. Ferrari, K. Parodi, O. Jakel, J. Debus, T. Haberer, A. Abdollahi., Next generation multi-scale biophysical characterization of high precision cancer particle radiotherapy using clinical proton, helium-,carbon- and oxygen ion beams., Oncotarget (aug. 2016). doi:10.18632/oncotarget.10996.
URL ttp://www.oncotarget.com/fulltext/10996

[12] Y.Cao, D.Tang, Y.Xiang, L.Men, C.Liu, Q.Zhou, J.Wu, L.Huo, T.Song, Y.Wang, Z.Li, R.Wei, L.Shen, J. Z. Hong, Study on the appropriate timing of postoperative adaptive radiotherapy for high-grade glioma, Cancer Manag Res. (2021). doi:https://doi.org/10.2147/CMAR.S300094.

[13] A. Knopf, A. Lomax, In vivo proton range verification: a review., Physics in Medicine and Biology, 58(15), R131-R160. (2013).

[14] A. Lühr, C. von Neubeck, M. Krause, E. G. Troost., Relative biological effectiveness in proton beam therapy. current knowledge and future challenges., Clinical and Translational Radiation Oncology (feb. 2018). doi:10.1016/j.ctro.2018.01.006.
URL http://linkinghub.elsevier.com/retrieve/pii/S2405630818300028

[15] C. Grassberger, A. Trofimov, A. Lomax, H. Paganetti, Variations in linear energy transfer within clinical proton therapy fields and the potential for biological treatment planning, International Journal of Radiation Oncology*Biology*Physics 80 (2011) 1559–1566. doi:https://doi.org/10.1016/j.ijrobp.2010.10.027.

[16] N. Peters, P. Wohlfahrt, C. Hofmann, C. Möhler, S. Menkel, M. Tschiche, M. Krause, E. G. Troost, W. Enghardt, C. Richter, Reduction of clinical safety margins in proton therapy enabled by the clinical implementation of dual-energy ct for direct stopping-power prediction, Radiotherapy and Oncology 166 (2022) 71–78.
URL https://doi.org/10.1016/j.radonc.2021.11.002

[17] R. Mohan, C. R. Peeler, F. Guan, L. Bronk, W. Cao, D. R. Grosshans, Radiobiological issues in proton therapy, Acta Oncologica (2017). doi:10.1080/0284186X.2017.1348621.

[18] Dudouet, Cussol, Daniel, Durand, Labalme, Benchmarking geant4 nuclear models for carbon-therapy at 95 mev/a, Physical Review C. 89. (2013). doi:10.1103/PhysRevC.89.054616.

[19] Cebr3 - cerium bromide scintillator crystal, Advatech UK Ltd.
URL https://www.advatech-uk.co.uk/cebr3.html

[20] M. E. Wolf, Robust optimization in 4d treatment planning for carbon ion therapy of lung tumors. phd thesis, technische universita t, darmstadt 2018.
URL http://tuprints.ulb.tu-darmstadt.de/8354/

[21] C.-A. Reidel, E. Pierobon, F. Horst, L. Gesson, A. Paz, C. Graeff, T. Steinberger, K. Zink, M. Witt, Y. Senger, C. Finck, M. Vanstalle, C. L. Tessa, M. Durante, U. Weber, C. Schuy, Feasibility study of 4d-online monitoring of density gradients induced by lung cancer treatment using carbon ions, Frontiers - under review (2024).

[22] Krishnan, Mayakannan, Ranjith, A narrative review of particle therapy in cancer. cancer research, statistics, and treatment (2023) 248–260doi:10.4103/crst.crst_272_22.

[23] M. Goitein, M. Jermann, The relative costs of proton and x-ray radiation therapy, Clin Oncol (R Coll Radiol) (2003). doi:10.1053/clon.2002.0174.

[24] R. L. Foote, H. Tsujii, R. Imai, H. Tsuji, E. B. Hug, T. Kanai, J. J. Lu, J. Debus, R. Engenhart-Cabillic, A. Mahajan, The majority of united states citizens with cancer do not have access to carbon ion radiotherapy, Front Oncol (jul 2022). doi:10.3389/fonc.2022.954747.

[25] H. Paganetti, Range uncertainties in proton therapy and the role of monte carlo simulations., Physics in Medicine and Biology, 57(11), R99-R117. (2012).

[26] R. Schulte, Experience with the phase ii particle ct imaging system built by the pct collaboration (2018).

[27] U. Amaldi, A. Bianchi, Y.-H. Chang, A. Go, W. Hajdas, N. Malakhov, J. Samarati, F. Sauli, D. Watts, Construction, test and operation of a proton range radiography system, Nuclear Instruments and Methods in Physics Research Section A : Accelerators, Spectrometers, Detectors and Associated Equipment (feb. 2011). doi:10.1016/j.nima.2010.11.096.
URL http://linkinghub.elsevier.com/retrieve/pii/S0168900210026318

[28] V. A. Bashkirov, R. P. Johnson, H. F.-W. Sadrozinski, R. W. Schulte, Development of proton computed tomography detectors for applications in hadron therapy., Nuclear Instruments and Methods in Physics Research Section A : Accelerators, Spectrometers, Detectors and Associated Equipment (feb. 2016). doi:10.1016/j.nima.2015.07.066.
URL http://linkinghub.elsevier.com/retrieve/pii/S0168900215009274

[29] H. F.-W. Sadrozinski, V. Bashkirova, B. Colby, G. Coutrakon, B. Erdelyi, D. Fusi, F. Hurley, R. P. Johnson, S. Kashiguine, S. McAllister, F. Martinez-McKinney, J. Missaghian, M. Scaringella, S. Penfold, V. Rykalin, R. Schulte, K. Schubert, D. Steinberg, A. Zatserklaniy, Detector development for proton computed tomography (pct) (oct. 2011). doi:10.1109/NSSMIC.2011.6152494.
URL http://ieeexplore.ieee.org/document/6152494/

[30] N. Arbor, D. Dauvergne, G. Dedes, J. M. Letang, K. Parodi, C. T. Q. nones, E. Testa, S. Rit, Monte carlo comparison of x-ray and proton ct for range calculations of proton therapy beams, M. Physics in Medicine and Biology (oct. 2015). doi:10.1088/0031-9155/60/19/7585.
URL http://stacks.iop.org/0031-9155/60/i=19/a=7585?key=crossref.57a1486c25f9eea1404e24c3be3deb7c

[31] M. Yang, G. Virshup, J. Clayton, X. R. Zhu, R. Mohan, L. Dong, Theoretical variance analysis of single- and dual-energy computed tomography methods for calculating proton stopping power ratios of biological tissues., Physics in Medicine and Biology (mars 2010). doi:10.1088/0031-9155/55/5/006.
URL http://stacks.iop.org/0031-9155/55/i=5/a=006key=crossref.dfc557bb88c6d3a5127ef1dd48a5f62f

[32] B. Li, H. C. Lee, X. Duan, C. Shen, L. Zhou, X. Jia, M. Yang., Comprehensive analysis of proton range uncertainties related to stopping-powerratio estimation using dual-energy ct imaging, Physics in Medicine Biology (aug. 2017). doi:10.1088/1361-6560/aa7dc9.
URL http://stacks.iop.org/0031-9155/62/i=17/a=7056?key=crossref.2fd0504410d46a976fcd0f750c586605

[33] N. Hunemohr, B. Krauss, C. Tremmel, B. Ackermann, O. Jakel, S. Greilich., xperimental verification of ion stopping power prediction from dual energy ct data in tissue surrogates, Physics in Medicine and Biology (jan. 2014). doi:0.1088/0031-9155/59/1/83.
URL http://stacks.iop.org/0031-9155/59/i=1/a=83?key=crossref.881694b2b96a7f29939baae0c5b34bb5

[34] W. R. Leo, Techniques for nuclear and particl physics experiments, Spriner-Verlag, 1994.

[35] X. Li, et al., Performance study of cerium bromide (cebr3) scintillation crystal for gamma-ray spectroscopy, Nuclear Instruments and Methods in Physics Research Section A: Accelerators, Spectrometers, Detectors and Associated Equipment 663 (2012) 404–408.

[36] T. Yamamoto, et al., Development of large-sized nai(tl) scintillator with digital sipm readout for high-energy gamma-ray astronomy, Journal of Instrumentation 15 (2020).

[37] M. Yoshino, et al., Performance of a labr3(ce) scintillator in high-resolution gamma-ray spectrometry, IEEE Transactions on Nuclear Science 56 (2009) 1219–1223.

[38] R. Wang, et al., Study on the performance of bismuth germanate scintillator for high energy gamma ray detection, Journal of Physics: Conference Series 1403 (2019).

[39] D. T. Tidrow, et al., Performance of ej-309 liquid scintillator in the detection of fast neutrons, IEEE Transactions on Nuclear Science 61 (2014) 1762–1768.

[40] C. Xu, et al., Performance of csi(tl) crystals and sipm readout for high-resolution gamma-ray spectroscopy, Nuclear Instruments and Methods in Physics Research Section A: Accelerators, Spectrometers, Detectors and Associated Equipment 953 (2020).

[41] H. Wang, et al., Characterization of gadolinium oxysulfide as a neutron-sensitive scintillator, Nuclear Instruments and Methods in Physics Research Section A: Accelerators, Spectrometers, Detectors and Associated Equipment 988 (2021).

[42] P. Zhang, et al., Characterization of zinc sulfide scintillator for high-energy photon detection, Journal of Instrumentation 16 (2021).

[43] J. Birks, Scintillations from organic crystals: Specific fluorescence and relative response to different radiations, Proceedings of the Physical Society. Section A (1951) 64–874doi:10.1088/0370-1298/64/10/303.

[44] Miller, Alex, Machrafi, Rachid, Fariad, Abuzar, Investigation of the labr3 scintillator response to heavy ions., Radiation Measurements (2018). doi:101016/jradmeas201806009.

[45] M. Toppi, A. Sarti, A. A. et al., Elemental fragmentation cross sections for a 16o beam of 400 mev/u kinetic energy interacting with a graphite target using the foot e-tof detectors, Frontiers in Physics 10 (2022). doi:10.3389/fphy.2022.979229.
URL https://www.frontiersin.org/articles/10.3389/fphy.2022.979229

[46] Millera, Alex, Machrafi, Rachid, Fariad, Abuzar, Investigation of the LaBr3 scintillator response to heavy ions, Radiation Measurements 115 (2018) 43–48. doi:10.1016/j.radmeas.2018.06.009.
URL https://linkinghub.elsevier.com/retrieve/pii/S1350448717306030

[47] F. Quarati, O. Alan, P. Dorenbos, J. de Haas, G. Benzoni, N. Blasi, C. Boiano, S. Brambilla, F. Camera, R. Alba, G. Bellia, C. Maiolino, D. Santonocito, M. Ahmed, N. Brown, S. Stave, H. Weller, Y. Wu, High energy gamma-ray spectroscopy with LaBr3 scintillation detectors, Nuclear Instruments and Methods in Physics Research Section A: Accelerators, Spectrometers, Detectors and Associated Equipment 629 (1) (2011) 157–169. doi:10.1016/j.nima.2010.11.035.
URL https://linkinghub.elsevier.com/retrieve/pii/S0168900210024976

[48] D. Breton, E. Delagnes, J. Maalmi, P. Rusquart, The wavecatcher family of sca-based 12-bit 3.2-gs/s fast digitizers (2014) 1–8doi:10.1109/RTC.2014.7097545.

[49] M. Vanstalle, Dosimétrie électronique et métrologie neutrons par capteur cmos a pixels actifs, Ph.D. thesis, Université de Strasbourg (2011).

[50] P. N. Truong, P. Marchand, C. Finck, F. Boisson, D. Boisson, et al.., F autoradiography with the mimosa-28: Characterisation and application, IEEE Transactions on Radiation and Plasma Medical Sciences (2020). doi:hal-02881292.

[51] J. Allison, et al., Recent developments in geant4, Nuclear Instruments and Methods in Physics Research Section A: Accelerators, Spectrometers, Detectors and Associated Equipment 835 (2016) 186–225. doi:https://doi.org/10.1016/j.nima.2016.06.125.

[52] J. Allison, et al., Geant4 developments and applications, IEEE Transactions on Nuclear Science 53 (2006) 270–278. doi:10.1109/TNS.2006.869826.

[53] S. Agostinelli, et al., Geant4—a simulation toolkit, Nuclear Instruments and Methods in Physics Research Section A: Accelerators, Spectrometers, Detectors and Associated Equipment 506 (2003) 250–303. doi:https://doi.org/10.1016/S0168-9002(03)01368-8.

[54] D.Sarrut, et al., he opengate ecosystem for monte carlo simulation in medical physics, Phys Med Biol. (2022). doi:10.1088/1361-6560/ac8c83.

[55] J. Constanzo, M. Vanstalle, C. Finck, D. Brasse, M. Rousseau, Dosimetry and characterization of a 25-MeV proton beam line for preclinical radiobiology research, Medical Physics 46 (5) (2019) 2356–2362. doi:10.1002/mp.13512.
URL c

[56] P. Hofverberg, M. Antunes, C. Armando, J.-M. Bergerot, E. Bourrel, J.-F. Dicarlo, G. Donadey, S. Dumas, D. Fayaud, J.-C. Grini, A. Giusto, Y. Payan, M. Rolion,

C. Salicis, G. Angellier, J. Hérault, D. Maneval, M. Vidal, P. Mandrillon, F. Bezerra, J. Mekki, R. Trimaud, A 60 MeV proton beam-line dedicated to research and development programs, Applied Radiation and Isotopes 184 (2022) 110190. doi:10.1016/j.apradiso.2022.110190.
URL https://linkinghub.elsevier.com/retrieve/pii/S0969804322000896

[57] [link].
URL https://www.gsi.de/en/work/project_management_fair/sis100sis18_sis/heavy_ion_synchrotron_sis18

[58] M. Pullia, et al., The Experimental Beam Line at CNAO, in: 7th International Particle Accelerator Conference, 2016, p. TUPMR038. doi:10.18429/JACoW-IPAC2016-TUPMR038.

[59] C. Finck, et al., Study for online range monitoring with the interaction vertex imaging method, hysics in Medicine Biology 62 (2017).

[60] G. Knoll, Radiation detection and measurement, John Wiley Sons. (2010).

[61] A. Bross, A. Pla-Dalmau, K. Mellott, M. Knott, New developments in plastic scintillators., IEEE Nuclear Science Symposium Conference Record (2007).

[62] R. A. Cecil, B. D. Anderson, R. Madey, Improved predictions of range-energy relations for heavy ions, Nuclear Instruments and Methods (1979).

[63] F. D. Brooks, Development of organic scintillators., Nuclear Instruments and Methods (1979).

[64] S. Agostinelli, J. Allison, K. Amako, J. Apostolakis, H. Araujo, P. Arce, M. Asai, D. Axen, S. Banerjee, G. Barrand, F. Behner, L. Bellagamba, J. Boudreau, L. Broglia, A. Brunengo, H. Burkhardt, S. Chauvie, J. Chuma, R. Chytracek, G. Cooperman, G. Cosmo, P. Degtyarenko, A. Dell'Acqua, G. Depaola, D. Dietrich, R. Enami, A. Feliciello, C. Ferguson, H. Fesefeldt, G. Folger, F. Foppiano, A. Forti, S. Garelli, S. Giani, R. Giannitrapani, D. Gibin, J. Gómez Cadenas, I. González, G. Gracia Abril, G. Greeniaus, W. Greiner, V. Grichine, A. Grossheim, S. Guatelli, P. Gumplinger, R. Hamatsu, K. Hashimoto, H. Hasui, A. Heikkinen, A. Howard, V. Ivanchenko, A. Johnson, F. Jones, J. Kallenbach, N. Kanaya, M. Kawabata, Y. Kawabata, M. Kawaguti, S. Kelner, P. Kent, A. Kimura, T. Kodama, R. Kokoulin, M. Kossov, H. Kurashige, E. Lamanna, T. Lampén, V. Lara, V. Lefebure, F. Lei, M. Liendl, W. Lockman, F. Longo, S. Magni, M. Maire, E. Medernach, K. Minamimoto, P. Mora de Freitas, Y. Morita, K. Murakami, M. Nagamatu, R. Nartallo, P. Nieminen, T. Nishimura, K. Ohtsubo, M. Okamura, S. O'Neale, Y. Oohata, K. Paech, J. Perl, A. Pfeiffer, M. Pia, F. Ranjard, A. Rybin, S. Sadilov, E. Di Salvo, G. Santin, T. Sasaki, N. Savvas, Y. Sawada, S. Scherer, S. Sei, V. Sirotenko, D. Smith, N. Starkov, H. Stoecker, J. Sulkimo, M. Takahata, S. Tanaka, E. Tcherniaev, E. Safai Tehrani, M. Tropeano, P. Truscott, H. Uno, L. Urban, P. Urban, M. Verderi, A. Walkden, W. Wander, H. Weber, J. Wellisch, T. Wenaus, D. Williams, D. Wright, T. Yamada, H. Yoshida, D. Zschiesche, Geant4 - a simulation toolkit, Nuclear Instruments and Methods in Physics Research Section A: Accelerators, Spectrometers, Detectors and Associated Equipment 506 (3) (2003) 250–303. doi:10.1016/S0168-9002(03)01368-8.

[65] Guide for physics lists, Cancer Rev7.1 (Realese 11.1) (Apr. July 31st, 2023).

[66] A. Miller, R. Machrafi, A. Fariad, Investigation of the labr3 scintillator response to heavy ions, Radiation Measurements 115 (2018). doi:https://doi.org/10.1016/j.radmeas.2018.06.009.

[67] R. Hamm, M. E. Hamm, Industrial Accelerators and Their Applications, 10.1142/7745, 2012.

[68] Buxton, V. George, Greenstock, L. Clive, W. Helman, Phillips, Ross, B. Alberta, Critical Review of rate constants for reactions of hydrated electrons, hydrogen atoms and hydroxyl radicals (OH/O in Aqueous Solution, Journal of Physical and Chemical Reference Data 17 (2) (1988) 513–886. arXiv:https://pubs.aip.org/aip/jpr/article-pdf/17/2/513/11730413/513_1_online.pdf, doi:10.1063/1.555805.
URL https://doi.org/10.1063/1.555805

[69] S. Salvador, et al, Timing performances of a time-of-flight detection system for the fracas large acceptance mass spectrometer, Journal of Applied Physics (2020). doi:10.1088/1748-0221/15/03/T03004.

[70] Rw3 slab phantom (may 2024).

[71] S. Biondi, et al., The fragmentation of target experiment (foot) and its daq system, IEEE REAL TIME CONFERENCE (2020). doi:https://doi.org/10.48550/arXiv.2010.16251.

[72] A. Koning, D. Rochman, J.-C. Sublet, N. Dzysiuk, M. Fleming, S. van der Marck, Tendl: Complete nuclear data library for innovative nuclear science and technology, Nuclear Data Sheets 155 (2019) 1–55.
URL https://doi.org/10.1016/j.nds.2019.01.002

[73] M. Abadi, A. Agarwal, P. Barham, E. Brevdo, Z. Chen, C. Citro, al., TensorFlow: Large-scale machine learning on heterogeneous systems, software available from tensorflow.org (2015).
URL https://www.tensorflow.org/

[74] F. Chollet, et al., Keras, https://keras.io (2015).

[75] C. Finck, Y. Karakaya, V. Reithinger, R. Rescigno, J. Baudot, J. Constanzo, D. Juliani, J. Krimmer, I. Rinaldi, M. Rousseau, E. Testa, M. Vanstalle, C. Ray, Study for online range monitoring with the interaction vertex imaging method, Physics in Medicine and Biology 62 (11 2017). doi:10.1088/1361-6560/aa954e.

[76] R. Siegel, K. Miller, A. Jemal, Cancer statistics, CA Cancer J Clin. 2020 (2020).

[77] World health organization.global cancer observatory. (2024).
URL https://gco.iarc.fr/

[78] W. Travis, E. Brambilla, A. Nicholson, et al., The 2015 world health organization classification of lung tumors: impact of genetic, clinical and radiologic advances since the 2004 classification., J Thorac Oncol. (2015).

[79] W. Travis, E. Brambilla, A. Burke, et al., Who classification of tumours of the lung, pleura, thymus and heart., th ed. Lyon, France: International Agency for Research on Cancer (2015).

[80] National comprehensive cancer network. nccn clinical practice guidelines in oncology: Non-small cell lung cancer. version 5.2021.
URL https://www.nccn.org/professionals/physician_gls/default.aspx#nscl

[81] C. Bert, E. Rietzel, 4d treatment planning for scanned ion beams., Radiotherapy and Oncology, 86(2), 209-217. (2007).

[82] Y. Seppenwoolde, et al., Precise and real-time measurement of 3d tumor motion in lung due to breathing and heartbeat, measured during radiotherapy., International Journal of Radiation Oncology, Biology, Physics, 53(4), 822-834. (2002).

[83] K. Parodi, W. Enghardt, Potential application of pet in quality assurance of proton therapy., Physics in Medicine and Biology, 45(11), N151-N156. (2000).

[84] S. Minohara, T. Kanai, M. Endo, K. Noda, Respiratory gated irradiation system for heavy-ion radiotherapy., International Journal of Radiation Oncology, Biology, Physics, 47(4), 1097-1103. (2000).

[85] J. W. Wong, M. B. Sharpe, D. A. Jaffray, V. R. Kini, J. M. Robertson, J. S. Stromberg, A. A. Martinez, The use of active breathing control (abc) to reduce margin for breathing motion., International Journal of Radiation Oncology, Biology, Physics, 44(4), 911-919. (1999).

[86] A. E. Lujan, E. W. Larsen, J. M. Balter, R. K. T. Haken., A method for incorporating organ motion due to breathing into 3d dose 518 calculations., Med. Phys., 26(5):715–720 (1999). doi:10.1118/1.598577.

[87] C. Finck, et al., Study for online range monitoring with the interaction vertex imaging method., 502 Phys. Med. Biol., 62(24):9220 (2017). doi:50310.1088/1361-6560/aa954e.

[88] C. Reidel, C. Finck, C. Schuy, M. Rovituso, U. Weber, Alignment procedure of silicon pixel detectors for ion-beam therapy applications., Nucl. Instrum. Meth. A, 931:142–150 (2019). doi:10.1016/j.nima.2019.03.042.

[89] M. Krämer, et al., Treatment planning for heavy-ion radiotherapy: physical beam model and dose optimization., Phys. Med. Biol., 45(11): 528 3299 (2000). doi:10.1088/0031-9155/45/11/313.

[90] Opengate version 10.
URL https://opengate-python.readthedocs.io/en/latest/index.html

Lévana GESSON

Données nucléaires pour la hadronthérapie

Résumé

La hadronthérapie, incluant la thérapie par ions lourds et protons, améliore le traitement du cancer en ciblant précisément les tumeurs tout en minimisant les dommages aux tissus sains. Cependant, les particules secondaires produites pendant le traitement influencent la distribution de dose, impactant l'efficacité et la sécurité. Cette thèse explore la production et l'impact de ces particules, et leur rôle dans la distribution de dose. Les calculs de dose reposent sur des simulations Monte Carlo, mais le manque de données expérimentales sur les réactions nucléaires limite leur précision. Le projet CLINM a pour but de combler ces lacunes en caractérisant les particules secondaires à l'aide d'un télescope ΔE-E. Des expériences menées au CNAO en 2023 ont révélé des écarts entre les données expérimentales et les simulations Geant4, surtout pour les particules d'hélium. L'algorithme DINo a été développé comme outils complémentaire pour améliorer la précision des prédictions de réactions nucléaires. Enfin, un dispositif de suivi CMOS a été créé pour améliorer la précision du traitement du cancer du poumon en suivant la densité tissulaire, soulignant le besoin de caractérisation et de technologies avancées en thérapie par particules.

Mots-clés : Hadronthérapie, Thérapie par ions lourds, Particules secondaires, Calcul de dose, Simulations Monte Carlo, Réactions nucléaires, scintillateur, Algorithme d'apprentissage profond, CMOS.

Résumé en anglais

Particle therapy, including heavy ion and proton therapy, advances cancer treatment by precisely targeting tumors while minimizing damage to healthy tissues. However, secondary particles produced during treatment affect dose distribution, impacting efficacy and safety. This thesis explores the production and impact of these particles, emphasizing their role in dose distribution. Dose calculations rely on Monte Carlo simulations, but limited experimental data on nuclear reactions reduces accuracy. The CLINM project addresses these gaps by characterizing secondary particles using a ΔE-E telescope. Experiments at the CNAO center in 2023 showed discrepancies between experimental data and Geant4 simulations, especially for helium particles. To enhance nuclear reactions prediction accuracy, the DINo algorithm was developed as a complementary tool, improving dose calculations. A CMOS tracking device was also created to enhance treatment precision for lung cancer by tracking tissue density, underscoring the need for advanced characterization and technologies in particle therapy.

Keywords : Hadrontherapy, Heavy ion therapy, Secondary particles, Dose calculation, Monte Carlo simulations, Nuclear reactions, scintillator, Deep learning algorithm, CMOS.